

AN ABSTRACT OF THE THESIS OF

Thomas L. George for the degree of Doctor of Philosophy in Mechanical Engineering presented on December 10, 1982

Title: A Model for the Mechanical Behavior of Irradiated Mixed Carbide Sphere Pac Fuel Pins

Abstract approved: Redacted for Privacy  
T. C. Kennedy, K.L. Peddicord

A model is developed that allows the prediction of the stress-strain distribution in a mixed carbide sphere pac fuel pin during irradiation. The model is coupled with a previously developed model for the thermal behavior of the pin. The one-dimensional (radial at various axial locations) solution is for quasi-steady pin operating conditions.

Generalized plane strain is assumed for the fuel and cladding separately so that slip at the fuel-cladding interface can be accommodated. The elasto-plastic equations are solved including elastic-plastic transition and unloading. A finite element solution scheme is used with an incremental approach to linearize the equations. The nonlinear effects of elastic and plastic material property changes are included. Elastic, plastic, creep, swelling, and thermal strains are considered separately in the analysis.

The elastic and plastic properties depend on the material properties of the spheres themselves and the geometry of the packed bed. The bed geometry changes during irradiation from a cohesionless random sphere array to a form resembling porous pellet fuel. Analytic expressions are derived for the fuel elastic constants and the yield strength parameters as functions of the bed geometry and the sphere material properties. Good agreement between available experimental data and the analytic prediction is observed.

The models used for the fuel creep and swelling are described. The fuel creep strain includes the standard deviatoric component along with a volumetric component to model the fuel densification as the geometry changes. Swelling is based on available correlations.

The numerical solution scheme as implemented in the SPECKLE-III code is discussed and results are presented for the simulation of a sphere pac pin irradiation experiment. The code predictions are in good agreement with post-irradiation examination results.

A Model for the Mechanical Behavior of  
Irradiated Mixed Carbide Sphere Pac Fuel Pins

by

Thomas L. George

A THESIS

submitted to

Oregon State University

in partial fulfillment of  
the requirements for the  
degree of

Doctor of Philosophy

Completed December 10, 1982

Commencement June 1983

APPROVED:

Redacted for Privacy

Professor of Mechanical Engineering in charge of major

Redacted for Privacy

Professor of Nuclear Engineering, second thesis advisor

Redacted for Privacy

Head of Department of Mechanical Engineering

Redacted for Privacy

Dean of Graduate School

Date thesis is presented December 10, 1982

Typed by Peggy Snyder and Cathy Darby for Thomas L. George

## ACKNOWLEDGEMENT

This research and thesis would not have been completed without the support and assistance of many people, a few of whom are mentioned here. I would like to thank my thesis advisors, Drs. Tim Kennedy and Lee Peddicord. Their many helpful suggestions and support are greatly appreciated.

Funding for this research supplied by the Swiss Federal Institute for Reactor Research, Fuel Development Program under the direction of R. W. Stratton, is gratefully acknowledged. Appreciation is also expressed to Dr. Don Trent and Battelle, Pacific Northwest Laboratory for financial support during my leave of absence.

I am deeply indebted to Peggy Snyder and Cathy Darby for putting this thesis in its present form.

Finally, I thank my wife, Joni, for her constant love and support that sustained me throughout this research.

TABLE OF CONTENTS

1.0	INTRODUCTION.....	1
1.1	SPHERE PAC FUEL PIN DESCRIPTION.....	4
1.2	SPHERE PAC FUEL PIN IRRADIATION BEHAVIOR.....	4
1.3	REVIEW OF PIN MODELING CODES.....	14
1.4	RESEARCH OBJECTIVES.....	15
2.0	ELASTO-PLASTIC EQUATIONS.....	18
3.0	STRESS-STRAIN RELATIONSHIPS.....	27
3.1	BACKGROUND.....	27
3.2	UNIT CELL.....	33
3.3	ELASTIC CONSTANTS FOR AN ISOTROPE MADE UP OF ANISTROPIC PARTS.....	37
3.4	UNIT CELL STRESS-STRAIN RELATIONSHIP.....	44
3.5	ELASTIC CONSTANTS FOR A RESTRUCTURING RANDOM PACKED BED OF UNIFORM SPHERES.....	53
3.6	COMPARISON WITH EXISTING MODELS AND EXPERIMENTAL DATA....	55
3.7	ELASTIC PROPERTIES FOR A BINARY ARRAY.....	62
3.8	ELASTIC PROPERTIES FOR RESTRUCTURED FUEL.....	76
4.0	CONSTITUTIVE RELATIONS FOR SPHERE PAC FUEL.....	78
4.1	PLASTIC CONSTITUTIVE EQUATIONS FOR GRANULAR MEDIA.....	78
4.1.1	Plastic Yield Functions.....	78
4.1.2	Plastic Potential Function.....	86
4.1.3	Micromechanical Models.....	87
4.1.4	Application to Restructuring Sphere Pac Fuel....	89

4.2	FRICTIONAL YIELDING.....	90
4.2.1	Cohesion of a Restructuring Fuel Bed.....	93
4.2.2	Binary Array Shear Strength.....	101
4.2.3	Shear Strain Ratio of Unrestructured Fuel.....	107
4.2.4	Internal Friction Angle for Unrestructured Fuel.....	108
4.2.5	Frictional Yield Parameters for Binary Sphere Array.....	108
4.2.6	Plastic Potential Function for Frictional Yielding.....	109
4.3	HYDROSTATIC YIELDING.....	111
4.3.1	Neck Growth and Shrinkage Associated with Hydrostatic Yielding.....	114
4.3.2	Neck Growth and Shrinkage in the Small Sphere Array due to Plastic Flow.....	115
4.4	YIELD STRESS OF (U,PU)C.....	116
4.5	PLASTIC MODULUS MATRIX.....	119
5.0	INITIAL STRAINS FOR SPHERE PAC FUEL.....	120
5.1	FUEL THERMAL STRAIN RATE.....	120
5.2	FUEL CREEP AND SHRINKAGE RATE.....	120
5.2.1	Restructured Fuel Creep.....	121
5.2.2	Creep Strain Components.....	124
5.2.3	Restructuring Fuel Shrinkage.....	126
5.3	FUEL SWELLING.....	129
5.4	NONLINEAR ELASTIC STRAIN RATE.....	133
5.4.1	Restructuring Fuel Nonlinear Elastic Strain Rate.....	134
5.4.2	Restructured Fuel Nonlinear Elastic Strain Rate.....	139

6.0	CLADDING MECHANICAL MODELS.....	140
6.1	CLADDING ELASTIC STRESS-STRAIN RELATION.....	140
6.2	CLADDING PLASTIC CONSTITUTIVE RELATION.....	141
6.3	INITIAL STRAIN RATE.....	142
7.0	NUMERICAL SOLUTION.....	145
7.1	FUEL AND CLADDING ELEMENT STIFFNESS EQUATION.....	147
7.2	INTERFACE ELEMENT STIFFNESS EQUATION.....	153
7.3	STIFFNESS EQUATION ASSEMBLAGE AND SOLUTION.....	162
7.4	STRESS AND STRAIN RATES.....	165
7.5	ELASTIC-PLASTIC TRANSITION.....	166
7.6	ADDITIONAL TIME STEP LIMITS.....	168
7.7	TIME INTEGRATION.....	169
7.8	CODE LAYOUT.....	171
7.9	CODE VERIFICATION.....	173
8.0	CODE APPLICATION.....	174
9.0	CONCLUSIONS AND RECOMMENDATIONS.....	187
9.1	RECOMMENDATIONS FOR FUTURE WORK.....	192
	BIBLIOGRAPHY.....	194
	APPENDICES 202	
	APPENDIX A.....	203
	APPENDIX B.....	219
	APPENDIX C.....	226

LIST OF FIGURES

	<u>Page</u>
FIGURE 1.1	Conceptual Diagram of an Unirradiated Sphere Pac Fuel Pin.....6
FIGURE 1.2	Conceptual Diagram of an Irradiated Sphere Pac Fuel Pin.....9
FIGURE 1.3	Interaction of Phenomena Occurring During Irradiation of a Sphere Pac Fuel Pin.....13
FIGURE 2.1	Coordinate System for Fuel Pin Analysis.....19
FIGURE 3.1	Schematic for Two Spheres in Contact.....29
FIGURE 3.2	Random Sphere Array Unit Cell.....34
FIGURE 3.3	Predicted Coordination Number Using the Unit Cell.....36
FIGURE 3.4	Coordinate System for Rotating Unit Cell.....39
FIGURE 3.5	Unit Cell Oriented in Stress Field $\{\sigma\}$ .....45
FIGURE 3.6	Effective Young's Modulus Versus Confining Pressure for a Random Array of Uniform Spheres.....54
FIGURE 3.7	Effective Poisson's Ratio Versus Confining Pressure for a Random Array of Uniform Spheres.....54
FIGURE 3.8	Effective Young's Modulus Versus Neck Ratio for a Random Array of Uniform Spheres.....56
FIGURE 3.9	Effective Poisson's Ratio Versus Neck Ratio for a Random Array of Uniform Spheres.....56
FIGURE 3.10	Elastic Property Model Comparison with Sonic Velocity in a Regular Sphere Array.....59
FIGURE 3.11	Elastic Property Model Comparison with Random Sphere Array Shear Modulus Versus Void Ratio.....61
FIGURE 3.12	Elastic Property Model Comparison with Random Sphere Array Shear Modulus Versus Confining Pressure.....61

FIGURE 3.13	Schematic Diagram of Binary Sphere Array.....	63
FIGURE 3.14	Effective Young's Modulus Versus Neck Ratio for a Binary Sphere Array.....	71
FIGURE 3.15	Effective Poisson's Ratio Versus Neck Ratio for a Neck Ratio for a Binary Sphere Array.....	71
FIGURE 3.16	Young's Modulus for Restructured Fuel as a Function of the Initial Porosity.....	73
FIGURE 3.17	$d\sigma_w/d\sigma_h$ Versus Small Sphere Neck Ratio.....	73
FIGURE 3.18	Young's Modulus for Restructuring Fuel with Shrinkage of Small Sphere Array.....	75
FIGURE 3.19	Poisson's Ratio for Restructuring Fuel with Shrinkage of Small Sphere Array.....	75
FIGURE 4.1	Stress-Strain Behavior of Granular Materials.....	79
FIGURE 4.2	Mohr-Coulomb and Drucker-Prager Yield Surfaces on the Octahedral Plane.....	83
FIGURE 4.3	Capped Yield Surfaces for Frictional Material....	84
FIGURE 4.4	Coordinate System for Rotations of the Unit Cell.....	94
FIGURE 4.5	Schematic of Four Spheres in Contact Oriented in a Shear Field.....	95
FIGURE 4.6	Schematic of Neck Region with Maximum Shear Plane and $\omega$ -Plane Orientation; Mohr's Circle for Neck Region Stress.....	99
FIGURE 4.7	Cohesion of a Single Size Sphere Array.....	101
FIGURE 4.8	Schematic Showing Relation Between Binary and Small Sphere Array Plastic Shear Strain....	102
FIGURE 4.9	Binary-to-Small Sphere Array Plastic Shear Strain Ratio.....	109
FIGURE 4.10	Binary Sphere Array Strength Parameters for Frictional Yielding.....	110
FIGURE 4.11	Capped Yield Surface for Sphere Pac Fuel.....	112

FIGURE 4.12	Fracture and Flow Stress for (U,Pu)C.....	117
FIGURE 5.1	Swelling of (U,Pu)C at Constant Temperature.....	132
FIGURE 5.2	Comparison of Two-Points Quadrature Formula and Simpson's Rule for Integration of Equation 5.37.....	138
FIGURE 7.1	Elements for Fuel Pin Modeling.....	146
FIGURE 7.2	Fuel or Cladding Ring Element.....	148
FIGURE 7.3	Fuel-Cladding Centerface Element.....	155
FIGURE 7.4	Yield Surface for Interface Element.....	158
FIGURE 7.5	SPECKLE-III Flow Diagram.....	172
FIGURE 8.1	D3P12 Centerline Temperature Stress History.....	178
FIGURE 8.2	D3P12 Inner and Outer Fuel Hydrostatic Stress History.....	178
FIGURE 8.3	D3P12 Radial Profiles of Small Sphere Neck Ratio.....	179
FIGURE 8.4	D3P12 Gas Pressure History.....	179
FIGURE 8.5	D3P12 Axial Strain History.....	180
FIGURE 8.6	D3P12 Hoop Stress History.....	180
FIGURE 8.7	D3P12 Cladding Tangential Strain History.....	181
FIGURE 8.8	D3P12 EOI Radial Temperature and Porosity Profiles.....	182
FIGURE A.1	Thermal-Elastic Check Problem Geometry.....	205
FIGURE A.2	Comparison of Analytic and SPECKLE-III Solutions for Tangential Stress in Thermal- Elastic Check Problem.....	214
FIGURE A.3	Comparison of Analytic and SPECKLE-III Solutions for Axial Strain in Thermal- Elastic Check Problem.....	214
FIGURE A.4	Elastoplastic Check Problem Geometry.....	215

FIGURE A.5	Comparison of Hodge and White and SPECKLE-III Solution for Elastoplastic Check Problem.....	217
FIGURE B.1	Schematic Diagram of Triaxial Compression Test Equipment.....	220
FIGURE B.2	Load Deflection Behavior for a Typical Triaxial Compression Test on a Random Array of Uniform Steel Spheres.....	222
FIGURE B.3	Mohr-Coulomb Envelopes for Triaxial Compression Tests on Sphere Arrays.....	225
FIGURE C.1	Coordinate System for Derivation of Equation 3.7.....	228
FIGURE C.2	Coordinate System for Derivation of Equation 3.12.....	228
FIGURE C.3	Random Sphere Array Unit Cell.....	235

## LIST OF TABLES

	<u>Page</u>
TABLE 3.1	Shrinkage and Neck Ratios Values for the Curves on Figures 3.18 and 3.19.....74
TABLE 3.2	Porosity and Temperature Effects on Elastic Properties of UC.....76
TABLE 8.1	DID03, Pin 12 Physical Characteristics.....175
TABLE 8.2	DID03, Pin 12 Assumed Irradiation History.....176
TABLE A.1	Parameters for Thermal-Elastic Check Problem.....213
TABLE A.2	Plasticity Problem Parameters.....216
TABLE B.1	Triaxial Compression Tests.....223

# A MODEL FOR THE MECHANICAL BEHAVIOR OF IRRADIATED MIXED CARBIDE SPHERE PAC FUEL PINS

## 1.0 INTRODUCTION

The safe and economical operation of a fast breeder reactor (FBR) is greatly influenced by the materials and design of the fuel pins. A pin consists of a cylindrical tube enclosing the reactor fuel and a plenum region to accommodate released gaseous fission products. From a safety standpoint the cladding represents the first barrier to contain the radioactive fuel and fission gases, and therefore the cladding integrity is a primary concern in the pin design. The economical operation of the reactor requires that the pin withstand high temperatures to maximize thermal efficiency, and high fluences to allow longer periods between reloading. It is also desirable to keep the cladding thickness as small as possible to reduce the overall core material requirements and the parasitic absorption of neutrons.

There are a variety of material and geometry choices for the fuel and cladding, each having particular qualities that make them attractive from an economic or safety viewpoint. To determine acceptable design parameters for various material choices, it is necessary either to run experiments covering the range of expected reactor steady-state and transient conditions or to use mathematical models to predict the behavior of a fuel pin during its in-reactor lifetime. The experimental method, though accurate and conclusive, is very expensive and time consuming. The mathematical model approach is an alternative that can provide useful design criteria as well as insight to the pin behavior. However, it is necessary to demonstrate that the model is in reasonable agreement with experimental results.

The present work is directed toward a more complete mathematical model for one particular fuel type (mixed carbide sphere pac). Previous work by Ades (1979) modeled the thermal behavior of sphere pac fuel. This model is herein extended to include the mechanical

response of an irradiated sphere pac pin. The mechanical model provides the fuel hydrostatic stress required in several of the thermal model components. It also predicts the cladding stresses and strains that are required to determine pin lifetimes. The thermal and mechanical models are so closely inter-related that a reasonable fuel pin model cannot be formulated without treating the two effects simultaneously.

Most FBR pins in use today employ a mixed oxide fuel  $[(U,Pu)O_2]$  in a 20% CW 316 stainless steel cladding. The mixed oxide fuel was chosen based on its high burnup potential and its known in-reactor behavior from experience in thermal reactor applications. The stainless steel cladding was chosen mainly because of its strength characteristics at high temperatures. There are other fuel and cladding combinations (known as advanced fuels and advanced claddings) that could lead to significant improvement in the economics and safety of FBR operation. Among the advanced fuels are the mixed carbides -  $[(U,Pu)C]$ , carbonitrides  $[(U,Pu)CN]$ , nitrides  $[(U,Pu)N]$ , and metal fuels. The advantage of the advanced fuels is due largely to their higher thermal conductivity, that allows higher linear power ratings, and to their shorter doubling time resulting from the lower specific fissile inventory and higher breeding gain (Waltar and Reynolds, 1981). These fuels are at a disadvantage, however, by their increased swelling due to retention of fission products. A variety of stainless steel alloys are being evaluated for use as FBR fuel pin cladding. Reduced swelling at high fluences is the main advantage of these advanced alloys.

The overall pin performance is also influenced by the fuel geometry. Usually the fuel is formed in sintered cylindrical pellets (90-95% TD) designed so that some nominal gap exists between the fuel and the cladding at room temperature. This gap is necessary to accommodate some of the differential thermal expansion of the fuel and cladding and to increase the initial pin average (smear) porosity so that some of the swelling due to fission products can be taken up

within the fuel. At some time after reactor startup, the initial gap closes and the resulting fuel-cladding mechanical interaction (FCMI) becomes an important phenomena that can determine the lifetime of the pin. Large cladding strains resulting from FCMI may lead to pin failure by a breach of the cladding or excessive cladding strain.

Vibro fuels are being investigated as an alternative fuel geometry. These fuels consist of either small irregular fuel particles (VIPAC fuel) or microspheres of various sizes (sphere pac). The pins are manufactured by loading the fuel particles into the cladding and vibrating the pin to ensure uniform and dense packing. In the case of FBR sphere pac fuel, the spheres are of two sizes mixed together so that packing densities around 75-80% TD are obtained. Besides providing a simpler and cleaner pin manufacturing process (Stratton, 1977), there is evidence that the sphere pac geometry has less detrimental FCMI than pellet pins of similar smear density (Fitts and Miller, 1974; Barner, et al., 1981; Smith, et al., 1974, 1977; Bart, 1982). This is especially beneficial for the advanced fuels that are prone to higher swelling rates.

A model for predicting the behavior of sphere pac mixed carbide fuels under steady-state operating conditions is described in this work. In the remainder of this first chapter the physical characteristics are given. The important phenomena occurring during irradiation are described including their interactions, and related modeling work is reviewed. The chapters that follow concentrate on the mechanical model for the sphere pac fuel pin including the governing equations, elastic and plastic constitutive relations, creep, swelling, sintering, and other important phenomena in the fuel and cladding. The numerical scheme used to solve the coupled thermal-mechanical model is described, and the results of the numerical simulations of a sphere pac fuel pin irradiation experiment are presented. Finally, some conclusions are drawn as to the model's strengths and weaknesses and recommendations are made for further experimental and analytic investigations.

## 1.1 SPHERE PAC FUEL PIN DESCRIPTION

The physical characteristics of a sphere pac fuel pin given in this section are taken from the more complete description by Ades (1979). The fuel microspheres are manufactured by the Swiss Federal Institute for Reactor Research (EIR) using a wet gelation process (Stratton, 1977). The fuel consists of two sphere sizes, the larger having diameters between 600 and 800 microns and the smaller in the range 40 to 60 microns. The smaller spheres are small enough to easily infiltrate a packed bed of large spheres. The mixed carbide fuel, (U, Pu)C, is usually produced with the heavy metal atoms consisting of 85% uranium and 15% plutonium. The spheres have nominally about 94% of the fuel theoretical density. The grain diameters of the smaller spheres range between 5 and 20 microns while those of the large spheres are between 20 and 60 microns.

For most of the experiments run so far, the cladding used was AISI M 316 stainless steel, 20% cold worked. A solid UC pellet is usually placed at the sealed end of the cladding before filling with the fuel spheres. The filled pin is vibrated resulting in fuel smear densities between 75% and 80% TD. Another UC pellet is placed at the top of the fuel column and a light retaining spring inserted to hold the fuel in place during shipping and handling. A gas plenum volume is included in the pin (usually above the fueled region) to provide space for the fission gas released during irradiation. The plenum and the void space in the fuel region are filled with helium at just above atmospheric pressure before sealing the cladding. The pin dimensions differ for the various experiments, but usually the outside cladding diameter is about 8 mm with a wall thickness of about 0.5 mm.

## 1.2 SPHERE PAC FUEL PIN IRRADIATION BEHAVIOR

The behavior of a sphere pac fuel pin during irradiation is briefly described in this section to provide an understanding for some

of the assumptions made in the model. Many complex and interacting phenomena are involved in the thermal-mechanical response of a fuel pin and none of them can be fully described without referring to others. Therefore, there is no way of ordering this discussion so that only previously defined concepts are referred to. In an attempt to order the phenomena, the following is a list of the most important phenomena as they occur chronologically during irradiation (keeping in mind that, at least to some extent, all the processes can occur simultaneously).

1. A conceptual diagram of the unirradiated sphere pac fuel is shown in Figure 1.1. The small microspheres are packed into the interstitial spaces of the large sphere array. The cross section shown does not pass through the equator of all the large spheres, giving the appearance that there are more than two sphere sizes.
2. As the reactor is brought to full power, the fission process begins to generate heat in a fresh sphere pac fuel pin. The heat density depends on the magnitude of the flux and the local fuel density, burnup, and chemical composition of the fuel. The resulting temperature profile depends on the fuel and cladding conductivity, the coolant temperature, and the heat density. As the reactor power rises the fuel temperature increases due to the increased fission rate and the rising coolant temperature.
3. The thermal expansion coefficients for the fuel and the cladding are about equal, but the higher fuel temperatures result in higher thermal expansion rates for the fuel. The interaction between the fuel and the cladding puts the fuel under a compressive load. If the fuel does not slip at the fuel-cladding interface, the cladding will be subject to axial tensile stress as well as the radial and tangential stress resulting from the internal radial pressure exerted by the fuel. Due to the radial temperature variation in the fuel and the no-slip condition at the interface, the fuel is put in some deviatoric stress state (the stress state less the hydrostatic stress). The

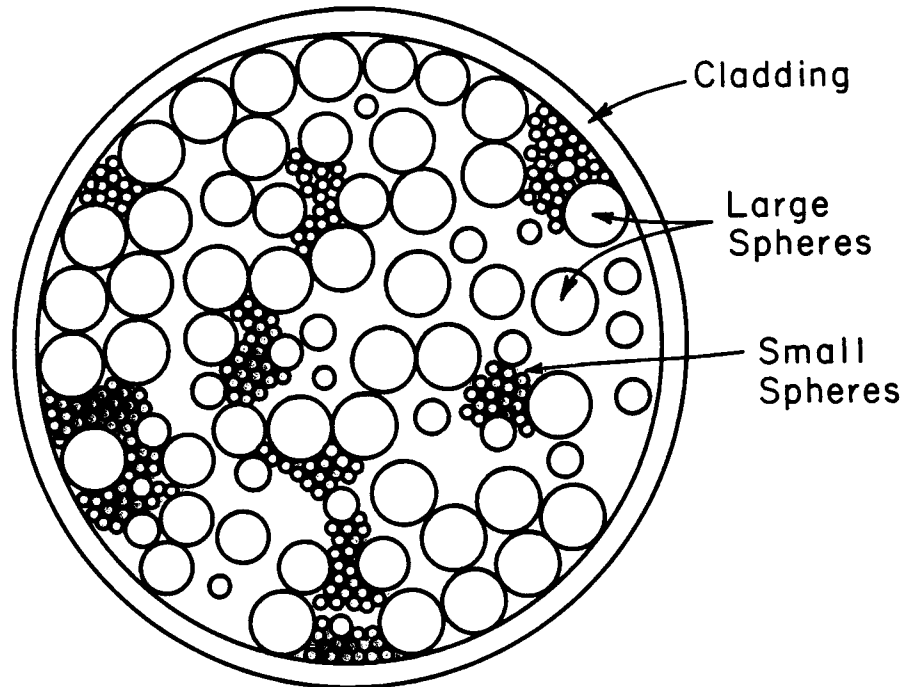


FIGURE 1.1. Conceptual Diagram of an Unirradiated Sphere Pac Fuel Pin

unrestructured sphere pac fuel, like any granular material, can support a shear load proportional only to the compressive hydrostatic stress. This implies that there is the potential for plastic flow in the fuel from the very beginning of the reactor startup. Plastic flow may also occur under hydrostatic compression because of the large contact stresses developed.

4. The high fuel temperatures and compressive loads on the sphere pac fuel results in the formation of neck regions between adjacent spheres (initial stage restructuring). The neck results from the migration of atoms by various mechanisms from the contact region or the free surfaces of the sphere. The necks have an important influence on the thermal and mechanical properties of the fuel. Before the necks are established most of the heat transfer in the fuel takes place through the gas occupying the voids between the

spheres. As the necks grow, more heat passes through the contact region, and the effective thermal conductivity is increased. The necks also make the bed elastically stiffer and increase the shear strength. If the neck growth mechanism takes atoms from the contact region, the sphere centers approach one another. This effectively shrinks the sphere bed, relieving some of the compressive stress imposed by the cladding. There is a negative feedback in this restructuring phenomena since the two driving forces (temperature and compressive stress) are reduced as the process continues. Another restructuring phenomena that occurs simultaneously is grain growth. At high temperatures, grains with convex boundaries are eliminated as their atoms pass across the boundaries to the more stable concave boundaries of larger grains. [See Ades (1979) and Matthews (1979) and Section 5.2 of this report for discussions on restructuring in mixed carbide sphere pac fuel.]

5. As the fuel temperature increases the temperature and, therefore, pressure of the free gas in the plenum and fuel void space increases. This tends to increase the effective thermal conductivity of the fuel bed and is an additional force acting on the cladding.
6. The fission events leave fission products (stable gas atoms and solid fission products) that accumulate in the fuel grains. The solid fission products result in immediate swelling of the fuel grains and therefore create additional FCMI. The gas atoms diffuse through the grains and collect in bubbles or existing pores in the fuel. The size of the pores and bubbles may be influenced by the hydrostatic stress in the fuel. Eventually the bubbles grow to such a size that they contribute significantly to the swelling of the fuel. The swelling is a function of fuel temperature and burnup.

7. The deviatoric stresses developed in the fuel and cladding are relieved to some extent by creep. Thermal and dislocation creep is important at high temperatures, but significant creep also occurs at low temperatures due to the fission process. In the cladding this fission-induced creep is the dominant mechanism. If the stresses are high enough, plastic flow may occur in the cladding. The cladding is also subject first to some initial densification and then to swelling resulting from the neutron flux.
8. In the central hotter region of the fuel, necks between spheres continue to grow and eventually begin to interfere with one another, marking the end of initial stage sintering. At this point the thermal mechanisms for neck growth rate begin to increase and closed pores are formed at the sphere interstitial spaces. The central region of the sphere pac fuel no longer looks like a sphere bed but rather like a porous pellet and, as such, has the thermal and mechanical properties of pellet fuel. The newly formed pores become more spherical in shape as they migrate up the temperature gradient toward the center of the pin. The fuel may continue to densify by hot pressing mechanisms. Figure 1.2 is a conceptual diagram of the sphere pac fuel when it has restructured to this extent. Blank (1977) has described the restructuring in mixed carbide pellet fuel in terms of four fuel zones, each with distinct restructuring characteristics. The same zones can also be recognized in sphere pac fuel and are noted in Figure 1.2. The characteristics of each zone are given below.

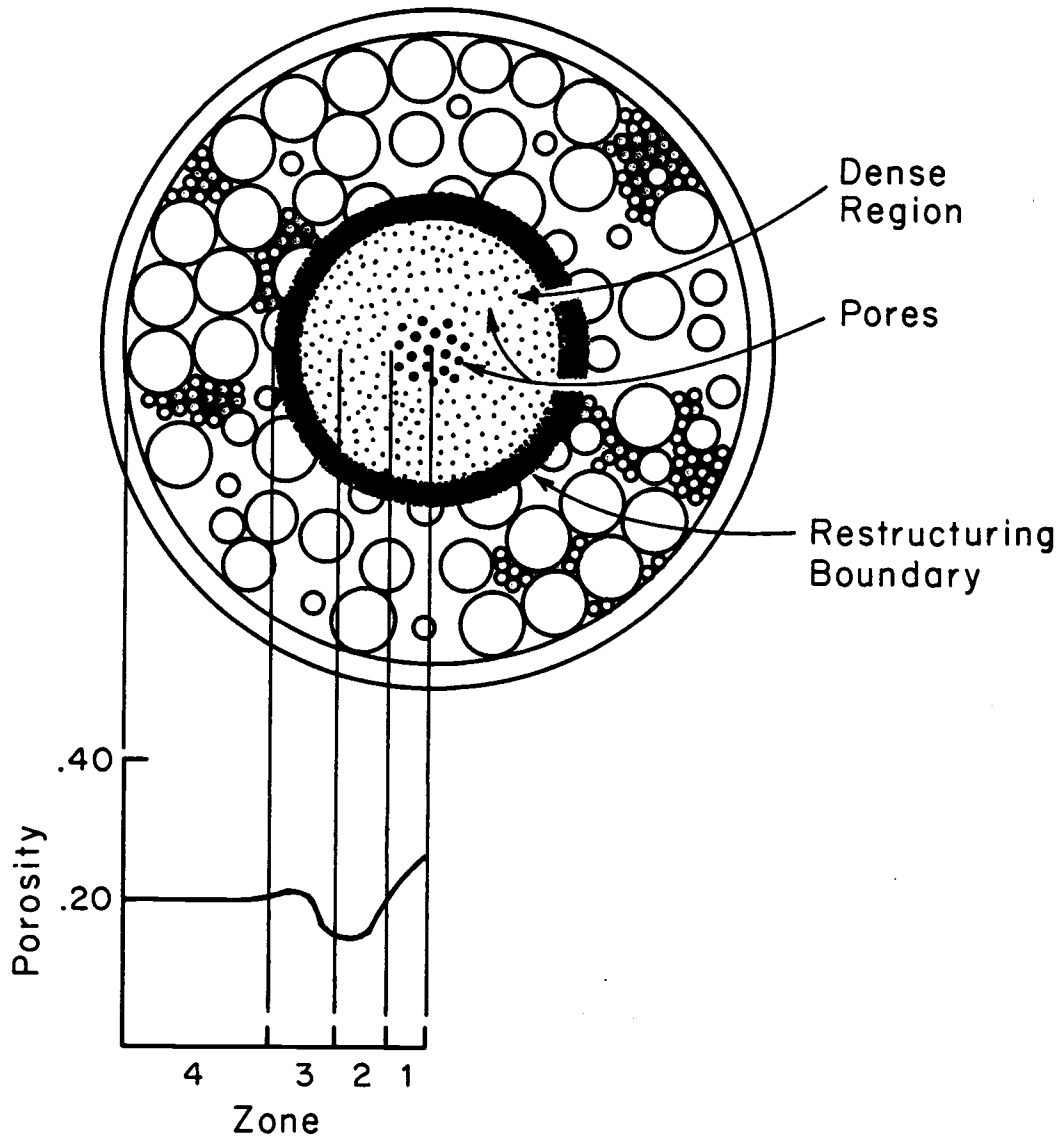


**FIGURE 1.2.** Conceptual Diagram of an Irradiated Sphere Pac Fuel Pin

- Zone I - This is the central region of the pin and fuel temperatures usually greater than 1300°C are needed for this zone to develop. The pores are large with diameters about the same as the grain diameter (20-50 $\mu$ m).
- Zone II - In this zone the pores and grains are large, but the pore diameter is less than the grain size. This region occurs at temperatures in the range 1150 to 1300°C, with slightly higher radial temperature gradients than in Zone I. The grains are elongated parallel to the temperature gradient. The porosity is less than the average initial fuel porosity since pores from this zone migrate into Zone I.
- Zone III - The outer edge of this zone corresponds to the outer edge of the restructured (pellet-like) region of the sphere pac fuel. The temperature is around 1100°C, and there is a heavy accumulation of fission gas on grain boundaries. The grains in this zone are equiaxed.
- Zone IV - In this zone the sphere pac fuel retains its particulate nature although there may be some neck growth between spheres. The grain structure and porosity are essentially the same as that for unirradiated fuel.
- The porosity profile associated with the depicted pin is also shown in Figure 1.2. In carbide fuel the central region may develop a large porosity, but no central hole develops as in oxide fuel. Whether or not all the zones develop in a given axial section of the fuel depends on the coolant temperature and linear power. In low power pins only Zones III and IV may be observed. The changes in porosity associated with the restructuring affect the thermal and mechanical properties of the fuel and the local heat generation.

9. The fission gas continues to accumulate in the fuel grain and diffuses into bubbles on grain boundaries. Small fission gas bubbles are swept up by migrating pores and bubbles and by moving grain boundaries. Eventually some of this gas is released from the fuel to the free gas. The introduction of fission gas into the free gas decreases the gas conductivity and, therefore, the effective fuel conductivity in the outer regions of the fuel where little restructuring occurs. This is partially offset by the conductivity increase due to increased gas pressure. The increased gas pressure also constitutes an additional load on the cladding.
10. The chemical components of the fuel can migrate from their initial location affecting the local power density. In mixed carbide fuel, plutonium has been observed to migrate down the temperature gradient (Kleykamp, 1977) resulting in a somewhat flattened radial temperature profile.
11. If the combined effects of the fuel shrinkage and cladding swelling are large enough, the radial load imposed on the cladding by the fuel may become small enough to allow slip at the interface. This affects the stress distribution in both the fuel and cladding. Further cladding swelling or fuel shrinkage could lead to an opening of a gap between the fuel and cladding, increasing the thermal resistance of the pin and causing the fuel temperature to increase.
12. The cladding mechanical properties are functions of the temperature and fluence. The stiffness and strength decrease with increasing temperature but increase with increasing fluence. If the cladding deforms plastically the effective yield strength increases slightly due to work hardening. The fuel mechanical properties are similarly affected by temperature.
13. If the accumulated inelastic strain in the cladding is large enough, then pin failure can occur through cladding rupture. The

cladding failure limit is given either by a maximum allowable inelastic strain or the cumulative damage function (CDF) that assigns a damage fraction for each period of time that the cladding operates at a given stress level and temperature. Failure is predicted when the cumulative damage fraction equals unity.

14. The thermal cycling resulting from normal reactor power cycles can also affect the mechanical performance of the pin. The cladding strength can be reduced by fatigue resulting from the cycling.
15. Finally, off-normal transients (undercooling, overpower, etc.) can result in premature pin failure due to large cladding stress and strains. The pin response during the transient depends on all of the pin conditions at the time of the transient as well as the particular imposed driving force (e.g., sudden rise in power).

This list represents the most important phenomena, either observed or postulated, occurring in a mixed carbide sphere pac fuel pin. There may be other phenomena that are equally important but not as yet identified. Figure 1.3 shows schematically the interaction of these phenomena. Only the direct influencing phenomena are indicated by arrows. An arrow with points at both ends indicates a direct feedback between two phenomena. The operating conditions and physical parameters (pin dimensions, etc.) influence all the phenomena in some way and are also included in the diagram.

Most of the phenomena are modeled using one or more differential equations so that the prediction of the overall pin thermal-mechanical behavior requires large computer codes and the development of such a code is one of the objectives of this research.

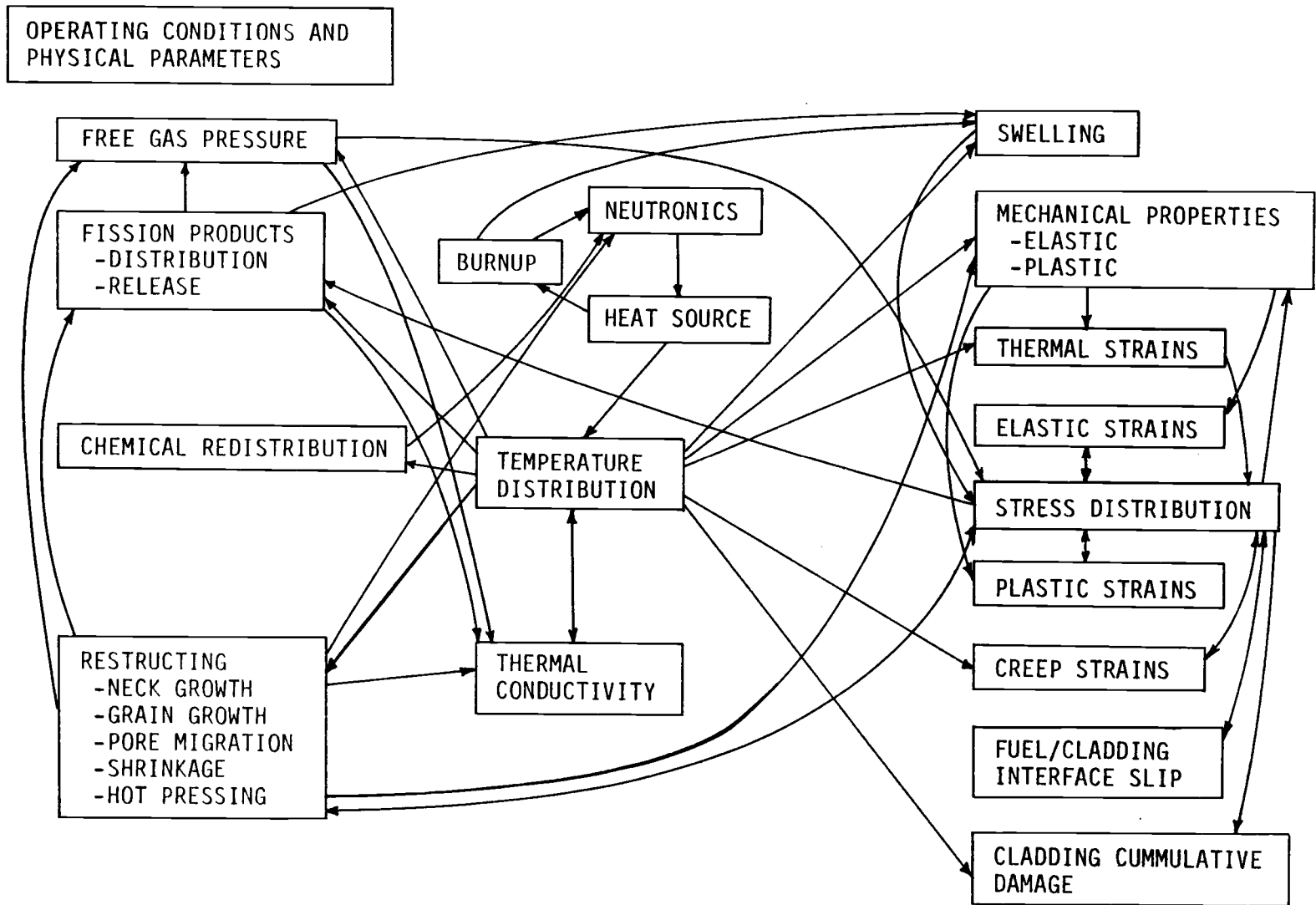


FIGURE 1.3. Interaction of Phenomena Occurring During Irradiation of a Sphere Pac Fuel Pin

### 1.3 REVIEW OF PIN MODELING CODES

A comprehensive review of codes developed to predict various aspects of fuel pin behavior is given by Ades and Peddicord (1978a, 1978b) and Ades (1979), so only a brief review is presented here with emphasis on the mechanical model. Most of the codes were developed for application to LMFBR oxide fuels in pellet form. The most comprehensive and widely used code in the U.S. is LIFE (Billone, et al., 1977). For the mechanical model the pin is divided into a number of annular rings and an analytic solution obtained for each ring that depends on the boundary conditions imposed by adjacent rings. The stress distribution throughout the fuel and cladding is obtained by solving for the interface loads and deformations. Generalized plain stress is assumed and the effects of creep, fuel cracking, and fuel-cladding slip are included. The CYGRO (Newman, et al., 1977) code solves the same equation set as LIFE but uses a finite-element method. In Germany the SATURN (Kummerer, et al., 1971) and URANUS (Lassman, 1977) codes have been developed and have capabilities similar to LIFE. There are several codes, including COMETHE (Godesar, et al., 1970) and DEFORM (Merckx, 1968) that treat most of phenomena modeled in LIFE but incorporate more empiricism for some of the models (e.g., swelling and gas release). There are also codes available that are concerned with only one or more aspects of the pin behavior. In particular the CRASH (Guyette, 1970) code models only the cladding and requires the fuel radial dimension or pin internal gas pressure from another code.

Modifications have been made to some of the above codes to make them applicable to carbide pellet fuel. The LIFE-4C (Liu and Zawadzki, 1981) code is a modified version of LIFE (via UNCLE) (Billone, 1979) for carbide fuel and treats all the phenomena considered in LIFE.

Since all of these codes were developed for pellet fuel pins, one of the main concerns is closure of the gap between fuel and cladding,

and much of the modeling is based on whether the gap is open or closed. Sphere pac fuel pins do not have an initial gap, so the modeling approach is considerably different. Further, although fuel structuring occurs in both pellet and sphere pac fuel, it plays a much more important role in the overall thermal-mechanical behavior in sphere pac fuel pins. Finally, the nature of the sphere pac material (granular versus solid) dictates that a different modeling approach be used. It is known that the FRUMP (Haynes and Wilmore, 1973) code is being developed to model advanced fuels, including sphere pac, but there has been no recent publication of its progress. For these reasons, none of the available mechanical models seemed suitable for modeling a sphere pac fuel pin, and it was evident that a mechanical model starting from basic principles was needed.

#### 1.4 RESEARCH OBJECTIVES

The primary objective of this research is to provide a capability to predict the thermal-mechanical behavior of an unirradiated mixed-carbide sphere pac fuel pin under steady-state operating conditions. As outlined by Ades (1979), the overall behavior can be broken down into four categories:

1. a neutronics model that provides the local heat generation rate in the pin
2. a thermal model that predicts the temperature distribution, fission gas behavior, and restructuring
3. a chemical redistribution model that predicts the local concentration of heavy metal atoms
4. a mechanical model that predicts the cladding stresses and strains and the hydrostatic fuel stress required in the thermal model.

The thermal model was developed by Ades (1979) and constituted the SPECKLE-I code. To eliminate the other three components of the model, it was assumed that the fission rate was radially uniform, that there was no chemical redistribution, and that the fuel hydrostatic stress was constant (50 MPa) through the operating history of the pin. The SPECKLE-II (George and Peddicord, 1981) code was essentially a rewrite of SPECKLE-I with improvements to the numerics, restructuring model, and user conveniences. A neutronics model has been developed by Robinson (1981) to be incorporated into the SPECKLE-III code and a chemical redistribution model is being developed.

The development of a mechanical model includes:

1. The important phenomena must be identified and the necessary equations developed to predict the response. Justifiable simplifying assumptions must be made so that a tractable solution may be obtained. The results and experiences of the developers of other fuel pin behavior codes can be used for much of the work required in this first step.
2. The elastic and plastic constitutive properties of the pin components must be obtained. This is not a major obstacle for the cladding, since these are in use in other pin behavior codes. For the fuel, however, there are no experimental data or analytic models that provide the mechanical material properties of a restructuring fuel bed. In this research, models are developed that give two elastic constants and the plastic constitutive relations of a restructuring fuel bed that depend on the material properties of the spheres themselves, neck growth, hydrostatic compression, bed porosity, and temperature. The model can be used for a randomly packed array of uniform spheres or the binary array of the EIR fuel.
3. Appropriate expressions must be obtained for the fuel and cladding creep and swelling rates. Here again, previous work in fuel pin modeling can be relied upon.

4. A numerical scheme must be devised that can solve the necessary equations for the mechanical model in a reasonable amount of computer time. This scheme must mesh with the previously developed thermal model solution scheme as the two models are closely coupled by the temperature and fuel hydrostatic stress.

The results of the above effort must be compared with existing experimental data and the other analytic or computer solutions to verify the basic assumptions and solution procedures. Conclusions can then be drawn concerning the range of application of the code and areas where more research is required.

The complete thermal-mechanical model in its coded form (SPECKLE-III) is not intended to be the definitive model for mixed carbide sphere pac fuel pins. Rather, it represents a first effort and provides a framework for the extension and improvement of the model segments as more experimental and analytic experience is obtained.

## 2.0 ELASTO-PLASTIC EQUATIONS

The set of equations required for the solution of general problems in elasto-plastic materials consists of 1) equilibrium equations to ensure force and momentum equilibrium, 2) kinematic relationships that give the strain in terms of the local deformation, and 3) constitutive equations that relate the strains to the stresses. The equilibrium equations are linear, but the kinematic and constitutive relationships are, in general, nonlinear. For the elasto-plastic analysis of a fuel pin, Figure 2.1, a number of assumptions are made that considerably simplify the equation set. These assumptions are:

1. The length of the pin can be broken up into a number of shorter segments and within each segment a state of generalized plane strain exists in the fuel and the cladding separately, i.e., the axial strains in the fuel and cladding are independent of radial position but not necessarily equal.
2. The solution is axisymmetric.
3. Both the fuel and cladding materials are isotropic.
4. The deformations are small, i.e., the nonlinear terms of the kinematic relations are neglected.

Under these assumptions the equilibrium equations for one axial segment reduce to

$$\frac{d\sigma_r}{dr} + \frac{\sigma_r - \sigma_\theta}{r} = 0 \quad 2.1$$

where  $\sigma_r$  and  $\sigma_\theta$  are the radial and tangential normal stress components.

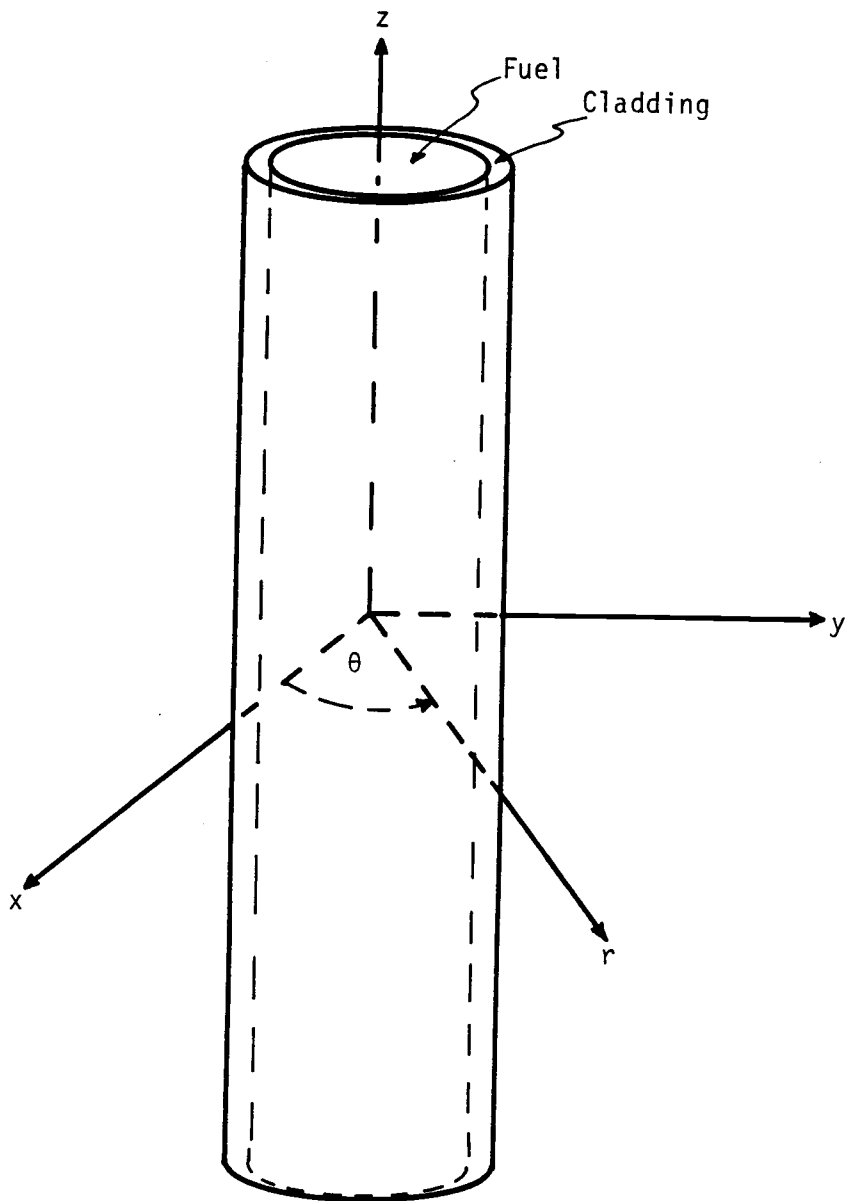


FIGURE 2.1. Coordinate System for Fuel Pin Analysis

The linear kinematic relations are

$$\{\epsilon\} = \begin{Bmatrix} \epsilon_r \\ \epsilon_\theta \\ \epsilon_z \end{Bmatrix} = \begin{Bmatrix} du/dr \\ u/r \\ \text{constant} \end{Bmatrix} \quad 2.2$$

where  $\epsilon_r$ ,  $\epsilon_\theta$  and  $\epsilon_z$  are the radial, tangential, and axial normal strain components respectively, and  $u$  is the radial displacement.

The nonlinearities in the kinematic relations have been removed by assumption 4 above, but the stress-strain constitutive relation is still nonlinear. This nonlinearity arises from the inclusion of plastic flow in the analysis and from the nonlinearity of the elastic stress-strain relationship. The elastic stress-strain relation can be written as

$$\{\epsilon^e\} = e(\{\sigma\}, \xi) \quad 2.3$$

where  $\{\epsilon^e\}$  is the elastic strain,  $\{\sigma\}$  is the stress state, and  $\xi$  represents a combination of parameters that affect the stress-strain relation, e.g., temperature, porosity and fuel restructuring effects on the elastic moduli.

The deformation of an elasto-plastic material depends on the stress-strain history as well as the current stress state. For this reason it is helpful to express the stress-strain relationship as a rate equation, thus

$$\{\dot{\epsilon}^e\} = \dot{e}(\{\sigma\}, \xi) \quad 2.4$$

where the overdot indicates a time rate of change. Carrying out the differentiation gives

$$\{\dot{\epsilon}^e\} = \frac{\partial e}{\partial \{\sigma\}} \{\dot{\sigma}\} + \frac{\partial e}{\partial \xi} \dot{\xi} \quad 2.5$$

An elastic modulus matrix is defined as

$$[E]^{-1} = \frac{\partial e}{\partial \{\sigma\}}$$

The specific form of  $[E]$  is discussed in Chapters 3 and 6. A strain rate due to elastic nonlinearities is defined as

$$\{\dot{\epsilon}^{en}\} = \frac{\partial e}{\partial \xi} \dot{\xi}$$

This strain rate results from some change in the material elastic properties at constant stress. Combining the above definitions with Equation 2.5 gives

$$\{\dot{\epsilon}^e\} = [E]^{-1} \{\dot{\sigma}\} + \{\dot{\epsilon}^{en}\} \quad 2.6$$

The total strain consists of elastic deformation, plastic flow, thermal expansion, creep and fission induced swelling giving

$$\{\dot{\epsilon}\} = [E]^{-1} \{\dot{\sigma}\} + \{\dot{\epsilon}^p\} + \{\dot{\epsilon}^t\} + \{\dot{\epsilon}^c\} + \{\dot{\epsilon}^s\} + \{\dot{\epsilon}^{en}\} \quad 2.7$$

The last four strain rate terms are combined to give an initial strain rate  $\{\dot{\epsilon}^0\}$ . In the numerical scheme used to solve the equation set it is assumed that  $\{\dot{\epsilon}^0\}$  can be specified from the previous time interval stress and strain state, i.e., this term is treated explicitly in time. For the remainder of the development in this section then, it is assumed that  $\{\dot{\epsilon}^0\}$  is specified. The various contributions to  $\{\dot{\epsilon}^0\}$  are discussed in Chapters 5 and 6. Using the definition of the initial strain rate

$$\{\dot{\epsilon}^0\} = \{\dot{\epsilon}^t\} + \{\dot{\epsilon}^c\} + \{\dot{\epsilon}^s\} + \{\dot{\epsilon}^{en}\}$$

the stress-strain relation can now be expressed as

$$\{\dot{\epsilon}\} = [E]^{-1} \{\dot{\sigma}\} + \{\dot{\epsilon}^p\} + \{\dot{\epsilon}^0\} \quad 2.8$$

Following the development by Zienkewicz (1969) the plastic strain rate can be related to the total strain rate as shown in the following.

From the generally accepted theory of plasticity (Mendelson, 1968), a material begins to yield plasticity upon loading when a surface in stress space (called the yield surface) is reached. The shape and position of the yield surface depends on the material properties and the loading history. The yield surface can be expressed as

$$f(\{\sigma\}, \{\varepsilon^P\}, \chi) = 0 \quad 2.9$$

where  $\chi$  represents a combination of parameters (e.g., restructuring, temperature, etc.) that influences the shape or location of the yield surface. If for a given set of conditions  $f < 0$ , then the material is in an elastic state and any loading or unloading will be elastic as long as  $f$  remains less than zero. Continued loading from this state causes  $f$  to increase (by definition). When  $f=0$  the material is in an elastoplastic state and further loading will result in plastic flow. Unloading ( $f$  decreasing) from a point on the yield surface will be accompanied by elastic strains only.

The yield function determines whether or not the material will yield upon loading but not how it yields, i.e., the relative magnitude of the plastic strain components are not determined. This information is obtained from a plastic potential function and the normality rule. The plastic potential function is another surface in stress space and the normality rule states that the plastic strain increments must be normal to the potential surface. The potential function can be expressed as

$$g(\{\sigma\}, \{\varepsilon^P\}, \chi) = 0 \quad 2.10$$

The normality condition requires that

$$\{\dot{\varepsilon}^P\} = d\lambda \left\{ \frac{\partial g}{\partial \sigma} \right\} \quad 2.11$$

where  $d\lambda$  is a non-negative scaling factor to be determined.

Loading from one elastic-plastic state produces another elastic-plastic state during which the yield function remains constant and equal to zero giving

$$df = 0 = \left\{ \frac{\partial f}{\partial \sigma} \right\}^T \{d\sigma\} + \left\{ \frac{\partial f}{\partial \epsilon^p} \right\}^T \{d\epsilon^p\} + \frac{\partial f}{\partial \chi} d\chi \quad 2.12$$

If Equation 2.12 is rewritten as a rate expression

$$0 = \left\{ \frac{\partial f}{\partial \sigma} \right\}^T \{\dot{\sigma}\} + \left\{ \frac{\partial f}{\partial \epsilon^p} \right\}^T \{\dot{\epsilon}^p\} + \frac{\partial f}{\partial \chi} \dot{\chi} \quad 2.13$$

and combined with Equations 2.8 and 2.11, then the scaling factor can be obtained giving

$$d\lambda = \frac{\left\{ \frac{\partial f}{\partial \sigma} \right\}^T [E] \{\dot{\epsilon}\} - \left\{ \frac{\partial f}{\partial \sigma} \right\}^T [E] \{\dot{\epsilon}^0\} + \frac{\partial f}{\partial \chi} \dot{\chi}}{\left\{ \frac{\partial f}{\partial \sigma} \right\}^T [E] \left\{ \frac{\partial g}{\partial \sigma} \right\} - \left\{ \frac{\partial f}{\partial \epsilon^p} \right\}^T \left\{ \frac{\partial g}{\partial \sigma} \right\}} \quad 2.14$$

If the plastic modulus matrix is now defined by

$$[P] = \frac{\left\{ \frac{\partial g}{\partial \sigma} \right\} \left\{ \frac{\partial f}{\partial \sigma} \right\}^T [E]}{\left\{ \frac{\partial f}{\partial \sigma} \right\}^T [E] \left\{ \frac{\partial g}{\partial \sigma} \right\} - \left\{ \frac{\partial f}{\partial \epsilon^p} \right\}^T \left\{ \frac{\partial g}{\partial \sigma} \right\}} \quad 2.15$$

then using the normality rule (Equation 2.11) the plastic strain rate can be given in terms of the total strain rate and the initial strain rate as

$$\{\dot{\epsilon}^p\} = [P] [\{\dot{\epsilon}\} - \{\dot{\epsilon}^0\}] + \{\dot{\epsilon}^{pp}\} \quad 2.16$$

The last term on the right hand side of Equation 2.16 is the plastic strain rate that results from a change in material properties (e.g., due to a temperature change) rather than a change in loading. It is defined by Equations 2.11 and 2.14 as

$$\{\dot{\epsilon}^{PP}\} = \frac{\frac{\partial f}{\partial \chi} \dot{\chi} \left\{ \frac{\partial g}{\partial \sigma} \right\}}{\left\{ \frac{\partial f}{\partial \sigma} \right\}^T [E] \left\{ \frac{\partial f}{\partial \sigma} \right\} - \left\{ \frac{\partial f}{\partial \epsilon^P} \right\}^T \left\{ \frac{\partial g}{\partial \sigma} \right\}} \quad 2.17$$

Finally, substitution of Equation 2.16 into Equation 2.8 gives the elasto-plastic stress-strain relation

$$\{\dot{\sigma}\} = [E] ([I] - [P]) (\{\dot{\epsilon}\} - \{\dot{\epsilon}^O\}) + [E] \{\dot{\epsilon}^{PP}\} \quad 2.18$$

where [I] is the identity matrix.

If the material is not in an elastic-plastic state then [P] and  $\{\dot{\epsilon}^{PP}\}$  are equal to zero and Equation 2.18 reduces to the elastic incremental stress-strain relation.

The expression for the plastic modulus matrix can be simplified if it is assumed that the material does not strain or work harden (perfect plasticity model) which implies that

$$\left\{ \frac{\partial f}{\partial \epsilon^P} \right\} = 0$$

For many materials experimental evidence indicates that the yield surface and the plastic potential surface are the same surface. The normality condition then is referred to as the associated flow rule. Under this assumption the plastic modulus matrix for a perfectly plastic material becomes

$$[P] = \frac{\begin{Bmatrix} \frac{\partial f}{\partial \sigma} \end{Bmatrix} \begin{Bmatrix} \frac{\partial f}{\partial \sigma} \end{Bmatrix}^T [E]}{\begin{Bmatrix} \frac{\partial f}{\partial \sigma} \end{Bmatrix}^T [E] \begin{Bmatrix} \frac{\partial f}{\partial \sigma} \end{Bmatrix}} \quad 2.19$$

Whether or not these two assumptions are valid for the materials of a sphere pac fuel pin is discussed in the sections on the plastic constitutive relations.

The equilibrium equations (Equation 2.1), the kinematic relations (Equation 2.2), and the stress-strain relationship (Equation 2.18) constitute the basic equation set to be solved. Before they can be solved the initial strain increment must be specified (Chapter 5) as well as the elastic modulus matrix, the yield function, and the plastic potential function. These later three constitutive relationships are the subject of the next two chapters.

### 3.0 STRESS-STRAIN RELATIONSHIPS

The stress-strain relationship (Equation 2.18) linearly relates the local stress and strain rates. The proportionality matrix is made up of the elastic and plastic modulus matrices. For sphere pac fuel these modulus matrices can be expected to depend on the elastic and plastic properties of the sphere material, load state, packing density, particle size distribution, particle packing arrangement, particle surface characteristics and, as the fuel begins to restructure, on the radius of the necks joining particles. As restructuring continues into the intermediate and final stages, the modulus matrices will be influenced by the fuel porosity, pore size and shape distributions, and the material properties of the continuous fuel matrix. The material properties of the fuel spheres will be functions of the local temperature and the intrasphere porosity introduced during the fabrication process.

Some experimental data exists for the temperature and porosity dependence of the elastic properties of (U,Pu)C. However, there is no data that provides the elastic properties for a sphere pac bed undergoing initial stage restructuring. Although very desirable, it does not appear that such data will be available in the near future. As an alternative, a model has been developed for the elastic properties of a restructuring sphere bed that depends only on the previously measured physical properties of the material that make up the (U,Pu)C spheres. Models for both single-size sphere arrays and binary arrays of the EIR fuel type are developed in this chapter.

#### 3.1 BACKGROUND

Several models have been proposed to describe the elastic behavior of a packed bed of spheres. All of these models rely on the work done by Hertz (Timoshenko and Goodier, 1951) on the contact between two spheres and the later extensions to this theory by Mindlin

(1949), Cattaneo (1938), and Mindlin and Deresiewicz (1953). According to Hertz, when two spheres (see Figure 3.1) of the same diameter are brought into close contact by opposing forces,  $N$ , that are directed along the line of the centers, the center-to-center approach is given by

$$\frac{n}{2R} = \left(\frac{a}{R}\right)^2 \quad 3.1$$

where  $n$  is the approach distance,  $R$  is the sphere radius, and  $a$  is the radius of the contact area. The contact area radius is given by

$$a/R = \left(\frac{QN}{R^2}\right)^{1/3} \quad 3.2$$

where  $Q = 3(1-\nu^2)/4E$  with  $\nu$  and  $E$  being Poisson's ratio and Young's modulus for the sphere material. The theory also predicts the normal stress distribution at the contact surface as

$$\sigma = \frac{3N}{2\pi a^3} (a^2 - \rho^2)^{1/2} \quad 3.3$$

where  $\rho$  is the distance from the contact center.

Equations 3.1 through 3.3 indicate the nonlinear nature of the elastic deformation of spheres in contact, with the center approach proportional to the 2/3 power of the normal force. Hertz's analysis was based on the assumptions that  $a/R \ll 1$ , the contact surface is planar, and there are no tangential components to the traction on the contact surface, i.e., the sphere surfaces are frictionless. Numerous experiments have confirmed the contact theory for cases that fall within the assumptions (Handbook of Eng. Mech., 1962).

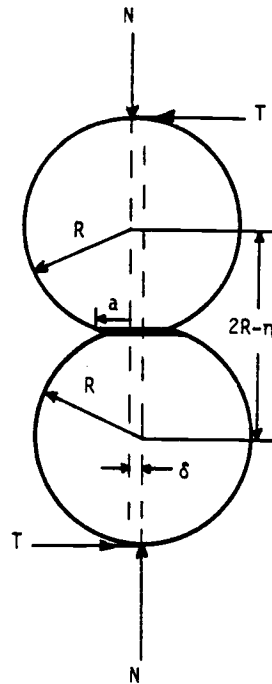


FIGURE 3.1. Schematic for Two Spheres in Contact

Cattaneo (1938) and Mindlin (1949) extended the Hertz contact theory to include tangential stress on the contact plane. For a set of spheres compressed by a normal force  $N$  and subject to a shearing force  $T$ , the sphere centers displacement in the direction of  $T$  is given by

$$\delta = \frac{2-\nu}{4Ga} T \quad 3.4$$

where  $G$  is the shear modulus.

This solution was based on the assumption that there is no slip at the contact plane. The solution predicts infinite shear stress at the outer edge of the contact area. To remove this physically unrealistic result, Cattaneo and Mindlin further extended the contact theory by allowing slip to occur in the outermost annular region of the

contact area. Within this annular region the shear stress,  $\tau$ , is related to the normal stress by the coefficient of static friction  $C_f$ , so that  $\tau/\sigma = C_f$ . Under this assumption the equation for the tangential displacement becomes

$$\delta = \frac{3(2-\nu)C_f N}{8Ga} \left[ 1 - \left( 1 - \frac{T}{C_f N} \right)^{2/3} \right] \quad 3.5$$

Johnson (1955) verified experimentally that the response to a cyclic tangential load was in agreement with Equation 3.5. Since a shear load is accompanied by some slip, the tangential displacement does not vanish when the load is removed, i.e., there remains some permanent displacement. The contact response to a normal and tangential load is therefore inelastic as well as nonlinear. Equation 3.5 was based on the assumption that the normal load was applied first and then the tangential load applied. Mindlin and Deresiewicz (1953) solved the problem for arbitrary rates of normal and tangential load application. In this case the tangential displacement depends on the entire loading history. The effect of twisting moments about the line through the sphere centers has also been investigated and torque-twist relations have been derived (Deresiewicz, 1954).

The results of the extended Hertz contact theory have been used to predict the behavior of sphere arrays. Duffy and Mindlin (1957) obtained differential stress-strain relations for an assembly of spheres in a face-centered cubic packing. The stress-strain relations were obtained by considering a face-centered cubic unit cell subject to some surface stresses  $\sigma_{ij}$ . Then by considering the additional deformation of each contact point when the surface stresses were changed by an amount  $d\sigma_{ij}$ , average displacements of the unit cell surfaces were obtained giving an incremental stress-strain relation. Due to the inelastic behavior of the sphere array, the initial contact forces and displacements (corresponding to surface stress  $\sigma_{ij}$ ) depend

on the entire loading history. For some simple loadings (hydrostatic stress, e.g.) the incremental stress-strain relations can be integrated to provide the initial contact forces and displacements. The theory was checked experimentally by constructing a bar made up of identical spheres in a face-centered array enclosed by a thin rubber membrane. The membrane was then evacuated to hold the spheres in place and provide an initial normal contact load for each sphere pair. Compression wave speeds through the bar were measured for various confining pressures. The theory-predicted wave speeds were lower than those observed experimentally when the forces tangent to the contact were neglected. Much better agreement was obtained when the theory included the effects of tangential forces. Both theories predicted the experimentally observed dependence on confining pressure (wave speed proportional to  $1/6$  power of confining pressure).

Similar incremental stress-strain relations were developed for simple cubic (Deresiewicz, 1957), hexagonal close packed (Duffy, 1959), tetragonal-sphenoidal and cubical-tetrahedral (Marklounf and Stewart, 1967) sphere arrays. All of these regular packings exhibit anisotropic behavior whereas a randomly packed bed is generally considered isotropic. There have been several attempts to predict the elastic constants for a randomly packed bed. Brandt (1955) considered a random sphere array with successively smaller spheres occupying the interstitial spaces left by the next larger size. Using the Hertz theory with normal contact loads only, Brandt calculated the volume change for each set of sphere sizes when the aggregate was subjected to some compressive hydrostatic load and obtained an expression for the bulk modulus. From the bulk modulus a linear wave speed was calculated and compared to data taken on sandstone. The results were in good agreement and again showed the  $1/6$  power dependence on the confining pressure. Brandt's model does not provide any information for the second elastic constant.

A randomly packed array can be considered to consist of small regions of various regular packings oriented at various angles with

respect to some reference coordinate system. The isotropic aggregate therefore consists of anisotropic parts oriented at various angles. Takahashi and Sato (1949) developed a relationship for the elastic constants of an isotrope made up of smaller parts each having the same anisotropic properties but at different orientations. The relationship was developed by assuming that each of the anisotropic parts was subjected to a common strain field and calculating the volume average strain energy. The volume average strain energy could then be used to obtain the isotropic elastic constants. This is analogous to the Voight (see eg, Wu and McCullough, 1977) model for composite materials and provides an upper bound for the material stiffness.

Yanagisawa (1978) attempted to extend the results of Takahashi and Sato by considering the random array to consist of various regular packings oriented at arbitrary angles. He quantified the distribution of regular packings by experimentally determining the distribution of the number of contacts per sphere (coordination number) in a random bed of glass spheres. Each of the regular packings has an associated coordination number so that the regular packing distribution could be obtained from the coordination number distribution. The elastic properties of the aggregate were then calculated by applying the results of Takahashi and Sato (1949) to anisotropic stress strain relations for each of the regular packings and taking an average weighted by the packing distribution. The theory predicted shear modulus was approximately 60% higher than experimental results on glass spheres and sand. The model did show, however, the correct dependence on the bed porosity and confining pressure.

More recently Digby (1981) developed a model for the elastic constants of a random sphere array where the spheres could be initially bonded together across small areas. The model considered a single sphere out of an array of spheres under hydrostatic compression. Using the Hertz contact theory Digby calculated the resultant force on the sphere when it was subjected to contact forces required to provide the contact deformation consistent with a uniform

strain increment in the sphere array. From these results he was able to obtain expressions for two elastic constants. The model reduced to Brandt's model for the case with no adhesion. Assumptions made for the model require that the radius of the initial bonding area is small compared to the sphere radius. No comparisons with experimental data were presented.

The models for the elastic behavior of sphere arrays and their comparisons with experimental data demonstrate that reasonable results can be obtained using models based on the Hertz contact theory. None of the models, however, can be used to model the binary sphere array in a sphere pac fuel pin. The model for the sphere pac fuel must account for two sphere sizes and fuel restructuring. The model should give elastic properties which approach those of a porous body as the second phase of the sintering process (pore closure) is completed. Brandt's model does account for more than one sphere size but only provides one elastic constant and does not consider bonded spheres. The model by Digby includes the effect of only very small necks and is developed for a single sphere size. In the following section a model is proposed that includes the effects of neck growth and two sphere sizes (the smaller spheres must infiltrate the large sphere array).

### 3.2 UNIT CELL

The model is based on the elastic response of a unit cell shown in Figure 3.2. The cell consists of two four-sided pyramids (forming an octahedron) sharing a common base and each having its apex at the center of one of two spheres in contact. The angle between the sphere center-to-center line and each of the sides of the octahedron is  $\beta$ . The cell includes the portions of the two spheres and the void space enclosed by the octahedron. It may be noted that a simple cubic array can actually be constructed of these unit cells (with  $\beta=45^\circ$ ) but other regular arrays and random packings cannot. The cell does, however, have the essential characteristics of a random or regular packing;

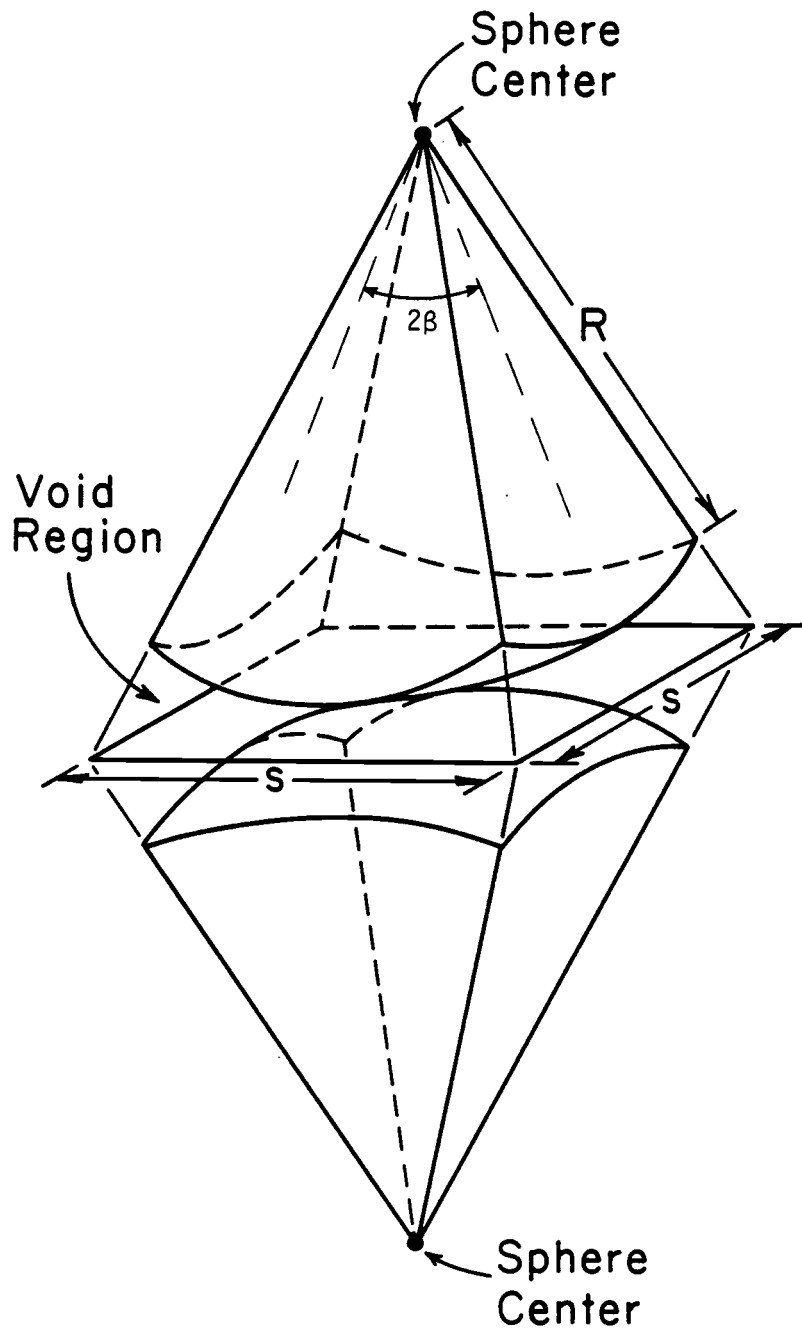


FIGURE 3.2. Random Sphere Array Unit Cell

contact point at a particular orientation, void space, and solid material. It also allows consideration of material deformation away from the contact point which becomes important when significant necks are established. The cell can be used as a reasonable approximation for the unit cell of any packing configuration, regular or random, as will be shown.

The dimensions of the unit cell, except for the angle  $\beta$ , are determined by the sphere radii. The angle  $\beta$  is chosen so that the unit cell has the same void fraction as the sphere array to be modeled. To obtain  $\beta$ , let CN be the average coordination number (number of contacts per sphere) of the sphere array. Then by associating equal surface areas of the sphere with each contact point,  $\beta$  can be obtained from

$$\frac{A(\beta)}{R^2} = \frac{4\pi}{\text{CN}} \quad 3.6$$

where,

$$\frac{A(\beta)}{R^2} = 4 \int_0^\beta \sin(\tan^{-1}(\cos \theta \tan \beta)) d\theta \quad 3.7$$

and  $A(\beta)$  is the surface area per contact. The packing factor (volume of solid/total volume) is related to the coordination number and  $\beta$  by

$$\text{pf} = \frac{V_s}{V_T} = \frac{\pi}{\text{CN} \tan^2 \beta} \quad 3.8$$

Equations 3.7 and 3.8 are derived in Appendix C. Thus, for any packing factor (or coordination number), Equations 3.6, 3.7, and 3.8 can be combined to yield the angle  $\beta$  and a coordination number (or packing factor). The form of Equation 3.7 dictates a numerical solution for the equation set. Figure 3.3 shows the predicted coordination number

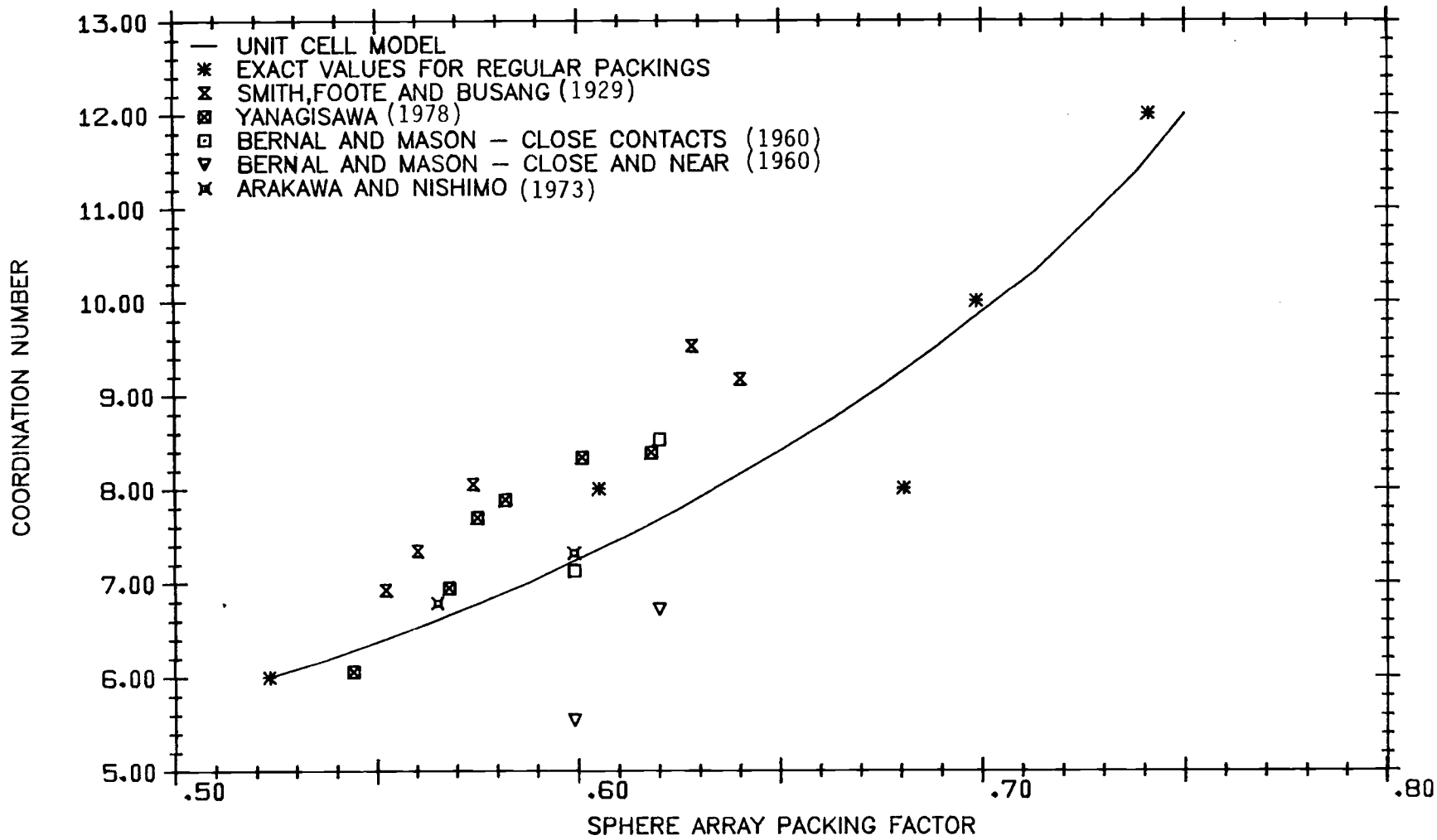


FIGURE 3.3. Predicted Coordination Number Using the Unit Cell

versus the sphere array packing factor using the octahedral unit cell. Included in the figure are the porosity and corresponding coordination number for some regular packings and some experimental data for random-packed beds. The present unit cell correlation predicts the packing factor for the regular packings very well except for a regular packing with a coordination number of eight. There are two regular packings with coordination number eight, cubical tetrahedral with packing factor 0.605, and body-centered cubic with packing factor of 0.68. For the same coordination number the unit cell correlation predicts an intermediate packing factor of 0.64. Most of the data falls above the unit cell curve except for the results of Bernal and Mason (1960). In their investigation, Bernal and Mason distinguished between close contacts (spheres actually touching) and near contacts (spheres located within a radius of 1.05 times the sphere radius). The data from the other investigators includes both the near and close contact points. With this consideration it can be seen that the octahedral unit cell reasonably represents any packing arrangement at least in terms of the packing factor versus the average number of contacts per sphere.

The octahedral pyramid unit cell can be used to develop an incremental stress-strain relationship for an aggregate assumed to be composed of these unit cells. The derivation of this stress-strain relationship is discussed in the next two sections.

### 3.3 ELASTIC CONSTANTS FOR AN ISOTROPE MADE UP OF ANISTROPIC PARTS

Some materials (e.g., polycrystals and granular media) are generally considered to behave isotropically although their smaller composing parts may be anistropic. The anistropic effects are washed out by the many orientations of the anistropic parts. To derive the properties of the isotropic aggregate from the known properties of the anistropic parts it is assumed that both the aggregate and the

individual parts behave linearly elastically. Thus an incremental form of Hooke's law can be expressed as

$$d\varepsilon_{ij} = D_{ijkl} d\sigma_{kl} \quad 3.9$$

where  $\varepsilon_{ij}$  is the linear strain tensor,  $D_{ijkl}$  is a fourth order tensor dependent on the material elastic properties, and  $\sigma_{ij}$  is the stress tensor. (It may be recalled that the general contact theory predicts inelastic behavior while the assumption here is that all behavior is elastic. In the next section an assumption will be made that removes the inelastic behavior making the results in this section applicable.) From thermodynamics it can be shown that for an adiabatic or isothermal process a strain energy density function exists (see e.g., Dym and Shames (1973)) and is defined as

$$dh = \sigma_{ij} d\varepsilon_{ij} \quad 3.10$$

where  $h$  is the strain energy per unit volume.

Now consider an anisotropic unit cell whose orientation with respect to a set of reference axis  $(X_1, X_2, X_3)$  is given by three rotations,  $\phi_1, \phi_2$  and  $\phi_3$  (see Figure 3.4). A set of coordinate axes fixed to the unit cell (one-half of the cell is shown in Figure 3.4) is identified as  $x_1, x_2$  and  $x_3$ . The transform tensor from the  $(x_1, x_2, x_3)$  system to the  $(X_1, X_2, X_3)$  systems is  $t_{iI}$  where

$$t_{iI} = \cos \theta_{iI}$$

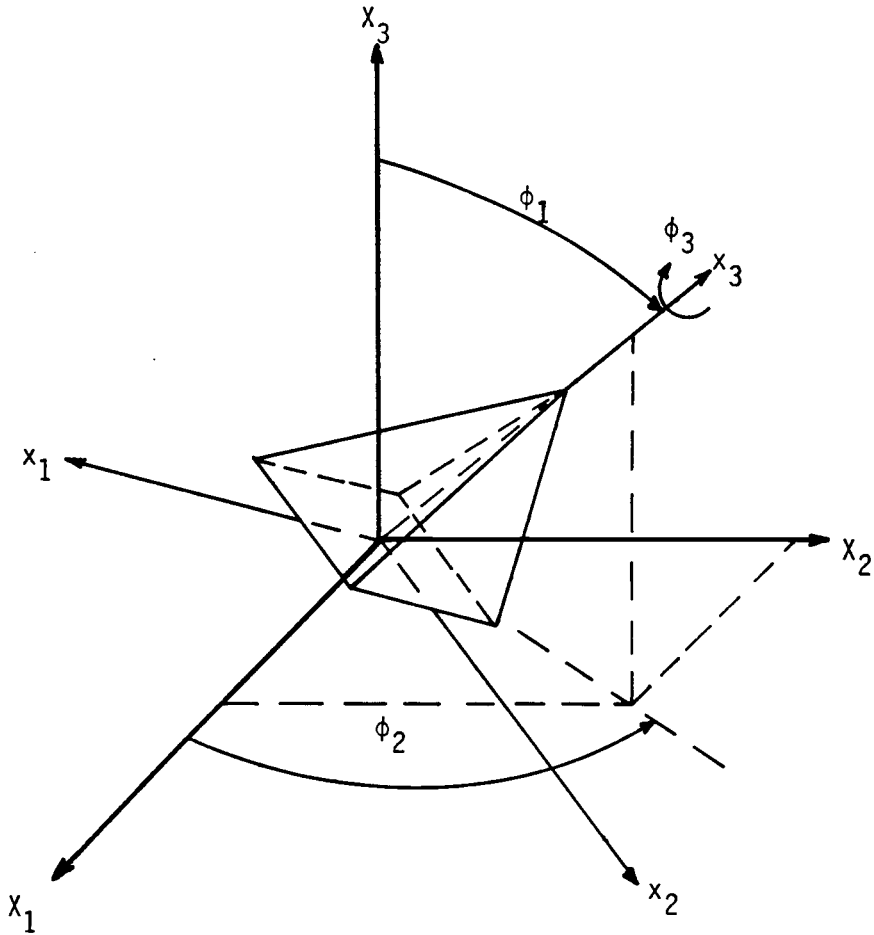


**FIGURE 3.4.** Coordinate System for Rotating Unit Cell

and  $\theta_{iI}$  is the angle between  $x_i$  and  $X_I$ . Further consider a stress field  $\sigma_{IJ}$  and differential stress field  $d\sigma_{IJ}$  referenced to the  $(X_1, X_2, X_3)$  system. Assume that these stress fields are constant within and on the surfaces of the unit cell. The differential strain energy of the unit cell resulting from the application of  $d\sigma_{IJ}$  is given by

$$dh(\phi_1, \phi_2, \phi_3) = \sigma_{ij} d\epsilon_{ij} \quad 3.11$$

where  $\sigma_{ij}$  and  $d\epsilon_{ij}$  are the stress and differential strain referenced to the  $(x_1, x_2, x_3)$  coordinate system.

Now it is assumed that the strain energy density of the aggregate is the volume average of the strain energy of the unit cells comprising the aggregate. Thus, assuming a uniform distribution of cell orientations, it is shown in Appendix C that

$$dh^0 = \frac{1}{8\pi^2} \int_0^{2\pi} \int_0^{2\pi} \int_0^{\pi} dh \sin \phi_1 d\phi_1 d\phi_2 d\phi_3 \quad 3.12$$

where  $h^0$  is the strain energy density of the aggregate.

Then substituting Equations 3.11 and 3.9 into 3.12 gives

$$dh^0 = \frac{1}{8\pi^2} \int_0^{2\pi} \int_0^{2\pi} \int_0^{\pi} \sigma_{ij} D_{ijk\ell} d\sigma_{k\ell} \sin \phi_1 d\phi_1 d\phi_2 d\phi_3 \quad 3.13$$

The elastic constants of the isotropic aggregate are defined as those that give the same value for the strain energy density as Equation 3.12. Thus

$$dh^0 = \sigma_{IJ} d\epsilon_{IJ} = \sigma_{IJ} D_{IJKL}^0 d\sigma_{KL} \quad 3.14$$

where  $D_{IJKL}^0$  is the elastic property tensor for the aggregate.

Applying the coordinate transformation to Equation 3.13 gives

$$dh^0 = \frac{1}{8\pi^2} \int_0^{2\pi} \int_0^{2\pi} \int_0^{\pi} \sigma_{IJ} t_{iI}^2 t_{jJ}^2 t_{kK}^2 t_{\ell L}^2 D_{ijk\ell} d\sigma_{KL} \sin \phi_1 d\phi_1 d\phi_2 d\phi_3$$

3.15

so that by comparison with Equation 3.14 the elastic property tensor for the aggregate is

$$D_{IJKL}^0 = \frac{1}{8\pi^2} \int_0^{2\pi} \int_0^{2\pi} \int_0^{\pi} t_{iI}^2 t_{jJ}^2 t_{kK}^2 t_{\ell L}^2 D_{ijkl} \sin \phi_1 d\phi_1 d\phi_2 d\phi_3$$

3.16

The strain energy calculated from Equation 3.14 with  $D_{IJKL}^0$  defined by Equation 3.16 is a lower bound on the actual strain energy of the aggregate as discussed by Paul (1960). It is analagous to the lower bound provided by the Reuss (see eg., Garg, et al, 1973) model for composite materials.

An upper bound on the aggregate strain energy can be found if the definition of complementary strain energy is used in place of Equation 3.11, i.e.,

$$dh^*(\phi_1, \phi_2, \phi_3) = \epsilon_{ij} d\sigma_{ij} \quad 3.17$$

with

$$d\sigma_{ij} = C_{ijkl} d\epsilon_{kl} \quad 3.18$$

Then if it is assumed that the unit cell exists in some constant strain state  $\epsilon_{IJ}$  and is subjected to surface displacements consistent with a constant differential strain field then the elastic properties for the aggregate are given by

$$C_{IJKL}^0 = \frac{1}{8\pi^2} \int_0^{2\pi} \int_0^{2\pi} \int_0^\pi t_{iI}^2 t_{jJ}^2 t_{kK}^2 t_{lL}^2 C_{ijkl} \sin\phi_1 d\phi_1 d\phi_2 d\phi_3 \quad 3.19$$

For the special case of an orthotropic material the stress-strain relation (Equation 3.9) can be written as

$$\{d\varepsilon\} = [D] \{d\sigma\} \quad 3.20$$

where

$$\{d\varepsilon\}^T = [d\varepsilon_{11}, d\varepsilon_{22}, d\varepsilon_{33}, d\gamma_{12}, d\gamma_{13}, d\gamma_{23}]$$

$$\{d\sigma\}^T = [d\sigma_{11}, d\sigma_{22}, d\sigma_{33}, d\tau_{12}, d\tau_{13}, d\tau_{23}]$$

and

$$[D] = \begin{bmatrix} D_{11} & D_{12} & D_{13} & 0 & 0 & 0 \\ D_{21} & D_{22} & D_{23} & 0 & 0 & 0 \\ D_{31} & D_{32} & D_{33} & 0 & 0 & 0 \\ 0 & 0 & 0 & D_{44} & 0 & 0 \\ 0 & 0 & 0 & 0 & D_{55} & 0 \\ 0 & 0 & 0 & 0 & 0 & D_{66} \end{bmatrix}$$

with  $D_{ij} = D_{ji}$

For an orthotropic unit cell it can be shown (see Appendix C) that Equation 3.16 reduces to

$$D_{11}^0 = D_{22}^0 = D_{33}^0 = \frac{1}{5} (D_{11} + D_{22} + D_{33}) + \frac{2}{15} (D_{12} + D_{23} + D_{13}) + \frac{1}{15} (D_{44} + D_{55} + D_{66})$$

$$D_{12}^0 = D_{23}^0 = D_{13}^0 = \frac{1}{15} (D_{11} + D_{22} + D_{33}) + \frac{4}{15} (D_{12} + D_{23} + D_{13}) - \frac{1}{30} (D_{44} + D_{55} + D_{66})$$

$$D_{44}^0 = D_{55}^0 = D_{66}^0 = 2 (D_{11} - D_{12})$$

3.21

$$D_{14}^0 = D_{15}^0 = D_{16}^0 = D_{24}^0 = D_{25}^0 = D_{26}^0 = D_{34}^0 = D_{35}^0 = D_{36}^0 = D_{45}^0 = D_{46}^0 = D_{56}^0 = 0$$

giving the aggregate differential stress-strain relation

$$\{d\varepsilon\} = [D^0] \{d\sigma\} \quad 3.22$$

with  $[D^0]$  symmetric.

The analogous results for  $[C^0]$  were obtained by Takahashi and Sato (1949) and are

$$\begin{aligned} C_{11}^0 &= \frac{3}{15} (C_{11} + C_{22} + C_{33}) + \frac{2}{15} (C_{12} + C_{23} + C_{13}) + \frac{4}{15} (C_{44} + C_{55} + C_{66}) \\ C_{12}^0 &= \frac{1}{15} (C_{11} + C_{22} + C_{33}) + \frac{4}{15} (C_{12} + C_{23} + C_{13}) - \frac{2}{15} (C_{44} + C_{55} + C_{66}) \\ C_{44}^0 &= \frac{1}{2} (C_{11} - C_{12}) \end{aligned}$$

3.23

The actual material elastic properties for the aggregate lie somewhere between  $[D^0]$  and  $[C^0]^{-1}$ . Some work has been done in the theory of composite materials to improve the bounds imposed by  $[D^0]$  and  $[C^0]$ . However, Wu and McCullough (1977) showed that these are the best possible bounds unless something is known about how the differential stresses (or strains) within the unit cell vary as the cell is rotated in the stress field. For the analysis of the sphere pac fuel the definitions for elastic properties are assumed to be those given by Equation 3.24. Comparisons with experimental data and previous models gave much closer agreement to the lower bound equations.

As necks begin to grow between the spheres the unit cell becomes more isotropic and  $[C^0]^{-1}$  and  $[D^0]$  approach each other. The largest errors in the constitutive relation resulting from the use of the lower bound will therefore be for the completely unrestructured fuel.

To obtain the two elastic constants for the isotropic aggregate,  $D_{11}^0$  and  $D_{12}^0$ , it is first necessary to develop the stress-

strain relationship for the octrahedral unit cell (Equation 3.20). This relationship is developed in the next section.

### 3.4 UNIT CELL STRESS-STRAIN RELATIONSHIP

The stress-strain relationship for the orthotropic unit cell is derived using again the concept of a strain energy density function. For the octahedral unit cell oriented in a stress field  $\sigma_{ij}$  with the represented sphere centers on the z-axis, as shown in Figure 3.5, the strain energy density function can be expressed as

$$dh = \{\sigma\}^T [D] \{d\sigma\} \quad 3.24$$

where h is the strain energy density and

$$\{\sigma\} = [\sigma_x, \sigma_y, \sigma_z, \tau_{xy}, \tau_{xz}, \tau_{yz}]$$

[D] is the compliance matrix to be derived that relates the stresses to the strains as

$$\{d\epsilon\} = [D] \{d\sigma\} \quad 3.25$$

where

$$\{d\epsilon\} = [\epsilon_x, \epsilon_y, \epsilon_z, \gamma_{xy}, \gamma_{xz}, \gamma_{yz}]$$

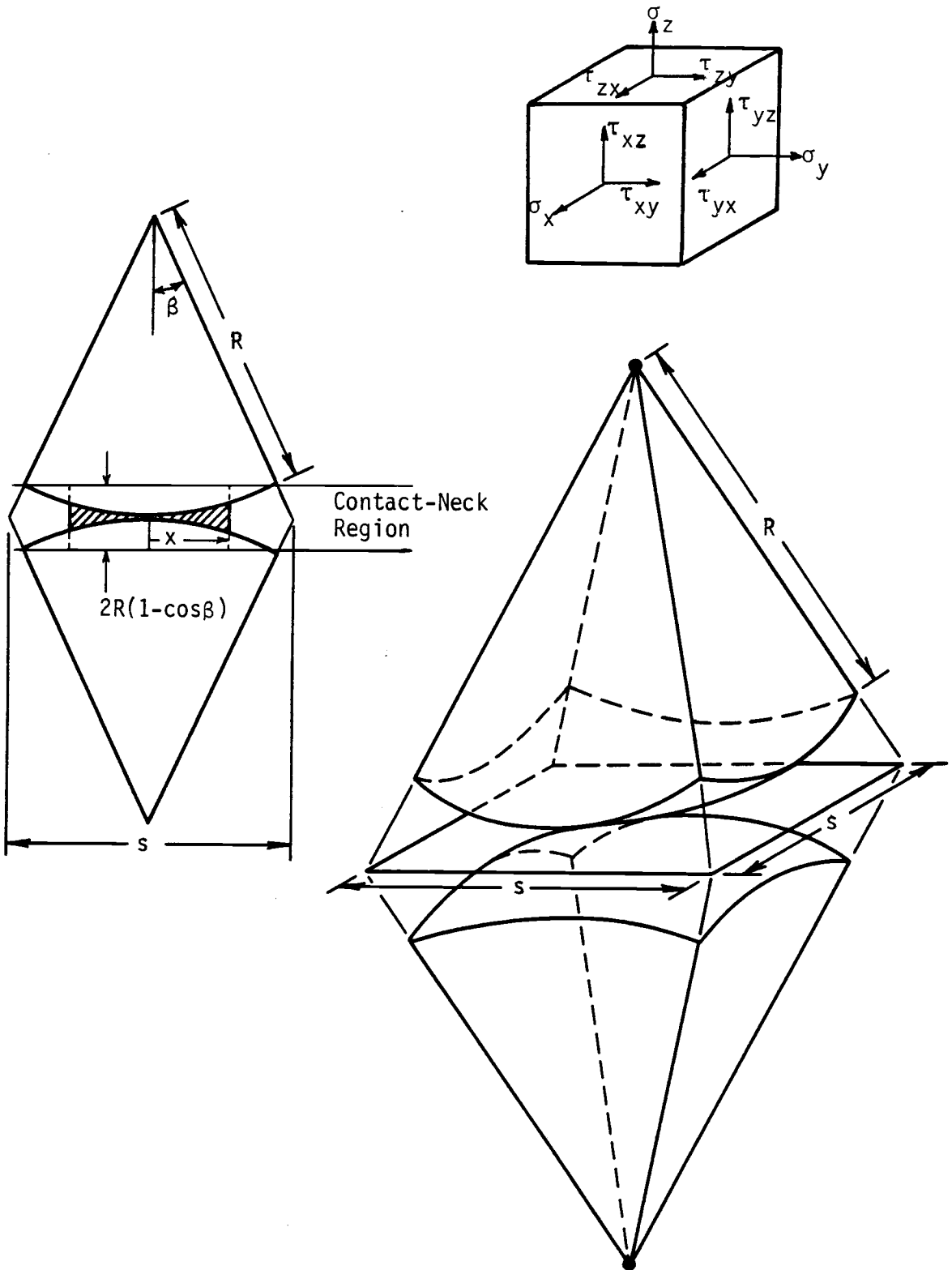


**FIGURE 3.5.** Unit Cell Oriented in Stress Field  $\{\sigma\}$

For two spheres in contact, the deformation (and stresses) resulting from the contact are localized in the contact region. At distances greater than  $3a$  ( $a$  is the contact radius) from the contact center, the stresses can be neglected (Handbook of Eng. Mech., 1962). It is assumed then that all of the strain energy associated with the contact deformation is located in the region between the set of planes parallel to the contact plane with each a distance  $R(1-\cos\beta)$  away from the contact plane as shown in Figure 3.5. It is also assumed that the strain energy associated with the accumulated neck material is localized in the contact-neck region shown in Figure 3.5. The rest of the unit cell can also deform in response to applied surface tractions. This deformation is referred to here as solid body (as opposed to contact) deformation. It is assumed then that the unit cell strain energy can be separated into two parts so that

$$Vdh = dH = dH_{CN} + dH_S \quad 3.26$$

where  $V$  is the unit cell volume,  $dH$  is the unit cell differential strain energy,  $dH_{CN}$  is the energy due to contact and neck deformation, and  $dH_S$  is the strain energy due to the solid body deformation.

To obtain a value for  $dH_S$  it is assumed that the stress distribution within the solid body portion of the unit cell is uniform and is given by the average surface stresses. The surface of the unit cell associated with the contact-neck region cannot support any load. For any particular surface of the unit cell the effective stress on the surface associated with the solid body portion is assumed uniform and is obtained from a simple force balance. For example

$$\sigma'_x = A_x/A'_x \sigma_x \quad 3.27$$



$$= \{\sigma\}^T \frac{V_S}{\cos^4 \beta} [D_m] \{d\sigma\}$$

where  $V_S$  is the solid volume and  $[D_m]$  is the compliance matrix for an isotropic material.

$$[D_m] = \frac{1}{E} \begin{bmatrix} 1 & -\nu & -\nu & 0 & 0 & 0 \\ -\nu & 1 & -\nu & 0 & 0 & 0 \\ -\nu & -\nu & 1 & 0 & 0 & 0 \\ 0 & 0 & 0 & E/G & 0 & 0 \\ 0 & 0 & 0 & 0 & E/G & 0 \\ 0 & 0 & 0 & 0 & 0 & E/G \end{bmatrix} \quad 3.30$$

The unit cell stress-strain relation must account for the increased stiffness due to the formation of necks in the contact region. Using the principle of virtual work, the strain energy in the contact-neck region can be written as

$$dH_{CN} = \{F\}^T \{\Delta\} \quad 3.31$$

where  $\{F\}$  is the effective force vector and  $\{\Delta\}$  is the corresponding displacement vector due to deformation in the contact-neck region.  $\{F\}$  and  $\{\Delta\}$  are given by

$$\{F\}^T = [\sigma_x A_x, \sigma_y A_y, \sigma_z A_z, \tau_{xy} A_x, \tau_{xz} A_z, \tau_{yz} A_z]$$

and

$$\{\Delta\}^T = [\Delta_x, \Delta_y, \Delta_z, \Gamma_{xy}, \Gamma_{xz}, \Gamma_{yz}]$$

where  $\Delta_x$  is the displacement at the point of application of  $\sigma_x A_x$ , etc. The only deflections considered in the contact neck region are deformations normal to the contact plane and shear deformations parallel to the contact plane. This implies that  $\Delta_x = \Delta_y = \Gamma_{xy} = 0$ . The displacements are related to the forces through the stiffness equation

$$\{dF\} = [C_{CN}]\{\Delta\} \quad 3.32$$

It is now assumed that the total contact neck region stiffness is the sum of the contact stiffness and the neck stiffness, i.e., the neck and the contact act as independent parallel springs. The contact-neck region stiffness matrix is then written as

$$[C_{CN}] = [C_C] + [C_N] \quad 3.33$$

where  $[C_C]$  is the stiffness matrix resulting from the Hertz contact theory and  $[C_N]$  is the stiffness matrix for the neck material.

It will be recalled that the generalized Hertz contact theory implies that the transverse deformations are inelastic because of slip along the contact plane. However, since in sphere pac fuel small necks are formed between adjacent particles very early in the loading process, it is reasonable to assume that there is no slip in the contact plane. The normal and transverse compliances can therefore be obtained by differentiating Equations 3.1 and 3.4 with respect to the loads giving

$$d\eta/dN = \frac{4}{3} Q/a$$

3.34

$$d\delta/dT = \frac{2-\nu}{4Ga}$$

The contact stiffness matrix can now be written as

$$[C_C] = \begin{bmatrix} 0 & & & & & \\ & 0 & & & & \\ & & \frac{3a}{4Q} & & & \\ & & & 0 & & \\ & & & & \frac{4Ga}{2-\nu} & \\ & & & & & \frac{4Ga}{2-\nu} \end{bmatrix} \quad 3.35$$

The stiffness of the neck material is assumed to be that of a circular column with radius  $x$  and height  $\ell_{\text{eff}}$  (see Figure 3.5). It is not clear what the effective column height should be, but as the neck gets large,  $\ell_{\text{eff}}$  should approach  $2R(1-\cos\beta)$  (the height of the contact region) so that all of the solid body type strain energy in the unit cell is accounted for. For very small necks the contact-neck stiffness should be dominated by the contact stiffness. By letting  $\ell_{\text{eff}} = 2R(1-\cos\beta)$ , independent of the neck radius, both of these requirements are satisfied. The neck stiffness matrix can be written as

$$[C_N] = \frac{\pi x^2}{\ell_{\text{eff}}} \begin{bmatrix} 0 & & & & & \\ & 0 & & & & \\ & & E & & & \\ & & & 0 & & \\ & & & & G & \\ & & & & & G \end{bmatrix} \quad 3.36$$



$$dH_{CN} = \{\sigma\}^T [A][D_{CN}][A]\{d\sigma\}/R \quad 3.39$$

where

$$[A] = \begin{bmatrix} A_x & & & & & & \\ & A_y & & & & & \\ & & A_z & & & & \\ & & & A_x & & & \\ & & & & A_z & & \\ & & & & & A_z & \\ & & & & & & A_z \end{bmatrix}$$

The projected areas are given by (see Appendix C)

$$\begin{aligned} A_x &= A_y = 2R^2 \tan\beta \\ A_z &= 4R^2 \tan^2\beta \end{aligned} \quad 3.40$$

The results of equations 3.26, 3.29 and 3.39 can now be combined to give the unit cell differential strain energy

$$dH = \{\sigma\}^T \left( \frac{1}{R} [A][D_{CN}][A] + V_s [A/A'] [D_m] [A/A'] \right) \{d\sigma\} \quad 3.41$$

Then, by comparison with Equation 3.24, the unit cell compliance matrix is given by

$$[D] = \frac{1}{VR} [A][D_{CN}][A] + \frac{V_s}{V} [A/A'] [D_m] [A/A'] \quad 3.42$$

It is shown in Appendix C that Equation 3.42 reduces to

$$[D] = A_{CN}[D_{CN}] + A_m[D_m] \quad 3.43$$

with

$$A_{CN} = 6 \tan^2 \beta$$

$$A_m = \frac{1}{\cos^4 \beta} \left[ \text{pf} - \pi/4 \frac{(1-\cos\beta)^2(2+\cos\beta)}{\tan^2 \beta} \right]$$

where pf is the sphere array packing factor. As will be shown, the first term of Equation 3.43 dominates for small neck growth but as the neck radius becomes significant the second becomes more important, and the compliance due to contact deformation decreases. The coefficient  $A_m$  determines the effective stiffness of the array at the end of initial stage sintering.

Equation 3.43 provides the results needed to obtain the effective elastic constant matrix  $[D^0]$  for the isotropic aggregate via Equation 3.21. In the next section some results are obtained for the elastic properties of a random packed bed of uniform spheres and compared to some experimental results and previous theories.

### 3.5 ELASTIC CONSTANTS FOR A RESTRUCTURING RANDOM PACKED BED OF UNIFORM SPHERES

A small computer program was written to solve the equations presented in Sections 3.2, 3.3 and 3.4 for two elastic constants of a sphere bed as a function of the confining pressure and the neck ratios. The elastic properties predicted by the model for a bed of uniform spheres at a packing factor of 0.61 are shown in Figures 3.6 through 3.9. Figures 3.6 and 3.7 show the effective elastic modulus ( $\bar{E}/E$  where  $E$  is the elastic modulus of the sphere material) and Poisson's ratio as a function of the normalized confining

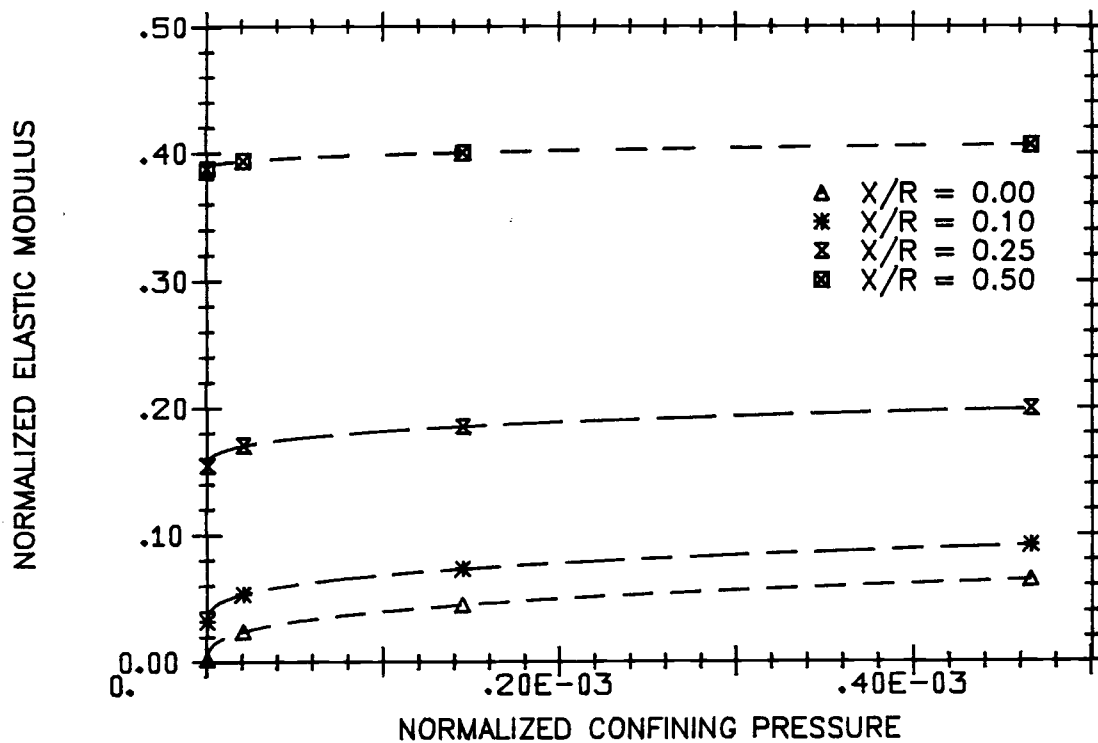


FIGURE 3.6. Effective Young's Modulus Versus Confining Pressure for a Random Array of Uniform Spheres

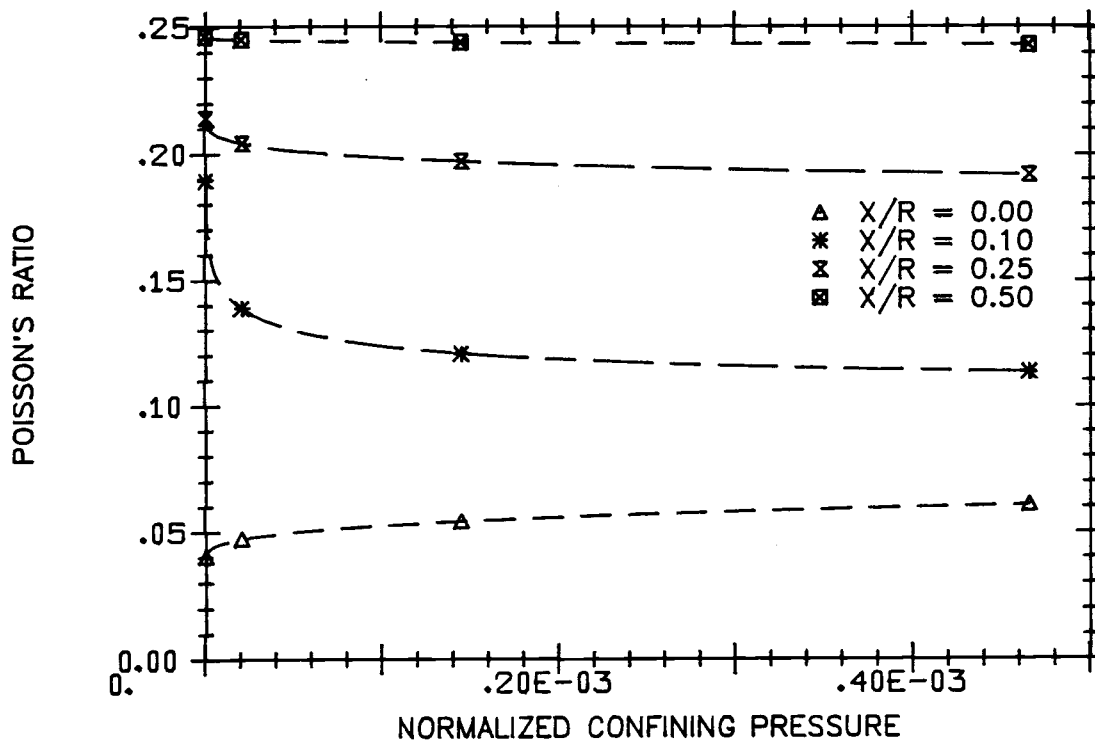


FIGURE 3.7. Effective Poisson's Ratio Versus Confining Pressure for a Random Array of Uniform Spheres

pressure ( $P/E$ ) for various neck ratios. When there is no neck growth the elastic modulus increases proportional to  $P^{1/3}$  while Poisson's ratio is essentially independent of  $P$  and is small ( $\sim 0.05$ ). This prediction for Poisson's ratio is in agreement with the analytic results for regular packed sphere arrays (see, e.g., Deresiewicz, 1957) and experimental evidence for cohesionless granular material (Lade and Duncan, 1975). As the neck radius becomes larger the initial stiffness increases and is less dependent on the confining pressure. Poisson's ratio also increases as the neck radius increases and approaches the value of Poisson's ratio for the sphere material ( $\nu = 0.3$ ). This again is in agreement with experimental evidence that indicates that Poisson's ratio for a porous body is not much less than that for solid material. For a sphere bed with small necks established, Poisson's ratio initially decreases with increasing pressure. In terms of the model equations, this is because the normal stiffness to shear stiffness ratio for the contact alone is greater than that for the neck alone. As the confining pressure increases the contact region stiffness becomes dominated by the Hertz contact terms. It is not known whether or not the behavior of Poisson's ratio with respect to pressure shown in Figure 3.7 is physically realistic.

Figures 3.8 and 3.9 show the elastic properties for the same bed as a function of neck ratio at three different confining pressures.

### 3.6 COMPARISON WITH EXISTING MODELS AND EXPERIMENTAL DATA

The model presented in Sections 3.3 and 3.4 can be compared to some experimental results and existing theories. Brandt (1955) derived an expression for the bulk modulus of a sphere array consisting of successively smaller infiltrating sphere sizes and included the possibility of a fluid filling the remaining void. For the case of one sphere size with a packing factor of 0.61 and no fluid, the expression for the bulk modulus reduces to

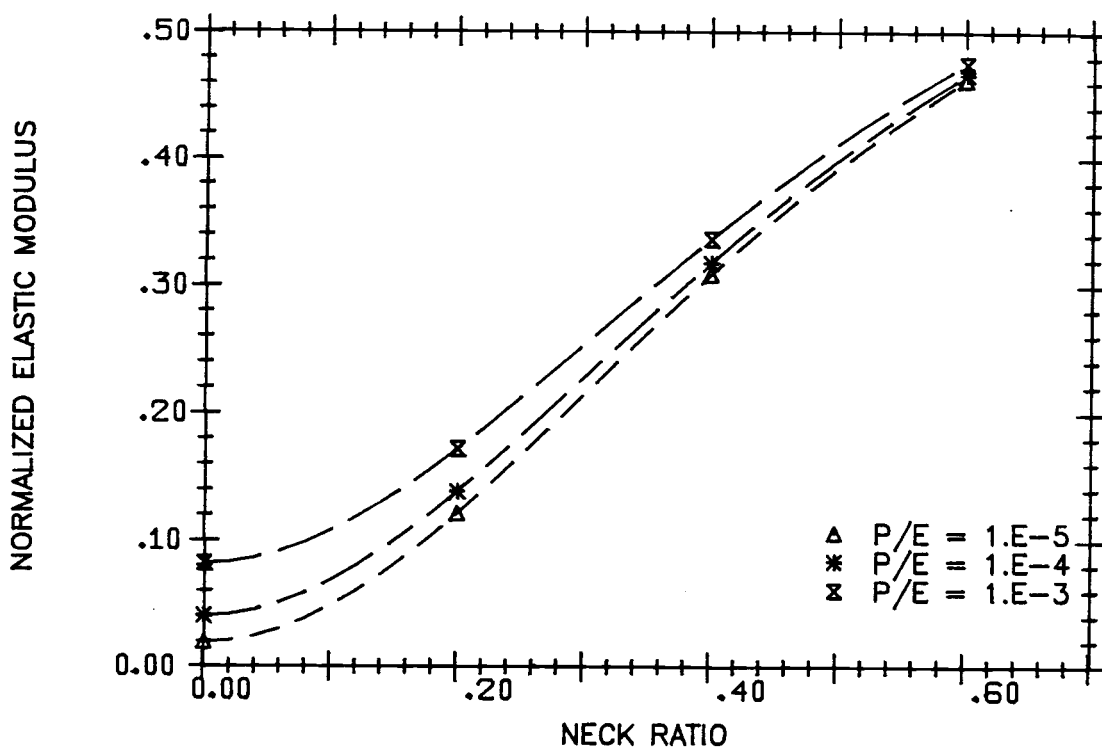


FIGURE 3.8. Effective Young's Modulus Versus Neck Ratio for a Random Array of Uniform Spheres

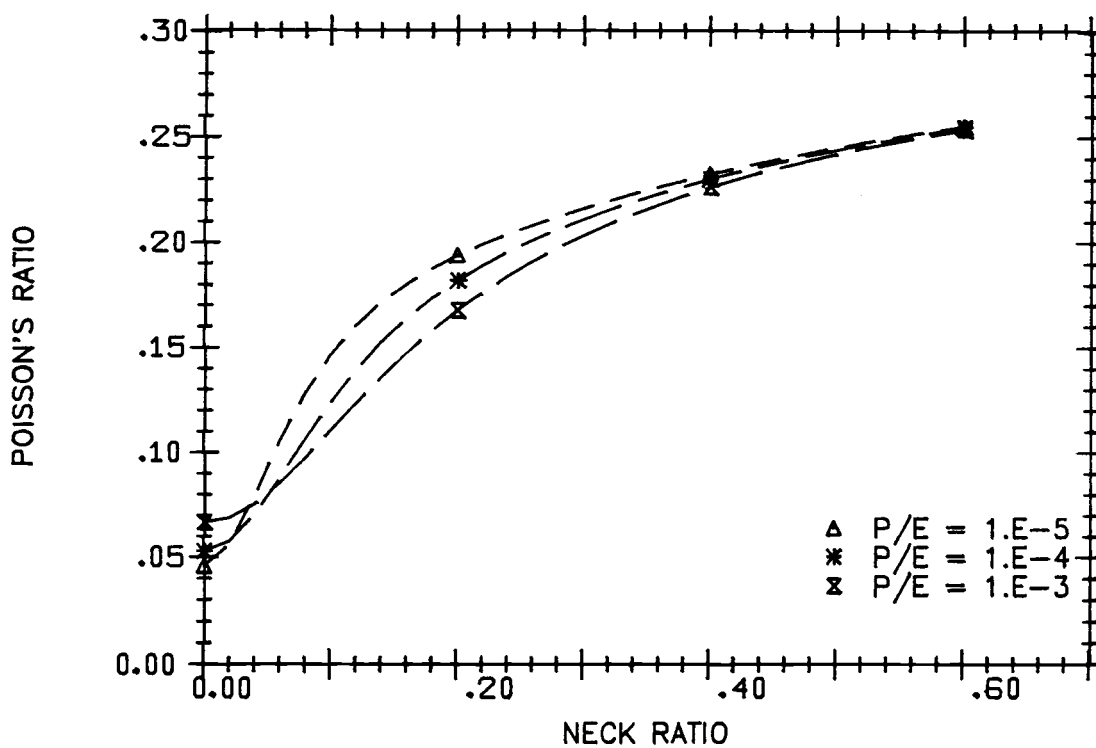


FIGURE 3.9. Effective Poisson's Ratio Versus Neck Ratio for a Random Array of Uniform Spheres

$$K/E = 0.3443 \left( \frac{P/E}{(1-\nu^2)^2} \right)^{1/3} \quad 3.44$$

The effective bulk modulus for an aggregate can be calculated from the present model by

$$K/E = \frac{1}{E(3D_{11}^0 + 6D_{12}^0)} \quad 3.45$$

resulting in

$$K/E = \frac{1}{A_m(3-4\nu) + (2A_{CN}^2)^{1/3} (1-\nu^2)^{2/3} (P/E)^{-1/3}} \quad 3.46$$

If the first term in the denominator (solid body compliance) is neglected and  $A_{CN}$  calculated using  $\beta = 39.5^0$  (corresponding to  $pf = 0.61$  from the unit cell correlation) then the effective bulk modulus is

$$K/E = 0.3114 \left( \frac{P/E}{(1-\nu^2)^2} \right)^{1/3} \quad 3.47$$

which is within 10% of the results obtained by Brandt. It has the same functional dependence on  $P$  and the sphere material elastic constants as Brandt's model as expected, since both were derived from the Hertz contact theory. Brandt's model predicts that the bulk modulus continually increases as the confining pressure,  $P$ , increases whereas the bulk modulus predicted by the present model is limited by

$$K/E < \frac{1}{A_m(3-4\nu)} = \frac{0.8}{3-4\nu} < \frac{1}{3(1-2\nu)} \quad 3.48$$

The last term in the above expression is the normalized bulk modulus for solid material. Thus the present model could potentially be used for very large confining pressures, where the Hertz theory may no longer be valid, to provide a reasonable estimate for the effective elastic properties. Brandt did not compare his model to experimental data directly, but he did compare an extension of the model for nonspherical particles, which included an arbitrary constant, to the confining pressure dependence of porosity and sound wave velocity in sand and sandstone. The agreement was good, indicating that the functional dependence (Equation 3.44) on pressure is essentially accurate.

Duffy and Mindlin (1957) measured the velocity of a compression wave in a sphere array. The array was constructed of steel spheres in a face-centered cubic arrangement. The spheres were held in place by a thin rubber membrane, evacuated to provide a range of confining pressures. The spheres were arranged so that the bar was parallel to [100] or the [110] direction of the array (i.e., parallel to an edge or face diagonal of a unit cube). The experimental results are given in Figure 3.10, that shows the wave velocity (normalized by twice the wave velocity in steel) as a function of the confining pressure for bars in the [100] and the [110] orientations. Excellent agreement is shown between the experiment and the present model at the higher confining pressures. Mindlin and Duffy attributed the decreasing pressure dependence as pressure increases to spheres not initially in contact. The effect was more pronounced when spheres of lower diameter tolerance were used. The present model predicts only one wave velocity, independent of the orientation of the bar. However, the experimental wave velocities are so close for the two orientations, it is not unreasonable to expect the wave velocity to be about the same for any orientation and therefore comparison with the present model is valid.

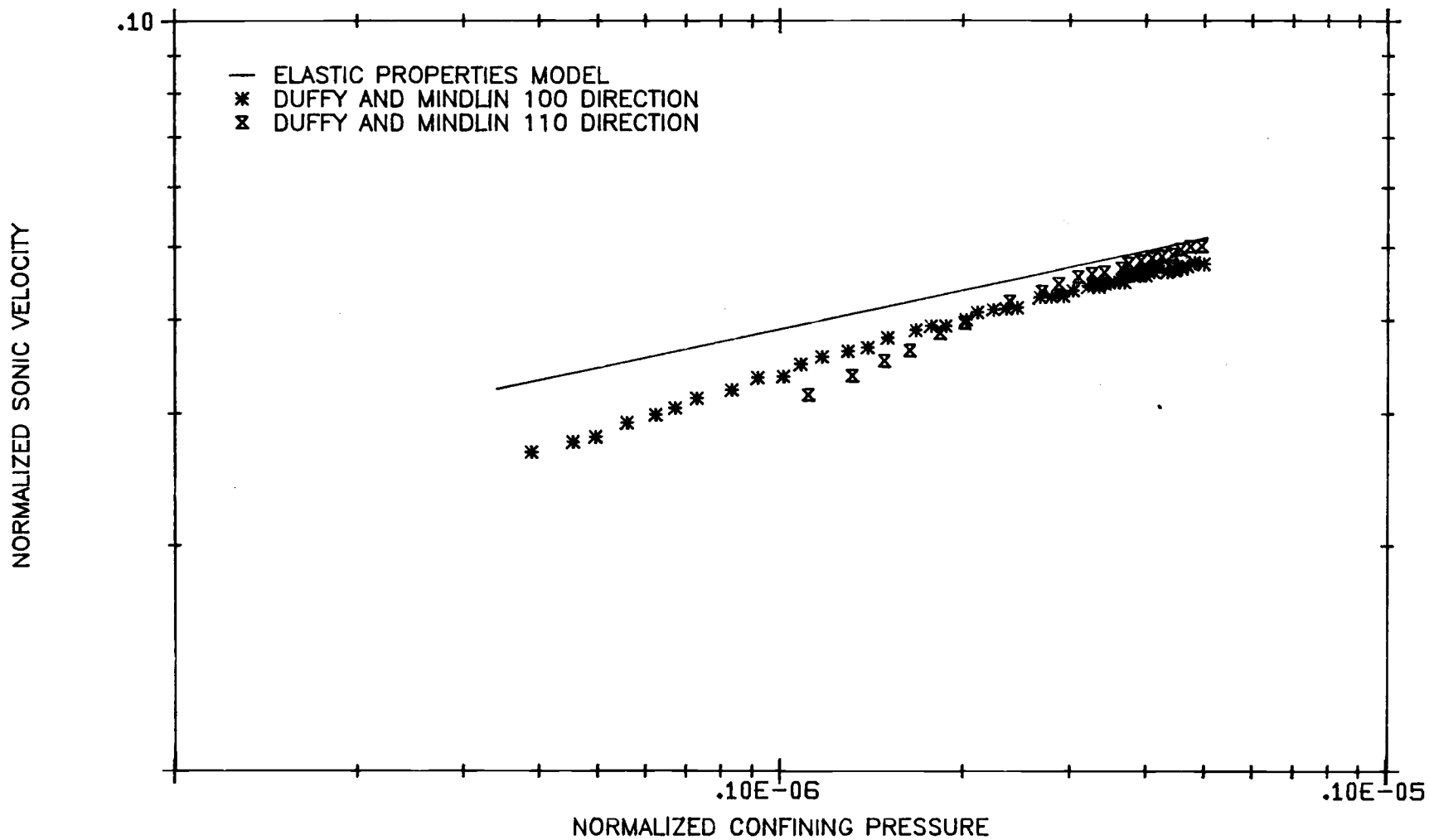


FIGURE 3.10. Elastic Property Model Comparison with Sonic Velocity in a Regular Sphere Array

Yanagisawa (1978) measured the shear modulus in random arrays of uniform glass beads and in packed sand. The resonant column method was used to obtain the frequency response to a torsional oscillation applied to a cylindrical sample under some confining pressure. The shear wave velocity and shear modulus can be calculated from the resonant frequency. The experimental data for the shear modulus (normalized by one-half of the shear modulus of glass) versus void ratio (void volume/solid volume) at a confining pressure of 0.1 MPa is shown in Figure 3.11. Also shown in the figure are results using the present model. The model accurately predicts the void ratio dependency but predicts shear moduli about 20 to 30% low at each pressure. This effect can also be seen in Figure 3.12 that shows the shear modulus of glass beads at a void ratio of 0.60 as a function of confining pressure. Again the predicted shear modulus is low and shows a  $1/3$  power dependence on confining pressure. The experimental data, however, increases in proportion to the 0.43 power of confining pressure. This may be the same effect seen in the wave speed experiments of Duffy and Mindlin where increased confining pressure brought more spheres into contact. Presumably, at higher contact pressures, the slope of the experimental curve would decrease to correspond to the Hertz contact theory. There may be several explanations as to why the model predictions are low. The elastic properties of the glass beads used in the experiment were not reported so there is some uncertainty in the values used in the model ( $E = 6.9 \times 10^4$  MPa,  $\nu = 0.2$ ). The model provides a lower bound on the strain energy which is consistent with the lower prediction of the shear modulus. Finally, the particular choice of the geometry of the unit cell could be an influencing factor since the unit cell underpredicts the number of contact points at a given packing factor for random packed beds. The fact that the model predicted the wave velocity in the steel sphere bar so closely (a case where the unit cell packing factor and coordination number closely match those of the experiment) indicates that the low predicted shear modulus could be attributed to the underprediction of coordination number for random beds.

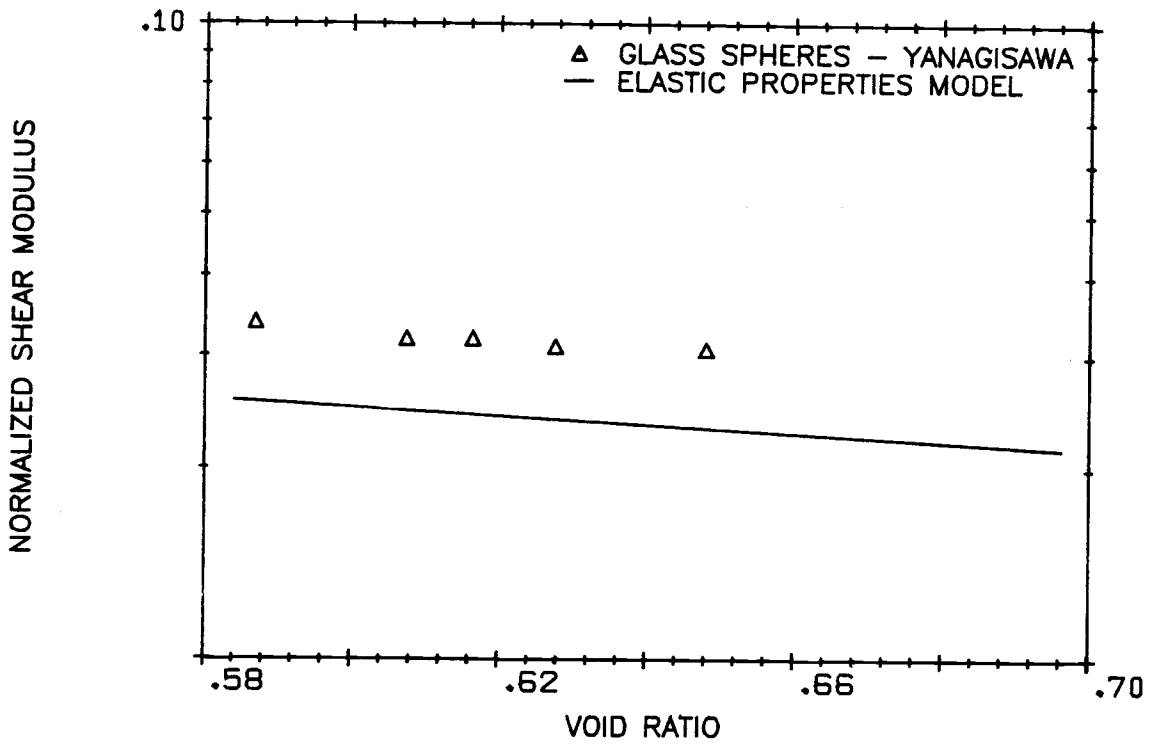


FIGURE 3.11. Elastic Property Model Comparison with Random Sphere Array Shear Modulus Versus Void Ratio

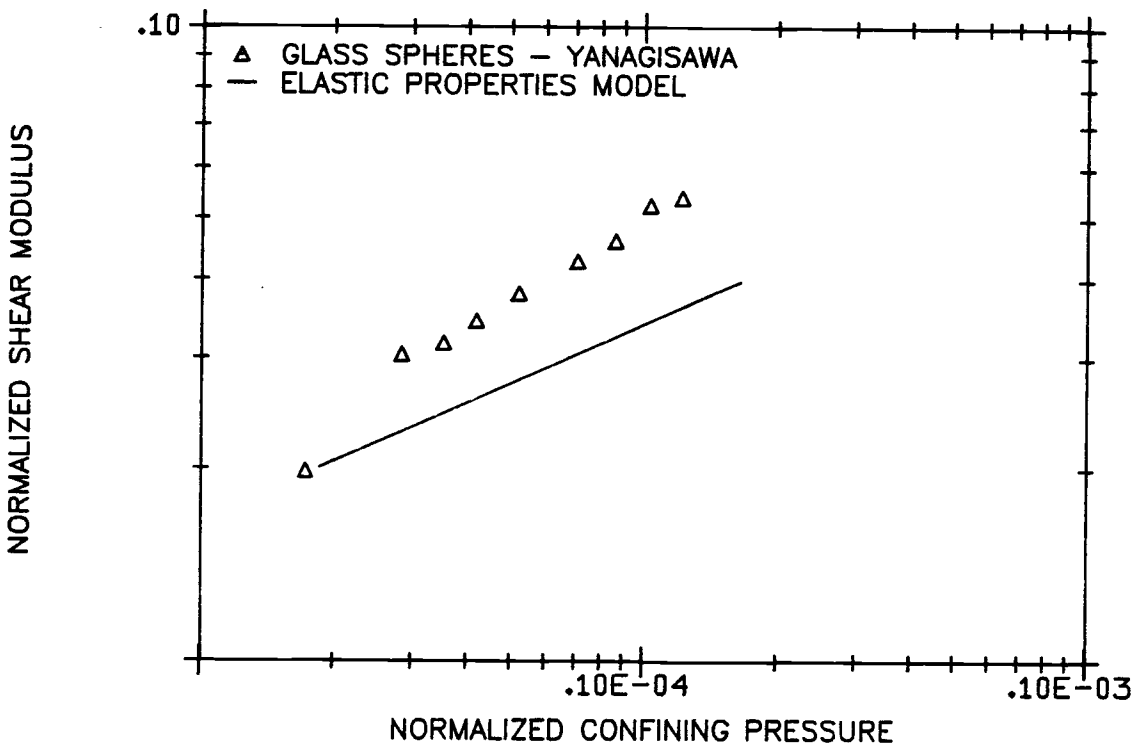


FIGURE 3.12. Elastic Property Model Comparison with Random Sphere Array Shear Modulus Versus Confining Pressure

Based on the above results, the model for predicting the elastic constants of a sphere bed provides reasonable estimates for sphere arrays without necks. No data has been found that gives the elastic properties of a bed with specified necks between particles. As the neck gets very large the elastic properties should approach those of a porous body for which there is some data available. Such a comparison is made in the next section after the extension of the model to a binary sphere array is described.

### 3.7 ELASTIC PROPERTIES FOR A BINARY ARRAY

The model described in Section 3.4 is here extended to provide estimates for the elastic properties of a binary sphere bed. For this model, it is assumed that the bed consists of uniform spheres of two sizes. The smaller spheres must be small enough to easily infiltrate the large sphere array. This will occur if the small-to-large sphere diameter ratio is less than 0.15 as is the case for the EIR sphere pac fuel (diameter ratio  $\sim 0.07$ ). Further, it is assumed that loading of the small spheres can only occur through deformation of the large sphere array. The effective stress on the large spheres are therefore the same as those described in Section 3.1.4 but there is an additional reaction force on the large spheres due to the interaction with the small spheres as depicted in Figure 3.13. As the large sphere array is compressed, the small sphere array is subjected to some boundary displacement due to the contact deformation of the large spheres. The resulting stress in the small sphere array acts to oppose the stress causing the contact deformation in the large sphere array. It is evident then that, under the above assumption, the stresses in the small sphere array will not be the same as those of the aggregate or the large sphere array.

The model for the elastic properties should account for the stresses in each of the large and small sphere arrays separately and relate them to the stresses in the aggregate. The restructuring of

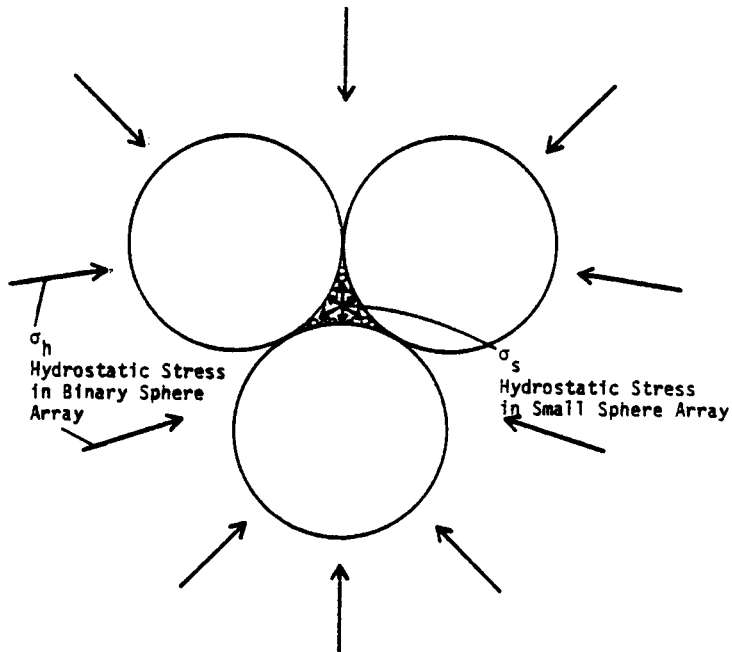


**FIGURE 3.13.** Schematic Diagram of Binary Sphere Array

the binary bed provides another complication in the binary elastic model. The neck growth is dependent (among other parameters) on the contact stresses and on the sphere diameter. The neck growth rate increases with increasing contact pressure and with decreasing sphere diameter. The initial neck growth can be expected to be considerably larger between the small spheres due to the small diameter influence. The neck growth is accompanied by sphere center-to-center approach resulting in shrinkage of the small sphere array. As the small sphere array contracts, the load on the small spheres will be relieved and the contact load on the large spheres will be correspondingly increased. The increased contact load on the large spheres results in increased neck growth between large spheres and more shrinkage of the large sphere array. The shrinkage of the large sphere array results in further interaction with the small sphere array.

A rather simplified model is proposed to account for all of these complex inter-related phenomena. It is much in line with the model

proposed by Brandt (1955) for the effective bulk modulus of a four-sphere size aggregate with a saturating fluid. The theory of composite materials is used to provide an estimate for the second elastic constant.

To obtain an estimate for the bulk modulus of a binary sphere array consider a volume,  $V_B$ , of the array under some hydrostatic stress,  $\sigma_h$ . The binary bulk modulus,  $K_B$ , can be defined by

$$K_B = V_B \frac{\delta\sigma_h}{\delta V_B} \quad 3.49$$

where  $\delta V_B$  is the change in volume  $V_B$  due to a change in the hydrostatic stress,  $\delta\sigma_h$ . Momentarily neglecting the small spheres, a volume change of a large sphere array consists of two parts: a volume change due to deformation in the contact-neck region, and a volume change due to compression of the solid sphere material. The compliance matrix for an array of uniform spheres considered an isotrope can be expressed as

$$[D^0] = A_{CN} [D_{CN}^0] + A_m [D_m^0] \quad 3.50$$

where  $A_{CN}[D_{CN}^0]$  and  $A_m[D_m^0]$  are the isotropic compliance matrices for the contact-neck region and solid body deformations obtained by applying the isotropic relationships (Equations 3.21) to the unit cell compliance matrices,  $A_{CN}[D_{CN}]$  and  $A_m[D_m]$ , derived in Section 3.4. The bulk modulus for each of the two volume change components can be obtained from the respective compliance matrix giving

$$K_L^C = \frac{1}{3A_{CN}(D_{CN11} + 2D_{CN12})} \quad 3.51$$

$$K_L^S = \frac{1}{3A_m \left( \frac{D}{m_{11}} + 2D \frac{1}{m_{12}} \right)}$$

where  $K_L^C$  and  $K_L^S$  are the bulk moduli corresponding to contact-neck deformation and solid body deformation, respectively. The total volume change of the large sphere array is given by

$$\delta V_L = \delta V_L^C + \delta V_L^S \quad 3.52$$

where  $\delta V_L^C$  and  $\delta V_L^S$  are the volume changes due to contact-neck deformation and solid body deformation, respectively.

Now consider again the small spheres in the interstitial spaces of the large sphere array. It is assumed that only contact-neck deformations of the large spheres are responsible for the interaction of the large and small sphere arrays. If the small sphere array has contracted due to sintering shrinkage, some initial load,  $\sigma^*$ , (positive in compression) on the large sphere array will be required before there is any interaction between the large and small spheres. Assume, for now, that the hydrostatic compression on the aggregate is larger than  $\sigma^*$  so that the large and small sphere arrays are interacting. Contact-neck deformations result in a reduction of the interstitial volume of the large sphere array. Therefore, it is assumed that the volume change of the small sphere array is given by

$$\delta V_S = \delta V_L^C \quad 3.53$$

and that the volume change of the binary array is equal to the volume change of the large sphere array.

$$\delta V_B = \delta V_L \quad 3.54$$

Let  $\sigma_s$  be the hydrostatic stress in the small sphere array resulting from the interaction with the large sphere array. Then the various volume changes can be related to the pressure changes by

$$\frac{\delta V_L^S}{V_B} K_L^S = \delta \sigma_h \quad 3.55$$

$$\frac{\delta V_L^C}{V_B} K_L^C = \delta \sigma_h - \delta \sigma_s \quad 3.56$$

$$\frac{\delta V_S}{(1 - pf_L)V_B} K_S = \delta \sigma_s \quad 3.57$$

where  $pf_L$  is the large sphere packing factor. Equation 3.56 relates the large sphere array volume change to the difference between the applied pressure increment and the small sphere stress increment. This is analogous to the effective pressure used in the mechanics of granular media where  $\sigma_s$  corresponds to the pore pressure developed in a saturating liquid. It should be noted that  $K_L^C$  is a function of  $\sigma_h - \sigma_s$  and  $K_S$  is a function of  $\sigma_s$  as these pressures are used to define the contact forces.

Equations 3.49, 3.52, 3.54, 3.55, and 3.56 can be combined to give

$$1/K_B = 1/K_L^S + \frac{1 - \delta \sigma_s / \delta \sigma_h}{K_L^C} \quad 3.58$$

and Equations 3.53, 3.56, and 3.57 combine to yield

$$\delta\sigma_s/\delta\sigma_h = 1 + \frac{K_L^C (1 - pf_L)}{K_S} \quad 3.59$$

Equation 3.59 represents the following differential equation for the small sphere array hydrostatic stress with the functional dependence of  $K_L^C$  and  $K_L$  indicated.

$$d\sigma_s/d\sigma_h = 1 + \frac{(1 - pf_L) K_L^C (\sigma_h - \sigma_s)}{K_S (\sigma_s)} \quad 3.60$$

Recalling that some initial hydrostatic stress on the binary array may be required before there is any interaction between the large and small sphere arrays, the small sphere array hydrostatic stress may be written as

$$\sigma_s = \int_{-\sigma^*}^{\sigma_h} d\sigma_s/d\sigma_h d\sigma_h \quad \text{for } -\sigma_h > \sigma^*$$

$$\sigma_s = 0 \quad \text{for } -\sigma_h < \sigma^* \quad 3.61$$

A numerical procedure is required to solve Equation 3.61 for given values of  $\sigma^*$ ,  $\sigma_h$ , the small and large sphere neck radii, and the temperature dependent elastic properties of the sphere material. In a computer simulation of a sphere-pac fuel pin lifetime irradiation there will be on the order of 10,000 such solutions required. Fortunately, for a given set of parameters,  $d\sigma_s/d\sigma_h$  is nearly independent of the binary array hydrostatic stress. Thus  $d\sigma_s/d\sigma_h$  is treated as an unknown constant and the small sphere array hydrostatic stress is given by

$$\sigma_s = \begin{cases} d\sigma_s/d\sigma_h (\sigma_h + \sigma^*) & -\sigma_h > \sigma^* \\ 0 & -\sigma_h < \sigma^* \end{cases} \quad 3.62$$

An iterative procedure is used to solve for  $d\sigma_s/d\sigma_h$  from Equations 3.60 and 3.62. Once  $\sigma_s$  is determined,  $K_L^c$  can be obtained from Equation 3.51 and the binary bulk modulus calculated from Equation 3.58.

To complete the solution for the binary bulk modulus the initial stress for interaction  $\sigma^*$  is still required. It is assumed that if there has been no shrinkage of either the large or the small sphere array then  $\sigma^* = 0$ , i.e., the initial sphere pack bed is tightly packed. The sintering model provides the sphere center-to-center approach, normalized by the sphere diameter, for the large and small sphere arrays. Let these be  $S_L$  and  $S_S$  respectively. The volume occupied by an array of  $M$  spheres is

$$V = M \frac{4\pi}{3} \frac{R^3}{\rho} \quad 3.63$$

The relative volume decrease associated with a shrinkage,  $S$  is

$$\frac{\delta V}{V} = \frac{1}{V} \frac{dV}{dR} R S = 3S \quad 3.64$$

For a given volume of the binary mixture,  $V_B$ , let  $\bar{\delta V}_S$  and  $\bar{\delta V}_L$  be the volume decreases of the small and large spheres, respectively, due to shrinkage. The volume of the binary must be reduced by an amount

$$\delta V^* = \bar{\delta V}_S - \bar{\delta V}_L \quad 3.65$$

before there will be any interaction between the large and small sphere arrays. Consistent with previous assumptions, the volume change  $\delta v^*$  must be due to large sphere contact-neck deformations only. Thus

$$\frac{\delta V^*}{V} = \int_0^{\sigma^*} \frac{dP}{K_L(P)} \quad 3.66$$

In terms of the large and small sphere shrinkages, the volume change is given by

$$\frac{\delta V^*}{V} = 3 S_S (1 - pf_L) - 3 S_L \quad 3.67$$

Equation 3.66 is easily solved numerically for  $\sigma^*$ . It is assumed that  $\sigma^* = 0$  if  $\delta V^*/V$  from Equation 3.67 is less than zero.

A second constant is required to determine the elastic behavior of the binary array. Paul (1960) derived an expression for Poisson's ratio for a two material composite. If it is assumed that for a composite subjected to uniaxial strain,  $\epsilon_x$ , the strains along the other two coordinates are

$$\epsilon_y = \epsilon_z = -\bar{\nu} \epsilon_x \quad 3.68$$

then the effective Poissons ratio for the composite is

$$\bar{\nu} = \frac{\nu_1(1+\nu_2)(1-2\nu_2)fE_1 + \nu_2(1+\nu_1)(1-2\nu_1)(1-f)E_2}{(1+\nu_2)(1-2\nu_2)fE_1 + (1+\nu_1)(1-2\nu_1)(1-f)E_2} \quad 3.69$$

where the subscripts refer to the two materials and  $f$  is the volume fraction of material 1. Equation 3.69 is used for the effective Poisson's ratio for the binary sphere mixture with  $f$  given by the large sphere packaging factor.

The stress-strain relation for the restructuring sphere bed is then

$$\begin{Bmatrix} \epsilon_x \\ \epsilon_y \\ \epsilon_z \\ \gamma_{xy} \\ \gamma_{xz} \\ \gamma_{yz} \end{Bmatrix} = \frac{1}{\bar{E}} \begin{bmatrix} 1 & -\bar{\nu} & -\bar{\nu} & 0 & 0 & 0 \\ -\bar{\nu} & 1 & -\bar{\nu} & 0 & 0 & 0 \\ -\bar{\nu} & -\bar{\nu} & 1 & 0 & 0 & 0 \\ 0 & 0 & 0 & 2(1+\bar{\nu}) & 0 & 0 \\ 0 & 0 & 0 & 0 & 2(1+\bar{\nu}) & 0 \\ 0 & 0 & 0 & 0 & 0 & 2(1+\bar{\nu}) \end{bmatrix} \begin{Bmatrix} \sigma_x \\ \sigma_y \\ \sigma_z \\ \tau_{xy} \\ \tau_{xz} \\ \tau_{yz} \end{Bmatrix}$$

3.70

where  $\bar{E} = K_B 3(1-2\bar{\nu})$ .

Thus, an elastic stress-strain relation has been obtained for restructuring sphere pac fuel that depends on sphere properties, packing, restructuring (neck growth), and hydrostatic stress in the fuel. No experimental data has been found for the elastic properties of a binary sphere array such as the one used for the EIR fuel. Some representative results are provided here to show the effect of the various parameters on the effective elastic properties.

Figures 3.14 and 3.15 show the effective elastic modulus and Poisson's ratio of a binary sphere array as a function of the neck radius of the small spheres. Results are plotted for three values of the normalized confining pressure,  $P/E$ , where  $E$  is the elastic modulus of the sphere material. Poisson's ratio for the sphere material represented in these plots is 0.3. The packing factors for the large and small spheres are 0.61 and 0.56 respectively. The neck ratio of the large spheres was assumed to be 1/2 the neck ratio for the small

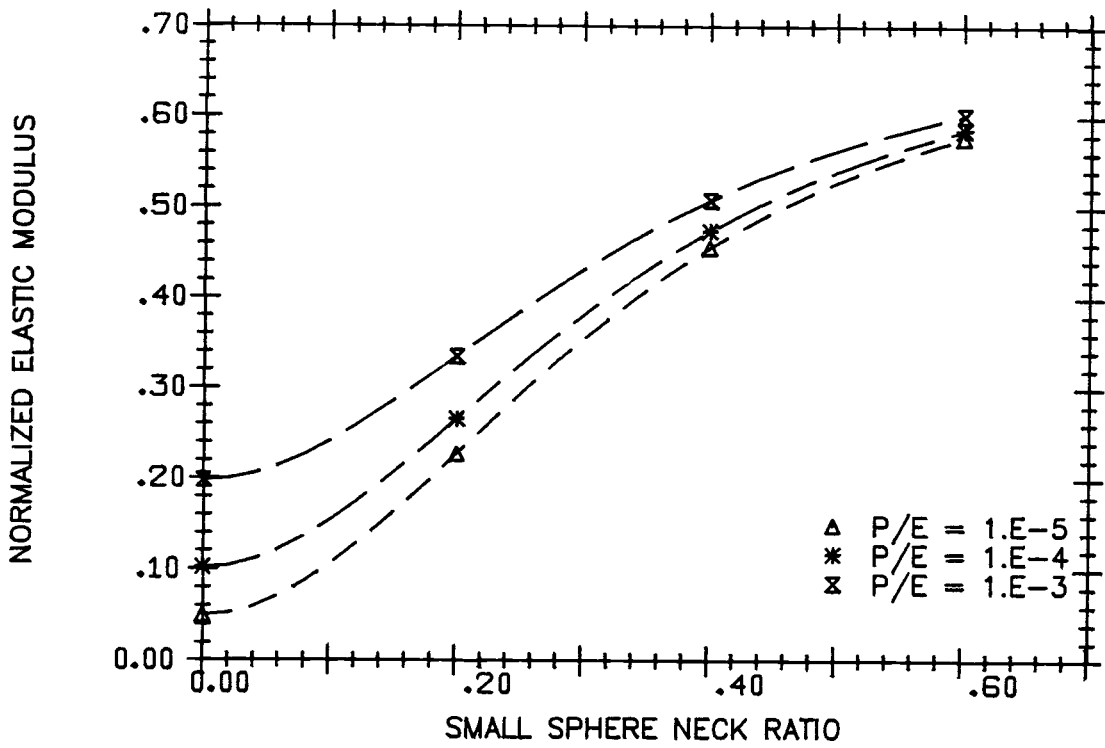


FIGURE 3.14. Effective Young's Modulus Versus Neck Ratio for a Binary Sphere Array

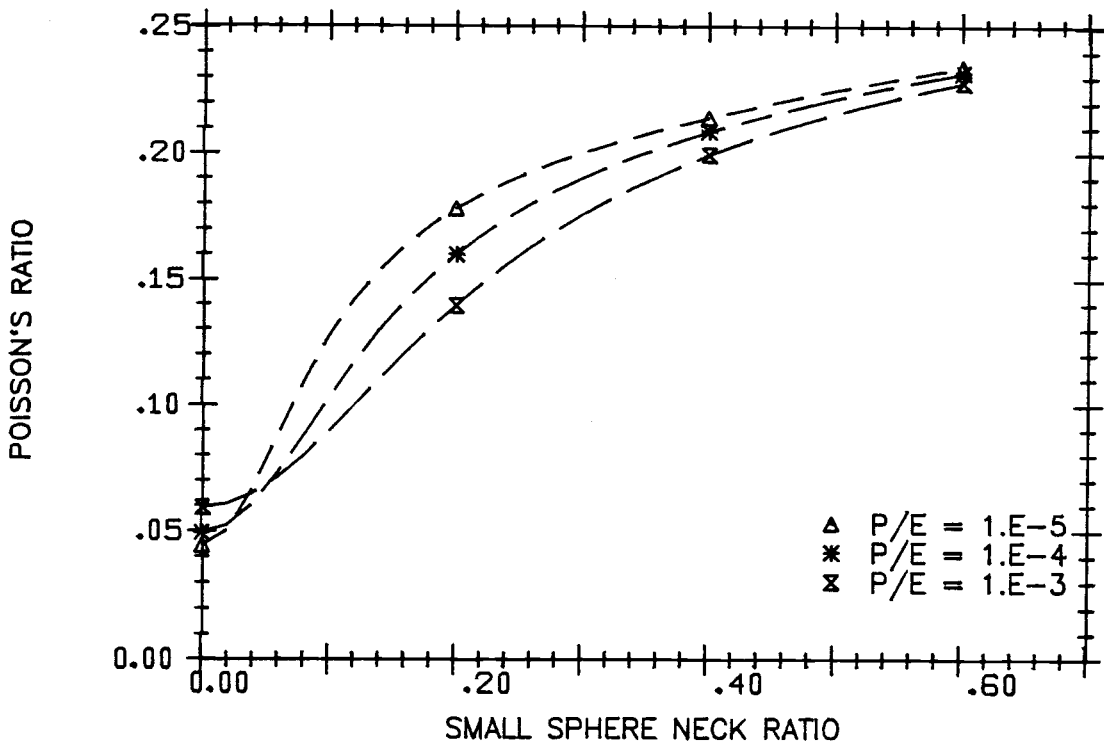


FIGURE 3.15. Effective Poisson's Ratio Versus Neck Ratio for a Binary Sphere Array

spheres. This approximates the fuel restructuring during the initial stages of the neck growth. For these simulations it was assumed that there was no shrinkage of the small or large sphere arrays. The general trends for the elastic modulus and Poisson's ratio of the binary sphere array are similar to those observed for the single size sphere array. The binary array elastic modulus is about a factor of two larger than that for the single size sphere array at small neck ratios and is about 20% larger at large neck ratios. Poisson's ratio is nearly the same for the binary and single size arrays.

The elastic constants appear to approach a limit as the neck ratio gets large. From geometry considerations, at neck ratios of about  $\sim 0.45$  closed pores begin to form and the fuel no longer resembles a sphere bed. An estimation of the elastic properties of a continuous material with distributed porosity can be obtained from the model by calculating the properties with both the small and large sphere neck ratios set to 0.5. Various material porosities can be modeled by changing the initial packing factors for the two sphere sizes. This procedure was used to obtain model-predicted elastic constants of porous material as a function of porosity. Results are shown in Figure 3.16 and compared to some existing theories and experimental results as presented by Marlowe and Wilder (1965). The model compares very well with the experimental data by Marlowe and Wilder for yttrium oxide and with Gatto's (1950) theory in the range of interest for sphere pac fuel.

Figure 3.17 shows the small sphere array pressure derivative,  $d\sigma_s/d\sigma_h$  as a function of the small sphere neck ratio. Here, again, the large sphere neck ratio was taken as 1/2 the small sphere neck ratio. As previously indicated, it can be observed in Figure 3.17 that the pressure derivative is fairly insensitive to the hydrostatic stress in the binary array. For  $\sigma^* = 0.$ , the hydrostatic stress in the smaller sphere array is between 75 and 85% (depending on neck ratio) of the binary array hydrostatic stress.

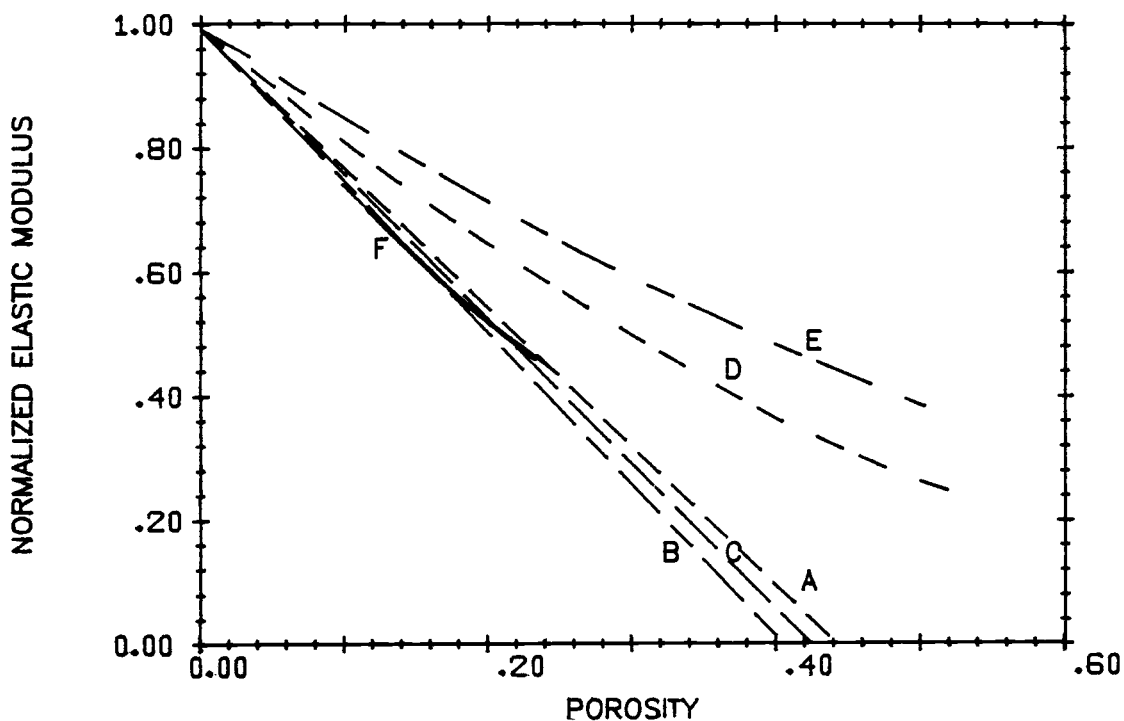


FIGURE 3.16. Young's Modulus for Restructured Fuel as a Function of the Initial Porosity. A) fit to data for UC (Padel, B) fit to data for  $Y_2O_3$  (Marlowe and Wilder), C) Gatto's theory, D) MacKenzie's Theory, E) Hashin's Theory, F) Present Model

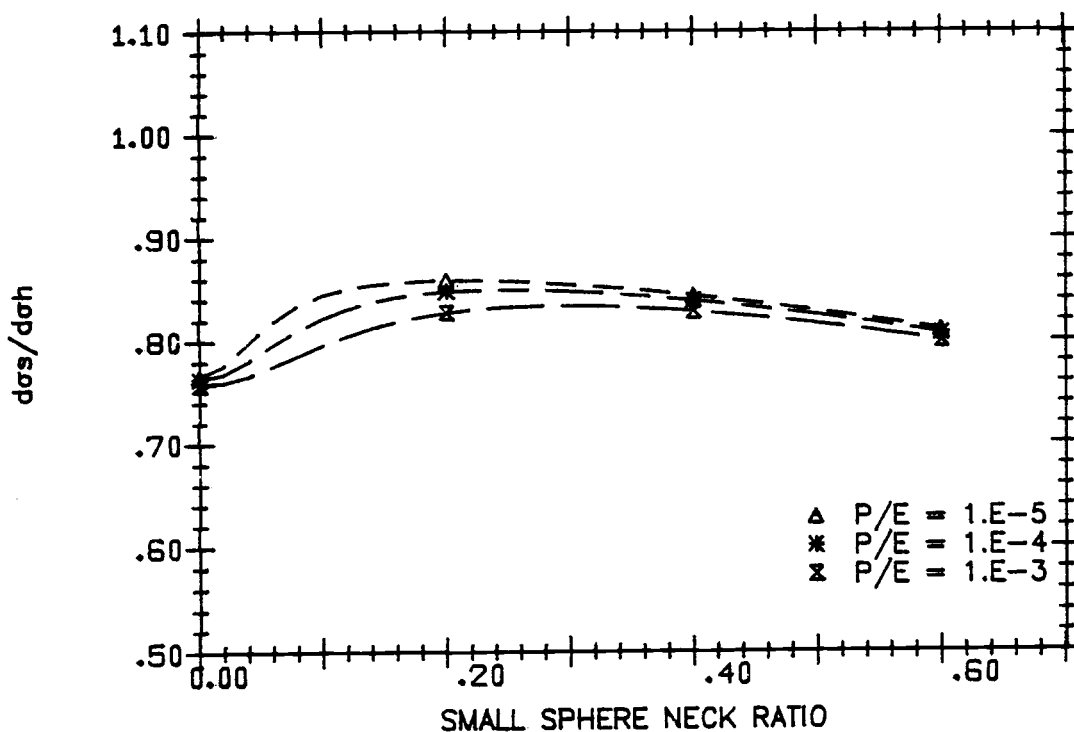


FIGURE 3.17.  $d\sigma_s/d\sigma_h$  Versus Small Sphere Neck Ratio

For the previous results it was assumed that there was no shrinkage of the large or small sphere arrays. Figures 3.18 and 3.19 show the effect on the elastic modulus and Poisson's ratio of some shrinkage in the small sphere array. The plots show the elastic property as a function of the normalized confining pressure on the binary array. Table 3.1 shows the values used for the large and small sphere neck radii and the small sphere array shrinkage for each of the three curves in Figures 3.18 and 3.19.

TABLE 3.1. Shrinkage and Neck Ratios Values for the Curves on Figures 3.18 and 3.19

<u>Curve</u>	<u>(X/R)<sub>S</sub></u>	<u>(X/R)<sub>L</sub></u>	<u>S<sub>S</sub></u>
1	0.05	0.025	0.005
2	0.10	0.05	0.01
3	0.20	0.10	0.02

The initial stress,  $\sigma^*$ , required to bring the large and small sphere arrays into contact is clearly evident in the first two cases shown in Figure 3.18. For the third case  $\sigma^*$  was never reached.

$\sigma^*$  increases as the small sphere array shrinkage increases and as neck radius in the large sphere array increases.

Although the data for elastic properties of sphere arrays is limited (and even more so for restructuring beds), there is enough evidence to indicate that the model presented here can be used to provide reasonable approximations for the elastic properties of a restructuring sphere pac fuel bed. It is difficult to determine whether or not the proposed model represents a conservative estimate of the elastic properties in terms of the effect on the overall pin behavior during irradiation. If the stiffness is too small, the cladding stresses due to fuel thermal expansion will be underpredicted. If the stiffness is too large, higher contact stress

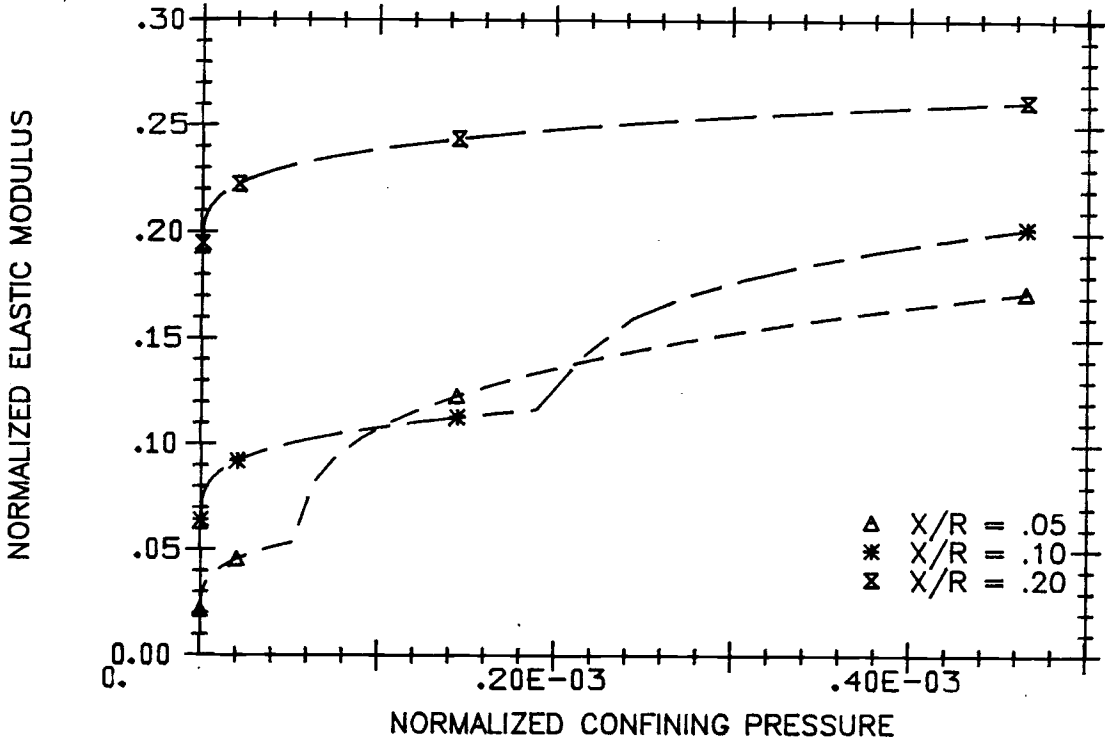


FIGURE 3.18. Young's Modulus for Restructuring Fuel with Shrinkage of Small Sphere Array

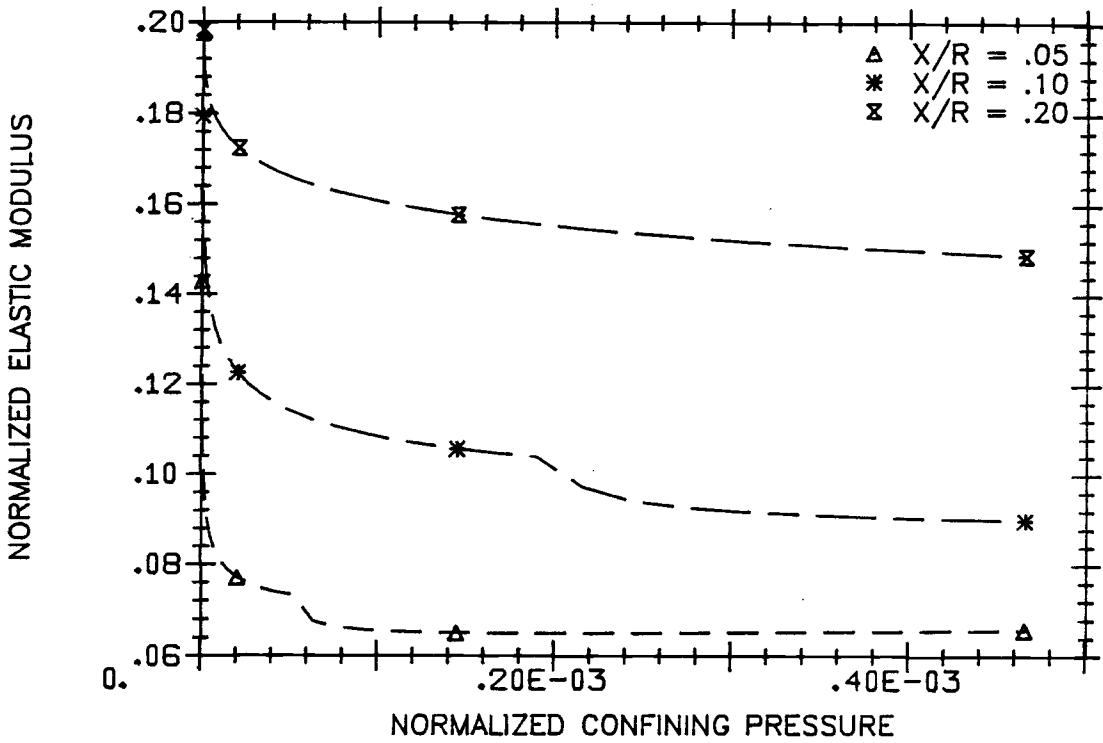


FIGURE 3.19. Poisson's Ratio for Restructuring Fuel with Shrinkage of Small Sphere Array

will result and the restructuring rate may be overpredicted and therefore give smaller cladding stress. Until experimental data is available, the proposed model must be accepted as a "best estimator" for the elastic properties.

### 3.8 ELASTIC PROPERTIES FOR RESTRUCTURED FUEL

Once the sintering process reaches the point where pores begin to close up, the fuel can be considered to have properties similar to those of a porous pellet. Since there is little data available for the elastic properties of (U,Pu)C, the properties of UC are used. The restructured fuel properties are assumed to depend only on the fuel temperature and porosity. Table 3.2 gives the temperature and porosity dependence for two sets of data.

TABLE 3.2. Porosity and Temperature Effects on Elastic Properties of UC

$E_0$ (at 25°C) (Mpa)	$-\frac{\partial E/E_0}{\partial T}$ (°C <sup>-1</sup> × 10 <sup>-4</sup> )	$-\frac{\partial E/E_0}{\partial p}$	$\nu_0$ (at 25°C)	$-\frac{\partial \nu/\nu_0}{\partial T}$	$-\frac{\partial \nu/\nu_0}{\partial \alpha_p}$	Reference
2.25 × 10 <sup>5</sup>	0.814	2.31	0.29	—	0.99	Padel and de Novon (1969)
	1.10	—	0.29-0.30	0.29	—	Hall (1970)

In addition, Padel, et al. (1970) reported the elastic modulus and Poisson's ratio of 90.1% dense (U,Pu)C at 25°C as 1.83 × 10<sup>5</sup> MPa and 0.265 respectively. From the results in Table 3.2, the elastic properties of (U,Pu)C are given by

$$E = 2.25 \times 10^5 (1.0 - 2.31p)(1.0 - 1.0 \times 10^{-4}T) \text{ MPa} \quad 3.71$$

$$\nu = 0.29 (1.0 - 0.99p)(1.0 - 0.29 \times 10^{-4}T) \quad 3.72$$

where  $p$  is the porosity and  $T$  is the temperature in degrees C.

Equations 3.71 and 3.72 are also used for calculating the elastic properties of individual fuel spheres, as this information is required in the model to predict the sphere array effective properties. In this case the as-fabricated porosity of the fuel spheres is used in Equations 3.71 and 3.72. The fuel is claimed to be restructured when the neck ratio of the small sphere array reaches 0.45. The elastic properties predicted by the model for restructuring fuel are about 10% lower than those given by Equations 3.71 and 3.72 when the  $X/R = .45$  limit is reached. This difference in stiffness is attributed to the formation of closed pores towards the end of initial stage sintering. This closure of pores is not accounted for in the restructuring fuel elastic property model. To provide a smooth transition from restructuring to restructured fuel properties, the restructuring fuel properties are averaged with the restructured fuel properties after the small sphere neck ratio reaches 0.4. The transition properties are given by

$$E_T = (\bar{x}_s - .4)20. (E_{rd} - E_{rg}) + E_{rg} \quad 3.73$$

$$\nu_T = (\bar{x}_s - .4)20. (\nu_{rd} - \nu_{rg}) + \nu_{rg} \quad 3.74$$

for  $.4 < \bar{x}_s < .45$ . The subscripts  $rg$  and  $rd$  refer to restructuring and restructured fuel, respectively and  $\bar{x}_s$  is the small sphere neck ratio.

#### 4.0 PLASTIC CONSTITUTIVE RELATIONS FOR SPHERE PAC FUEL

The elasto-plastic stress-strain relation given by Equation 2.18 requires the plastic modulus matrix. This matrix is defined in terms of a yield function and a plastic potential function (Equation 2.15). The yield and potential functions may depend on the material properties, load state, and accumulated plastic strain. For the restructuring fuel, the yield and potential function will also depend on the changes in the macroscopic material properties due to the restructuring process. Yielding and plastic flow for completely unrestructured fuel is expected to be similar to the plastic behavior of granular materials while the completely restructured fuel should exhibit plastic behavior similar to that of porous ceramic solids. The yield and potential functions developed in this chapter reflect this transition from granular to solid material and provides a first estimate for the plastic modulus matrix.

#### 4.1 PLASTIC CONSTITUTIVE EQUATIONS FOR GRANULAR MEDIA

##### 4.1.1 Plastic Yield Functions

The stress-strain behavior of typical granular material samples is shown in Figure 4.1. Figure 4.1a shows a stress-strain curve for a triaxial compression test where the sample is first loaded with some hydrostatic compression  $P$ , and then an additional load,  $\sigma_1$  is applied uniaxially. The response to the initial loading up to point 2 is similar to that of solid materials in that there is first some linear relationship between stress and strain to point 1, followed by some nonlinear response to point 2. Unloading at point 2 reveals that the nonlinear strain between points 1 and 2 is irrecoverable and therefore plastic. From point 2 the material is unloaded and, after recovering the elastic strain, begins to deform plasticly in the reverse direction even before the uniaxial load is completely removed. Reloading from 3 brings the sample back onto the initial loading curve at 2. From the stress-strain curve it can be observed that the yielding is

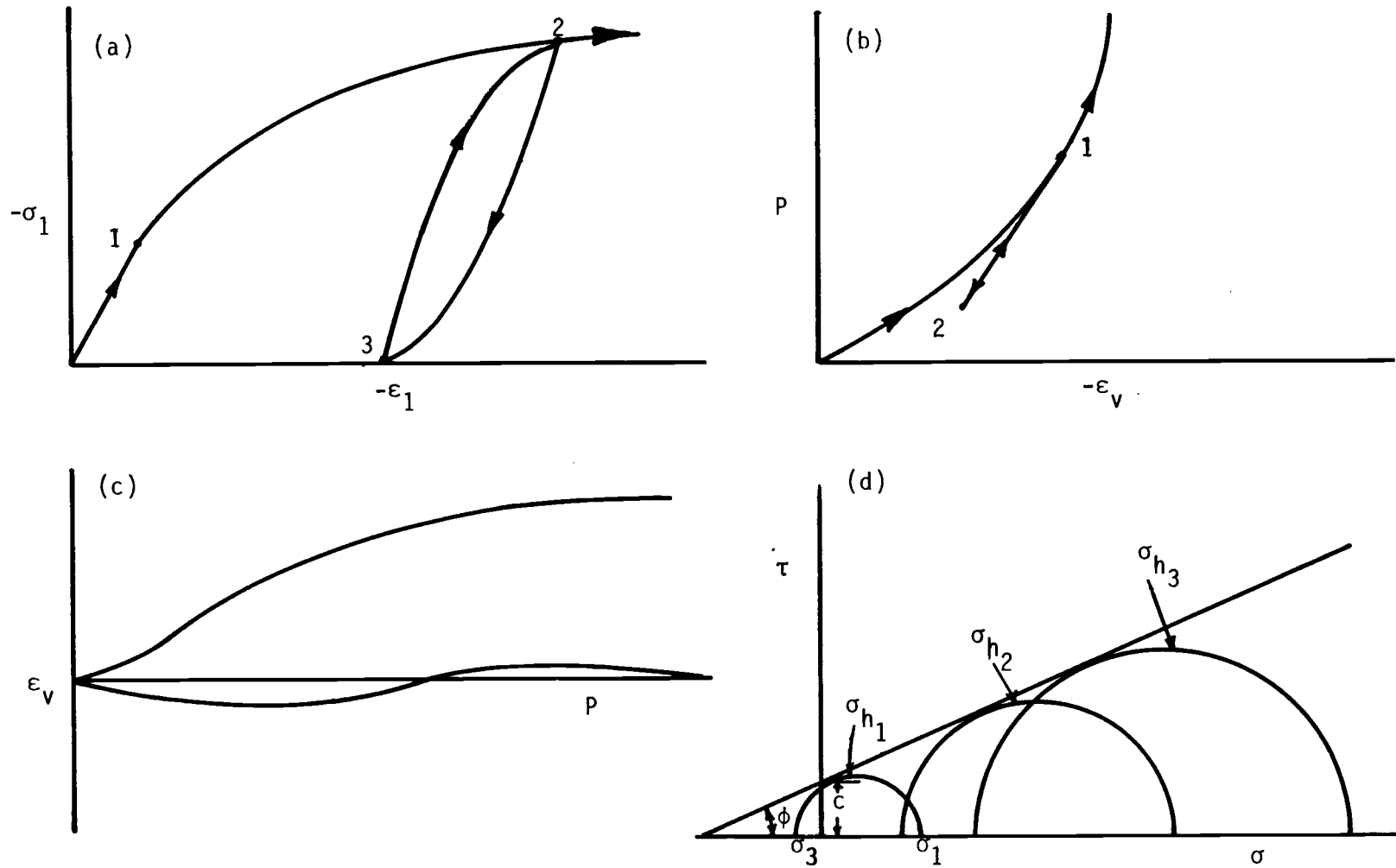


FIGURE 4.1. Stress-Strain Behavior of Granular Materials  
 a) triaxial compression, b) hydrostatic compression,  
 c) dilatation under shearing, d) Mohr-Coulomb envelope

anisotropic (i.e., yielding in compression is not the same as yielding in tension) and there is some kinematic hardening of the sample. Depending on the initial compaction of the sample the material may experience some kinematic softening rather than hardening after the initial yield point is reached. Figure 4.1b (Christian and Desari, 1977) shows the volumetric strain response to hydrostatic compression of a previously uncompacted sample. The sample contracts nonlinearly in response to the hydrostatic compression up to 1. Unloading from 1 follows a linear elastic response curve indicating that some of the initial volume change is irrecoverable or plastic. Figure 4.1c (Harr, 1977) shows the response of a granular sample when it is strained under some shearing force. A sample that is initially densely compacted will expand in volume under the shearing action. This response is termed dilatancy and is a major difference between granular and solid materials which generally maintain constant volume during plastic deformation. A loosely compacted sample may initially contract during the shearing process. Samples that do not change volume appreciably during plastic shear are said to be at the critical void ratio.

The plastic deformation of granular material involves individual grains sliding across one another. The surface friction and the contact load between particles are therefore important factors in determining the plastic behavior of granular material. Figure 4.1d shows the Mohr circles at yield plotted for a series of triaxial compression tests at various levels of hydrostatic compression. The shear strength increases linearly with increasing hydrostatic compression. Mohr and Coulomb (see, e.g., Zienkiewicz and Humpheson, 1977) proposed a yield criteria that describes the envelope of the Mohr's circles shown in Figure 4.1d. The yield function can be written as

$$f = \tau_{\max} + \left( \frac{\sigma_1 + \sigma_3}{2} - \frac{C}{\tan \phi} \right) \sin \phi \quad 4.1$$

where  $\tau_{\max}$  is the maximum shear stress,  $\sigma_1$  and  $\sigma_3$  are the maximum and minimum principal stresses,  $C$  is the cohesion, and  $\phi$  is the internal friction angle. For a friction angle of zero, Equation 4.1 reduces to the Tresca or maximum shear yield criteria if  $C$  is the shear yield strength. Mathematically, Equation 4.1 is difficult to work with since the minimum and maximum stresses must be found before the yield criteria can be applied and the surface has sharp corners. Drucker and Prager (1952) proposed a von Mises form of the frictional yield criteria given by

$$f = \alpha I_1 + J_2^{1/2} - k \quad 4.2$$

where  $\alpha$  and  $k$  are parameters that depend on the friction angle and cohesion of the material.  $I_1$  is the first invariant of the stress tensor

$$I_1 = \sigma_{ij} \quad 4.3$$

and  $J_2$  is the second invariant of the stress deviator tensor

$$J_2 = 1/2 s_{ij}s_{ij} = 1/2 [(\sigma_1 - \sigma_h)^2 + (\sigma_2 - \sigma_h)^2 + (\sigma_3 - \sigma_h)^2]$$

4.4

where  $s_{ij}$  is the stress deviator tensor,  $\sigma_h$  is the hydrostatic stress and  $\sigma_1, \sigma_2, \sigma_3$  are the principal stresses. The Drucker-Prager criteria has been used extensively in soil and rock mechanics because of

its mathematically convenient form even though there is evidence that the Mohr-Coulomb criteria better predicts the yielding of granular material (Bishop, 1966). Assuming that the Mohr-Coulomb surface is a true representation of the material yield surface, then the parameters  $\alpha$  and  $k$  in the Drucker-Prager criteria should be chosen so that the Mohr-Coulomb surface is closely approximated. In stress space, the Mohr-Coulomb surface is a six-sided pyramid while the Drucker-Prager surface is a circular cone. Figure 4.2 shows the intersection of the Mohr-Coulomb surface with the octahedral plane along with some possible choices for the Drucker-Prager surface. By choosing the external envelope for the Drucker-Prager criteria the yield surface reduces to the von Mises surface for zero friction angle. The proper definitions for  $\alpha$  and  $k$  for this surface are given by (Zienkiewicz and Humpheson, 1977)

$$\alpha = \frac{2 \sin \phi}{\sqrt{3} (3 - \sin \phi)} \quad k = \frac{6C \cos \phi}{\sqrt{3} (3 - \sin \phi)} \quad 4.5$$

Drucker and Prager (1952) proposed other definitions for  $\alpha$  and  $k$  by matching the Mohr-Coulomb criteria for plane strain. These Drucker-Prager parameters define a lower bound on the Mohr-Coulomb criteria. The upper bound parameters can be as much as 50 percent larger than the lower bound parameters for reasonable values of the friction angle ( $\phi < 35^\circ$ ).

The yield surface described so far cannot account for the experimentally observed kinematic hardening or the plastic deformation under hydrostatic stress. Drucker, Gibson and Henkel (1957) proposed that the Drucker-Prager yield surface should have a spherical end cap, the position and size of which would depend on the plastic volumetric strain. The model predicted qualitatively the experimentally observed behavior of soils, but no mathematical definition of the yield surface was given. The hardening predicted by the model results from the

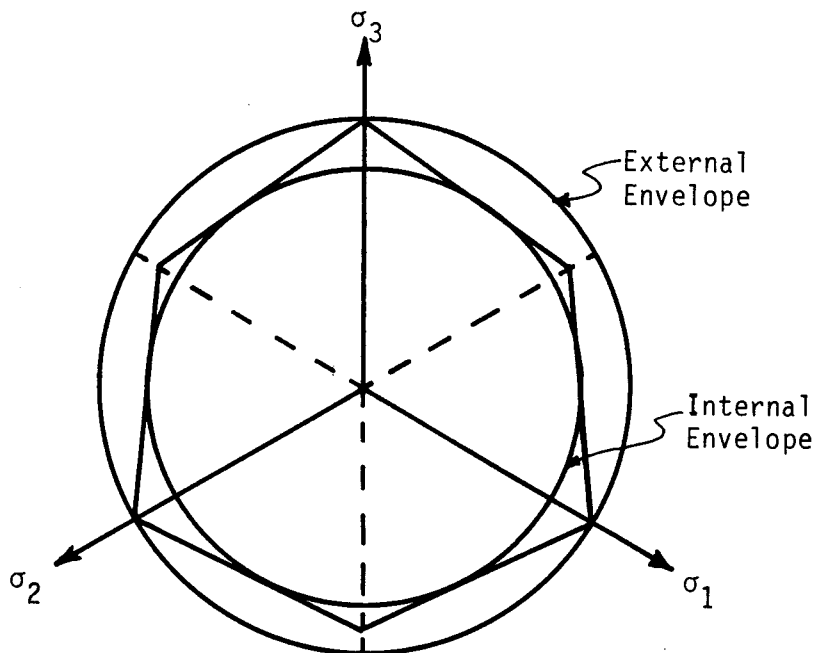
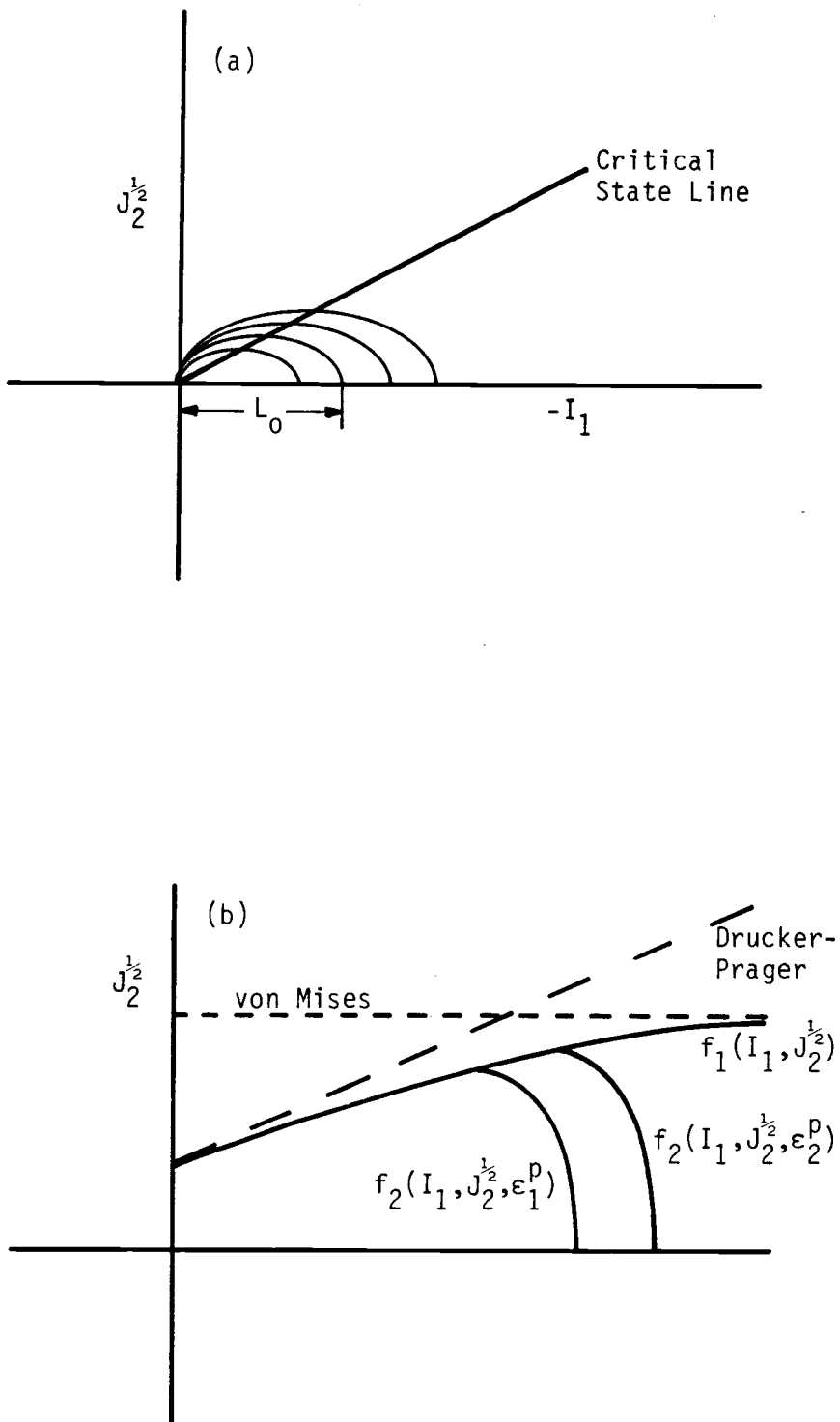


FIGURE 4.2. Mohr-Coulomb and Drucker-Prager Yield Surfaces On the Octahedral Plane

movement of the end cap away from the cone vertex as the plastic volumetric strain increases negatively.

There have been several variations on the capped end model. Roscoe and Burland (1968) proposed that the yield surface could be represented as an ellipse in the  $I_1, \sqrt{J_2}$  plane. Figure 4.3 shows a series of elliptic yield functions for a frictional material undergoing plastic deformation. The size of each ellipse is determined by the critical state line which passes through the end of the minor axis of each ellipse. Loading at points to the right of the critical state line result in negative volumetric plastic strain while loading at points to the left cause positive volumetric strain. The major axis of each ellipse depends on the volumetric plastic strain, and experimentally determined values for the initial void ratio, swelling and compression indices, and an initial value for the length of the major



**FIGURE 4.3.** Capped Yield Surfaces for Frictional Material  
 a) Roscoe and Burland, b) Dimaggio and Sandler

axis,  $L_0$ . The initial major axis length depends on the preconsolidation pressure to which the material was subjected. As the material is subjected to larger and larger compressive hydrostatic stress the major axis length increases and the minor axis length is determined by the critical state line.

Dimaggio and Sandler (1971) proposed a capped model that uses two yield functions as shown in Figure 4.3b. The first function,  $f_1$ , assumes perfect plasticity and defines a failure envelope similar to the Mohr-Coulomb envelope. The second function,  $f_2$ , accounts for the strain hardening and volumetric strains under hydrostatic load. A total of eight experimentally determined parameters, including two effective elastic constants, are required to explicitly define the yield surface. The model was in good agreement with experimental results on dry sand.

The capped models can predict the hardening (or softening) behavior of granular materials, but all hardening is assumed isotropic. Mroz, Norris and Zienkiewicz (1978) proposed a hardening model that accounts for the anisotropic behavior. The model uses a bounding surface determined by the preconsolidation of the material. The yield surface (similar to that proposed by Roscoe) translates and contracts within the bounding surface. The translation and contraction depends on the hardening parameters of the materials. If the yield surface contracts the bounding surface expands isotropically in accordance with a consolidation hardening parameter. The model qualitatively predicts the anisotropic behavior of granular materials for some assumed functional forms of the hardening parameters.

Recent literature (Tatsuoka, 1980; Mullenger and Davis, 1981) indicates that there is still ongoing work to determine a yield criteria that encompasses all of the observed behavior of granular materials with a minimum of experimentally obtained parameters.

#### 4.1.2 Plastic Potential Function

The specification of the plastic behavior of any material depends not only on the yield function but also on the plastic potential function that prescribes the relative magnitude of the plastic strain components. The standard practice of assuming that the yield and potential surface are the same predicts plastic behavior that is not in satisfactory agreement with experiment when using such yield models as the Mohr-Coulomb or Drucker-Prager surfaces. Since the plastic strain direction is normal to the plastic potential surface, these theories always predict some dilation. While tightly compacted samples do expand when sheared plasticly, the volumetric strain is generally less than that predicted by the Mohr-Coulomb type models, and loosely compacted samples may contract rather than expand. This fact led to the formulation of the critical state models that predict contraction or expansion depending upon which side of the critical state line the material resides. The critical state models for yielding were developed with the idea that they would also provide the plastic potential surface giving an associated flow law. Most plasticity models for granular material incorporate an associated flow law regardless of the yield criteria chosen. However, there have been some attempts to formulate nonassociated flow laws.

Poorooshasb, Holubec and Sherbourne (1966, 1967) obtained a plastic potential surface from experimental results on sand in triaxial compression tests. The potential surface shape was very close to the yield surface proposed by Roscoe. An experimentally determined yield surface was similar to the Mohr-Coulomb surface. Lade and Duncan (1975) fitted yield and deformation results for dry sand using a yield function of the form

$$f = I_1^3 / I_3 - k_1 \quad 4.6$$

and a potential function

$$g = I_1^3/I_3 - k_2 \quad 4.7$$

where  $I_3$  is the third invariant of the stress tensor ( $I_3 = \sigma_1 \sigma_2 \sigma_3$ ) and  $k_1$  and  $k_2$  are experimentally determined parameters.  $k_1$  and  $k_2$  were found to be linearly related as

$$k_2 = Ak_1 + 27(1 - A) \quad 4.8$$

Both  $A$  and  $k_1$  can be determined from triaxial tests only. Work hardening was also considered and an expression given for  $k_1$  that again involved parameters determinable from triaxial compression tests. One advantage of the yield function chosen by Lade and Duncan is that the surface shape closely approximates the shape of the Mohr-Coulomb surface. The model does not have a capped end but was applied only to preconsolidated samples so that the Mohr-Coulomb type yield surface was adequate.

It is not yet clear whether a nonassociated flow law is required to predict the deformation of granular material or if a more versatile yield criteria with associated flow will suffice. Most of the effort has been toward developing a yield surface that can also be used as the potential surface.

#### 4.1.3 Micromechanical Models

The previously discussed models for a yield surface and plastic potential surface are based on experimental results from samples of granular material treated as a continuum. Another possible approach is to try to predict the macroscopic behavior of a granular material

by considering the behavior of individual grains. This approach was taken by Rowe (1962) (and further developed by Horne (1965)) when he derived a stress-dilatancy law by considering the interaction of individual spheres in regular packings under triaxial test conditions. By minimizing the amount of energy lost to heat during intergrain sliding, Rowe obtained a stress-dilatancy law which relates the dilation to the stress ratio,  $\sigma_1/\sigma_3$  and the friction angle,  $\phi_\mu$ .  $\sigma_1$  is maximum principal stress and  $\sigma_3$  is the principal stress in the orthogonal directions. The friction angle,  $\phi_\mu$ , is not the internal friction angle of the Mohr-Coulomb criteria but is the static friction angle for a sphere on a flat surface. The stress-dilatancy law worked well for regular packings, but for random packings it was necessary to replace  $\phi_\mu$  by  $\phi_f$  which was allowed to vary to fit the dilatancy for various loading and initial packing densities. Presumably, this was to account for the rearrangement of particles and the corresponding change in the number of active contacts (contacts where sliding occurs) as a random packing is loaded.

Recently, there have been several micromechanical models [Christoffersen, Mehrabadi and Nemat-Nasser (1981); Tokue (1979); Matsuoka and Takeda (1980); Nemat-Nasser (1980); and Uda, Konishi and Nemat-Nasser (1980)] that at least qualitatively predict the macroscopic stress-strain behavior of granular systems. Generally these theories consider an individual rigid grain, or cluster of grains which act as one grain, together with the direction and magnitude of the contact forces at active contacts. By assuming various spatial distributions of the active contact orientations and applying force and moment equilibrium for individual grains, macroscopic stresses can be related to the contact force distribution. Macroscopic kinematic relationships can also be obtained from the contact orientation distribution. A stress-displacement relationship is obtained by assuming that energy is dissipated only by frictional sliding. The external work by the macroscopic stresses can therefore be equated to the internal frictional sliding work. Some of the theories also account

for variations in the active contact distribution as loading proceeds to model the experimentally observed strain hardening or softening.

#### 4.1.4 Application to Restructuring Sphere Pac Fuel

The plastic stress-strain theory for granular materials is still clearly in a development stage. There is no fundamental agreement as to the best yield criteria or plastic potential or even if the classical continuum plasticity theory applies to granular material. For sphere pac fuel, the sintering mechanism further complicates the situation since any model must be able to account for the changing cohesion. Further, since the stresses and temperatures anticipated in a fuel pin are much larger than those generally considered in soil mechanics, the yielding under hydrostatic stress may be of an entirely different nature. In the mechanics of granular material, yielding under hydrostatic stress is considered to be associated with particle rearrangement. In sphere pac fuel the high temperatures and high contact stress can result in local yielding at contacts when the aggregate is under hydrostatic compression.

Based on the review of the plastic behavior of granular materials and the above observations, a plasticity model for sphere pac fuel is developed in accordance with the following:

1. Since the loading of the fuel is in one direction (with possible unloading only to the initial load state) the anisotropic yielding can be ignored and the Drucker-Prager yield criteria applies.
2. Large hydrostatic stresses can result in local yielding at contacts and a cap is provided for the surface to account for this yielding.
3. A plastic potential function is chosen that does not allow dilation under shear.
4. The parameters  $\alpha$  and  $k$  in the Drucker-Prager yield law can be suitably modified to account for the neck growth effects so that

the yield law becomes the von Mises criteria for completely restructured fuel.

#### 4.2 FRICTIONAL YIELDING

Under the above assumptions the frictional yield surface for an array of uniform spheres undergoing restructuring can be given by a generalization of Equation 4.2:

$$f_1 = \alpha I_1' + J_2^{1/2} - k(\bar{x}) \quad 4.9$$

The functional dependence of the parameter  $k$  on the neck ratio,  $\bar{x}$ , is noted and  $I_1'$  is the effective stress invariant (three times the effective hydrostatic stress) for computing the frictional effect on yielding. Since Equation 4.9 should approach the von Mises yield law as the neck ratio gets large, the relationship between  $\alpha$  and  $k$  and the friction angle and cohesion are chosen as Equations 4.4 where the cohesion,  $C$ , depends on the neck ratio.

The effective hydrostatic stress for friction effects is assumed to be that portion of the stress supported by the contact (the neck supporting the rest). Assuming again that the neck and contact stiffnesses act in parallel, that the contact-neck load is proportional to the hydrostatic stress, and that the neck and contact deformation are equal, the expression for the stress supported by the contact can be obtained. Let  $F_T$  be the total contact-neck load,  $F_N$  the portion of  $F_T$  supported by the neck and  $F_C$  the portion of  $F_T$  supported by the contact. Then

$$I_1/I_1' = F_T/F_N = 1 + F_C/F_N \quad 4.10$$

and assuming equal deformation of the neck and contact gives

$$I_1/I'_1 = 1 + k_N/k_C \quad 4.11$$

where  $k_N$  and  $k_C$  are the neck and contact stiffnesses, respectively. The stiffness ratio is obtained from the elastic stress-strain model (Equation 3.37) resulting in

$$k_N/k_C = \frac{E\pi x^2}{\lambda_{\text{eff}}} \frac{4Q}{3a} \quad 4.12$$

Thus, as the neck ratio gets large,  $I'_1$  approaches zero and the frictional effects in the yield law become small. Equation 4.9 can be rewritten in terms of an effective friction angle (or the equivalent  $\alpha$  parameter) as

$$f = \alpha' I_1 + J_2^{1/2} - k(\bar{x}) \quad 4.13$$

where

$$\alpha' = \alpha / (1 + k_N/k_C) \quad 4.14$$

The effective friction angle,  $\phi_e$ , is then computed from Equation 4.5 so that

$$\alpha' = \frac{2 \sin \phi_e}{\sqrt{3} (3 - \sin \phi_e)} \quad 4.15$$

Then, dividing Equation 4.15 by Equation 4.5, the effective friction angle is given in terms of the stiffness ratio and the initial friction angle ( $\bar{x} = 0$ ) as

$$\alpha'/\alpha = \frac{1}{1 + k_N/k_C} = \frac{\sin \phi_e}{(3 - \sin \phi_e)} \frac{(3 - \sin \phi)}{\sin \phi} \quad 4.16$$

or

$$\frac{\sin \phi_e}{3 - \sin \phi_e} = \frac{\sin \phi}{3 - \sin \phi} \frac{1}{1 + k_N/k_C} \quad 4.17$$

Equation 4.17 implies that as the neck radius increases, the effective friction angle decreases as required.

The second parameter,  $k$ , in Equation 4.13 is now defined in terms of the material cohesion and the effective friction angle via Equation 4.5 giving

$$k = \frac{6 C(\bar{x}) \cos \phi_e}{\sqrt{3} (3 - \sin \phi_e)} \quad 4.18$$

As  $\phi_e$  approaches zero,  $k$  approaches  $2/\sqrt{3} C$  so that if  $C$  is the shear strength of the material, then the yield law becomes the von Mises criteria

$$f = J_2^{1/2} - \frac{2C}{\sqrt{3}} \quad 4.19$$

It remains to develop an estimate for the cohesion,  $C$ , as a function of the neck radius.

#### 4.2.1 Cohesion of a Restructuring Fuel Bed

Consider a sphere array made up of various rotations of the unit cells shown in Figure 3.2 and a pure shear field applied to the array. If the array is sheared plastically a series of parallel shear surfaces (not necessarily planar) will develop in the material. For arrays with small neck growth these surfaces will be discrete, separated, on the average, by a distance at least as large as the sphere diameter, since the shear surface will pass mainly through the neck region of the unit cells. As the neck radius increases, the shear surfaces become less distinct and the shear strain approaches a constant value throughout the media. The model for cohesion described in this section reflects this transition in the shearing properties of the restructuring fuel.

The shear field is referenced to a fixed coordinate system  $(x,y,z)$  as shown in Figure 4.4. The orientation of a particular unit cell is determined by the orientation of the  $z'$  axis of the unit cell (the  $z'$  axis passes through the represented sphere centers) given by the angles  $\psi$  and  $\theta$  as shown. Since the neck region is cylindrical and determines the shear strength of the cell, it is not necessary to consider rotations of the unit cell about the  $z'$  axis. The cohesion of the restructuring array is now assumed to be the average frictionless shear strength of all the unit cells that a typical shear surface passes through. Considering all possible orientations of the unit cells intersected by the shear surface, the average cohesion can be represented by

$$C = \frac{\int_0^{\pi/2} \int_0^{\psi_{\max}} S_{yu} \sin \psi \, d\psi d\theta}{\int_0^{\pi/2} \int_0^{\psi_{\max}} \sin \psi \, d\psi d\theta} \quad 4.20$$

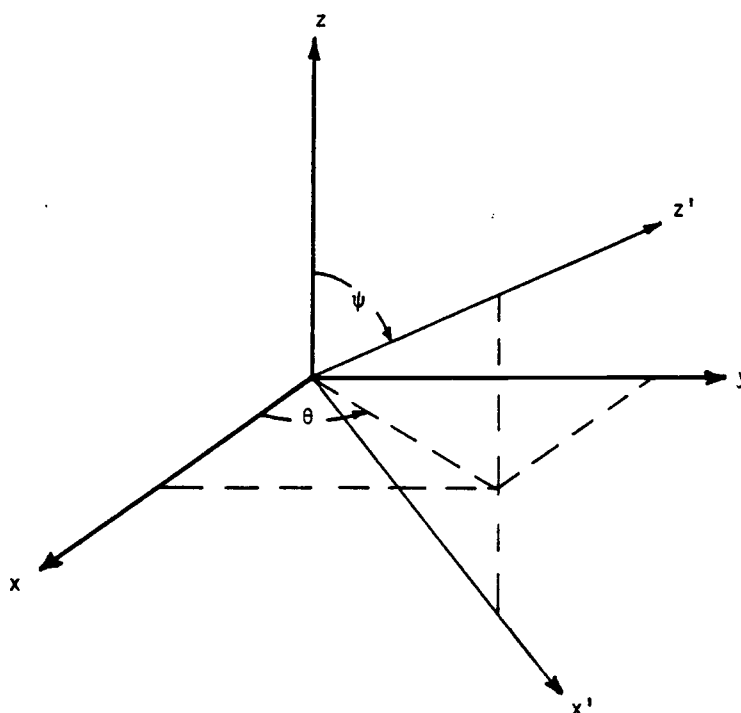


FIGURE 4.4. Coordinate System for Rotations of the Unit Cell

where  $\psi_{\max}$  is the maximum rotation (in the  $\psi$  direction) made by any of the unit cells intersected by the shear surface and  $S_{yu}$  is the shear strength of a unit cell oriented at  $(\psi, \theta)$  in the pure shear field.

If the array is considered to be made up of spheres arranged as tetrahedrons as shown in Figure 4.5, then the  $\psi_{\max}$  is  $60^\circ$ . If the rotation is greater than  $60^\circ$  then the shear surface will pass between some other pair of spheres with smaller shear strength. In the present model  $\psi_{\max}$  is assumed to be equal to  $60^\circ$ . It is now necessary to obtain the shear strength of a unit cell as a function of  $\psi$  and  $\theta$ .

The coordinate transformation from  $(x, y, z)$  to  $(x', y', z')$  as shown in Figure 4.4 is

$$[T] = \begin{bmatrix} \cos \theta \cos \psi & \sin \theta \cos \psi & -\sin \psi \\ -\sin \theta & \cos \theta & 0 \\ \cos \theta \sin \psi & \sin \theta \sin \psi & \cos \psi \end{bmatrix} \quad 4.21$$

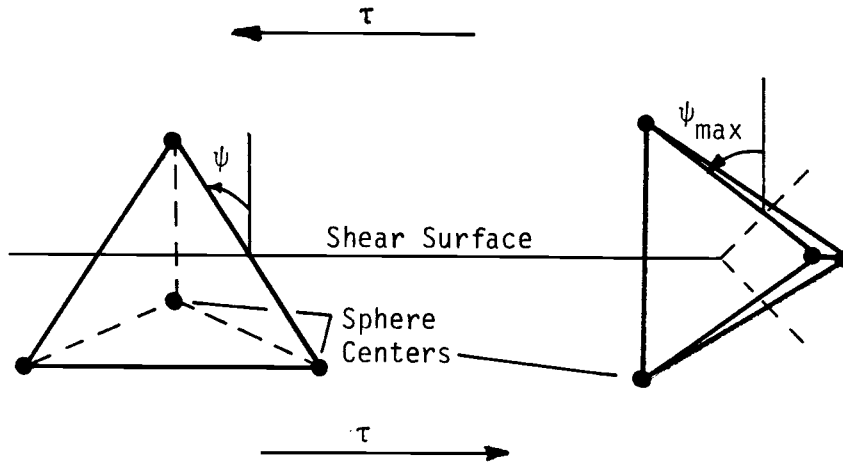


FIGURE 4.5. Schematic of Four Spheres in Contact Oriented in a Shear Field

Given a pure shear stress field,  $\tau$ , referenced to the unprimed coordinates, the stress field in the primed coordinates is given by

$$[\sigma]' = [T][\sigma][T]^T \quad 4.22$$

where

$$[\sigma] = \tau \begin{bmatrix} 0 & 0 & 0 \\ 0 & 0 & 1 \\ 0 & 1 & 0 \end{bmatrix}$$

so that

$$[\sigma]' = \tau \begin{bmatrix} -2 \sin\psi \sin\theta \cos\psi & -\cos\theta \sin\psi & \sin\theta(\cos^2\psi - \sin^2\psi) \\ -\cos\theta \sin\psi & 0 & \cos\theta \cos\psi \\ \sin\theta(\cos^2\psi - \sin^2\psi) & \cos\psi \cos\theta & 2\sin\theta \cos\psi \sin\psi \end{bmatrix} \quad 4.23$$

It is required to find  $\tau$  that results in yielding of a unit cell when subjected to the stress field  $[\sigma]'$ .

It is assumed that the unit cell will yield when the maximum shear stress in the unit cell reaches the shear strength of the sphere material. For most orientations of the unit cell the yield strength will be determined by the shear stress in the neck region. For cells at a large angle,  $\psi$ , and with a large neck radius the shear strength of the cell may be limited only by the shear strength of a solid sphere. From the discussion on the elastic constitutive model, the effective shear stress in the solid body portion of the sphere is

$$\tau' = \tau / \cos^2 \beta \quad 4.24$$

Thus, regardless of the cell orientation, the unit cell shear strength is limited by

$$S_{yu} < S_y \cos^2 \beta \quad 4.25$$

where  $S_y$  is the shear strength of the sphere material.

As in the elastic constitutive model, it is assumed that  $\sigma'_x$ ,  $\sigma'_y$ , and  $\tau'_{xy}$  are zero in the neck region. Then, from Equation 4.23 the stress in the neck region is

$$[\sigma'_N]' = \tau A_f \begin{bmatrix} 0 & 0 & \sin\theta(\cos^2\psi - \sin^2\psi) \\ 0 & 0 & \cos\theta\cos\psi \\ \sin\theta(\cos^2\psi - \sin^2\psi) & \cos\theta\cos\psi & 2\sin\theta\cos\psi\sin\psi \end{bmatrix} \quad 4.26$$

where  $A_f$  is the area factor given by the ratio of the projected areas of the unit cell and the neck in the  $z'$  direction. The area factor is given by

$$A_f = \frac{4 \tan^2 \beta}{\pi X^2}$$

From Equation 4.26 the principal stresses in the neck can be obtained and are

$$\sigma'_1 = 0, \quad \sigma'_{2,3} = \frac{\sigma'_z \pm \sqrt{\sigma'^2_z + 4(\tau'^2_{xz} + \tau'^2_{yz})}}{2} \quad 4.27$$

where  $\sigma'_z$ ,  $\tau'_{xz}$  and  $\tau'_{yz}$  are the nonzero components of  $[\sigma'_N]'$ . The maximum shear stress in the neck is then

$$\tau'_{\max} = \frac{\sigma'_2 - \sigma'_3}{2} = \tau A_f \sqrt{\cos^2\psi - \cos^4\psi + \sin^2\theta(1 - 2\sin^2\psi)^2}$$

$\tau'_{\max}$  will limit the shear strength of the unit cell as long as the corresponding shear plane can pass through the neck region only. For some orientations of  $\tau'_{\max}$  and some neck radius the shear plane will pass through the solid body portion of the sphere (see Figure 4.6a). If this occurs,  $\tau'_{\max}$  will not limit the unit cell shear strength since the shear stress on the  $\tau'_{\max}$  shear plane will be much lower in the solid body portion of the sphere and yielding would not occur over the entire plane. In this case the maximum shear stress for determining yield in the neck region is the shear stress on the  $\omega$ -plane that passes through the extreme boundaries of the neck regions indicated in Figure 4.6a. The angle between the  $x'y'$  plane and the  $\tau'_{\max}$  shear plane can easily be obtained from the Mohr circle representation, Figure 4.6b, and is given by

$$\tan 2 \xi = \frac{\sigma'_z}{2\tau'_r} = \frac{\sin \theta \cos \psi \sin \psi}{\sqrt{\cos^2 \psi \cos^2 \theta + \sin^2 \theta (1-2 \sin^2 \theta)^2}} \quad 4.29$$

where  $\tau'^2_r = \tau'^2_{xz} + \tau'^2_{yz}$

The angle  $\omega$  can be computed from the neck ratio as

$$\tan \omega = \frac{1 - \sqrt{1 - \bar{x}^2}}{\bar{x}} \quad 4.30$$

and the shear stress on the  $\omega$ -plane is given by

$$\tau'_\omega = \tau'_{\max} \cos (2\xi - 2\omega) \quad 4.31$$

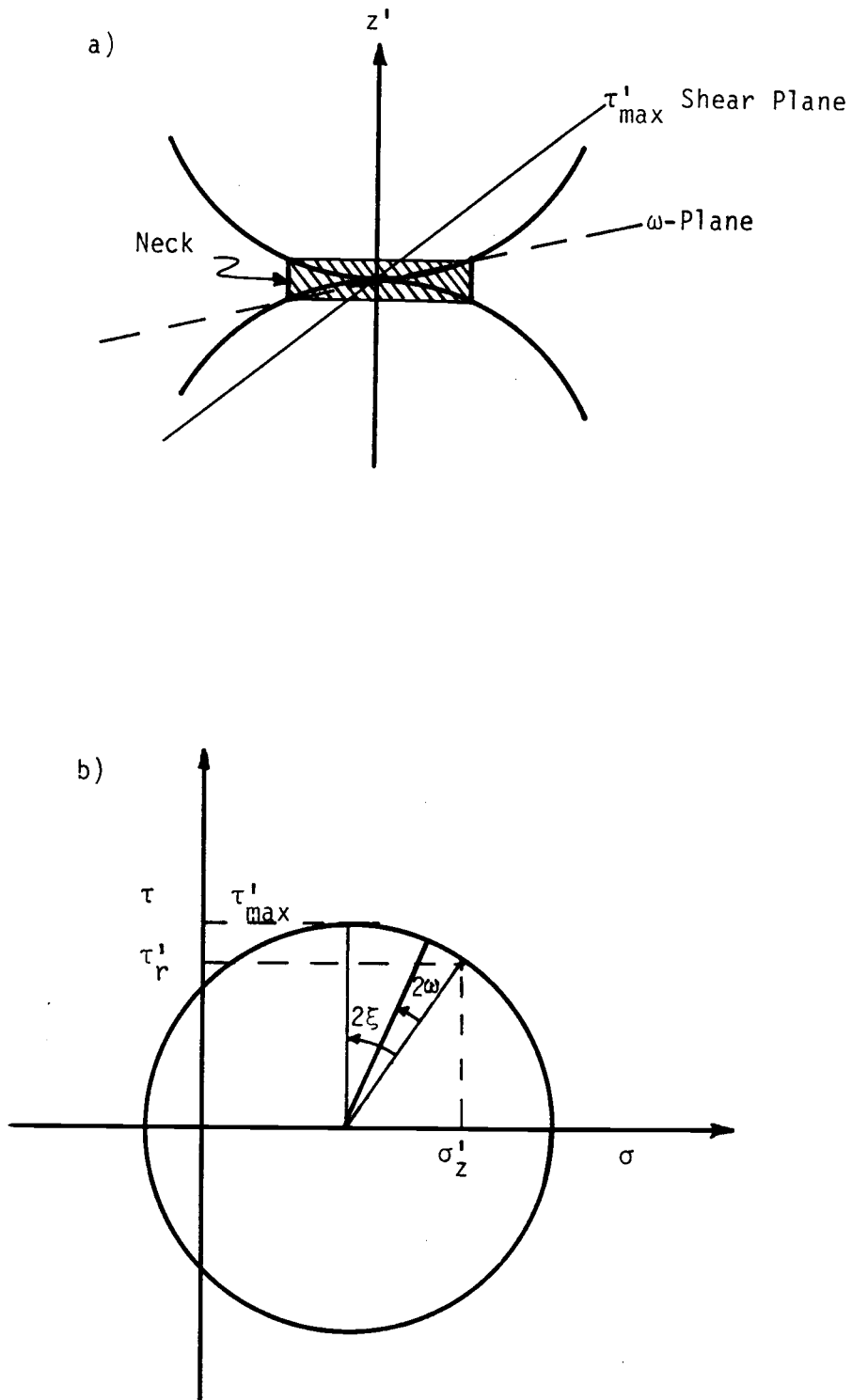


**FIGURE 4.6.** a) Schematic of Neck Region with Maximum Shear Plane and  $\omega$ -Plane Orientation. b) Mohr's Circle for Neck Region Stress

Then by combining the results given in Equations 4.25, 4.28, and 4.31, the unit cell shear strength can be expressed as

$$S_{yu} = \frac{S_y}{A_f \sqrt{\cos^2 \psi - \cos^4 \psi + \sin^2 \theta (1 - 2 \sin^2 \psi)^2}} \begin{pmatrix} 1 & \text{if } \xi < \omega \\ \frac{1}{\cos(2\xi - 2\omega)} & \text{if } \xi > \omega \end{pmatrix}$$

subject to

$$S_{yu} < S_y \cos^2 \beta \quad 4.32$$

Equation 4.20 can now be integrated numerically for a given value of the neck radius to give the effective cohesion of an array of uniform spheres with connecting necks. The normalized cohesion ( $C/S_y$ ) as a function of neck ratio is plotted in Figure 4.7 for two values of  $\beta$  (corresponding to packing factors of 0.56 and 0.62). The curves show that the array has no cohesion at zero neck ratio and approaches a limiting value as the neck ratio gets large. This is the model predicted value of the shear strength of a porous material with uniform pores uniformly distributed throughout the body. The model-predicted porous body effective shear strengths are  $0.59 S_y$  and  $0.54 S_y$  for initial packing factors of 0.62 and 0.56 respectively. The limiting value is closely approached at a neck ratio of 0.55. This is reasonably close to the suggested end of initial stage sintering limit.

Using this model for the cohesion as a function of the neck radius together with the effective friction angle from Equation 4.17,

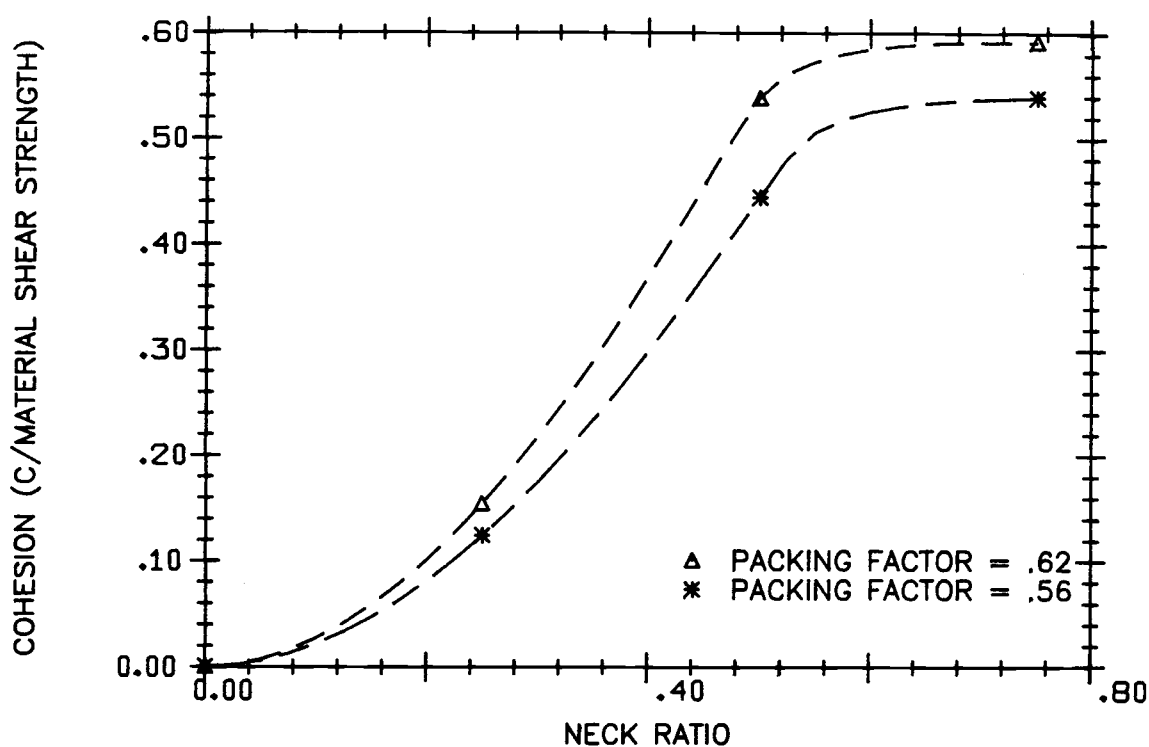


FIGURE 4.7. Cohesion of a Single Size Sphere Array

the strength parameters,  $\alpha'$  and  $k$  required in the yield function (Equation 4.13) can be determined. This provides the yield condition for a restructuring array of uniform spheres. The model must now be extended to the case of smaller spheres in the large sphere array interstitial spaces.

#### 4.2.2 Binary Array Shear Strength

Consider a binary array with only small necks between the large spheres. Under plastic shear, shear surfaces will be established that pass through the contact-neck regions of the large sphere array. The relative displacement of large spheres on opposite sides of the shear surface will result in shear stress applied to the small sphere arrays and accompanying plastic shear. Due to this rigid body motion of the large spheres (with respect to the small sphere array) the plastic shear strain in the small sphere array is expected to be larger than that of the binary mixture (see Figure 4.8). The small sphere array

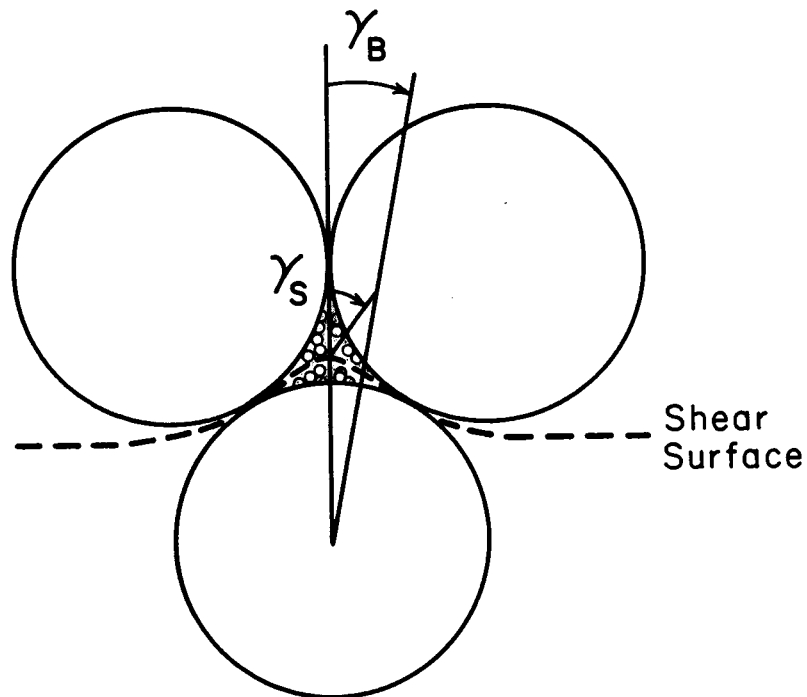


FIGURE 4.8. Schematic Showing Relation Between Binary and Small Sphere Array Plastic Shear Strain

shear strain is assumed to be proportional to the binary array strain giving

$$\gamma_S = \zeta \gamma_B \quad 4.33$$

The proportionality constant  $\zeta$  is expected to be a function of the initial packing factors of the two sphere sizes and of the large-to-small sphere diameter ratio. When the neck radius becomes large in the large sphere array, the shear surface does not necessarily pass only through the neck regions of the large sphere array as discussed in the previous section. If the large spheres themselves are shearing plastically the small sphere array is not subject to the rigid body motion of the large spheres and the strain in the small spheres is assumed to be equal to the binary array strain.

So, for unit cells that shear in the neck region,  $\zeta$  has a value determined by the packing parameters, say  $\zeta_0$ , while for unit cells that shear through the solid body portion  $\zeta$  is equal to 1. The effective value of  $\zeta$  is assumed to be the average value over all unit cells along the shear surface, giving

$$\zeta = \frac{\int_0^{\pi/2} \int_0^{\psi_{\max}} \zeta_u \sin\psi d\psi d\theta}{\int_0^{\pi/2} \int_0^{\psi_{\max}} \sin\psi d\psi d\theta} \quad (4.34)$$

$$\text{where } \zeta_u = \begin{cases} \zeta_0 & \text{if the unit cell shears in the neck region} \\ 1 & \text{if the unit cell shears in the solid body region} \end{cases}$$

The specification of  $\zeta_0$  is described in the next section.

The binary array shear strength can be obtained by assuming that the work required to shear the binary array is equal to the sum of the work involved in shearing the large and small sphere arrays. This can be expressed by

$$dW_B = dW_L + (1 - pf_L) dW_S \quad 4.35$$

where

$$dW_L = S_L d\gamma_B \quad 4.36$$

$$dW_S = S_S d\gamma_S \quad 4.37$$

$dW_B$  is the work per unit volume required to shear the binary array an amount  $d\gamma_B$ ,  $pf_L$  is the large sphere packing factor,  $S_L$  and  $S_S$  are the large and small sphere array shear strengths respectively, and  $dW_L$  and  $dW_S$  are the large and small sphere shear work per unit of binary volume. The shear strength of the binary array is related to the binary shear work by

$$dW_B = S_B d\gamma_B \quad 4.38$$

Then combining Equation 4.33 with Equations 4.35, 4.36, 4.37 and 4.38, the binary array shear strength is given by

$$S_B = S_L + (1 - pf_L) \tau S_S \quad 4.39$$

Equation 4.39 relates the shear strength of the binary array in pure shear to the large and small sphere array shear strengths. The shear strengths of the various sphere arrays is given by the Drucker-Prager yield criteria (Equation 4.13) and is

$$S = (\alpha' I_1 + k) \frac{\sqrt{3}}{2} \quad 4.40$$

Substituting Equation 4.40 for the large, small, and binary sphere arrays into Equation 4.39 results in

$$k_B - \alpha'_B I_{1B} = k_L - \alpha'_L I_{1L} + (1 - pf_L) \tau (k_S - \alpha'_S I_{1S}) \quad 4.41$$

where  $I_{1B}$ ,  $I_{1L}$ , and  $I_{1S}$  are the stresses for computing frictional effects in the binary, large and small sphere array respectively. The effective stress for frictional effects in the large sphere array is assumed to be

$$I_{1L} = I_{1B} - I_{1S} \quad 4.42$$

and  $I_{1B}$  and  $I_{1S}$  are three times the hydrostatic stresses computed for the binary and small sphere arrays from the solution of the elastoplastic equations.

By separating the frictional and nonfrictional strength terms in Equation 4.41, the binary array strength parameters can be defined by

$$k_B = k_L + \zeta(1 - pf_L)k_S \quad 4.43$$

and

$$\alpha'_B = (1 - I_{1S}/I_{1B}) \alpha'_L + (1 - pf_L) \zeta I_{1S}/I_{1B} \alpha'_S \quad 4.44$$

Equations 4.43 and 4.44 give reasonable results when the neck ratio for the large spheres is not too much less than that of the small sphere. For the more typical case where the small sphere neck ratio is considerably larger than the large sphere neck ratio, the predicted shear strength (related to  $k_B$  in Equation 4.43) may be larger than the shear strength of solid material. For this case the model predicts that shear surfaces pass mainly through the neck regions of the large spheres resulting in solid body motion of the

large spheres and therefore large plastic work done on the small sphere array ( $\zeta$  is close to  $\zeta_0$ ). When the strength of the small sphere array becomes large it is more likely that the large spheres themselves will shear rather than impose large strains on the small spheres, i.e., the value of  $\zeta$  should be closer to unity. A limiting value for  $\zeta$  may be obtained by considering the maximum possible plastic shear work for a restructuring binary array. It is assumed that this maximum would be obtained when both the large and the small sphere arrays are shearing through the solid body portion of the unit cell. Thus, from Equations 4.32 and 4.35

$$dW_{B_{\max}} = S_y \cos^2 \beta_L d\gamma_B + (1 - pf_L) S_y \cos^2 \beta_S d\gamma_B \quad 4.45$$

where  $\beta_L$  and  $\beta_S$  are the unit cell defining angles for the large and small sphere arrays. The maximum binary shear strength is then

$$S_{B_{\max}} = S_y (\cos^2 \beta_L + (1 - pf_L) \cos^2 \beta_S) \quad 4.46$$

The limiting value for  $\zeta$  can now be obtained by combining Equations 4.39 and 4.46 giving

$$\zeta_{\max} = \frac{S_y (\cos^2 \beta_L + (1 - pf_L) \cos^2 \beta_S) - S_L}{(1 - pf_L) S_S} \quad 4.47$$

Now substituting the shear strength definition of Equation 4.40 the limiting value of  $\zeta$  is given by

$$\zeta_{\max} = \frac{2/\sqrt{3} S_y (\cos^2 \beta_L + (1 - pf_L) \cos^2 \beta_S) - (k_L - \alpha'_L I_{1L})}{(1 - pf_L)(k_S - \alpha'_S I_{1S})}$$

4.48

The shear strain ratio is then given by Equation 4.34 subject to the limit imposed by Equation 4.48.

Several parameters are still required to complete the model for the restructuring fuel frictional yield strength. These are the small and large sphere array internal friction angles, the small-to-large sphere plastic shear strain ratio,  $\zeta_0$ , and the yield stress of the sphere material itself. The specification of these parameters is discussed in the following sections and Section 4.4.

#### 4.2.3 Shear Strain Ratio of Unstructured Fuel

Equation 4.44 together with some triaxial compression test data was used to determine  $\zeta_0$ . Triaxial compression tests (see Appendix B) were performed on samples of steel spheres, alumina spheres, and a binary sample of the steel and alumina spheres. The steel-to-alumina sphere diameter ratio was 15.6 which is in the range of the large-to-small sphere diameter ratio of the sphere pac fuel (~10 - 20). In the binary mixture the large and small sphere packing factors were both 0.58. From tests on the steel spheres and the alumina spheres individually, the angle of internal friction was found to be 13.5° for the steel and 18.5° for the alumina spheres. The binary mixture had a friction angle of 27°. Using the elastic constitutive model the small-to-binary stress ratio was given as  $I_{1S}/I_{1B} = 0.911$ . Equation 4.15 provided values for  $\alpha'$  for each of the sphere arrays giving  $\alpha'_L = .0974$ ,  $\alpha'_S = 0.1221$ , and  $\alpha'_B = 0.2059$ . Substituting these values in Equation 4.44 and solving for  $\zeta$  results in  $\zeta = 4.22$ . This is the value used for  $\zeta_0$ .

Figure 4.9 shows  $\zeta$  as a function of the large sphere array neck radius. For small necks  $\zeta$  has the value of  $\zeta_0$  indicating that the shear surface passes mainly through the neck regions of the unit cells. As the cohesion approach its limiting value (see Figure 4.7)  $\zeta$  approaches unity indicating that the shear surfaces pass through the solid body portion of many of the unit cells.

For some values of the large and small sphere neck ratios the value of  $\delta$  used for calculating the binary strength parameters may be limited by Equation 4.48 and will not be as large as the value shown in Figure 4.9.

#### 4.2.4 Internal Friction Angle for Unrestructured Fuel

The frictional yield model requires values for the internal friction angles for the large and small sphere arrays for unrestructured fuel. A value of  $\phi = 20^\circ$  was chosen for both the large and small sphere arrays. This value was based on the measured angle of repose of a conical pile of  $UO_2$  spheres. The angle of repose gives a reasonable estimate for the internal friction angle (Gray, 1968). Soil mechanics tests (e.g., triaxial compression, shear box, angle of repose) are required on the mixed carbide sphere pac fuel to improve the estimate for the internal friction angle.

#### 4.2.5 Frictional Yield Parameters for Binary Sphere Array

As described in the preceding, the strength of the binary array depends on the yield stress of the sphere material, the internal friction angles, neck ratios, and effective hydrostatic compression in each of the large and small sphere arrays. Figure 4.10 shows the binary strength parameters as a function of the small sphere neck radius. For this representative plot the large sphere neck ratio was taken as 0.5 times the small sphere neck ratio. No shrinkage of the large or small sphere arrays was assumed and so the small-to-binary hydrostatic stress ratio was taken as a constant equal to 0.8. The internal friction angle for both arrays was  $20^\circ$ .

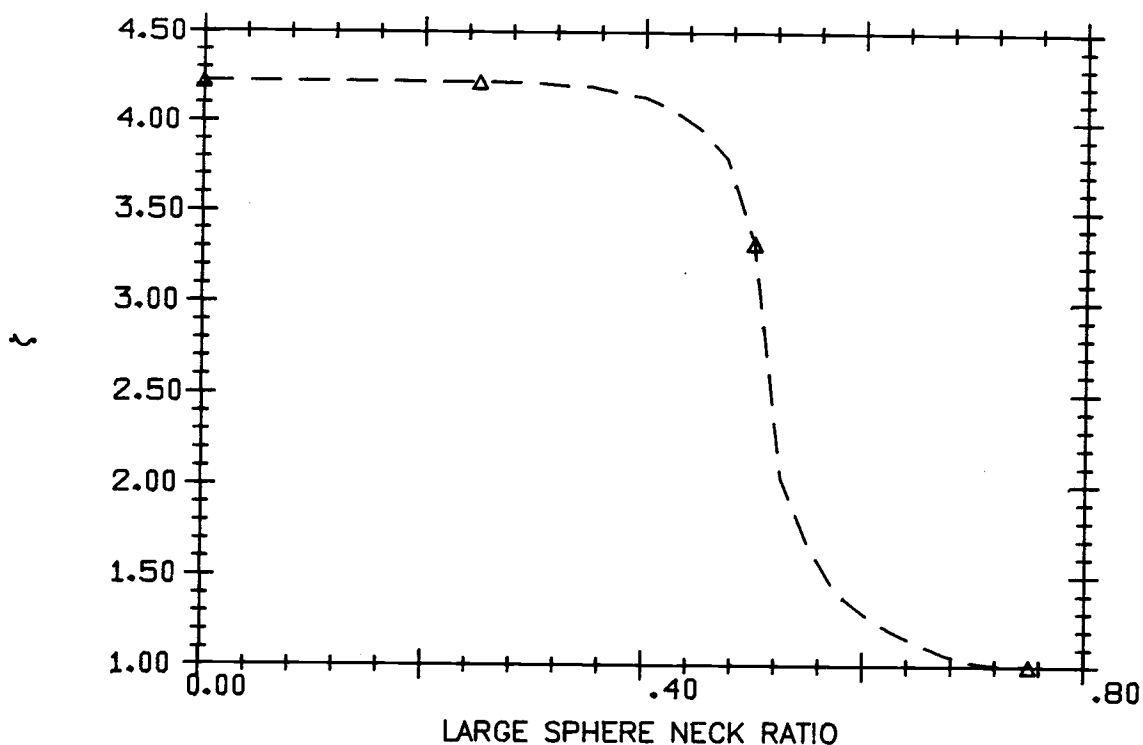


FIGURE 4.9. Binary-to-Small Sphere Array Plastic Shear Strain Ratio

The curves in Figure 4.10 show that as the neck ratio increases  $\alpha_B'$  decreases, thereby decreasing the frictional effects in the yield function. The value of  $k_B$ , (normalized by the sphere material shear strength) however, increases with increasing neck ratio reflecting the increased cohesion of the sphere array. The predicted equivalent shear strength of restructured fuel is approximately 0.85  $S_y$ .

The quantitative accuracy of the yield model cannot be assessed at this time due to the lack of experimental data. The model does, however, provide a means of estimating the shear yield strength as a continuous function of the restructuring from a cohesionless sphere bed to a material with closed pores.

#### 4.2.6 Plastic Potential Function for Frictional Yielding

The use of an associated flow law for granular material generally leads to an overprediction of the dilation under plastic shear. Plastic potential functions have been proposed (Christian and Desai, 1977)

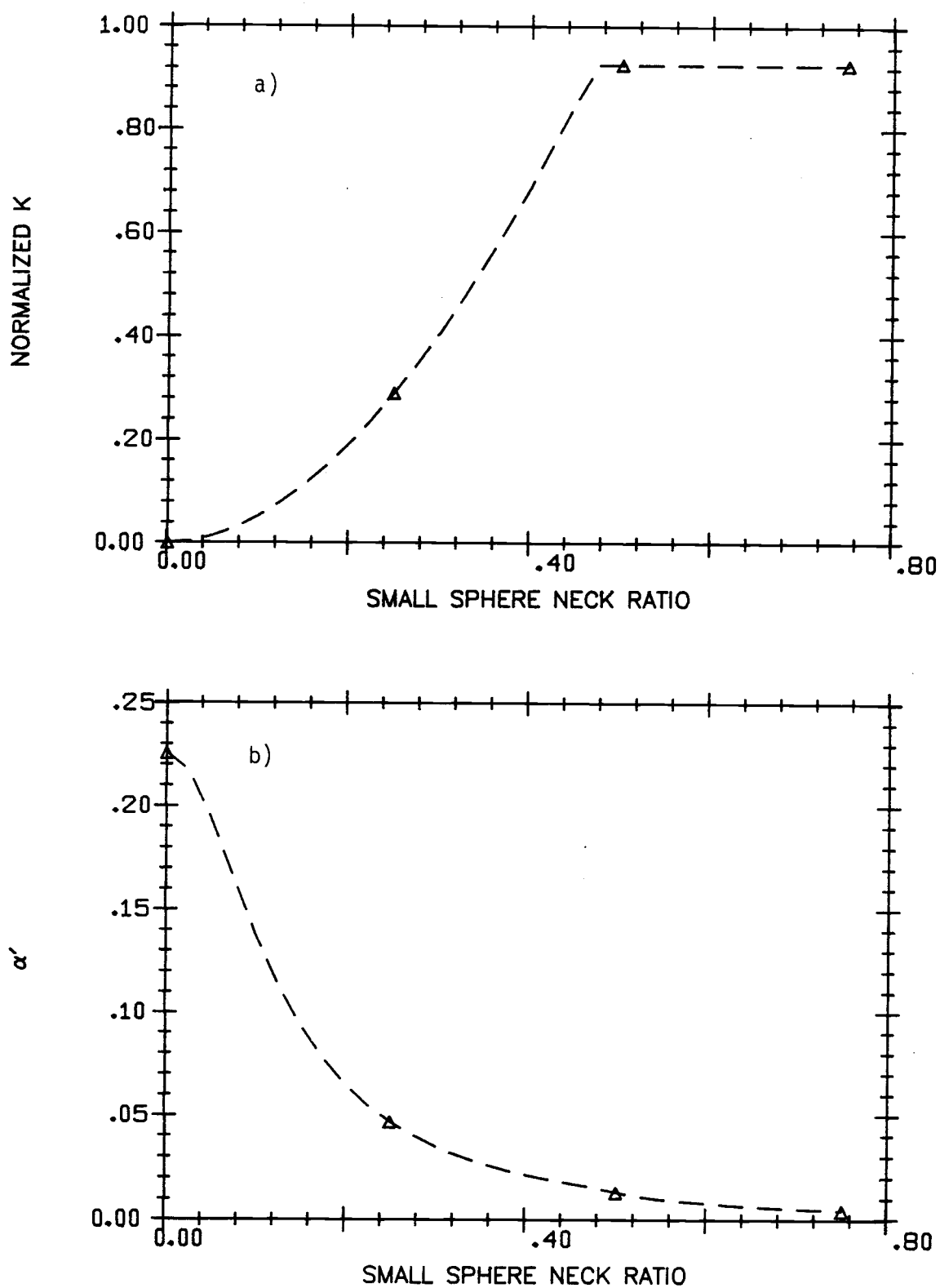


FIGURE 4.10. Binary Sphere Array Strength Parameters for Frictional Yielding. a) Parameter  $k$ , b) Parameter  $\alpha'$

that eliminate the volumetric strain. Such a plastic potential function is chosen for this analysis and is obtained by ignoring the frictional effects in the yield function. Thus the plastic potential function becomes

$$g_1 = J_2^{1/2} - k(x) \quad 4.49$$

Equation 4.49 is equivalent to the von Mises yield law so that as the fuel restructures, and the frictional effects become small, the yield function approaches the plastic potential function and associated flow is obtained.

### 4.3 HYDROSTATIC YIELDING

Yielding under hydrostatic load is an important phenomena that occurs during the very early stages of restructuring. It results from the large localized stresses at the sphere contacts. Most of the early densification of the fuel is due to the plastic flow under hydrostatic stress. This plastic flow also contributes to the neck growth between spheres and therefore increases the effective thermal conductivity. Without plastic flow under hydrostatic stress the cladding would yield before the fuel could densify through the other shrinkage mechanisms.

The hydrostatic yield surface is represented by a cap on the frictional yield surface as shown in Figure 4.11. The exact shape of the surface is unknown but the point where the surface intersects the hydrostatic stress axis can be estimated. It is known that when a flat piece of material is loaded by a hard spherical or cylindrical punch, the punch begins to deform the material plastically when the average pressure across the punch face is 2.5 to 3.0 times the yield stress (Tabor, 1951). It is assumed that the punch analysis can be applied to two spheres in contact, and that plastic flow will not occur as long as

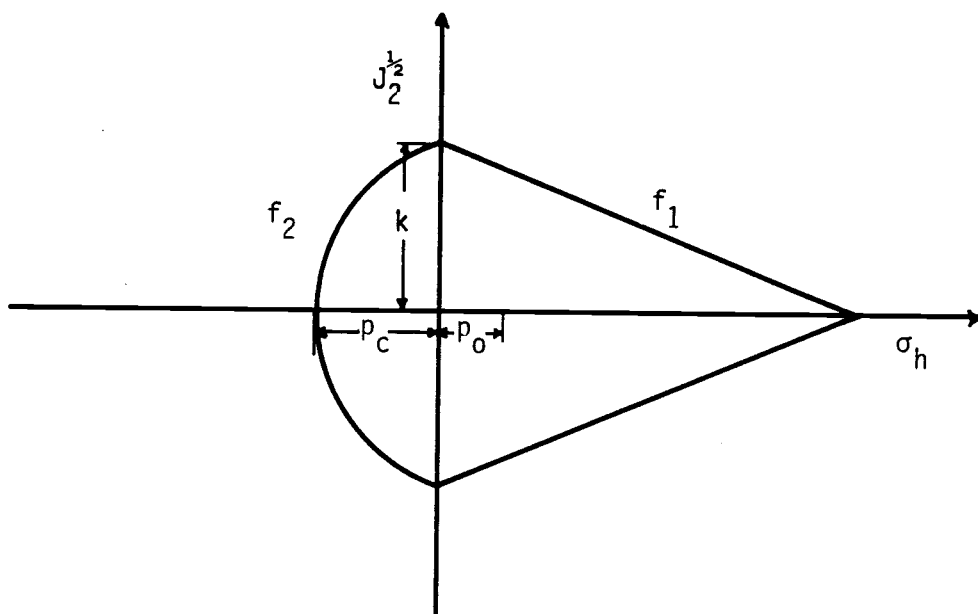


FIGURE 4.11. Capped Yield Surface for Sphere Pac Fuel

$$N/A_c < 2.5 \sigma_y \quad 4.50$$

where  $N$  is the load normal to the contact area,  $A_c$  and  $\sigma_y$  is the sphere material yield strength. The normal force is obtained from Equation 3.38 giving the yield condition

$$\frac{-\sigma_h 4 R^2 \tan^2 \beta}{A_c} < 2.5 \sigma_y \quad 4.51$$

The contact area is assumed to be either that obtained from the current value of the neck ratio or from the Hertzian contact radius, whichever is larger.

It is assumed that the binary sphere mixture can yield plastically under hydrostatic stress only if the large sphere array yields. The hydrostatic stress used for computing the contact force on the large sphere array is

$$\sigma_{hL} = \sigma_{hB} - \sigma_{hS} \quad 4.52$$

where  $\sigma_{hB}$  and  $\sigma_{hS}$  are the hydrostatic stresses for the binary mixture and the small sphere array respectively. The maximum allowable hydrostatic compression on the binary mixture can now be obtained by replacing  $\sigma_h$  in Equation 4.51 by  $\sigma_{hL}$  and combining with Equation 4.52 to give

$$-\sigma_{hB} < \frac{2.5 A_c \sigma_y}{4 R_L^2 \tan^2 \beta_L} - \sigma_{hS} \quad 4.53$$

Equation 4.53 gives the point of intersection of the hydrostatic yield surface with the hydrostatic stress axis. The parameter  $p_c$  identified in Figure 4.12 is therefore given by

$$p_c = \frac{2.5 A_c \sigma_y}{4 R_L^2 \tan^2 \beta_L} - \sigma_{hS} \quad 4.54$$

The hydrostatic yield surface is assumed to be spherical with its center of curvature on the hydrostatic axis. It is somewhat arbitrarily assumed that the surface intersects the  $J_2$  axis at  $k$ , the strength parameter for the frictional yield surface. This insures that there will never be yielding on the hydrostatic surface if the hydrostatic stress is positive. From geometry, the center of curvature is located at

$$p_0 = \frac{1}{2} (k^2/p_c - p_c) \quad 4.55$$

The yield function is then the equation of a circle in the  $\sigma_h, J_2^{1/2}$  space and is given by

$$f_2 = (J_2 + (\sigma_{hB} - p_0)^2) - (p_c + p_0)^2 \quad 4.56$$

It is assumed that the plastic flow under hydrostatic yielding is associated so that

$$g_2 = f_2 \quad 4.57$$

#### 4.3.1 Neck Growth and Shrinkage Associated with Hydrostatic Yielding

When the fuel yields on the  $f_2$  surface there is some center-to-center approach of the spheres (shrinkage). The shrinkage rate of the large sphere array,  $\dot{S}_L$  is related to the plastic volumetric strain rate,  $\dot{\epsilon}_V^P$ , by (see Equation 3.64)

$$\dot{S}_L = - \dot{\epsilon}_V^P / 3 \quad 4.58$$

The relation between neck growth rate and shrinkage rate due to plastic flow is assumed to be the same as that for viscous flow and is given by (Kingsley, et al. 1976)

$$\dot{S}_L = \frac{\dot{\bar{x}}_L}{\bar{x}_L} \quad 4.59$$

where  $\bar{x}_L$  is large sphere neck ratio.

#### 4.3.2 Neck Growth and Shrinkage in the Small Sphere Array due to Plastic Flow

The model discussed in the previous two sections can only account for neck growth due to plastic flow in the large sphere array. However, plastic flow can also be an important mechanism for neck growth between small spheres and effectively limits the maximum compressive stress developed in the small sphere array. Since the yield stress of the binary mixture is a function of the small sphere array hydrostatic stress (inequality 4.53), yielding of the small sphere array indirectly influences the yielding of the binary mixture.

From inequality 4.51 the hydrostatic compression in the small sphere array is limited by

$$-\sigma_{hS} < \frac{2.5 \sigma_y A_c}{4 R_S^2 \tan^2 \beta_s} = \sigma_m \quad 4.60$$

If the hydrostatic compression in the small sphere array is less than  $\sigma_m$  then there is no shrinkage or neck growth due to plastic flow. If the hydrostatic compression exceeds  $\sigma_m$  it is assumed that sufficient shrinkage occurs to make  $-\sigma_{hS} = \sigma_m$ .

The small sphere hydrostatic stress is given by Equation 3.62. The shrinkage of the small sphere array is related to  $\sigma^*$  through Equations 3.65 and 3.66. It is required to find the the small sphere array shrinkage (or equivalent,  $\sigma^*$ ) that makes  $-\sigma_{hS} = \sigma_m$ . Substituting  $\sigma_m$  for the small sphere array hydrostatic compression and solving for  $\sigma^*$  from Equation 3.62 gives

$$\sigma^* = (-\sigma_{hB} - \sigma_m) / d\sigma_s/d\sigma_h \quad 4.61$$

Now Equations 3.66 and 3.67 can be solved for the required small

sphere shrinkage giving

$$S_S = \left[ \frac{1}{3} \int_0^{\sigma^*} \frac{d\sigma_h}{K_L^c} + S_L \right] \frac{1}{(1 - pf_L)} \quad 4.62$$

For a finite time increment the shrinkage rate is approximated by

$$\dot{S}_S = \frac{S_S^1 - S_S^0}{\Delta t} \quad 4.63$$

where  $S_S^1$  is the shrinkage calculated from Equations 4.62 and  $S_S^0$  is the shrinkage at the end of the previous time step. Equation 4.59 can be applied to obtain the corresponding neck growth rate due to plastic flow.

#### 4.4 YIELD STRESS OF (U,Pu)C

The yield stress of mixed carbide is required in the model described for the restructuring fuel yield functions. There is only limited data available for the yield stress for (U,Pu)C. Werner and Blank (1981) reported the yield stress of (U<sub>0.8</sub>P<sub>0.2</sub>)C (93% TD) in the temperature range 1400 < T < 1550°C. They also obtained the yield stress of mixed nitride and carbonitride over a larger temperature range. These results can be used to infer the qualitative behavior of the mixed carbide over a large temperature range. Their results indicate that mixed carbonitride ceramics (MC<sub>0.8</sub>N<sub>0.2</sub>) fail in brittle fracture at temperatures below about 1100°C and flow plastically above this temperature.

In the present model the mixed carbide fracture and flow stress is assumed to parallel the results for the mixed carbonitride as shown in Figure 4.12. For temperatures above 1600°C the yield stress is

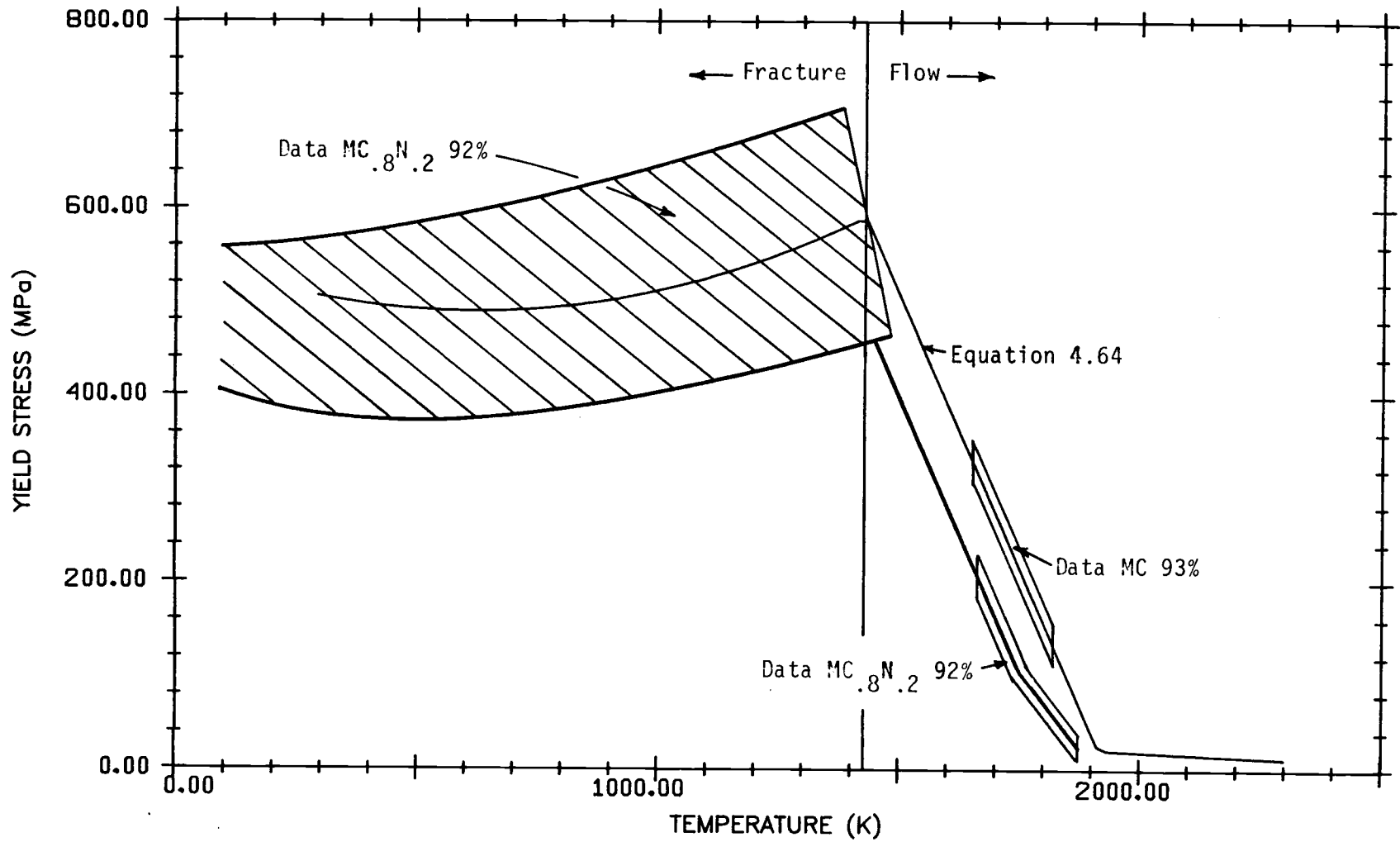


FIGURE 4.12. Fracture and Flow Stress for (U,Pu)C

expected to be very small as it is for UC (Routbort and Singh, 1975) which has a yield stress of ~20 MPa at temperatures above 1500°C. The yield stress is assumed to linearly approach zero as the fuel temperature approaches the melting temperature. The yield (or fracture) stress assumed for the mixed carbide fuel is given by

$$\sigma_y = \begin{cases} 546. - 0.19T + 1.549 \times 10^{-4}T^2 & 0 < T < 1413K \\ 2263. - 1.17T & 1413 < T < 1917K \\ 20.(2753. - T)/836. & T > 1917K \end{cases}$$

4.64

where T is in degrees K and  $\sigma_y$  is in MPa. The shear strength required for the cohesion is assumed to be  $\sigma_y/2$ .

The plasticity model is based on an assumption that the material flows plastically and does not fracture. In the central portion of the pin where most of the densification occurs through plastic yielding on the hydrostatic surface the temperature is above the transition temperature and the plastic flow assumption is acceptable. In the outer regions of the fuel yielding can occur on either the hydrostatic or the frictional surface. In these regions the strength of the fuel may be overestimated since fracture in the neck region would result in a new contact with no necks. This possible shortcoming of the model is recognized and should be investigated in the continuing effort to provide an accurate mechanical behavior model.

#### 4.5 PLASTIC MODULUS MATRIX

All the functions required for the plastic-modulus matrix have now been presented. The matrix can easily be constructed by taking the required derivatives of the plastic yield and potential functions (see Equation 2.15). If the fuel is yielding according to the frictional yield law then  $f_1$  and  $g_1$  are used to define [P] while  $f_2$  and  $g_2$  are used if yielding is on the hydrostatic surface. The explicit form of [P] is rather cumbersome and is not presented here.

The plastic strain rate due to changes in the yield stress is defined by Equation 2.17. The derivative of the yield function with respect to  $\chi$  cannot be obtained analytically, nor is  $\dot{\chi}$  explicitly known. However, the required strain rate can be approximated by

$$\{\dot{\epsilon}^{pp}\} = \frac{[f_i(\sigma_t, \chi_{t+\Delta t}) - f_i(\sigma_t, \chi_t)] \left\{ \frac{\partial g}{\partial \sigma} \right\}}{\Delta t \left\{ \frac{\partial f}{\partial \sigma} \right\}^T [E] \left\{ \frac{\partial g}{\partial \sigma} \right\} - \left\{ \frac{\partial f}{\partial \epsilon P} \right\}^T \left\{ \frac{\partial g}{\partial \sigma} \right\}} \quad 4.65$$

where the  $i$  subscript on  $f$  is either 1 or 2 depending on which yield surface the fuel is on and  $f_i(\sigma_t, \chi_t)$  is the yield function evaluated at the time  $t$  values of stress and the material property parameters (temperature and neck ratio).

## 5.0 INITIAL STRAINS FOR SPHERE PAC FUEL

The total stress-strain relation (Equation 2.7) requires the initial strain rate consisting of the thermal, creep, and swelling strain rates and the elastic strain rate resulting from changes in the elastic properties (nonlinear elastic strain rate). Each of these strain rates is specified for the fuel in the following sections.

### 5.1 FUEL THERMAL STRAIN RATE

The fuel thermal strain rate is assumed to be isotropic and is given by

$$\dot{\epsilon}_r = \dot{\epsilon}_\theta = \dot{\epsilon}_z = C_t (T) \dot{T} \quad 5.1$$

where  $C_t$  is the coefficient of linear thermal expansion and  $\dot{T}$  is the time rate of temperature change. Ogard, Land, and Leary (1965) experimentally determined the expansion coefficient for  $(U_{0.87}Pu_{0.13})C$  in the temperature range 25 - 900°C. The expansion coefficient is

$$C_t = 8.7 \times 10^{-6} + 6.0 \times 10^{-9}T, 1/^\circ C \quad 5.2$$

with T in degrees centigrade. Equation 5.2 is assumed to apply at all calculated fuel temperatures.

### 5.2 FUEL CREEP AND SHRINKAGE RATE

In the restructuring fuel the sintering-induced shrinkage is assumed to dominate over any creep within the sphere themselves. For

most of the initial critical stage sintering the dominant shrinkage mechanism is expected to be the irradiation and temperature-induced viscous flow (Matthews 1979) which is essentially a creep phenomena that occurs locally in the contact-neck region. In the fully restructured regions of the fuel, shrinkage is due to hot pressing under hydrostatic compression. Creep to relieve the deviatoric stress is also considered.

### 5.2.1 Restructured Fuel Creep

The shrinkage in the restructured fuel is due to hot pressing. Under a compressive load and high temperatures the fuel porosity is reduced as the pores shrink and become more spherical. The hot pressing model used to simulate this effect is the same as that found in the UNCLE code (Billone 1979) for carbide pellet fuel. The volumetric strain due to hot pressing is given by

$$\dot{\epsilon}_V^{hp} = 9./4. A_{hp} \frac{p}{1-p} \frac{\sigma_h}{\mu}, 1/s \quad 5.3$$

where  $p$  is the fuel porosity and  $\mu$  is the fuel viscosity given by

$$1/\mu = 202./d^2 \exp(-80,000/RT) + 6.944 \times 10^{-25} \dot{F}, \text{MPa} \cdot \text{s} \quad 5.4$$

$d$  is the grain diameter in microns,  $\sigma_h$  is the hydrostatic stress in MPa and  $\dot{F}$  is the fission rate in neutrons/cm<sup>3</sup> s.

The parameter  $A_{hp}$  was fitted to pin strain data for pellet fueled pins giving  $A_{hp} = 15.0$ . The same value is used for the restructured portion of sphere pac fuel. The hot pressing strain rate is assumed to be isotropic giving

$$\dot{\epsilon}_r^{hp} = \dot{\epsilon}_\theta^{hp} = \dot{\epsilon}_z^{hp} = \dot{\epsilon}_v^{hp}/3. \quad 5.5$$

A deviatoric creep is also considered in the restructured fuel. The usual assumption for pellet fuel analysis is that most of the creep strain is due to secondary creep that is independent of the total creep strain. This assumption is also used in the present model although there is evidence that, for mixed carbide fuel, primary creep may represent a significant portion of the total creep strain (Singh 1967). The creep data for mixed carbide fuel is so limited and scattered that it is not reasonable to model the more complicated primary creep at this time. The secondary creep rate is assumed to be the sum of a thermal creep rate and a fission-induced creep rate. The rate expressions chosen for this model are based mainly on a review of carbide fuel properties by Routbort and Singh (1975).

The thermal creep rate is taken from the work of Tokar (1973) who measured the compressive creep of  $(U_{0.79}Pu_{0.21})C_{1.02}$  at temperatures of 1300, 1400, and 1500°C and stresses of 13.8, 27.6, and 41.4 MPa. The initial porosity of the sample was 0.14, and densification of the samples occurred during the primary creep phase reducing the porosity to as low as 0.08 at the onset of secondary creep. It should be noted that the steady-state creep of mixed carbides is sensitive to small variations in the stoichiometry with hypostoichiometric samples creeping faster than hyperstoichiometric samples (Routbort and Singh 1975). The secondary rate expression obtained by Tokar is

$$\dot{\epsilon}_t = 4.15 \times 10^6 \sigma^{2.44} \exp(-126.4 \text{ kcal/mol}/RT), \text{ 1/hr} \quad 5.6$$

For a slightly different stoichiometry [(U<sub>0.8</sub>Pu<sub>0.2</sub>) C<sub>1.0</sub>] Singh (1977) obtained a creep rate dependent on stress to the 3.0 power and with an activation energy of 296.6 kcal/mol. The creep rate was a factor of 5 greater than that observed by Tokar indicating the sensitivity to stoichiometry.

Other workers have obtained values of the stress exponent in the range 0.35 - 1.9 and activation energy in the range 45 - 117 kcal/mol for samples of various porosities and Pu contents between 13 and 15%. There is not enough data to determine the strain rate dependence on porosity or Pu content although samples with higher Pu content generally have higher thermal creep rates.

Below a certain temperature the creep rate predicted by Equation 5.6 becomes small compared to the fission-induced creep rate. The usual form for fission-induced creep is

$$\dot{\epsilon}_f = C_f \sigma^3 \dot{F} \quad 1/\text{hr} \quad 5.7$$

For UC the temperature at which  $\dot{\epsilon}_f$  dominates is  $\sim 1200^\circ\text{C}$  (Solomon 1973). The fission-induced creep is independent of temperature for carbides. From the data of Dienst (1977) the proportionality constant for Equation 5.7 is estimated at  $C_f = 2.5 \times 10^{-21}$  with  $\sigma$  given in MPa and  $\dot{F}$  in fissions/cm<sup>3</sup>·s.

The creep rate is a function of porosity although there is not enough data to determine the functional dependence for  $\dot{\epsilon}_t$  and  $\dot{\epsilon}_f$ . Until more data becomes available the total deviatoric creep rate is assumed to be linearly related to the porosity according to

$$\dot{\epsilon}_{cd} = C_p (1 - p)(\dot{\epsilon}_t + \dot{\epsilon}_f) \quad 5.8$$

The porosity coefficient is determined from the steady-state creep results of Tokar assuming a porosity of 0.08. This gives a value for  $C_p = 1.087$ . Combining Equations 5.6, 5.7, and 5.8, the total deviatoric creep rate is given by

$$\dot{\epsilon}_{cd} = 1.087 (1 - p) (4.15 \times 10^6 \sigma^{2.44} \exp(-126.4/RT) + 2.5 \times 10^{-21} \sigma^5), \text{ 1/hr} \quad 5.9$$

### 5.2.2 Creep Strain Components

Equation 5.9 gives the uniaxial creep rate in response to an applied uniaxial stress,  $\sigma$ . To get the three-dimensional deviatoric strain rate (see Kraus 1980) in response to an arbitrary three-dimensional stress state the components of the creep rate are assumed to be proportional to the deviatoric stress as

$$\dot{\epsilon}_{ij}^{cd} = \lambda s_{ij} \quad 5.10$$

If the effective stress for use in Equation 5.9 is defined by

$$\sigma_e = \sqrt{3J_2} \quad 5.11$$

and the resulting effective creep rate is related to the creep rate components by

$$\dot{\epsilon}_{cd} = \left( \frac{4\dot{\epsilon}_{ij}^{cd} \dot{\epsilon}_{ij}^{cd}}{3} \right)^{1/2} \quad 5.12$$

then substitution of Equation 5.10 into 5.13 yields a value for  $\lambda$  given by

$$\lambda = \frac{3}{2\sigma_e} \dot{\epsilon}_{cd} \quad 5.13$$

For the axisymmetric case Equations 5.10 and 5.12 reduce to

$$\begin{Bmatrix} \dot{\epsilon}_r^{cd} \\ \dot{\epsilon}_\theta^{cd} \\ \dot{\epsilon}_z^{cd} \end{Bmatrix} = \frac{3\dot{\epsilon}_{cd}}{2\sigma_e} \begin{Bmatrix} \sigma_r - \sigma_h \\ \sigma_\theta - \sigma_h \\ \sigma_z - \sigma_h \end{Bmatrix} \quad 5.14$$

with

$$\sigma_e^2 = \frac{3}{2} [(\sigma_r - \sigma_h)^2 + (\sigma_\theta - \sigma_h)^2 + (\sigma_z - \sigma_h)^2]$$

These equations are analogous to the Prandtl-Reuss equations for plastic flow using the von Mises yield criteria and the associated flow rule. They provide the deviatoric creep rate components in the restructured fuel. The total creep rate in the restructured fuel is the sum of the deviatoric creep and the hot pressing creep giving

$$\dot{\epsilon}_r^c = \dot{\epsilon}_r^{hp} + \dot{\epsilon}_r^{cd}, \text{ etc} \quad 5.15$$

### 5.2.3 Restructuring Fuel Shrinkage

The initial stage sintering model provides a value for the center-to-center approach rate of two spheres. The modeled mechanisms are the same as those described by Ades (1979), except for the viscous flow mechanism. Matthews (1979) obtained an expression for the viscous flow neck growth rate that corresponds to the creep law of the solid material. If the material creep law is of the form

$$\dot{\epsilon} = B_C \sigma^n \quad 5.16$$

then the viscous flow neck growth rate is given by

$$\dot{\bar{x}}_{VF} = \frac{9\pi B_C}{8} \left[ \frac{(2n - 1) F_a}{6n \bar{x}^2 R^2} \right]^n \quad 5.17$$

where  $F_a$  is the applied force ( $F_a = \sigma_h A_z$ ) on the contact area. Matthews also included a driving force term proportional to the surface tension of the material but this requires an assumption that the material at the neck surface is redistributed by some surface diffusion mechanism. Since the surface diffusion is small compared to the neck growth rate due to viscous flow, the surface tension term is neglected in this analysis.

The creep law for mixed carbide is discussed in Section 5.2.1. The creep rate is the sum of a thermal induced and a fission induced creep and so there are two corresponding terms for the viscous flow neck growth rate. The viscous flow neck growth rate is assumed to be given by the sum of these terms.

The shrinkage rate corresponding to the viscous flow neck growth rate is given by (Kingery, et al, 1976)

$$\dot{S}_{VF} = \bar{x} \dot{x}_{VF} \quad 5.18$$

There have been some attempts to determine the dominate sintering mechanism for mixed carbide fuel (Guenther, 1978; Ades, 1979; Matthews, 1979). Since the fuel operates over such wide ranges of temperature and stress and consists of two sphere sizes, these studies have not been conclusive. While viscous flow is the major contributor during most of initial stage sintering there is potential for any one of the mechanisms to contribute significantly at certain points in the restructuring process. Rather than try to anticipate the dominate mechanism it is assumed that the total instantaneous neck growth rate is the sum of the growth rate from each of the mechanisms giving

$$\dot{x}_{Total} = \dot{x}_{Volume} + \dot{x}_{Grain} + \dot{x}_{Surface} + \dot{x}_{Evaporation} + \dot{x}_{Viscous} \\ \text{Diffusion} \quad \text{Boundary} \quad \text{Diffusion} \quad \text{Condensation} \quad \text{Flow} \\ \text{Diffusion} \quad \text{Diffusion} \quad \text{Diffusion} \quad \text{Condensation} \quad \text{Flow} \quad 5.19$$

For Equation 5.19 to hold it must be assumed that the processes do not interfere with each other. This is not totally valid since, for example, grain boundary diffusion must be accomplished by surface diffusion to distribute the material at the neck surface. Further, when considering processes with and without shrinkage simultaneously, the basic neck geometry assumption (which is different for the two processes) it is not valid for either type of mechanism. Nevertheless, should one mechanism clearly dominate at any particular point in the sintering process, Equation 5.19 will reflect that dominance and provide a reasonable estimate for the neck growth rate.

A similar assumption is made for the shrinkage so that the total center-to-center approach rate is given by

$$\dot{S}_{\text{Total}} = \dot{S}_{\text{Volume Diffusion}} + \dot{S}_{\text{Grain Boundary Diffusion}} + \dot{S}_{\text{Viscous Flow}} \quad 5.20$$

The shrinkage and neck growth that occurs due to plastic flow in the neck region has been discussed in Chapter 4. The plastic neck growth and shrinkage are added to the contributions from Equation 5.19 and 5.20. Neck growth and shrinkage are calculated for both the large and the small sphere arrays. The effective hydrostatic stress is required for the volume diffusion, grain boundary diffusion and viscous flow mechanisms. For the large spheres it is calculated from Equation 4.42 and for the small spheres from Equation 3.62.

It is assumed that the shrinkage of the binary sphere array is only as large as the shrinkage of the large sphere array. The binary array shrinkage is therefore related to the large sphere shrinkage by (see Equation 3.64)

$$\dot{\epsilon}_v^{\text{sh}} = -\dot{S}_L \quad 5.21$$

where  $\dot{S}_L$  is the large sphere shrinkage rate (a positive quantity).

It is assumed that the shrinkage is isotropic giving

$$\dot{\epsilon}_r^{\text{sh}} = \dot{\epsilon}_\theta^{\text{sh}} = \dot{\epsilon}_z^{\text{sh}} = \dot{\epsilon}_v^{\text{sh}}/3. \quad 5.22$$

Equation 5.22 gives the creep strain rate components in the restructuring fuel.

### 5.3 FUEL SWELLING

The swelling of advanced fuels has been separated into four categories:

1. swelling due to solid fission products
2. microscopic swelling resulting from the nucleation and growth of fission gas bubbles within and on fuel grain boundaries
3. local swelling resulting from pore shrinkage (hot pressing), pore growth due to fission gas precipitation, grain growth, pore coalescence, crack healing, and gas release
4. crack formation and propagation.

The bubble and pore growth in mixed carbide fuels is not yet fully understood or quantified. Ronchi and Sari (1975) and Blank (1977) have qualitatively related the compressible gas swelling to the four restructuring zones described in Chapter 1 as follows:

- Zone IV very small bubbles (diameter  $< 0.1 \mu\text{m}$ ) only at higher burnups
- Zone III grain boundary bubbles (diameter  $> 0.5 \mu\text{m}$ ) ranging from small isolated bubbles on cold side of Zone III to interlinked bubbles on hot side
- Zone II large pores and bubbles (less than grain diameter) although overall porosity on the cold side may be lower than Zone III and IV porosity. Small pores and bubbles are eliminated by grain growth and pore migration.
- Zone I large pores (20 - 50  $\mu\text{m}$ ), high porosity region

Ronchi, et al (1978) and Blank (1975) identified a critical fuel temperature, located within Zone III that is an important parameter in determining the fission gas bubble growth. In fuel regions at temperatures below the critical temperature,  $T_C$ , the fission gas bubbles remain small and their effect on fuel swelling is small. Above  $T_C$  there is a large increase in the larger bubbles (diameter  $> 0.1 \mu\text{m}$ )

concentration which represents a main portion of the microscopic swelling. The critical temperature decreases with increasing burnup.

Recently Blank, et al have obtained some quantitative results for the microscopic swelling in mixed carbide pellet fuel. By measuring the bubble diameters in pellets at various burnup levels and at various radial locations in each pellet, they were able to get a bubble size distribution function that gives the bubble concentration for a particular size bubble as a function of fuel temperature and burnup. In this study they only considered intragranular bubbles. Expressions were obtained for the swelling of two bubble classes as a function of burnup and temperature. The bubble classes considered were the intragranular bubbles with diameters in the 0.03 - 0.4  $\mu\text{m}$  range and below the transition temperature where large bubble growth begins, and the intragranular bubbles in the same diameter range but above the critical temperature. Only bubbles in Zone IV and in Zone III near the Zone IV boundary were considered. The results were based on experimental data from sodium-bonded carbide pellet pins that experience little or no fuel cladding interaction. The predicted swelling using this model is therefore stress-free swelling.

There have been other correlations for the swelling in mixed carbide fuel that do not separate the swelling into its four contributing parts. Dienst (1979) obtained a swelling correlation that depends on the fuel centerline temperature and gives the overall swelling of a pellet. For a centerline temperature of 1050°C the overall swelling rate was found to be about 1.7%/FIMA (Fissions per Initial Metal Atom, unit of burnup). This increased to about 2.5%/FIMA at 1400°C and 3.5%/FIMA at 1600°C. At lower temperatures Clottes, et al (1973) observed a swelling rate of 1.45%/FIMA in mixed carbide pellets with centerline temperatures between 830 and 880°C.

This data based on centerline temperatures is not too useful for the sphere pac fuel since the centerline temperatures change considerably over the pin lifetime due to the restructuring. Further,

the swelling rate is a function of burnup as observed by Blank. A recent correlation by Zimmerman (1982) gives the swelling rate as a function of local temperature and burnup. His correlation is based on data taken on annular and solid pellet fuel (94 - 96%TD) in both stress-free and restrained conditions (confining pressure up to 40 MPa). The  $(U_{0.85}Pu_{0.15})C$  pellets were irradiated at spatially uniform temperatures in the range 280 - 1750°C and over a range of burnup up to 5.5 %FIMA. For mixed carbide fuel at constant temperature he obtained a swelling correlation given by

$$SW = 0.8B + C_1[1 - \exp(-C_2B)], \% \quad 5.23$$

where B is the burnup (%FIMA) and

$$C_1 = 10 + \frac{24}{1 + \exp\left(\frac{1400 - T}{74}\right)} \quad 5.24$$

$$C_2 = 0.06 + 8.025 \times 10^3 \exp(-2.027 \times 10^4/T) \quad 5.25$$

The first term in Equation 5.23 describes the swelling due to solid fission products, and the second term results from the fission gas-induced swelling. The influence of applied stress was found to be small. The solid fission product swelling is greater than the value determined by Blank et al (1976) (0.5%/FIMA). Figure 5.1 shows the swelling predicted by Equation 5.18 as a function of burnup at several temperatures. The temperatures and burnups have been extended beyond the range of the data and the validity of the correlation outside of the data range is unknown.

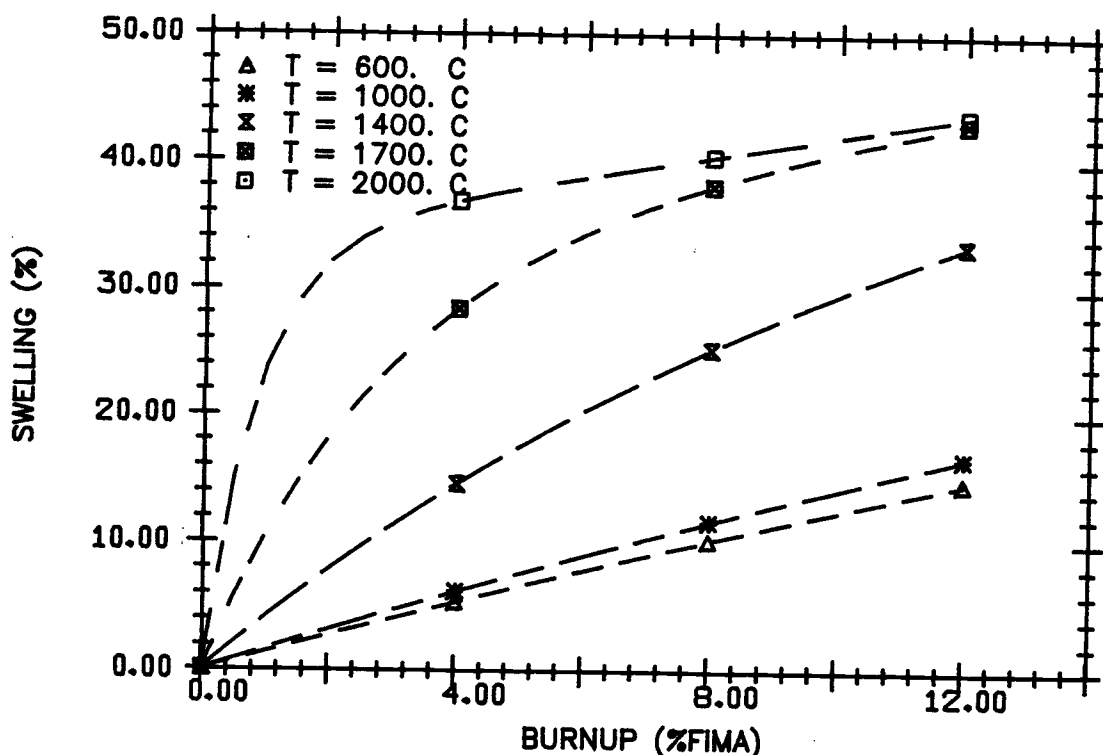


FIGURE 5.1. Swelling of (U,Pu)C at Constant Temperature

Until more detailed swelling correlations are derived (such as an extension of Blank's model) the fuel swelling is assumed to be given by Equation 5.23. The swelling strain rate is obtained by differentiating Equation 5.23 resulting in

$$\frac{\dot{\epsilon}_{sw}}{v} = 0.01 \left( 0.8 + \frac{C_1 C_2}{1 + C_2} \exp(-C_2 B) \right) \dot{B}, \text{ 1/sec} \quad 5.26$$

where  $\dot{B}$  is the burnup rate in %FIMA/sec. Since the swelling correlation was obtained for 94 - 96% TD fuel, which is approximately the as-fabricated porosity of the spheres, there is no porosity correction factor for the swelling rate. The swelling correlation does not exhibit any anomalies at temperatures and burnup outside the data range, so Equation 5.26 is used to estimate the fuel swelling rate at all fuel temperatures and burnups. This equation is used in both the

restructured and unrestructured regions of the fuel. The swelling is assumed to be isotropic, implying

$$\dot{\epsilon}_r^{SW} = \dot{\epsilon}_\theta^{SW} + \dot{\epsilon}_z^{SW} = \frac{1}{3} \dot{\epsilon}_V^{SW} \quad 5.27$$

#### 5.4 NONLINEAR ELASTIC STRAIN RATE

Changes in the elastic properties of a body under some nonzero constant load will result in some strains to satisfy the elastic stress-strain relationship. These changes in the elastic properties can result from temperature changes, if the properties are temperature dependent, and in the case of sphere pac fuel, changes in the material geometry through restructuring. From Chapter 2 the elastic stress-strain relation can be expressed as

$$\dot{\epsilon}^e = \frac{\partial e}{\partial \{\sigma\}} \dot{\{\sigma\}} + \frac{\partial e}{\partial \xi} \dot{\xi} \quad 5.28$$

where  $e$  is the elastic stress-strain function that relates the total elastic strain to the total stress and a combination of influencing parameters represented by  $\xi$ . The second term in Equation 5.28 is the strain rate due to changes in  $\xi$  at constant stress and is the nonlinear elastic strain rate giving

$$\dot{\epsilon}^{en} = \frac{\partial e}{\partial \xi} \dot{\xi} \quad 5.29$$

### 5.4.1 Restructuring Fuel Nonlinear Elastic Strain Rate

In the restructuring fuel an explicit form for the elastic stress-strain relation is not available. The nonlinear elastic strain rate must be calculated from the differential stress strain relation. This can be evaluated by calculating the total elastic strain rate at constant stress expressed as

$$\{\dot{\epsilon}^{en}\} = \{\dot{\epsilon}_{\sigma=C}^e\} \quad 5.30$$

For a constant  $\xi$ , the elastic strain rate is given by

$$\{\dot{\epsilon}^e\} = [D]\{d\tilde{\sigma}\} \quad 5.31$$

where  $[D] = [E]^{-1}$  is the elastic compliance matrix derived in Chapter 3. Recall that  $[D]$  depends on the hydrostatic stress as well as  $\xi$ . Integrating both sides of Equation 5.31 with respect to time and assuming that  $\{\epsilon\} = \{\sigma\} = 0$  at  $t = 0$  gives

$$\{\epsilon^e\} = \int_0^{\{\sigma\}} [D] \{d\tilde{\sigma}\} \quad 5.32$$

Equation 5.32 gives the total elastic strain for given values of  $\xi$  and  $\{\sigma\}$ . The nonlinear strain rate can now be obtained by differentiating Equation 5.38 with respect to time at constant stress giving

$$\{\dot{\varepsilon}^{en}\} = \{\dot{\varepsilon}_{\sigma=C}^e\} = \frac{d}{dt} \int_0^{\{\sigma\}} [D] \{d\tilde{\sigma}\} \quad 5.32$$

For a finite time increment Equation 5.32 becomes

$$\{\varepsilon^{en}\} = \frac{1}{\Delta t} \left[ \int_0^{\{\sigma\}} [D(\xi_{t+\Delta t})] \{d\tilde{\sigma}\} - \int_0^{\{\sigma\}} [D(\xi_t)] \{d\tilde{\sigma}\} \right] \quad 5.33$$

where  $\xi_t$  is the value of  $\xi$  at time  $t$ . Thus it is required to evaluate integrals of the form

$$I = \int_0^{\{\sigma\}} [D(\xi)] \{d\tilde{\sigma}\} \quad 5.34$$

Since here  $[D]$  depends only on the hydrostatic stress, it is convenient to make the change of variable

$$\{\tilde{\sigma}\} = \tilde{I}_1 / I_1 \{\sigma\} \quad 5.35$$

where  $I_1$  and  $\tilde{I}_1$  are the first stress invariants associated with  $\{\sigma\}$  and  $\{\tilde{\sigma}\}$ . Equation 5.42 defines a particular loading path from zero stress to  $\{\sigma\}$ . This does not cause any difficulty, since only elastic strains are considered and the integral is path independent. The integral then becomes

$$I = \int_0^1 [D] d\lambda \{\sigma\} \quad 5.36$$

where  $\lambda = \tilde{I}_1/I_1$ . The functional form of the compliance matrix  $[D]$  changes at  $\sigma^*$  (the hydrostatic compression at which the large and small sphere arrays begin to interact) so the integral is separated into two parts

$$I = \left[ \int_0^{\lambda^*} [D]d\lambda + \int_{\lambda^*}^1 [D]d\lambda \right] \{\sigma\} \quad 5.37$$

where  $\lambda^* = \sigma^*/I_1$

The functional dependence of  $[D]$  on the hydrostatic stress is deeply buried by the algebra in the derivation of the binary array stress-strain relation in Chapter 3 making the analytic evaluation of Equation 5.37 virtually impossible. The integral must be evaluated for each fuel region at every time step so that any numerical scheme used must be extremely fast. To obtain a suitable quadrature formula to evaluate the integral it is observed that for a single-size sphere array the entries in  $[D]$  are of the form (see Equations 3.2, 3.30, 3.37, and 3.42).

$$A + \frac{B}{C\lambda^{1/3} + D}$$

It is also observed (see Section 3.7) that the functional dependence of the binary array on hydrostatic stress is not too much different than that of the single-size sphere array. It is therefore expected that the compliance matrix for the binary could be approximated by terms having the above form. Any quadrature formula that could integrate terms of the above form exactly should provide a good approximation to the integrals given by Equation 5.37. Equivalently, the quadrature formula should integrate

$$1 + \frac{1}{\lambda^{1/3} + D/C}$$

exactly. This requires a quadrature formula that depends on the unknown value  $D/C$  which is unfeasible. For large  $D/C$  (equivalent to material approaching a porous body) the above term approaches unity and for small  $D/C$  it approaches

$$1 + \lambda^{-1/3}$$

A quadrature formula can easily be found (see Appendix C) that integrates terms of this form exactly and is given by

$$\int_0^1 f d\lambda = 0.4149993 f_{.1} + 0.5850007 f_{.9} \quad 5.38$$

where  $f_{.1}$  is  $f(\lambda = 0.2)$  and  $f_{.9}$  is  $f(\lambda = .9)$ .

This two-point quadrature formula provides a reasonable approximation to the two integrals in Equation 5.37 as can be seen in Figure 5.2. This figure compares one strain component evaluated according to Equation 5.36 or 5.32 using Simpson's rule and using the two-point quadrature formula. The integral was evaluated for a case of uniaxial compression and a variety of combinations (randomly chosen) of stress,  $\sigma^*$ , and large and small fraction neck ratios. The good agreement between the two integration schemes for all points indicates that the simple two-point quadrature scheme is sufficient to evaluate the required integrals. For sphere arrays with no necks the compliance

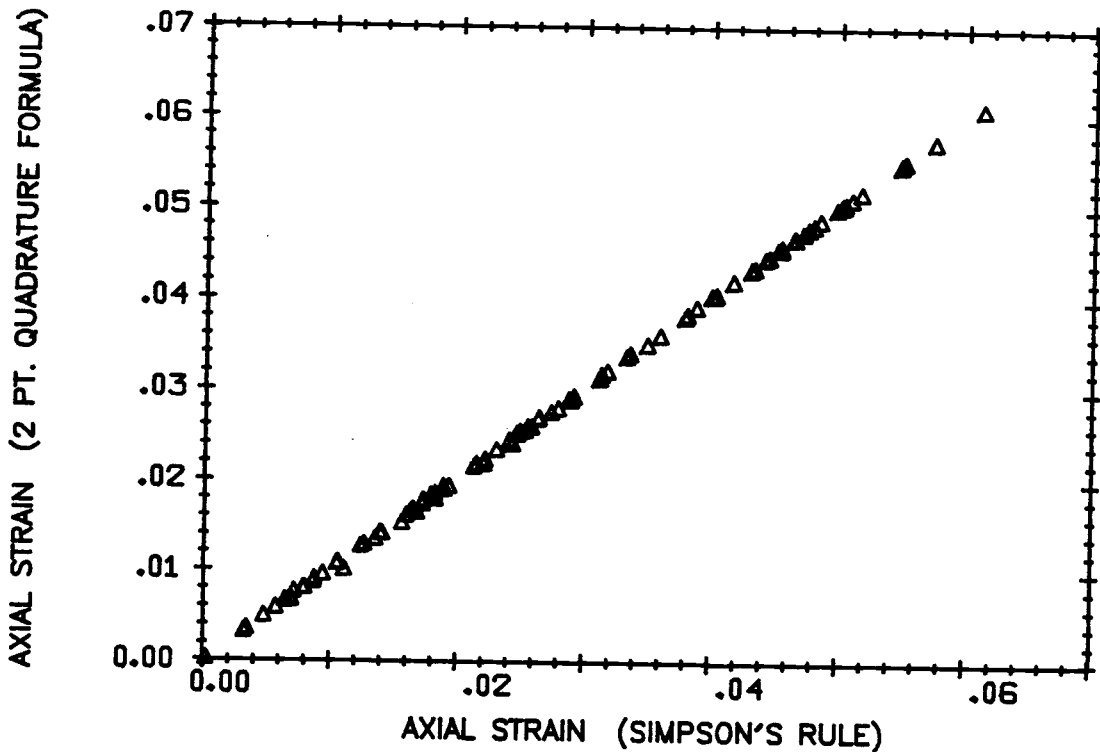


FIGURE 5.2. Comparison of Two-Points Quadrature Formula and Simpson's Rule for Integration of Equation 5.37

at zero stress is infinite. For these cases Simpson's rule does not provide a good estimate of the total strain. The few points where the two integration schemes differ by more than 2 or 3% have been identified as being associated with an array with very small necks.

Once the integration has been carried out, the nonlinear elastic strain rate can be obtained from

$$[\dot{\epsilon}^{en}] = \frac{1}{\Delta t} [I'_{t+\Delta t} - I'_t] \{\sigma\} \quad 5.39$$

where

$$I'_t = \int_0^1 [D \{\xi_t\}] d\lambda$$

#### 5.4.2 Restructured Fuel Nonlinear Elastic Strain Rate

In the restructured fuel an explicit form for the total stress-strain relation is available and is given by

$$\{\varepsilon\} = [D]\{\sigma\} \quad 5.40$$

From Equation 5.28 and 5.29 the nonlinear elastic strain rate is easily seen to be

$$\{\dot{\varepsilon}^{en}\} = [\dot{D}]\{\sigma\} \quad 5.41$$

where  $[\dot{D}]$  is the time rate of change of the compliance matrix.

## 6.0 CLADDING MECHANICAL MODELS

The mechanical models for the cladding are much simpler than those for the restructuring fuel and, in most cases, are a reduced form of the fuel mechanical models presented in Chapters 3, 4, and 5. The governing equations for the cladding are the same as those given in Chapter 2. In this chapter the models for each of the total strain components (elastic, plastic, etc.) are presented.

### 6.1 CLADDING ELASTIC STRESS-STRAIN RELATION

The cladding is assumed to be elastically isotropic and the elastic strain rate is given by

$$\{\dot{\epsilon}^e\} = [D]\{\dot{\sigma}\} + [\dot{D}]\{\alpha\} \quad 6.1$$

where

$$[D] = \frac{1}{E_c} \begin{bmatrix} 1 & -\nu_c & -\nu_c \\ -\nu_c & 1 & -\nu_c \\ -\nu_c & -\nu_c & 1 \end{bmatrix}$$

and  $E_c$  and  $\nu_c$  are Young's modulus and Poisson's ratio for the cladding.  $E_c$  and  $\nu_c$  are not specified here since there is a variety of choices possible for the cladding material. Elastic properties for stainless steel are available in the Nuclear Systems Materials Handbook (NSMH 1976) and properties for advanced alloys can be found in the Advanced Alloys Databook (AAD) (Laidler 1980). Generally, these two elastic constants are functions of the temperature only.

## 6.2 CLADDING PLASTIC CONSTITUTIVE RELATION

The cladding yield function is assumed to be given by the von Mises criteria

$$f = J_2^{1/2} - \frac{\sigma_y}{\sqrt{3}} \quad 6.2$$

where  $\sigma_y$  is the yield strength of the material in uniaxial tension. The yield strength depends on temperature, strain rate, and reactor fluence. As is usually done for metals, associated flow is assumed for the cladding implying that the plastic potential and yield function are identical. Thus

$$g = J_2^{1/2} - \frac{\sigma_y}{\sqrt{3}} \quad 6.3$$

Strain hardening of 20% cold worked stainless steel and the advanced alloys is generally small and is neglected in this analysis.

Under the above assumptions, the plastic modulus matrix for the cladding can be obtained from Equation 2.19 and is given by

$$[P_c] = \frac{1}{2J_2} \begin{bmatrix} s_r s_r & s_r s_\theta & s_r s_z \\ s_\theta s_r & s_\theta s_\theta & s_\theta s_z \\ s_z s_r & s_z s_\theta & s_z s_z \end{bmatrix} \quad 6.3$$

where  $s_r$ ,  $s_\theta$ , and  $s_z$  are the stress deviator components. The plastic modulus matrix is required in Equation 2.16 to relate the plastic strain rate to the total strain rate, the initial strain rate, and the

plastic strain rate due to changes in the yield stress of the material. The plastic strain rate due to changes in the yield stress is defined by Equation 2.17. Without knowing the explicit form of  $\partial f / \partial \chi \dot{\chi}$ , the strain rate can be defined for a finite time increment by

$$\{\dot{\epsilon}^{pp}\} = \frac{(1 + \nu_c)}{\Delta t} \frac{f(\sigma_t, \chi_{t+\Delta t}) - f(\sigma_t, \chi_t)}{E_c} \begin{Bmatrix} s_r \\ s_\theta \\ s_z \end{Bmatrix} \quad 6.4$$

where  $f(\sigma_t, \chi_t)$  is the yield function evaluated at the stress at time  $t$  and other influencing parameters (temperature, fluence) also at time  $t$ .

### 6.3 INITIAL STRAIN RATE

Like the fuel, the initial strain rate for the cladding consists of thermal, creep, and swelling strain rates and an elastic strain rate resulting from changes in the elastic constants in the material at constant stress.

The thermal strain rate is given by Equation 5.1 where the coefficient of expansion is taken from NSMH or AAD. As implied by Equation 5.1, the thermal strains are assumed to be isotropic.

The creep strain rate is given by Equation 5.14 where the effective uniaxial creep strain rate  $\dot{\epsilon}_c$  is for the specific cladding material being modeled. The uniaxial creep rate is generally given as the sum of thermal and irradiation-induced creep rates. The creep rate is generally a function of the effective stress, the fast fluence, and the temperature. The correlations usually provide a total creep correlation giving

$$\epsilon_c = \epsilon_c^t(t, \sigma_e, T) + \epsilon_c^i(\phi t, \sigma_e, T) \quad 6.5$$

where  $\epsilon_C^t$  and  $\epsilon_C^i$  are the thermal and irradiation-induced components, respectively, and  $t$  is time.  $\sigma_e$  is the effective stress (defined with Equation 5.14),  $T$  is temperature and  $\phi t$  is the fast fluence. The creep rate is obtained from these correlations by differentiating with respect to time giving

$$\dot{\epsilon}_C = \dot{\epsilon}_C(t, \sigma_e, T) + \frac{\partial \epsilon_C^i}{\partial \phi t}(\phi t, \sigma_e, T) \phi \quad 6.6$$

where  $\phi$  is the fast flux.

The swelling correlation for cladding materials is usually given as the sum of two components: a densification term and a swelling term. The densification occurs early in the pin lifetime and decreases as the fluence increases. The swelling increases with fluence and overtakes the densification at fast fluences of about  $1 \times 10^{22}$  n/cm<sup>2</sup>. The available swelling correlations are for stress-free material. According to a theoretical swelling model by Brailsford and Bullough (1973) the effect of stress on swelling is small for stainless steel cladding at temperatures below 600°C. Data reported by Bates, et al (1981) however, indicates that stress does influence swelling at temperatures below 600°C, but the dependence has not been quantified.

The swelling correlations are generally given in the form

$$\epsilon_V^{SW} = S_0(\phi t, T) - D(\phi t) \quad 6.7$$

where  $S_0$  is the swelling term and  $D$  is the densification term. The swelling rate is then given by

$$\dot{\epsilon}_V^{SW} = \frac{\partial \epsilon_V^{SW}}{\partial \phi t} \phi$$

6.8

For cold worked stainless steel the stress-free swelling is slightly anisotropic with the growth in the axial direction generally larger than that in the other two directions, as observed by Bates, et al. (1981). For stressed cladding the anisotropy was smaller. Until the anisotropy can be quantified for the various cladding materials and stress dependence, the swelling is assumed to be isotropic. The components of the swelling strain rate vector can then be obtained from Equation 5.27.

The final contribution to the initial strain rate is the nonlinear elastic strain rate. As in the case of the restructured fuel, a total elastic stress-strain relation is available so the strain rate is simply obtained from Equation 5.41.

All the strain rates and material properties for the fuel and cladding have now been specified, so the stress-strain relationship (Equation 2.18) has been completely established. It remains to solve the equilibrium and strain displacement equations coupled by the stress-strain relationship. The numerical procedure used to solve the equations is described in the next chapter.

## 7.0 NUMERICAL SOLUTION

The solution of the elastoplastic equations described in Chapter 2 is accomplished through the use of a finite-element method (see e.g., Zienkiewicz 1971 or Bathe and Wilson 1976) incorporated in the SPECKLE-III code. The numerical schemes used for the thermal models (temperature distribution, fission gas model, etc.) were discussed by Ades (1979) and George and Peddicord (1981) and are not considered here. It is assumed that, for purpose of the mechanical model numerics, the required input from the thermal model (temperature rate of change, neck radius, etc.) are available in the required form.

The finite-element method chosen is based on the principle of virtual work that states that for a body in equilibrium subject to small additional displacement with external loads held constant, the internal work done on the body is equal to the work done by the external loads. This can be expressed as

$$\int_V \{\delta\epsilon\}^T \{\sigma\} dV = \int_A \{\delta U\}^T \{F\} dA \quad 7.1$$

where  $V$  and  $A$  are the volume and surface area of the body considered,  $\{\delta U\}$  is the small displacement,  $\{\delta\epsilon\}$  is the strain increment consistent with  $\{U\}$ ,  $\{\sigma\}$  is the equilibrium stress state and  $\{F\}$  is the external load. The pin is subdivided into a number of finite elements as shown in Figure 7.1. The pin is divided axially into segments, each of length  $\Delta z$ . The fuel and cladding are further divided into cylinders of equal wall thickness ( $\Delta r_c$  for the cladding and  $\Delta r_f$  for the fuel). There is also a fuel-cladding interface element that allows slip between the fuel and the cladding as described later in this chapter. The interface element radial dimension is  $0.001r_f$  and is not considered in the thermal model.

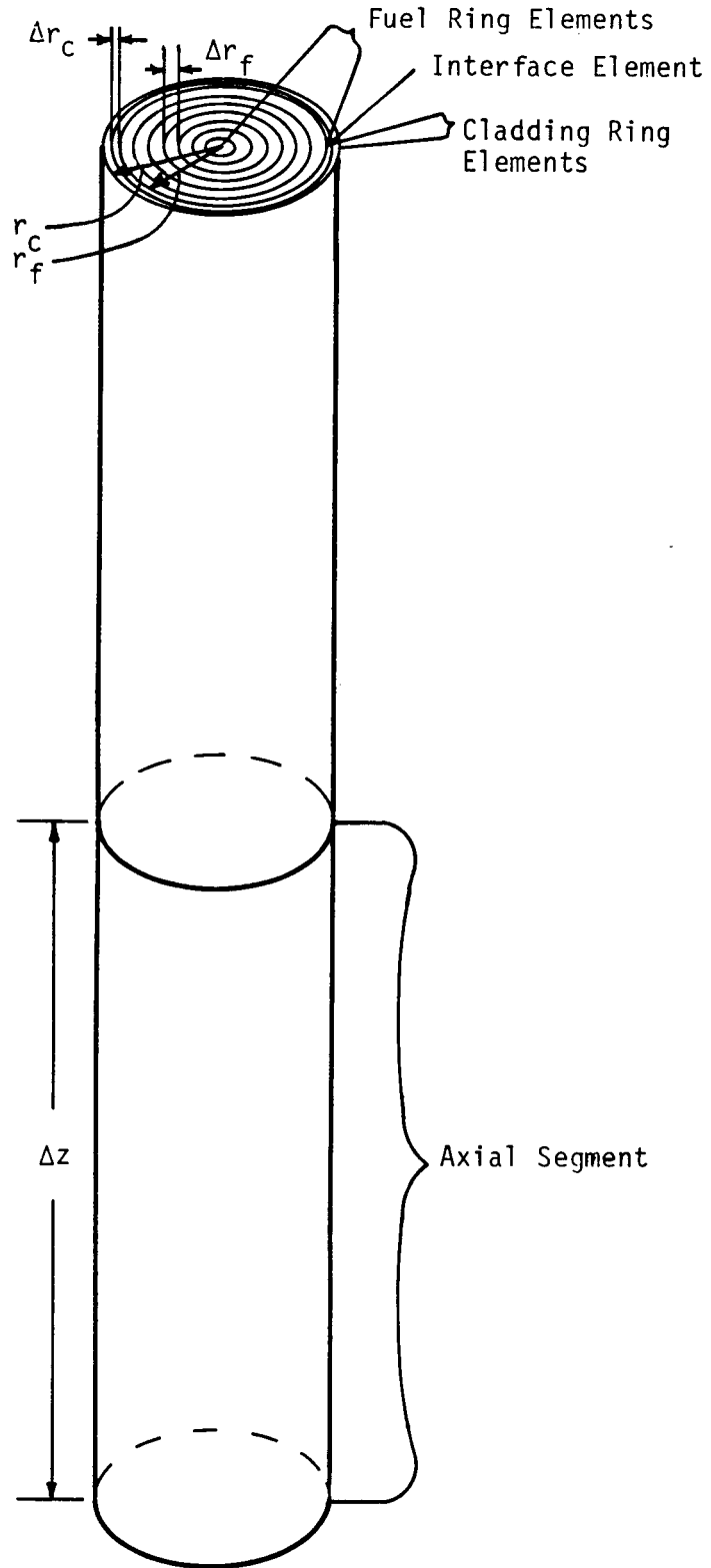


FIGURE 7.1. Elements for Fuel Pin Modeling

Since the system pressure in an LMFBR is low, it is assumed that there is no radially applied external force at the cladding outer surface. The bottom end of the pin is assumed fixed axially and the top end is assumed to be free and without any axial load. The only force considered that enters the right hand side of Equation 7.1 is the force exerted by the gas in the pin on the cladding interior and the outermost restructured fuel ring. The integration of Equation 7.1 is carried out over the individual ring elements giving

$$\sum_n \int_{V_n} \{\delta \epsilon_n\}^T \{\sigma_n\} dV_n = \sum_n \int_{A_n} \{\delta U_n\}^T \{F_n\} dA_n \quad 7.2$$

where  $V_n$  and  $A_n$  are the volume and surface area for an individual element.

### 7.1 FUEL AND CLADDING ELEMENT STIFFNESS EQUATION

An individual fuel element is shown in Figure 7.2 (the cladding elements are analogous). Under the general assumption listed in Chapter 2 the fuel element has only four degrees of freedom: the inner and outer radial displacement and the axial displacement at either end. An isoparametric formulation is used and the radial and axial displacements are assumed to vary linearly in the radial and axial directions, respectively. The radial and axial displacements at any point in an element are given by

$$U_n(s_1) = \frac{1}{2} [U_1^n(1 - s_1) + U_2^n(1 + s_1)]$$

$$V_n(s_2) = \frac{1}{2} [V_1^n(1 - s_2) + V_2^n(1 + s_2)] \quad 7.3$$

where  $s_1$  and  $s_2$  are coordinates that run in the radial and axial directions, respectively, and range from -1.0 (at the inner radius and element bottom) to +1.0 (at the outer radius and element top).

For any displacement field  $(U_n, V_n)$  the corresponding strain field can be obtained from the kinematic relations (Equation 2.2) and

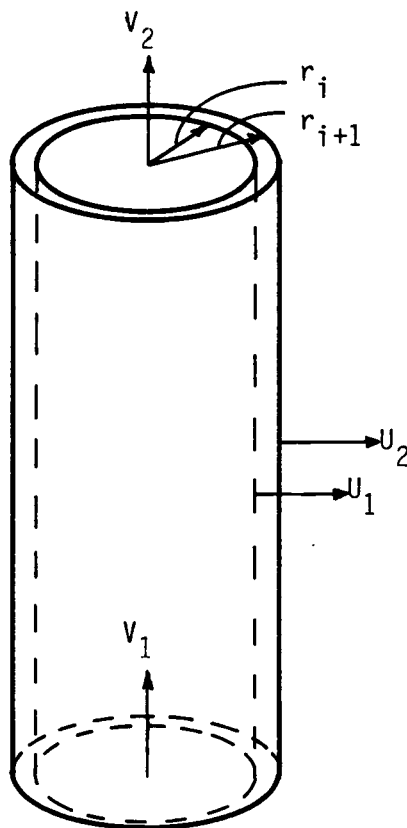


FIGURE 7.2. Fuel or Cladding Ring Element

Equations 7.3. This gives

$$\{\epsilon_n(s_1, s_2)\} = [B_n] \{U_n\} \quad 7.4$$

where

$$[B_n] = \begin{bmatrix} 0 & 0 & -1/\Delta z_n & 1/\Delta z_n \\ -1/\Delta R_n & 1/\Delta R_n & 0 & 0 \\ 1/R2_n & 1/R2_n & 0 & 0 \end{bmatrix}$$

$$\{U_n\}^T = [U_1^n, U_2^n, V_1^n, V_2^n]$$

$$\{\epsilon_n\}^T = [\epsilon_z^n, \epsilon_r^n, \epsilon_\theta^n]$$

with  $R2_n = r_n + r_{n+1}$  and  $\Delta R_n = r_{n+1} - r_n$ .

The strain increment corresponding to an incremental change in the displacement field is given by

$$\{\delta\epsilon_n\} = [B_n] \{\delta U_n\} \quad 7.5$$

From Equation 2.18 the stress vector at time  $t$  can be written as

$$\{\sigma_n\} = \{\sigma_n^0\} + \int_0^t [E_n] ([I] - [P_n]) (\{\dot{\epsilon}_n\} - \{\dot{\epsilon}_n^0\}) + [E_n] \{\dot{\epsilon}_n^{pp}\} dt \quad 7.6$$

where  $\{\sigma_n^0\}$  is the stress at time  $t = 0$ .

The total strain rate is related to the displacement rate by

$$\{\dot{\epsilon}_n\} = [B_n] \{\dot{U}_n\} \quad 7.7$$

Substituting Equations 7.5, 7.6 and 7.7 into Equation 7.2 gives

$$\begin{aligned} & \sum_n \int_{V_n} \{\delta U_n\}^T [B_n]^T \int_0^t [E_n] ([I] - [P_n]) [B_n] \{\dot{U}_n\} dt dV_n \\ &= \sum_n \int_{V_n} \{\delta U_n\}^T [B_n]^T \int_0^t [E_n] ([I] - [P_n]) \{\dot{\epsilon}_n^0\} - [E_n] \{\dot{\epsilon}_n^{PP}\} dt - \{\sigma_n^0\} dV_n \\ & \quad + \sum_n \int_{A_n} \{\delta U_n\}^T \{F_n\} dA_n \end{aligned} \quad 7.8$$

In the following discussion, the displacements  $U_1^n, U_2^n, V_1^n, V_2^n$  are referred to as node point displacements even though the displacement actually applies to an entire surface of the element. For the assemblage of elements the incremental node point displacements are arbitrary and it can therefore be shown (e.g., Bathe and Wilson 1976) that Equation 7.8 reduces to

$$\begin{aligned} & \sum_n \int_{V_n} [B_n]^T \int_0^t [E_n] ([I] - [P_n]) [B_n] \{\dot{U}_n\} dt dV_n \\ &= \sum_n \int_{V_n} [B_n]^T \int_0^t [E_n] ([I] - [P_n]) \{\dot{\epsilon}_n^0\} - [E_n] \{\dot{\epsilon}_n^{PP}\} dt - \{\sigma_n^0\} dV_n \\ & \quad + \sum_n \int_{A_n} \{F_n\} dA_n \end{aligned} \quad 7.9$$

Then differentiating Equation 7.9 with respect to time gives

$$\begin{aligned}
 & \sum_n \int_{V_n} [B_n]^T [E_n] ([I] - [P_n]) [B_n] \{\dot{U}_n\} dV_n \\
 &= \sum_n \int_{V_n} [B_n]^T [E_n] ([I] - [P_n]) \{\dot{\epsilon}_n^0\} - [E_n] \{\dot{\epsilon}_n^{pp}\} dV_n \\
 &+ \sum_n \int_{A_n} \{\dot{F}_n\} dA_n
 \end{aligned}$$

This expression can be simplified by introducing the element stiffness matrix  $[K_n]$  and forcing vector  $\{Q_n\}$  defined by

$$[K_n] = \int_{V_n} [B_n]^T [E_n] ([I] - [P_n]) [B_n] dV_n \quad 7.11$$

$$\begin{aligned}
 \{\dot{Q}_n\} &= \int_{V_n} [B_n]^T [E_n] ([I] - [P_n]) \{\dot{\epsilon}_n^0\} - [E_n] \{\dot{\epsilon}_n^{pp}\} dV_n \\
 &+ \int_{A_n} \{\dot{F}_n\} dA_n
 \end{aligned} \quad 7.12$$

The elastic and plastic modulus matrices are assumed constant within an individual element and  $[B_n]$  is also constant over the element so that

$$[K_n] = V_n [B_n]^T [E_n] ([I] - [P_n]) [B_n] \quad 7.13$$

and

$$\begin{aligned} \{\dot{Q}_n\} = & V_n ([B_n]^T [E_n] ([I] - [P_n]) \{\epsilon_n^o\} - [E_n] \{\epsilon_n^{pp}\}) \\ & + A_n \{\dot{F}_n\} \end{aligned} \quad 7.14$$

The last term of  $\{\dot{Q}_n\}$  is due to gas pressure force on the cladding or restructured fuel. For the inner most cladding element this term has the form

$$A_n \{\dot{F}_n\} = 2\pi r_f \Delta z \dot{P}_g \begin{Bmatrix} 1 \\ 0 \\ 0 \\ 0 \end{Bmatrix} \quad 7.15$$

where  $\dot{P}_g$  is the rate of change of the gas pressure. The force for the outermost restructured fuel region is

$$A_n \{\dot{F}_n\} = -2\pi r_r \Delta z \dot{P}_g \begin{Bmatrix} 0 \\ 1 \\ 0 \\ 0 \end{Bmatrix} \quad 7.16$$

where  $r_r$  is the radius of the restructured region.

The gas also exerts an axial force on the cladding transmitted through the end plug. The end plug is not explicitly modeled but the resulting axial force is applied to the innermost cladding element at the top axial level. The force term for this element is

$$A_n \{ \dot{F}_n \} = \pi r_f \dot{p}_g \begin{Bmatrix} 2\Delta z \\ 0 \\ 0 \\ r_f \end{Bmatrix} \quad 7.17$$

For an individual element a stiffness equation is thus obtained that relates the node point displacement rate to the forcing function given by

$$[K_n] \begin{Bmatrix} \dot{u}_1^n \\ \dot{u}_2^n \\ \dot{v}_1^n \\ \dot{v}_2^n \end{Bmatrix} = \begin{Bmatrix} \dot{Q}_1^n \\ \dot{Q}_2^n \\ \dot{Q}_3^n \\ \dot{Q}_4^n \end{Bmatrix} \quad 7.18$$

An equation of the above form can be constructed for each of the fuel and cladding elements. The stiffness matrix for the interface element is somewhat different and is developed in the following section.

## 7.2 INTERFACE ELEMENT STIFFNESS EQUATION

It will be recalled from the assumptions in Chapter 2 that the fuel and cladding are each separately in a state of generalized plane strain. Slip between the fuel and cladding would result in different axial strains for the fuel and the cladding. The slip/no-slip condition at the interface can easily be included in the general elastoplastic model. To accomplish this a special interface element has been devised. When the element is in the purely elastic state, a no-slip condition is imposed at the interface, while when it is in the elastic-plastic state, slip is allowed until the interface frictional force balances the difference in axial force across the interface.

The degrees of freedom for the interface element are shown in Figure 7.3. The vertical surfaces of the cylinder can displace radially and axially. The element is not connected to adjacent interface elements at the top or the bottom and axial strain of the elements is not considered. With the degrees of freedom shown in Figure 7.3 the possible strains are

$$\begin{Bmatrix} \epsilon_r^n \\ \epsilon_\theta^n \\ \gamma^n \end{Bmatrix} = [B_n^I] \begin{Bmatrix} U_1^n \\ U_2^n \\ W_1^n \\ W_2^n \end{Bmatrix} \quad 7.19$$

The shear strain is given by

$$\gamma = dW/dr \quad 7.20$$

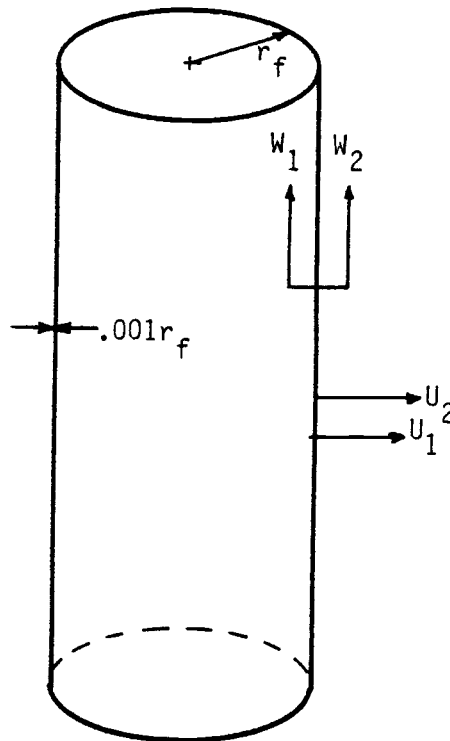


FIGURE 7.3. Fuel-Cladding Interface Element

so that the  $[B_n^I]$  matrix is defined by

$$[B_n^I] = \begin{bmatrix} -1/\Delta R & 1/\Delta R & 0 & 0 \\ 1/R_2 & 1/R_2 & 0 & 0 \\ 0 & 0 & -1/\Delta R & 1/\Delta R \end{bmatrix}$$

In the solution for the node point displacements it is assumed that  $W_1$  is equal to  $V_2$  for the adjacent fuel element and that  $W_2$  is equal to  $V_2$  for the adjacent cladding element. Any slip between the fuel and cladding therefore results in shear strain of the interface element. The elastic stress-strain relation for the interface element is chosen so that it will provide the proper fuel cladding interface pressure and shear stress but will not artificially restrain the fuel

or cladding. This is accomplished by setting the radial elastic modulus and the shear modulus to arbitrarily large values, the elastic modulus for tangential strains to an arbitrary small value, and Poisson's ratio to zero. The element is therefore very stiff radially and in shear and effectively provides a matched displacement condition for the fuel and cladding. By making the elastic modulus for tangential strains small, the element cannot contribute significantly to hoop restraint provided by the cladding. The stress-strain relation is

$$\begin{Bmatrix} \sigma_r^n \\ \sigma_\theta^n \\ \tau_n \end{Bmatrix} = \begin{bmatrix} E_R & 0 & 0 \\ 0 & E_T & 0 \\ 0 & 0 & G \end{bmatrix} \begin{Bmatrix} \epsilon_r^n \\ \epsilon_\theta^n \\ \gamma^n \end{Bmatrix} \quad 7.21$$

where  $E_R = G = 1 \times 10^7$  MPa and  $E_T = 1.0$  MPa.

As long as the interface element is in an elastic state the difference in axial displacement of the fuel and cladding will be very small (but not zero) due to the large shear modulus and the thinness of the element.

Fuel cladding slip occurs when the interface element goes to an elastoplastic state. It is assumed that the interface shear stress developed in a sphere pac pin is constant over the length of an axial segment. This shear stress is represented by the shear stress developed in the interface element. Slip at the interface will not occur as long as

$$|\tau_I| < \mu_I \sigma_{r_I} \quad 7.22$$

where  $\tau_I$  and  $\sigma_{r_I}$  are the interface shear and radial stresses and  $\mu_I$  is the coefficient of static friction for the sphere pac fuel against the

cladding. The yield function chosen to represent this slip/no-slip condition is

$$f_1 = |\tau| + \mu_I \sigma_{r_I} + C_1 \quad 7.23$$

where  $C_1$  is a small positive stress. The intersection of the yield surface with the  $(\tau_I, \sigma_{r_I})$  plane is shown in Figure 7.4.  $C_1$  is included in Equation 7.23 to avoid difficulties in going around the sharp point at apex of the yield surface. The value of  $C_1$  is chosen small enough so that when  $|\tau| < C_1$  the amount of axial strain in the cladding resulting from a complete release of the shear stress would be negligible. By the assumption of generalized plane strain, the cladding does not experience the interface shear force directly, but it shows up as an axial stress through the element coupling. The total axial force experienced by the cladding elements for one axial level is

$$\tau_I A_I = \bar{\sigma}_C A_C \quad 7.24$$

where  $A_I$  is the interface area,  $A_C$  is the cladding cross section area, and  $\bar{\sigma}_C$  is the average axial stress across the cladding cross section. The axial strain in the cladding resulting from the interface shear is then

$$\epsilon_C = \bar{\sigma}_C / E_C = \frac{\tau_I A_I}{A_C E_C} \quad 7.25$$

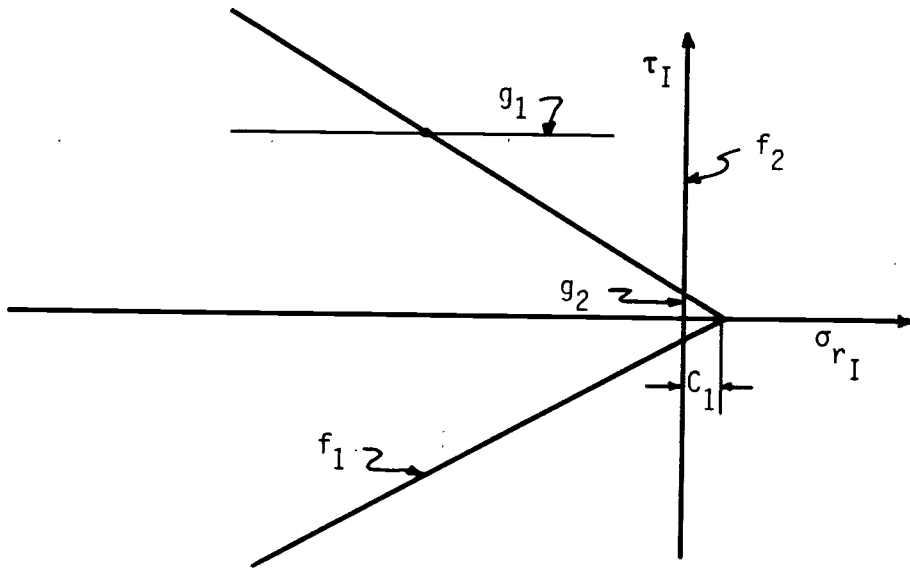


FIGURE 7.4. Yield Surface for Interface Element

where  $E_C$  is Young's modulus for the cladding.

A value for  $C_1$  can now be obtained by setting  $\tau_I = C_1$  and letting  $\epsilon_C^{\max}$  be the maximum allowable unrecovered axial strain, giving

$$C_1 = \frac{\epsilon_C^{\max} E_C A_C}{A_I} \quad 7.26$$

A value of  $\epsilon^{\max} = 1 \times 10^{-6}$  is used to calculate  $C_1$ .

A second yield surface represents the situation when the interface radial stress is greater than or equal to zero and a gap is opening between the fuel and the cladding. This surface is given by

$$f_2 = \sigma_{r_I} \quad 7.27$$

and is shown in Figure 7.4. Yielding occurs whenever  $f_1$  or  $f_2$  exceeds zero.

Equation 7.23 cannot be used for the plastic potential function because the plastic flow would always include some radial strain along with the plastic shear strain that simulates the slip. The plastic potential function should predict only plastic shear when the stress state is on  $f_1$  and only radial strains when yielding on  $f_2$ . A plastic potential function that has these properties is given by

$$g = \begin{cases} g_1 = |\tau| & \text{when on } f_1 \\ g_2 = \sigma_{r_I} & \text{when on } f_2 \end{cases} \quad 7.28$$

and is shown in Figure 7.4.

The plastic flow rule resulting from application of Equation 2.11 to Equation 7.21 is

$$\begin{Bmatrix} \dot{\epsilon}_r \\ \dot{\epsilon}_\theta \\ \dot{\gamma} \end{Bmatrix}_{\text{plastic}} = d\lambda \begin{Bmatrix} \begin{pmatrix} 0 & \text{on } f_1 \\ 1 & \text{on } f_2 \end{pmatrix} \\ 0 \\ \begin{pmatrix} \text{sign}(\tau) & \text{on } f_1 \\ 0 & \text{on } f_2 \end{pmatrix} \end{Bmatrix} \quad 7.29$$

giving the desired plastic strain rate components.

From Equations 7.23, 7.27, 7.28, and 2.15 the plastic modulus matrix can be obtained and is given by

$$[P_I] = \begin{bmatrix} \begin{pmatrix} 0 & \text{on } f_1 \\ 1 & \text{on } f_2 \end{pmatrix} & 0 & 0 \\ 0 & 0 & 0 \\ \begin{pmatrix} E_r/G \mu \text{ sign}(\tau) & \text{on } f_1 \\ 0 & \text{on } f_2 \end{pmatrix} & 0 & \begin{pmatrix} 1 & \text{on } f_1 \\ 0 & \text{on } f_2 \end{pmatrix} \end{bmatrix} \quad 7.30$$

There are no initial strain rates for the interface element and the strain rate due to the changes in the yield properties can be obtained from Equation 2.17. For finite time increments the parameter change rate term required in Equation 2.17 is given by

$$\frac{\partial f}{\partial \chi} \dot{\chi} = \frac{1}{\Delta t} (f(\sigma_t, \chi_{t+\Delta t}) - f(\sigma_t, \chi_t)) \quad 7.31$$

where  $f(\sigma_t, \chi_t)$  is the yield function evaluated using the time  $t$  values for  $\sigma$  and  $\chi$ . In the present model it is assumed that  $\mu_1$  is constant, which implies that  $\dot{\chi} = 0$  and Equation 7.31 appears unnecessary. However, due to all of the nonlinearities in the equations, when plastic flow is predicted, the stress state does not always remain precisely on the yield surface, i.e., the yield function,  $f$ , has a value not equal to zero after a time increment is completed. This error in the stress state is corrected at the next time step by solving

$$df(\sigma_{t+\Delta t}, \chi_{t+\Delta t}) = -f(\sigma_t, \chi_t) \quad 7.32$$

rather than  $df = 0$  as stated in Equation 2.12. Starting with Equation 7.32 and following through the steps in going from Equation 2.12 to 2.17 results in a modification to the strain rate due to changes in the yield parameters given now by

$$\{\dot{\epsilon}^{pp}\} = \frac{\frac{\partial f}{\partial \chi} \dot{\chi} + \frac{1}{\Delta t} f(\sigma_t, \chi_t) \left\{ \frac{\partial g}{\partial \sigma} \right\}}{\left\{ \frac{\partial f}{\partial \sigma} \right\}^T [E] \left\{ \frac{\partial g}{\partial \sigma} \right\} - \left\{ \frac{\partial f}{\partial \epsilon} \right\}^T \left\{ \frac{\partial g}{\partial \sigma} \right\}} \quad 7.33$$

Then, by substituting Equation 7.31 into 7.33 and assuming perfect plasticity, the above strain rate becomes

$$\{\dot{\epsilon}^{pp}\} = \frac{\frac{1}{\Delta t} f(\sigma_t, \chi_{t+\Delta t}) \left\{ \frac{\partial g}{\partial \sigma} \right\}}{\left\{ \frac{\partial f}{\partial \sigma} \right\}^T [E] \left\{ \frac{\partial g}{\partial \sigma} \right\}} \quad 7.34$$

Equation 7.34 applies to the fuel and cladding as well as the interface element. For the interface element the strain rate due to yield parameter changes is

$$\{\dot{\epsilon}_I^{pp}\} = \frac{\frac{1}{\Delta t} f(\sigma_t)}{(G \text{ on } f_1, E_r \text{ on } f_2)} \left\{ \begin{array}{l} (0 \text{ on } f_1) \\ (1 \text{ on } f_2) \\ 0 \\ (\text{sign}(\tau) \text{ on } f_2) \\ (0 \text{ on } f_2) \end{array} \right\} \quad 7.35$$

The interface element stiffness equation can be expressed in a form similar to that for the fuel and cladding and is given by

$$[K_I] \left\{ \begin{array}{l} \dot{U}_1^I \\ \dot{U}_2^I \\ \dot{W}_1^I \\ \dot{W}_2^I \end{array} \right\} = \left\{ \begin{array}{l} \dot{Q}_1^I \\ \dot{Q}_2^I \\ \dot{Q}_3^I \\ \dot{Q}_4^I \end{array} \right\} \quad 7.36$$

with

$$[K_I] = V_I [B_I]^T [E_I] ([I] - [P_I] [B_I])$$

and

$$\{\dot{Q}_I\} = - [E_I] \{\epsilon_I^{pp}\}$$

This treatment of the interface provides the slip simultaneously with the solution for the fuel and cladding response so that it is not necessary to use an iterative process to obtain the slip.

### 7.3 STIFFNESS EQUATION ASSEMBLAGE AND SOLUTION

The element stiffness equations given by Equations 7.18 and 7.36 must be solved simultaneously to get the node point displacement rates over the entire pin. The inclusion of slip at the fuel cladding interface couples the elements axially as well as radially. If all the element stiffness equations were assembled into a single stiffness equation the solution would require inversion (or iterative solution) of a sparse  $n \times n$  matrix where  $n$  is the number of radial rings times the number of axial segments. The problem is somewhat simplified and storage requirements reduced by using a matrix condensation scheme. In this scheme the element stiffness equations for one axial level are assembled in a level stiffness equation and this equation is condensed to a  $4 \times 4$  matrix equation that involves only axial displacement rates of the fuel and cladding. The condensed level stiffness equations are then assembled into a pin stiffness equation and the axial displacement rates obtained. The radial displacement rates can then be solved for using the level stiffness equations.

The assumption that the fuel and cladding are in a state of generalized plane strain requires that for all fuel elements

$$\dot{v}_1^n = \dot{v}_1^F$$

7.37

$$\dot{v}_2^n = \dot{v}_2^F$$





this solution the displacement rates at the bottom end of the pin are taken as zero, fulfilling the fixed end boundary condition. Having obtained the axial displacement rates, the radial displacement rate can be found by back substitution in the previously stored reduced level stiffness equations.

#### 7.4 STRESS AND STRAIN RATES

Once the displacement rates have been calculated the strain and stress rates can be obtained. The strain rates are calculated from Equation 7.7 for the fuel and cladding elements and from the rate expression corresponding to Equation 7.19 for the interface elements. For all elastic-plastic elements the plastic strain rate is obtained using Equation 2.16. Finally, using the previously stored initial strain rates, the stress rate for each element is calculated using the total stress strain relation (Equation 2.18).

Once the strain rates have been obtained, all plastic elements must be checked for unloading (i.e., return to an elastic state). Unloading occurs when  $d\lambda$  as calculated from Equation 2.14 is negative. If this criteria alone is used the nonlinearities in the equations and the explicit solution scheme lead to frequent switching between elastic and plastic states for some of the elements. Some further checks for unloading are made to ensure that the element should truly be in an elastic state. According to Drucker (1950, 1952), for a material in a plastic state the plastic work done on the material through the application of some load increment should be positive. Negative plastic work is used as a second criteria for unloading. In calculating the plastic work only the plastic strain increments due to the stress increments are used and the plastic strains due to changes in material properties are ignored. The plastic work done during a time interval  $\Delta t$  is then given by

$$dW_p = \Delta t^2 \{\dot{\sigma}\}^T (\{\dot{\epsilon}^p\} - \{\dot{\epsilon}^{pp}\}) \quad 7.42$$

If  $dW_p$  is negative for a particular element then a final check for unloading is made. In this final check the element plastic strains are converted to elastic strains and the resulting stress increment calculated. If these stress increments, when added to the total stress, cause the yield function to decrease (compared to its value when the plastic strains do not contribute to the stress increment) then the element is assumed to unload. The elastic/plastic flag for the element is switched and the deformation rates are recalculated for the entire pin. If more than one element appears to be unloading during a time increment then the element with the largest value of negative work is switched to elastic first and the displacement rates recalculated.

### 7.5 ELASTIC-PLASTIC TRANSITION

At each time step it is necessary to determine if the stress state of any of the elastic elements moves outside of the elastic region during a finite time increment. It is assumed that the stresses increase linearly with time during the time step so that the element stress at the end of the time increment is given by

$$\{\sigma\}_{t+\Delta t} = \{\sigma\}_t + \{\dot{\sigma}\}\Delta t \quad 7.43$$

It is also assumed that the strength parameters change linearly with time so that

$$x_{t+\Delta t} = x_t + \dot{x}\Delta t \quad 7.44$$

where  $\chi$  may represent temperature or neck ratio. Having calculated the stress rate, the yield functions are evaluated at  $\{\sigma\}_{t+\Delta t}$  and  $\chi_{t+\Delta t}$  for all elastic elements. For every elastic element in which the yield function is positive, the time to yielding is calculated from

$$f(\{\sigma\}_{t+h\Delta t}, \chi_{t+h\Delta t}) = 0 \quad 7.45$$

where

$$\{\sigma\}_{t+h\Delta t} = \{\sigma\}_t + \{\dot{\sigma}\}h\Delta t$$

$$\chi_{t+h\Delta t} = \chi_t + \dot{\chi}h\Delta t$$

Either a direct or an iterative solution is used, depending on the form of  $f$ , to obtain a value for  $h$  for each element that yields during the time step. The yield function can take on some unusual forms due to its dependence on  $\chi$  and care must be taken to ensure that the first root (i.e., the minimum  $h$  value) is found.

For the fuel and interface elements the treatment is somewhat different since there are two yield functions. If the element is elastic both  $f_1$  and  $f_2$  are evaluated at  $\{\sigma\}_{t+\Delta t}$ . If only one of the two yield functions is positive then  $h$  is solved for as described above. If both  $f_1$  and  $f_2$  are positive then corresponding  $h_1$  and  $h_2$  are found. The appropriate yield surface is determined by the smaller of  $h_1$  and  $h_2$ .

For an interface or fuel element already in a plastic state it is necessary to determine whether or not the stress state moves to the other yield surface during the time step. If, for instance, the element is plastic and on  $f_1$ , then  $f_2$  is evaluated at  $\{\sigma\}_{t+\Delta t}$ . If  $f_2$

returns a positive value then the stress state moves to  $f_2$  during the time step and the time to transition is found by solving

$$f_2(\{\sigma\}_{t+h\Delta t}) = 0.$$

From all elements in elastic-plastic transition, the one with the smallest  $h$  value is found. The time step is then limited by

$$\Delta t' = h\Delta t \quad 7.46$$

and the elastic-plastic flag for the transition element is switched so that at the beginning of the next time step the element will be considered in an elastic-plastic state. This process effectively allows the purely elastic stress increment to the point where the stress state falls on the yield surface with subsequent stress increments calculated so that the stress state remains on the yield surface.

## 7.6 ADDITIONAL TIME STEP LIMITS

Since the initial strain rate components are calculated explicitly and some of them depend on the stress state, it is necessary to limit the time step so that the change in stress is not too great. The time step is limited so that the maximum change in any stress component in any element is less than  $\sigma_{\max}$ . The time step is also limited by maximum permissible increments in the swelling, creep, neck growth, shrinkage and plastic strains. The limited time step is given by

$$\Delta t'' < \min \left[ \frac{\sigma_{\max}}{\dot{\sigma}_{\max}}, \frac{\epsilon_{\max}^{sw}}{\dot{\epsilon}_{\max}^{sw}}, \frac{\epsilon_{\max}^c}{\dot{\epsilon}_{\max}^c}, \frac{\bar{x}_{\max}}{\dot{x}_{\max}}, \frac{\epsilon_{\max}^{sh}}{\dot{\epsilon}_{\max}^{sh}}, \frac{\epsilon_{\max}^p}{\dot{\epsilon}_{\max}^p} \right] \quad 7.47$$

where the denominators are the maximum rate of change over all elements and the numerators are the maximum permissible changes. No attempt has been made to analytically determine appropriate values for the maximum permissible changes and, due to the complex interaction of the equations, it is not probable that this will ever be accomplished. With

$$\sigma_{\max} = 10 \text{ MPa}, \quad \epsilon_{\max}^{\text{sw}} = \epsilon_{\max}^{\text{sh}} = \epsilon_{\max}^{\text{c}} = \epsilon_{\max}^{\text{p}} = 5.E-4 \quad \text{and} \quad \bar{x}_{\max} = .05,$$

the code has reasonable execution times and does not exhibit any numerical instabilities. More refined time step limits may be possible but not without much experience in running the code for a variety of problems. The time step limit given by Equation 7.47 is actually applied before that given by Equation 7.46 to eliminate unnecessary searches for elastic-plastic transition times.

## 7.7 TIME INTEGRATION

The final major step required to complete the solution for a single time increment is to calculate the time integrated values of all the fundamental variables. The integrated value for each required variable is obtained according to

$$y_{t+\Delta t} = y_t + \dot{y} \Delta t_{\text{lim}} \quad 7.48$$

where  $y$  represents some variable and  $\Delta t_{\text{lim}}$  is the time step limited by input, elastic-plastic transition, or the stress or strain increment. The integrated variables include the axial and radial displacements, stresses, elastic strains, temperature, large and small

sphere neck ratio and shrinkage, thermal strain, swelling, and fast fluence. In addition, the porosity is adjusted to account for the shrinkage of the large sphere array, plastic flow on the hydrostatic stress yield surface and swelling due to gaseous fission products.

The porosity is defined by

$$P = 1 - V_S/V_T \quad 7.49$$

where  $V_S$  and  $V_T$  are the solid and total volume, respectively, so that assuming the solid volume remains constant the porosity change rate is

$$\dot{P} = \frac{V_S}{V_T^2} \dot{V}_T = (1-P) \frac{\dot{V}_T}{V_T} \quad 7.50$$

Substituting in the appropriate volumetric strain results in

$$\dot{P} = (1-P) \left( \dot{\epsilon}_{V,S}^{sh} + \dot{\epsilon}_{V,S}^p + \dot{\epsilon}_{V,S}^{sw} - \dot{\epsilon}_{V,S}^{sw} \right) \quad 7.51$$

where  $\dot{\epsilon}_{V,S}^{sw}$  is the swelling rate due to the solid fission products. The new porosity is then obtained from Equation 7.48. At this point the solution for the time increment has been completed and the calculations continue at the next time increment with new values for the driving functions (heat density, cladding temperature) obtained from code input.

## 7.8 CODE LAYOUT

A brief description of the SPECKLE-III code layout is given here with more attention given to the mechanical model than to the thermal model. A flow diagram is given in Figure 7.5.

A typical run begins with processing the user input and initializing all the variables. A time step is chosen based on input and the volumetric heat source is calculated. Since the conductivity is temperature dependent, an iterative loop is used to calculate the conductivity, temperature distribution and temperature rate change. The free gas pressure and temperature are also calculated within the iterative loop. Neck growth and shrinkage rates are then calculated for both the large and small sphere arrays and the pore migration and accompanying porosity change obtained in the restructured regions of the fuel. The time step may be limited at this point if the neck growth rate is large.

Using the neck ratio and hydrostatic stress from the end of the previous time step, the elastic properties for the fuel and cladding are calculated including the effective values for the fuel Young's modulus and Poisson's ratio,  $\sigma^*$ , and the small sphere to binary array hydrostatic stress ratio. Thermal creep, swelling, and elastic nonlinear strain rates are obtained and combined into the initial strain rate for each finite element.

For each element the stiffness equation is formed and these are combined into the level stiffness equations that are reduced and combined to give the pin stiffness equation. This equation is solved for the displacement rates from which the strain and then the stress rates are obtained. If any plastic elements are found to be unloading, the element is switched to elastic and the displacement rate solution is repeated. The time step may be limited at this point depending on the maximum stress or strain rate. All elastic elements are checked for elastic-plastic transition and the time step limited

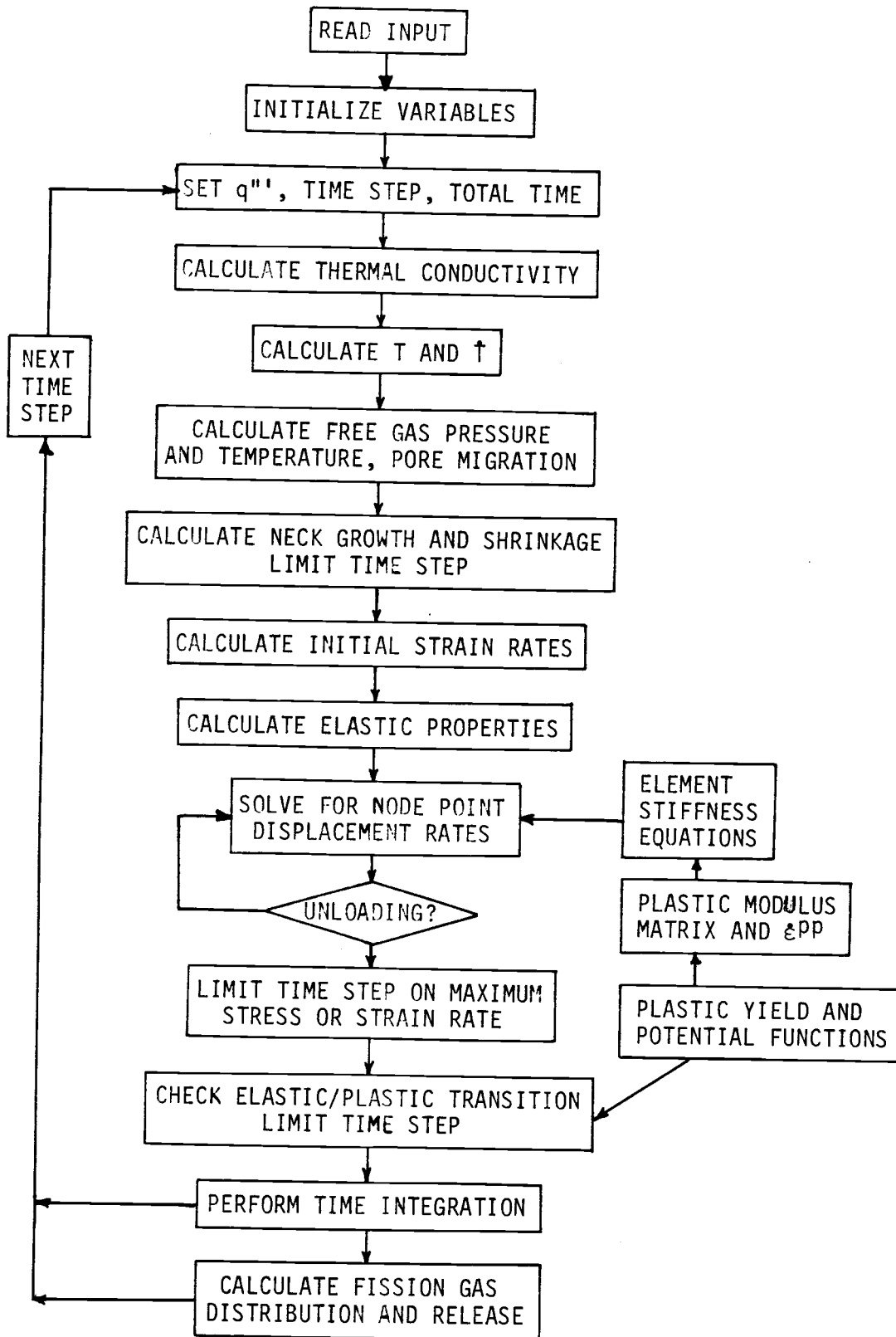


FIGURE 7.5. SPECKLE-III Flow Diagram

accordingly. The time integration is then carried out for required variables and the fuel swelling rate due to fission products is updated.

The fission gas diffusion process occurs slowly in time and therefore operates on a different time increment than the rest of the code. Typically a time step of 50 hours is adequate for the fission gas model. The fission gas model calculates the fission gas distribution and gas release.

### 7.9 CODE VERIFICATION

The code contains so many interrelated models that it is difficult to verify the code as a whole. Parts of the mechanical model have been checked out against analytic or other established codes. In Appendix A the results of the code are compared with an analytic solution for two concentric thermal elastic cylinders with slip, giving excellent agreement. The plasticity model was checked against a finite-difference solution for an internally pressurized cylinder using the von Mises yield criteria. A further check was made against a finite-element solution for an externally pressurized hollow cylinder using the Drucker-Prager yield criteria. In all cases agreement was excellent.

The complete thermal mechanical model has been used to model several experiments using sphere pac fuel. The results of one of these simulations are discussed in the next chapter.

## 8.0 CODE APPLICATION

The SPECKLE-III Code (George and Peddicord 1982) has been applied to a variety of test problems to simulate the in-reactor behavior of sphere pac fuel pins. The results from one of these test problems is presented in this chapter to demonstrate the computational capability of the code and to show qualitatively the behavior of the fuel and cladding during irradiation. The test problem models one pin out of a series of tests in the DIDO reactor at Harwell, U.K. (Bart 1982). The particular pin modeled was one of four pins in the third of the test series and is identified as DID03, pin 12 (D3P12). A pin from this irradiation test was chosen because all of the required modeling information was readily available and the post irradiation information examination (PIE) included measurements of the diametral strain. Pin 12 was modeled because the axial power profile was relatively flat so that the pin could be adequately modeled using only one axial section.

The DID03 pins each had a fuel stack length of 7.486 cm and a total pin length of 10.0 cm. Each was encapsulated in a sodium filled container with electrical heaters to control the sodium temperature. D3P12 was irradiated for 230 days at  $\sim 760$  W/cm and reached a burnup of  $\sim 5.0\%$  FIMA. The physical characteristics for D3P12 are listed in Table 8.1.

The initial ramp to full power was accomplished over a period of 2.25 hours but the electrical heater rods were not switched on until after  $\sim 24$  hours. The rise to full power was assumed to be linear with time and the outer cladding temperature at 2.25 hours was assumed to be 10% lower than that at 24 hours. The reactor was shut down and returned to full power a number of times during the course of the experiments but these power changes were not modeled. The total full power time was assumed to be uninterrupted in the SPECKLE-III model. The operating history, based on data given by Diess and Reindl (1982), is listed in Table 8.2. The end of irradiation (EOI) occurred after 5520 hours of full power operation.

TABLE 8.1. DID03, Pin 12 Physical Characteristics

Cladding

Material - AISI M 316/18% CW

ID/OD - .700/.802 cm

Fueled length - 7.486 cm

Plenum Volume - .531 cm<sup>3</sup>

Fuel (U<sub>.85</sub>-Pu<sub>.15</sub>) C

Large Fraction

sphere diameter 724±5 μm

packing factor .6330

sphere density .9467 TD

Small Fraction

sphere diameter 40-80 μm

packing factor .5670

sphere density .9280

Smear Density .7920 TD

Fill Gas

Temperature 25. C

Pressure .122 MPa (1.2 atm)

TABLE 8.2. DID03, Pin 12 Assumed Irradiation History

Irradiation Time (hours)	Linear Power (W/cm)	Cladding Outer Temperature (C)	Plenum Temperature (C)
0	0	25.	25.
2.25	760.	533.	412.
24.0	760.	590.	455.
5520.0	760.	590.	455.

The measured fast flux was  $6.83 \times 10^{12}$  n/sec-cm<sup>2</sup>. The fast flux-to-linear power ratio was calculated at  $8.99 \times 10^9$  n/cm-W-sec and assumed constant over the irradiation history. The friction factor for sphere pac fuel on stainless steel is unknown. A value of .5 was used based on results for UO<sub>2</sub> and Al<sub>2</sub>O<sub>3</sub> on zircaloy (Nakatsuka 1981).

The pin was modeled using one axial section for the fueled region with six rings in the fuel and two rings in the cladding. The requested time step over the first 2.25 hours was .2 hours. It was then increased to 2.0 hours until 24 hours of irradiation time was reached. From 24 to 50 hours the requested time step was 5 hours, increasing to 20 and then 50 hours at 50 and 200 hours irradiation time, respectively. The time step for the fission gas model was set to 50 hours. The requested time steps were limited by the code as described in Chapter 7.

The creep and swelling correlations for the stainless steel cladding were taken from NSMH (1976). Initial application of the SPECKLE-III code with these correlations included resulted in the prediction of very large cladding creep strains. Inspections of the creep equation revealed that a term of the form

$$\bar{\epsilon}_c \sim t^3 \sinh \frac{\bar{\sigma} A}{(1 + \sqrt{\phi t})}$$

was responsible for the large creep predictions. In the above term  $\bar{\epsilon}_c$  is the effective creep strain,  $t$  is the irradiation time,  $\bar{\sigma}$  is the effective stress,  $A$  is a constant and  $\phi t$  is the fast fluence. The first factor ( $t^3$ ) introduces time softening while the second factor gives time hardening to the creep strain. The DIDO reactor is a thermal reactor so that the fast fluence is very small. However the creep correlation was based on data from pins irradiated in fast reactors. The second factor has a nonzero value even for zero fluence so that overall the term represents considerable time softening if the fast fluence is small. The softening was so unreasonably large for the D3P12 pin that the above term was neglected entirely.

Some results from the SPECKLE-III simulation of the D3P12 experiment are presented in Figures 8.1 through 8.8. Figure 8.1 shows the predicted centerline temperature as a function of irradiation time. A peak temperature of 1604°C was reached at 24 hours when the outer cladding temperature first reached its maximum value. The temperature gradually decreased throughout the remainder of the irradiation due to the increasing fuel conductivity brought about by the restructuring process. The predicted EOI centerline temperature is 1250°C. These values can be compared to the 1820°C peak and 1505°C EOI temperatures predicted by SPECKLE-II without the mechanical model. The main reason for the difference between the two codes is that the restructuring (hence, conductivity) can be more accurately predicted with the mechanical model included.

Figure 8.2 shows the predicted fuel centerline and outermost ring hydrostatic stress. During the initial start-up the centerline compression increases very rapidly reaching a peak value of ~30 MPa at 1.7 hours. This rise in stress is due mainly to the differential thermal expansion between the fuel and cladding. After 1.7 hours, the fuel centerline temperature reaches a temperature (1350°C) that is high enough to allow rapid restructuring due to viscous and plastic flow resulting in a sharp drop in compression to almost zero stress. The restructuring makes the fuel stiffer, both elastically

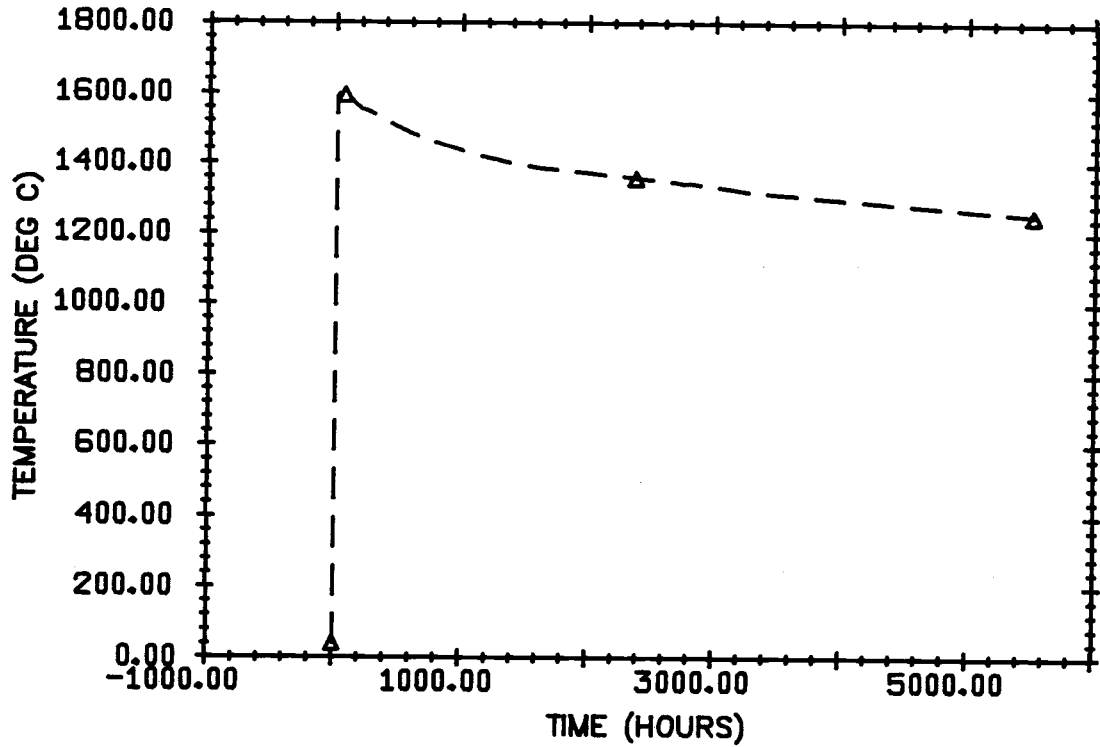


FIGURE 8.1. D3P12 Centerline Temperature History

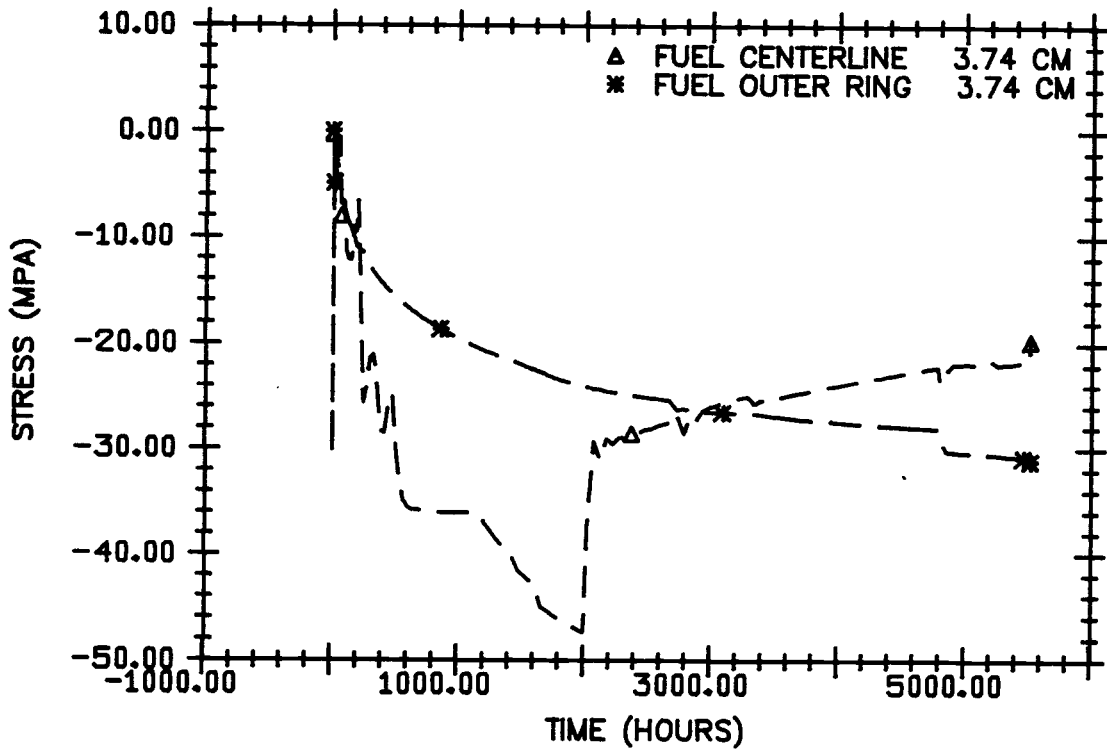


FIGURE 8.2. D3P12 Inner and Outer Fuel Hydrostatic Stress History

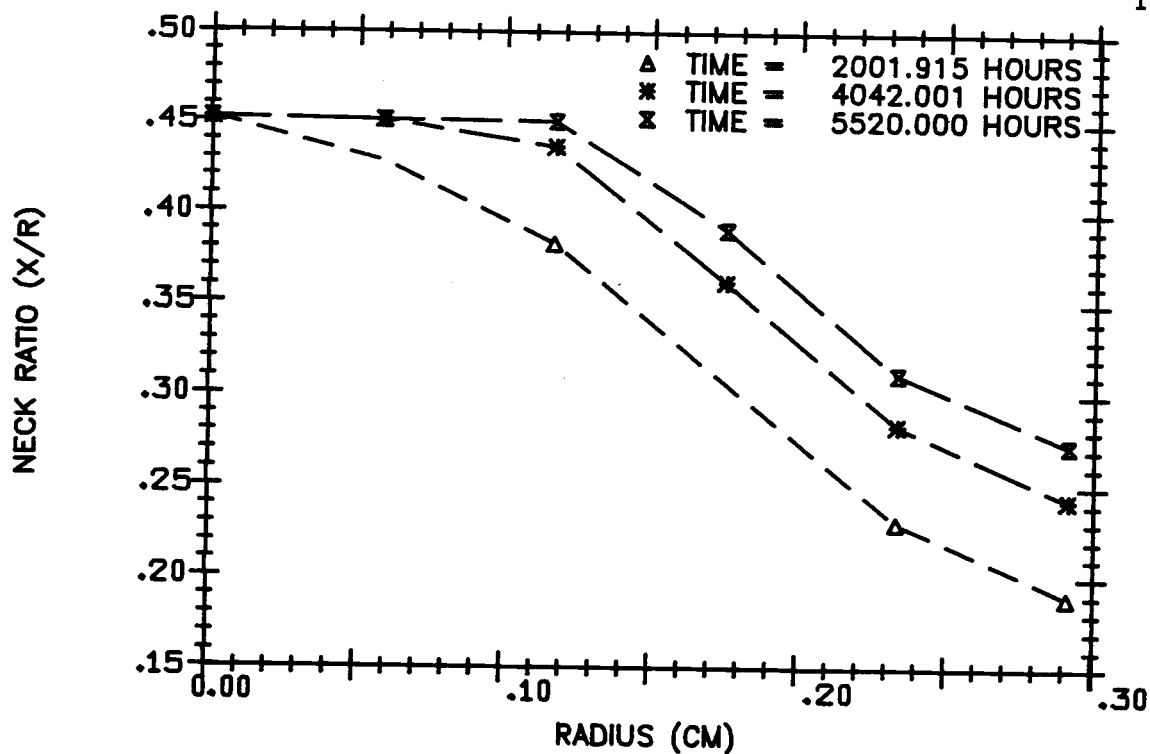


FIGURE 8.3. D3P12 Radial Profiles of Small Sphere Neck Ratio

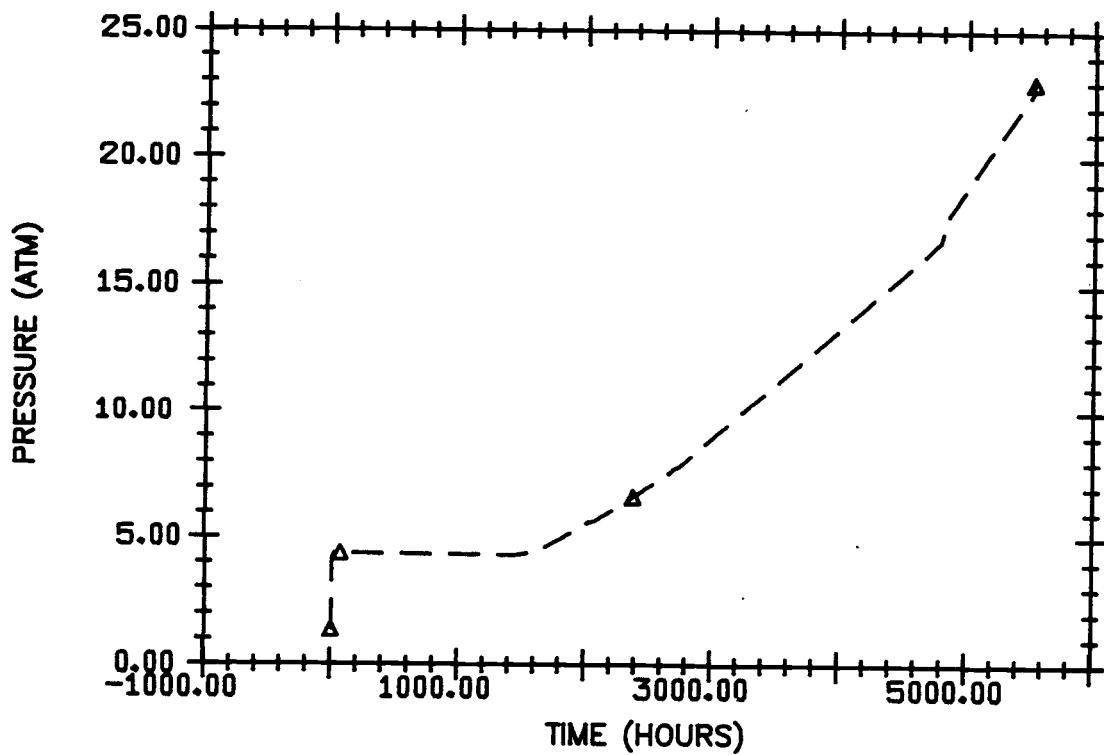


FIGURE 8.4. D3P12 Gas Pressure History

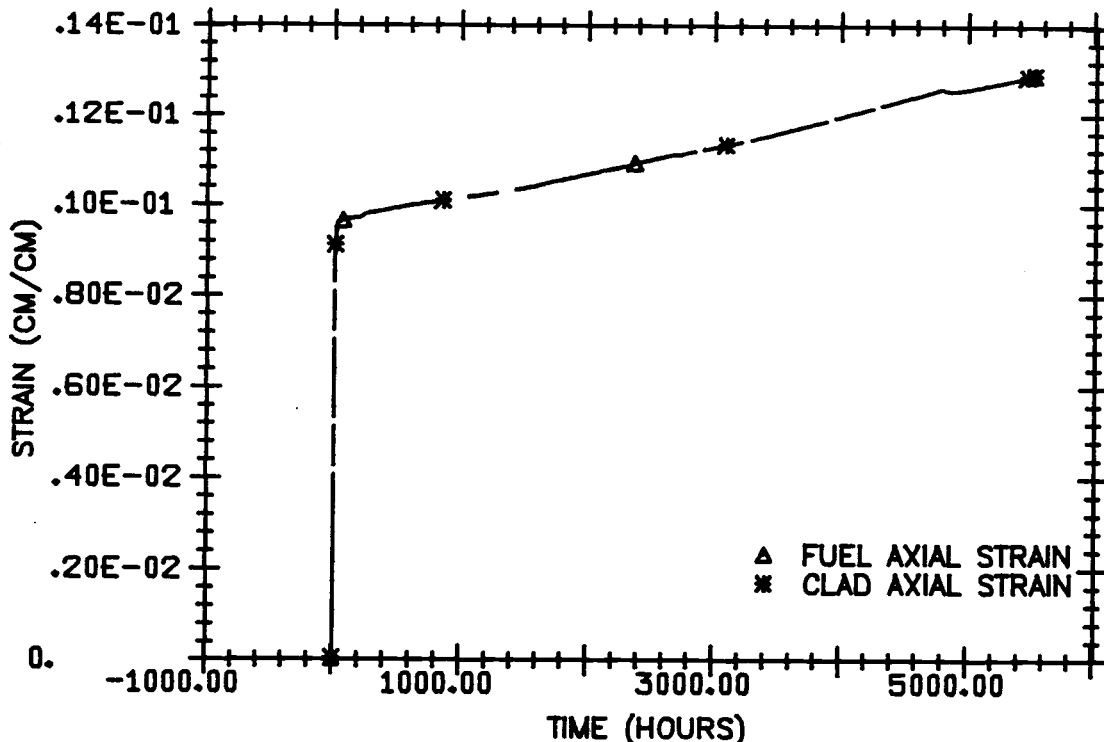


FIGURE 8.5. D3P12 Axial Strain History

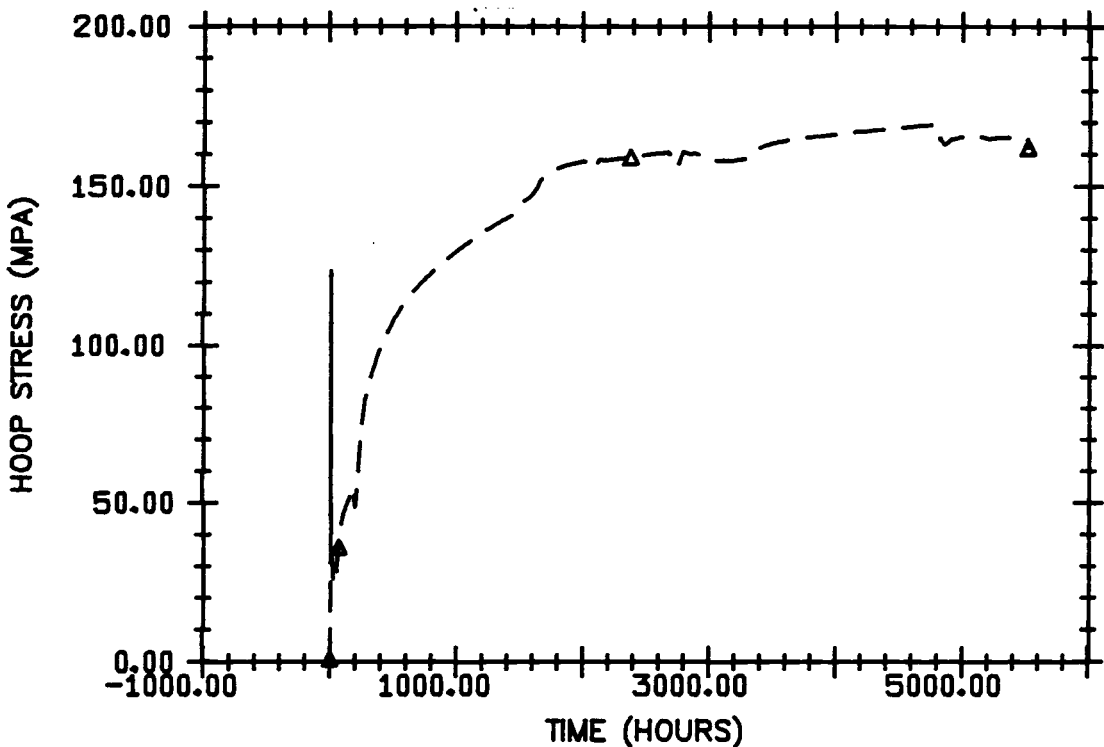


FIGURE 8.6. D3P12 Hoop Stress History

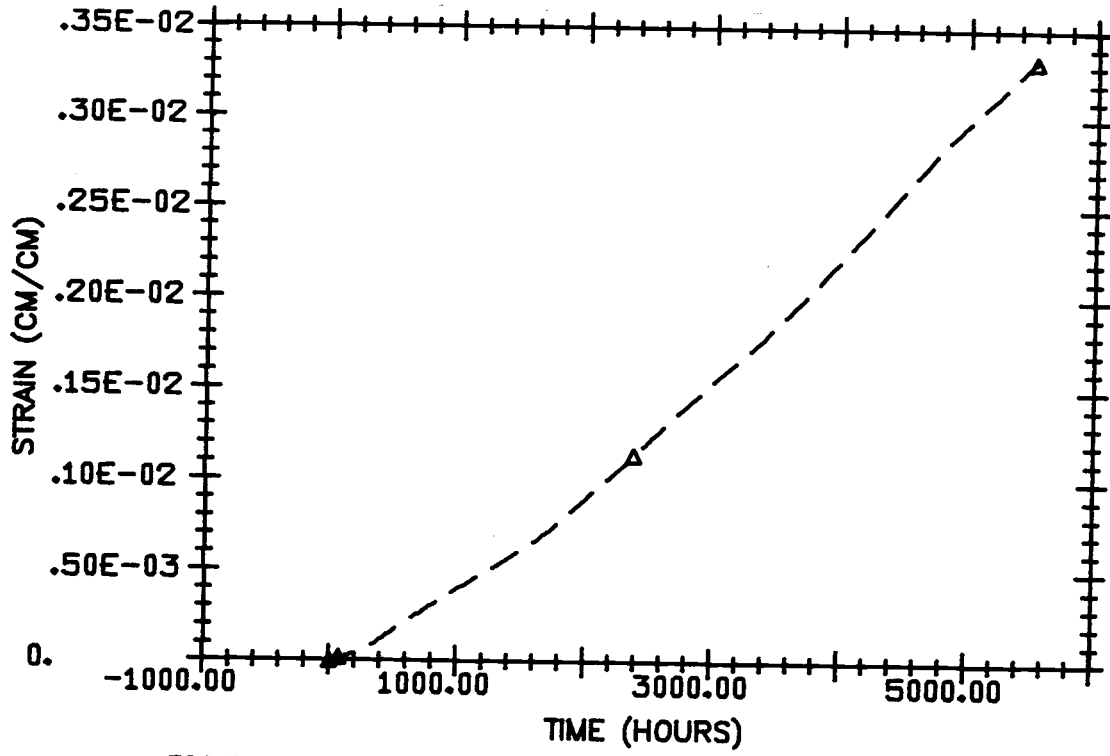


FIGURE 8.7. D3P12 Cladding Tangential Strain History

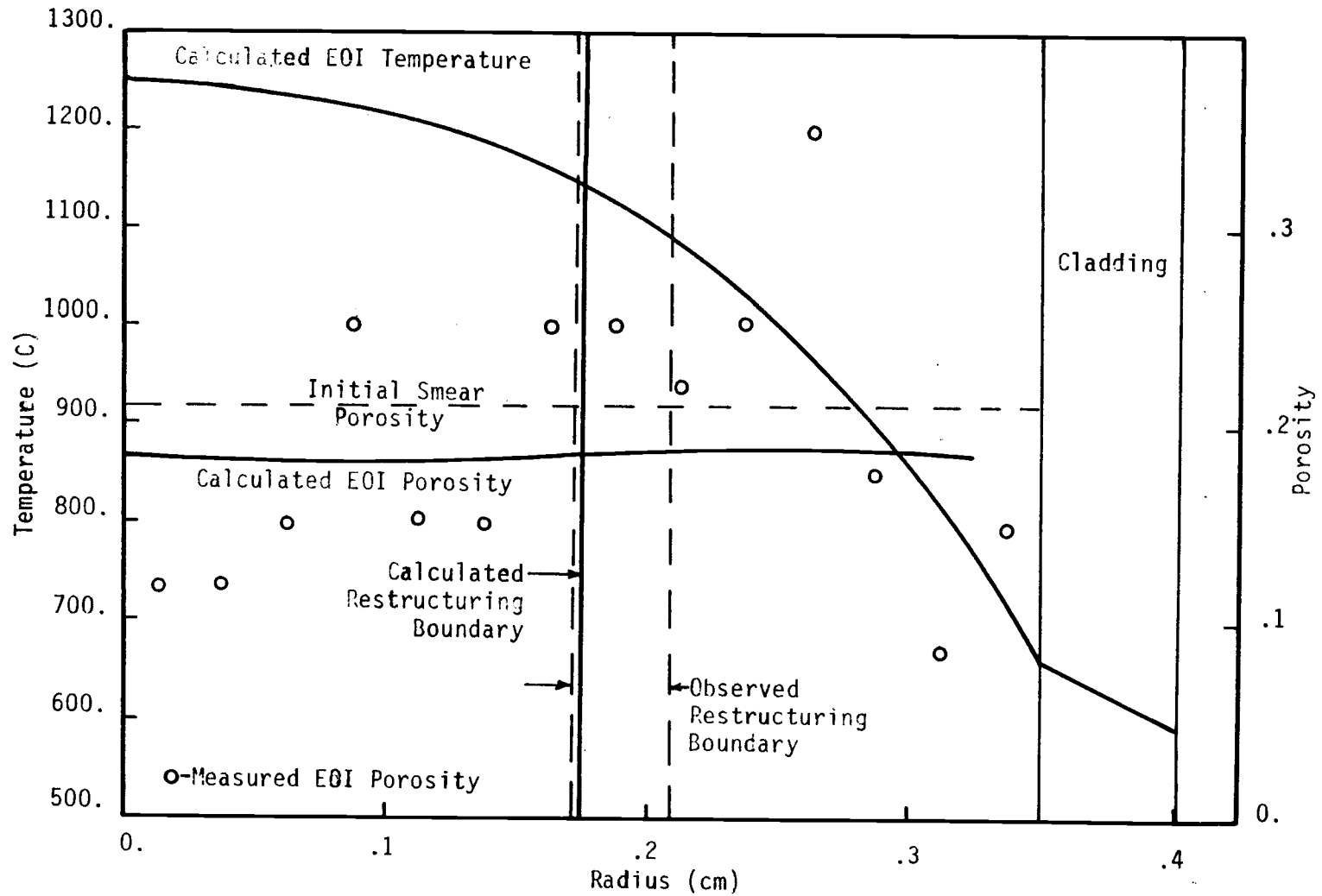


FIGURE 8.8. D3P12 EOI Radial Temperature and Porosity Profiles

and plastically, so that as the swelling starts the fuel compression increases. Three more reversals in the center ring loading can be observed in Figure 8.2. These have been identified as resulting from the explicit treatment of the plastic yielding of the small sphere array under hydrostatic compression. When the small sphere array yield criteria is exceeded the small sphere array is allowed to shrink. This results in a decrease in the small sphere array compressing and therefore increase in the effective compression on the large sphere array. This increased compression is relieved by plastic densification of the binary array resulting in a smaller binary array hydrostatic compression.

The centerline compression reaches a maximum value of ~48 MPa as ~2000 hours. At ~2000 hours the center ring element satisfies the criteria for restructured fuel and is allowed to densify by hot pressing. The rapid change in stress is not unreasonable since the fuel restructuring rate increases near the end of the neck growth phase. Small, rapid changes in the hydrostatic stress can also be noted at ~2700 hours and 4800 hours. These correspond to the transition to fully restructured fuel in the second and third rings.

The hydrostatic stress in the outer ring is relatively unaffected by the dramatic changes in the interior of the fuel, although the restructuring transition of the second and third elements is still evident. These stress histories can be compared to an assumed value of 50 MPa compression used in SPECKLE-II for all fuel regions.

The restructuring history can be observed in Figure 8.3 that shows the radial profile of the small sphere neck ratio at three times during the irradiation. By the end of the irradiation time, SPECKLE-III predicted that the inner three rings were fully restructured ( $\bar{x}_S > .45$ ). This compares very well with the post irradiation examination PIE that determined the radius of the fully restructured region as ~.21 cm (SPECKLE-III predicted .18 cm).

Figure 8.4 shows the predicted gas pressure as a function of the irradiation time. The initial pressure jump is due to the gas temperature change during start up. The gas pressure remains nearly constant until ~1600 hours when fission gas release from the fuel begins. The predicted EOI gas pressure (hot) is 23.0 atm (2.33 MPa) which is small compared to the outer ring fuel radial compression of 23.6 MPa implying that the fuel is responsible for most of the load placed on the cladding. The change in slope of the gas pressure curve at 4800 hours results from the removal of some of the free gas volume as the fuel becomes fully restructured.

The fuel and cladding axial strains versus irradiation time are shown in Figure 8.5. The fuel and cladding axial strains are identical throughout the irradiation indicating no-slip between the fuel and cladding. The thermal and elastic strains make up the first .96% strain at the initial ramp to full power. At the EOI the total strain is 1.29% giving .33% total permanent axial strain. The reported PIE results do not include axial strain measurements.

The cladding hoop stress history is shown in Figure 8.6. The hoop stress is defined here as

$$\sigma_{\text{hoop}} = - \sigma_{r_I} r_f / (r_c - r_f) \quad 8.1$$

where  $\sigma_{r_I}$  is the interface element radial stress and  $r_f$  and  $r_c$  are the cladding inner and outer radius. Some of the perturbations observed in the hydrostatic stress are reflected in the hoop stress although their magnitudes are greatly reduced. A spike in the hoop stress occurs during the initial rise to power before the fuel temperature is large enough to cause major restructuring. The maximum attained hoop stress is ~170 MPa, a factor of 2.5 less than the cladding yield stress.

The permanent tangential strain history in the outermost ring element is plotted in Figure 8.7. It is defined by

$$\epsilon_{\theta}^p = \epsilon_{\theta} - \epsilon_{\theta}^e - \epsilon_{\theta}^t \quad 8.2$$

where  $\epsilon_{\theta}$ ,  $\epsilon_{\theta}^e$ ,  $\epsilon_{\theta}^t$  are the total, elastic and thermal tangential strains. The permanent diametral strain (permanent radial displacement of cladding outer radius divided by cladding outer radius) is also estimated by the code using linear extrapolation from the strain results of the two outermost cladding ring elements. Permanent diametral strain is slightly larger than the strain plotted in Figure 8.7 with an EOI value of .344% or .07%/FIMA. From PIE results the peak (over the length of the pin) diametral strain of D3P12 was .1%/FIMA. The neglect of the time softening creep strain term, the large uncertainty in the creep strain correlation (the standard deviation equals .3 times the predicted creep strain), and the use of only one axial segment to model the pin could all contribute to the underprediction of the diametral strain.

Figure 8.8 shows the EOI predicted radial temperature and porosity profile and the restructured fuel boundary. PIE results for the fuel porosity and the observed restructured fuel boundary are also plotted. As previously noted the predicted restructuring boundary is in good agreement with PIE results. The radial temperature and porosity profiles agree very well with the definitions of the restructuring zones described in Section 1.2. For a central porous region (Zone I) to develop temperatures greater than 1300°C are required and clearly this zone did not develop. The temperatures in the region (Zones II and III) are in the range of 1100 to 1300°C with the restructuring boundary located where the temperature is 1100 to 1150°C. The predicted radial temperature profile is consistent with the zone definitions.

The large variations in the measured porosity near the cladding results from the way the large spheres pack against the cladding. Generally, a rather uniform layer of large spheres is packed against the cladding. The minimum porosity measurement is at a distance from the cladding of about one large sphere radius while the peak measurement is at just over one sphere diameter. The model assumes a random distribution of spheres so these variations of porosity are not predicted. The wall effect tends to propagate in towards the pin center (Benenati and Brosilow 1962) and could be responsible for some of the porosity variation in the pin interior. The PIE results indicate more densification at the pin center than predicted by SPECKLE-III. In the current model the densification achieved by the hot pressing mechanism is nearly balanced by the porosity produced by fission gas retention. To achieve better agreement with the data either one or both of these models must be improved.

Based on the D3P12 simulation and other test problems run the SPECKLE-III code appears to give reasonable results for mixed carbide sphere pac fuel pins. However many more experiment simulations and comparisons are required before the accuracy of the code can be assessed.

## 9.0 CONCLUSIONS AND RECOMMENDATIONS

A model has been developed to predict the mechanical behavior of mixed carbide sphere pack fuel pins. The model was coupled with a thermal model that provides the fuel temperature, fission gas behavior and fuel restructuring. The mechanical model includes components to predict the elastic and plastic constitutive relations for restructuring fuel. Thermal, creep, swelling, elastic and plastic strains of the fuel and cladding and slip at the fuel/cladding interface are each considered separately in the model to predict the fuel and cladding stresses. The fuel hydrostatic stress is an important parameter in many of the thermal models so that the thermal and mechanical behavior are tightly coupled. The thermal and mechanical model equations are solved numerically in the SPECKLE-III code.

The elastic properties of a restructuring sphere bed depend on the elastic properties of the sphere material and the bed geometry. The elastic properties of the sphere material are known but an analytic model was required to obtain the properties as a function of bed geometry. The factors that influence the bed geometry are the initial packing factors of the two sphere sizes and the neck growth and center-to-center approach between adjacent spheres as part of the restructuring process.

Elastic properties were first obtained for a random array of uniform spheres adjoined by a neck region. For this purpose a unit cell was devised whose exact configuration depends on the packing factor of the sphere bed. An incremental elastic stress-strain relation was obtained for the unit cell. The relationship was necessarily incremental because the elastic stiffness depends on the load normal to the contact plane between two spheres and therefore on the stress state. The Hertz contact theory (Timoshenko and Goodier 1951) and strain energy principles were used to obtain the stress-strain relation. The unit cell is elastically anisotropic but the

macroscopic behavior of a random sphere array can be considered isotropic. The elastic properties of an isotropic aggregate of spheres were obtained by considering the aggregate to be made up of unit cells with a uniform distribution of orientations. The stress-strain relation could then be derived from the volume-average strain energy of the aggregate through the application of strain energy principles.

An approach similar to Brandt's (1955) was used to obtain the bulk modulus of a binary mixture of large and small spheres. Brandt's model was extended to account for the possibility of shrinkage of the sphere arrays and the presence of necks between spheres. A second elastic constant for the binary mixture was obtained using results from the theory of composite materials. The model is formulated so that the hydrostatic stress in the binary array and the small sphere array are calculated separately.

Results from the elastic properties model were compared to available experimental data and theories for the speed of sound, bulk modulus and shear modulus of cohesionless (no neck) sphere arrays and to theories and data for elastic modulus of porous materials (large neck). Good agreement was shown between the model and data.

A two surface yield model was developed to describe the plastic behavior of restructuring sphere pac fuel. The first surface incorporates the frictional behavior of granular material and is an extension of the Drucker-Prager yield law (1952). The Drucker-Prager yield law depends on the experimentally determined internal friction angle and cohesion of the granular aggregate. The sphere pac fuel begins irradiation as a cohesionless bed but as neck growth proceeds the cohesion increases and the frictional effects diminish. Analytic expressions were derived for the cohesion and effective friction angle of a random array of uniform spheres. These expressions are functions of the packing factor, neck ratio, sphere material yield strength, and an experimentally determined friction angle of unrestructured fuel.

The results of some triaxial compression tests on single size and binary sphere arrays were used in the derivation of the two yield strength parameters for a restructuring binary array. As the neck growth increases the yield law approaches the von Mises yield criteria for frictionless material. A nonassociated flow law was used to remove the excessive dilation encountered with the Drucker-Prager yield law and associated flow.

The second yield surface was required to allow plastic deformation under hydrostatic compression. Hydrostatic compression results in high localized stresses near the sphere contact points. Results from punch analysis (Tabor 1951) were used to obtain one yield parameter. The second yield surface was assumed to form a spherical cap to the open end of the conical yield surface obtained previously. The second parameter required to define the radius of curvature was chosen so that the cap and the cone intersect when the hydrostatic stress is zero. The yielding under hydrostatic compression is treated separately in the large and small sphere arrays. An associated flow law is assumed for yielding on the second yield surface.

There is virtually no experimental data for the plastic properties of sphere pac fuel either with or without restructuring. Further, there is only very limited data for the yield strength of mixed carbide. This data covers only a very small temperature range and a single value of fuel porosity. Therefore, the validity of the proposed plastic constitutive model cannot be assessed at this time. The model incorporates features that should, at least qualitatively, describe the plastic behavior of sphere pac fuel. It considers the frictional yield of unrestructured fuel and continuously tends toward von Mises yielding for fully restructured fuel. The actual shape of the second yield surface (hydrostatic compression yielding) is unknown and the proposed surface can only be considered a reasonable guess. Yielding on this surface is the most important restructuring and densification mechanism during the initial startup period. The one indication that the model is correctly formulated is the good comparison with EOI results from sphere pac fuel experiments.

The proposed plasticity model offers a starting point for further development as more experimental data from separate effects tests becomes available and as more comparisons are made between the SPECKLE-III code and irradiation experiments.

The elastoplastic equations were rederived for the case of restructuring sphere pac fuel. These equations take into account the changes in elastic and plastic properties as the geometry and temperature of the fuel changes. They also allow thermal, creep and swelling strains to be included in this analysis.

The fuel creep model includes hot pressing densification and deviatoric strains to relieve the deviatoric stresses in the fully restructured region of the fuel. In the restructuring fuel only a densification creep is considered and is associated with the sintering induced shrinkage.

The swelling model is based on an empirical correlation by Zimmerman (1982) developed from experiments on mixed carbide pellets. In this correlation the swelling rate depends on the local temperature, burnup and burnup rate. Fuel stress effects are not included and the effects of fuel geometry (sphere pac versus pellet) are unknown. The correlation by Zimmerman is recognized as a significant contribution to fuel pin modeling efforts since it was based on separate effect tests rather than the end results of pin irradiations. More work of this nature is needed to determine the effects of stress and geometry.

The swelling strain and the creep densification were assumed to be isotropic. This is probably not the case since the densification (swelling) should be largest in the direction of maximum (minimum) compression. However, if these strains are not considered isotropic then, in the case of densification, the sintering and hot pressing must become vector rather than scalar quantities. This greatly increases the complexity of the entire thermal-mechanical model since almost every component depends on the restructuring. The current isotropic strain assumption appears to give reasonable results and

isotropic strain assumption appears to give reasonable results and should be retained.

The elastic-plastic equations were solved using a finite element approach. An explicit scheme is used to obtain the driving force consisting of the thermal, creep and swelling strain increments. The stress increments are then solved for simultaneously with the elastic and plastic strain increments. The incremental approach allows transition from elastic to plastic regimes at the end of a time increment. This avoids the difficulties involved in trying to solve the equations across a discontinuity if there is transition within a time step. The plastic yielding of the small sphere array was treated explicitly after the binary stress distribution has been obtained. This appears to cause some unphysical perturbations in the fuel hydrostatic stress near the center of the pin. This does not represent a major difficulty since the effect on the cladding stress is minimal.

A specialized fuel cladding interface element was devised that handles the fuel-cladding slip problem within the context of the elastoplastic model. This is an improvement over any of the schemes used in pellet pin codes that require some type of iterative solution to determine the relative axial strains of the fuel and cladding. In test problems run so far fuel cladding slip has not been observed but may be an important phenomena in transient analysis.

A SPECKLE-III simulation of a sphere pac fuel pin irradiation experiment was presented to demonstrate the computational capability of the code. The code was in good agreement with the PIE results for restructuring and cladding diametral strain. No firm conclusions can be drawn at this time regarding the overall accuracy of the thermal-mechanical model. Many more experiment simulations are required to establish the code's validity. However, since the code predictions are in reasonable agreement with observed behavior, it appears that the necessary phenomena have been included and that close agreement can be obtained by improvement of individual model components.

### 9.1 RECOMMENDATIONS FOR FUTURE WORK

As in any substantial research effort, the development of a sphere pac fuel thermal-mechanical model served to point out areas where further work is needed. A few of these are listed here.

1. For the elastic properties model a more rigorous treatment of the stress-strain relation for two spheres joined by a neck is needed. An analytic solution for the normal and shear stiffness as functions of the neck ratio and plastic center-to-center approach is desirable. This could be checked against experimental results on steel spheres for relevant conditions. The experiments could be carried out by welding two hemispheres together at the contact and taking stress-strain measurements.
2. A method should be devised for obtaining samples of random sphere arrays with nearly uniform neck growth throughout the array. The amount of restructuring in these samples should be controllable. The resulting samples could be used for a variety of experiments including measurements of conductivity, stress-strain, yield strength and plastic flow. The data would be invaluable for checking analytic models.
3. For the proposed plasticity model the internal friction angles for arrays of large and small spheres of mixed carbide fuel are needed. The binary array friction angle should also be measured and checked against the value predicted by the plasticity model.
4. More data is needed for the yield or fracture stress for mixed carbide. This data should be obtained for the range of temperatures and porosities anticipated in fuel pin irradiations.
5. Primary creep has been identified as potentially significant in mixed carbide fuel. It could be responsible for some of the very early restructuring now accounted for by plastic flow. More data is needed to quantify the primary and secondary creep behavior as a function of temperature and porosity.

6. The current mechanical models assume plastic flow when the yield stress is reached. At low temperatures the fuel is more likely to fail in brittle fracture. A method for incorporating fracture into the mechanical model should be investigated.
7. The dislocation creep of mixed carbide fuel is very sensitive to small changes in the effective stress, causing some numerical difficulties in the explicit solution scheme. These were solved in SPECKLE-III by using a semi-implicit formulation of the creep strain (see George and Peddicord 1982). A better method may be to extract the first order stress dependence from the creep strain equation and form a creep modulus matrix (much like the plastic modulus matrix) so that the creep strains can be obtained simultaneously with the stress increments.
8. Models for the pin neutronics and the redistribution of the fuel chemical components need to be incorporated in the SPECKLE-III code.
9. Finally, specific model improvements required can only be identified after the SPECKLE-III code has been compared to more of the available irradiation experiment data.

## BIBLIOGRAPHY

- Ades, M. 1979. Modeling of the Thermal Behavior of Irradiated Sphere-Pac Mixed Carbide Fuel. PhD. Thesis, OSU-NE-7902.
- Ades, M. and K. L. Peddicord. 1978a. "Modeling of the Thermal and Mechanical Behavior of LMFBR Fuel Elements. Part I. Oxide Fuels." OSU-EIR-31, Oregon State University, Dept. of Nucl. Eng.
- Ades, M. and K. L. Peddicord. 1978b. "Modeling of the Thermal and Mechanical Behavior of LMFBR Fuel Elements. Part II. Carbide Fuels." OSU-EIR-33, Oregon State University, Dept. of Nucl. Eng.
- Anselin, F. 1969. "The Role of Fission Products in the Swelling of Irradiated  $UO_2$  and  $(U,Pu)O_2$  Fuel." USAEC Report GEAP-5583.
- Arakawa, M. and M. Nishino. 1973. Zairyo 22:658.
- Barner, J. O., et al. 1981. "Elongation Behavior of PCI-Resistant LWR Fuel Designs During Power Ramping." Trans. Am. Nucl. Soc. Annual Meeting, Miami, Florida, 273.
- Bart, G. 1982. "The Post Irradiation Examination of Four Sphere-Pac (U,Pu)C Fuel Pins Irradiated in the Harwell DIDO Reactor." EIR Report 450. Swiss Federal Institute for Reactor Research, Wurenlingen, Switzerland.
- Rates, J. F., W. V. Cummings and E. R. Gilbert. 1981. "Anisotropic Growth of Reactor Pin Cladding." J. Nucl. Mat. 99:75-84.
- Rathe, K-J. and E. L. Wilson. 1976. Numerical Methods in Finite Element Analysis. Prentice-Hall, New Jersey.
- Bathe, K-J., E. L. Wilson and R. H. Iding. 1974. "NONSAP: A Structural Analysis Program for Static and Dynamic Response of Nonlinear Systems." UCSESM 74-3. Structural Eng. Lab., U. of Cal., Berkeley.
- Benenati, R. F. and C. B. Brosilow. 1962. "Void Fraction Distribution in Beds of Spheres." AIChE J. 8,3:359-361.
- Bernal, J. D. and J. Mason. 1960. "Coordination of Randomly Packed Spheres." Nature 188:910-911.
- Billone, M. C. 1979. "UNCLE-T: A Computer Code for the Analysis of Steady-State and Transient Performance of (U,Pu)C and (U,Pu)N Fuels." ANL-AFP-79.
- Billone, M. C., et al. 1977a. "LIFE-III Fuel Element Performance Code." ERDA-77-56, Argonne National Laboratory.

- Billone, M. C., et al. 1977b. "Progress in Modeling Carbide and Nitride Fuel Performance in Advanced LMFBR's." Advanced LMFBR Fuels Topical Meeting Proceedings, Tucson, Arizona, 516.
- Bishop, A. W. 1966. "The Strength of Soils as Engineering Materials." Geotechnique 16:91-128.
- Blackburn, L. D., D. L. Greenslade and A. L. Ward. 1981. "Mechanical Properties of Type 316 Stainless Steel Materials After Irradiation at 515C and 585C." HEDL-TME81-4,UC-77, Hanford Engineering and Development Laboratory.
- Blank, H. 1975. "On the Driving Forces for Bubble Growth and Swelling in MX-Type Fast Breeder Fuels." J. Nucl. Mat. 58:123.
- Blank, H. 1977. "Correlation Between Properties and Irradiation Behavior for Carbide, Carbonitride and Nitride Fuels." Advanced LMFBR Fuels Topical Meeting Proceedings, Tucson, Arizona, 482-500.
- Blank, H., R. Lindner, Hj. Matzke. 1976. "Behavior of Advanced Fast Breeder Fuels at High Power Density." IAEA-CN-36/369, Vienna, 511.
- Roley, B. A. and J. H. Weiner. 1960. Theory of Thermal Stresses. John Wiley and Sons, Inc., New York.
- Brailsford, A. D. and R. Bullough. 1973. "The Stress Dependence of High Temperature Swelling." J. Nucl. Mat. 48:87.
- Brandt, H. 1955. "A Study of the Speed of Sound in Porous Granular Media." J. Appl. Mech. 22:479-486.
- Cattaneo C. 1938. "Sul Contatto di due Corpi Elastici." Rend. R. Accad. dei Lincei (Ser. 6) 27:342-348,434-436.
- Christian, J. T. and C. S. Desai. 1977. "Constitutive Laws for Geological Media." Numerical Methods in Geotechnical Engineering. C. S. Desai and J. T. Christian, eds. McGraw-Hill, New York, 65-115.
- Christoffersen, J., M. M. Mehrabadi, S. Nemat-Nasser. 1981. "A Micromechanical Description of Granular Material Behavior." J. Appl. Mech. 48:339-344.
- Clottes, G., et al. 1973. "Experience d'Irradiation de Combustible Carure a Joint Sodium dans Rapsodie." Fuel and Fuel Elements for Fast Reactors, Symp. Proc., Brussels, Belgium 2:113-127.

- Deiss, E. and J. Reindl. 1982. "SPECKLE Code Results Compared with the Available Data of the Carbide Sphere Pac Irradiation Experiments." TM-45-82-28. Swiss Federal Institute for Reactor Research, Wurenlingen, Switzerland.
- Deresiewicz, H. 1954. "Contact of Elastic Spheres Under an Oscillating Torsional Couple." J. Appl. Mech. 21:52-56.
- Deresiewicz, H. 1958. "Stress-Strain Relations for a Simple Model of a Granular Medium." J. Appl. Mech. 25:402-406.
- Dienst, W. 1977. "Irradiation Induced Creep of Ceramic Nuclear Fuels." J. Nucl. Mat. 65:1-8.
- Dienst, W., I. Mueller-Lyda and H. Zimmerman. "Swelling, Densification and Creep of Oxide and Carbide Fuels under Irradiation." 1979. Proc. Int. Conf. Fast Breeder Reactor Fuel Performance, ANS, Monterey, California, 166.
- Digby, P. J. 1981. "The Effective Moduli of Porous Granular Rocks." J Appl. Mech. 48:803-808.
- DiMaggio, F. L. and I. Sandler. 1971. "Material Model for Granular Soils." J. Eng. Mech. Div. ASCE 97 no. EM3.
- Drucker, D. C. 1950. "Some Implications of Work Hardening and Ideal Plasticity." Quarterly of Appl. Math. 7:411-418.
- Drucker, D. C. 1952. "A More Fundamental Approach to Plastic Stress-Strain Relations." Proc. First U.S. Cong. of Appl. Mech., ASME, New York, 487-491.
- Drucker, D. C. and W. Prager. 1952. "Soil Mechanics and Plastic Analysis or Limit Design." Quarterly of Appl. Math. 10:157-165.
- Drucker, D. C., R. E. Gibson and D. J. Henkel. 1957. "Soil Mechanics and Work Hardening Theories of Plasticity." Trans. ASCE 122:338-346.
- Duffy, J. 1959. "A Differential Stress-Strain Relation for the Hexagonal Close-Packed Array of Elastic Spheres." J. Appl. Mech. 26:88-94.
- Duffy, J. and R. D. Mindlin. 1957. "Stress-Strain Relations and Vibrations of a Granular Medium." J. Appl. Mech. 24:585-593.
- Dym, C. L. and I. H. Shames. 1973. Solid Mechanics: A Variational Approach. McGraw-Hill, New York.
- Fitts, R. B. and F. L. Miller. 1974. "A Comparison of Sphere-Pac and Pellet (U,Pu)O<sub>2</sub> Fuel Pins in Low-Burning Instrumented Irradiated Tests." Nucl. Tech. 21:26.

- Garg, S. K., V. Svalbonas and G. A. Gurtman. 1973. Analysis of Structural Composite Materials. Marcel Dekker, Inc., New York.
- Gatto, F. 1950. "Influence of Small Cavities on Velocity of Sound in Metals." Alluminio 19:19-26.
- George, T. L. and K. L. Peddicord. 1981. "SPECKLE-II: A Computer Code for Calculating the Thermal Behavior of Sphere-Pac Fuel Pins." OSU-EIR-54, Oregon State University, Corvallis, Oregon.
- George, T. L. and K. L. Peddicord. 1982. "SPECKLE-III: A Computer Code for Calculating the Thermal-Mechanical Behavior of Sphere-Pac Fuel Pins." OSU-EIR-64, Oregon State University, Corvallis, Oregon.
- Gray, W. A. 1968. The Packing of Solid Particles. Chapman and Hall, Ltd., London. 28.
- Godesar, R., M. Guyette and N. Hoppe. 1970. "COMETHE II - A Computer Code for Predicting the Mechanical and Thermal Behavior of a Fuel Pin." Nucl. Appl. Tech. 9:205.
- Guenther, R. J. 1978. "The Applicability of Sintering Mechanisms in the Initial Stage Restructuring and Preferential Pore Migration of Irradiated ( $U_{0.85}Pu_{0.15}$ )C Sphere Pac Fuel." M. S. Thesis. Dept. of Nucl. Eng., Oregon State University.
- Guyette, M. 1970. "CRASH - A Computer Program for the Evaluation of the Creep and Plastic Behavior of Fuel Pin Sheaths." Nucl. Appl. Tech. 9:60.
- Hall, A. R. 1970. "Elastic Moduli and Internal Friction of Some Uranium Ceramics." J. Nucl. Mat. 37:314-323.
- Handbook of Engineering Mechanics. 1962. W. Flugge, ed. McGraw-Hill, New York.
- Harr, M. E. 1977. Mechanics of Particulate Media. A Probabilistic Approach. McGraw-Hill, New York.
- Horne, M. R. 1965. "The Behavior of an Assembly of Rotund, Rigid, Cohesionless Particles, I and II." Proc. Roy. Soc., London, Series A 286:62-97.
- Hayns, M. R. and D. Wilmore. 1973. "FRUMP - A Computer Programme for the Calculation of Stresses in Reactor Fuel Pins." AERE-R7380.
- Hodge, P. G. and G. N. White. 1950. "A Quantitative Comparison of Flow and Deformation Theories of Plasticity." J. Appl. Mech. 180-183.
- Kingery, W. D., H. K. Bowen and D. R. Uhlman. 1976. Introduction to Ceramics, 2<sup>nd</sup> ed. John Wiley and Sons, New York.

- Kleykamp, H. 1977. "The Chemical State of Irradiated Carbide Fuel Pins." Topical Meeting Proc. on Advanced LMFRR Fuels, Tucson, Arizona, 167.
- Kraus, H. 1980. Creep Analysis. John Wiley and Sons, New York.
- Kummerer K., et al. 1971. "The SATURN Codes and Material Data Evaluation." Proc. Conf. on Fast Reactor Fuel Element Tech., New Orleans. 211.
- Johnson, K. L. 1955. "Surface Interaction Between Elastically Loaded Bodies Under Tangential Forces." Proc. Roy. Soc. (London) Ser. A 230:531-548.
- Lade, P. V. and J. M. Duncan. 1975. "Elastoplastic Stress-Strain Theory for Cohesionless Soil." J. of the Geotechnical Eng. Div. of ASCE, Oct.:1037-1053.
- Laidler, J. J. 1980. Advanced Alloys Databook. TC-293 Rev.5. Hanford Engineering and Development Laboratory.
- Lassmann, M. 1977. "URANUS, A Computer Code for the Thermal and Mechanical Analysis of Fuel Rod Behavior." Trans. Fourth Int. Conf. on Structural Mechanics in Reactor Tech., San Francisco. Paper D1/2.
- Liu, Y. Y. and S. Zawadzki. 1981. Unpublished Work.
- Makhlouf H. M. and J. J. Stewart. 1967. "Elastic Constants of Cubical-Tetrahedral and Tetragonal-Sphenoidal Arrays of Uniform Spheres." Proc. Int. Symp. on Wave Propagation and Dynamic Properties of Earth Materials, Univ. of N. M.:825-837.
- Marlowe, M. O. and D. R. Wilder. 1965. "Elasticity and Internal Friction of Polycrystalline Yttrium Oxide." J. Amer. Cer. Soc. 48:227-233.
- Matsuoka H. and K. Takeda. 1980. "A Stress-Strain Relationship for Granular Materials Derived from Microscopic Shear Mechanism." Soils and Foundations 20:45-58.
- Matthews, J. R. 1979. "The Initial Stages of Sintering and Hot-Pressing in Vibro-Compacted Fuels." J. Nucl. Mat. 87:356-366.
- Mendelson, A. 1968. Plasticity: Theory and Application. MacMillan Co., New York.
- Merckx, K. R. 1968. "A Program for Calculating the Steady-State Deformation Rates for Cylindrical Fuel Elements." BNWL-663. Battelle Northwest Laboratories.

- Mindlin, R. D. 1949. "Compliance of Elastic Bodies in Contact." J. Appl. Mech. 16:259-268.
- Mindlin, R. D. and H. Deresiewicz. 1953. "Elastic Spheres in Contact Under Varying Oblique Forces." J. Appl. Mech. 20:327-344.
- Mroz, Z., V. A. Norris and O. C. Zienkiewicz. 1978. "An Anisotropic Hardening Model for Soils and Its Application to Cyclic Loading." Int. J. Numer. Anal. Methods Geomech. 2,3:203-221.
- Mullenger, G. and R. O. Davis. 1981. "A Unified Yield Criterion for Cohesionless Granular Materials." Int. J. Numer. Anal. Methods Geomech. 5,3:285-294.
- Nakatsuka, N. 1981. "Measurement of the Coefficient of Friction Between  $UO_2$  and  $Al_2O_3$  Pellets and Unirradiated Zircaloy Cladding." J. Nucl. Mater. 96:205-207.
- Nemat-Nasser, S. 1980. "On Behavior of Granular Materials in Simple Shear." Soils and Foundations 20:59-73.
- Newman, J. B., J. F. Gioving and L. P. Comden. 1977. "The CYGR0-4 Fuel Rod Analysis Computer Program." Trans. Fourth International Conf. on Structural Mechanics in Reactor Technology, San Francisco. Paper D1/1.
- Nuclear Systems Materials Handbook, Vol. 1. 1976. TID 2666.  
Compiled by Hanford Engineering and Development Laboratory.
- Oda, M., J. Konishi and S. Nemat-Nasser. 1980. "Some Experimentally Based Fundamental Results on the Mechanical Behavior of Granular Materials." Geotechnique 30:479-495.
- Ogard, A. E., C. C. Land and J. A. Leary. 1965. "The Thermal Expansion of PuC and UC-PuC Solid Solution." J. Nucl. Mat. 15:43.
- Olander, D. R. 1976. Fundamental Aspects of Nuclear Reactor Fuel Elements. TID-26711-P1, Technical Information Center, ERDA.
- Padel, A. and Ch. de Novion. 1969. "Constantes Elastiques des Carbures, Nitrures et Oxydes d'Uranium et de Plutonium." J. Nucl. Mat. 33:40-51.
- Padel, A., A. Groff and Ch. de Novion. 1970. "Constantes Elastiques des Carbonitrides d'Uranium et de Plutonium  $UC_{1-x}N_x$  et  $(U_{0.85}Pu_{0.15})C_{1-x}N_x$ ." J. Nucl. Mat. 36:297-303.
- Paul, B. 1960. "Prediction of Elastic Constants of Multiphase Material." Trans. Metallurgical Soc. of AIME 218:36-41.

- Poorooshasb, H. B., I. Holubec and A. N. Sherbourne. 1966. "Yielding and Flow of Sand in Triaxial Compression, Part I." Canadian Geotechnical Journal 3:179-190.
- Poorooshasb, H. B., I. Holubec and A. N. Sherbourne. 1967. "Yielding and Flow of Sand in Triaxial Compression, Parts II and III." Canadian Geotechnical Journal 4:376-397.
- Robinson, C. A. 1981. "Burnup Dependent Neutron Flux and Heat Source Distributions in Sphere-Pac Mixed Carbide Fuels." OSU-NE-8105. Oregon State University.
- Ronchi, C. and C. Sari. 1975. "Swelling Analysis of Highly Rated MX-Type LMFBR Fuels: I. Restructuring and Porosity Behavior." J. Nucl. Mat. 58:140-152.
- Ronchi, C., et al. 1978. "Swelling Analysis of Highly Rated MX-Type LMFBR Fuels: II. Microscopic Swelling Behavior." J. Nucl. Mat. 74:193-211.
- Roscoe, K. H. and J. B. Burland. 1968. "On the Generalized Stress-Strain Behavior of Wet Clay." Engineering Plasticity. J. Heyman and F. A. Leckie, eds. Cambridge Univ. Press 535-609.
- Rowe, P. W. 1962. "The Stress-Dilatancy Relations for Static Equilibrium of an Assembly of Particles in Contact." Proc. Roy. Soc., London, Series A 269:500-527.
- Routbort, J. L. and R. N. Singh. 1975. "Elastic, Diffusional and Mechanical Properties of Carbide and Nitride Nuclear Fuels - A Review." J. of Nucl. Mat. 58:78-114.
- Singh, R. 1977. "Creep Behavior of Mixed-Carbide Advanced Nuclear Fuel." Advanced LMFBR Fuels Topical Meeting Proceedings, Tucson, Arizona, 257-266.
- Smith, L., et al. 1974. "The Post Irradiation Examination of Four (U,Pu)C Sphere-Pac Fuel Pins Irradiated in DIDO Reactor at Harwell." EIR Report 265. Swiss Federal Institute for Reactor Research, Wurenlingen, Switzerland.
- Smith, L., et al. 1977. "DIDO II, The Post Irradiation Examination of Four (U,Pu)C Fuel Pins." EIR Report 317. Swiss Federal Institute for Reactor Research, Wurenlingen, Switzerland.
- Smith, W. O., P. D. Foote and P. F. Busang. 1929. "Packing of Homogeneous Spheres." Phys. Rev. 34:1271-1274.
- Soloman, A. A. 1973. "Radiation-Induced Creep of  $UO_2$ ." J. Am. Cer. Soc. 56:164.

- Stratton, R. W. 1977. "Development of Advanced Fuels in Switzerland." Proc. Topical Meeting on Advanced LMFBR Fuels, Tucson, Arizona 74.
- Tabor, D. 1951. The Hardness of Metals. Oxford Press, London.
- Takahashi, T. and Y. Sato. 1949. "On the Theory of Elastic Waves in Granular Substance." Bull. Earthquake Res. Inst. (Tokyo Univ.) 27:11-16.
- Tatsuoka, F. 1980. "Stress-Strain Behavior of an Idealized Anisotropic Granular Material." Soils and Foundations 20,3:75-90.
- Timoshenko, S. and J. N. Goodier. 1951. Theory of Elasticity, 2<sup>nd</sup> ed. McGraw-Hill, New York 372-382.
- Tokar, M. 1973. "Compressive Creep and Hot Hardness of U-Pu Carbides." J. Am. Cer. Soc. 56:173-177.
- Tokue, T. 1979. "A Stress-Dilatancy Model of Granular Material under General Stress Conditions." Soils and Foundations 19:63-78.
- Waltar, A. E. and A. B. Reynolds. 1981. Fast Breeder Reactors. Pergamon Press, New York.
- Werner, P. and H. Blank. 1981. "Mechanical Properties of Advanced Fuels under Compressive Deformation." Nucl. Tech. 52:73-84.
- Wu, C.-T. D. and R. L. McCullough. 1977. "Constitutive Relationships for Heterogeneous Materials." Developments in Composite Materials. G. S. Holister, ed. Applied Science Pub. Ltd., London 119-187.
- Yanagisawa, E. 1978. "Relation between the Shear Modulus and Void Ratio in Granular Media." Technology Reports, Tohoku Univ. 43:211-220.
- Zienkiewicz, O. C. 1971. The Finite Element Method in Engineering Science. McGraw-Hill, New York.
- Zienkiewicz, O. C. and C. Humpheson. 1977. "Viscoplasticity: A Generalized Model for Description of Soil Behavior." Numerical Methods in Geotechnical Engineering. C. S. Desai and J. T. Christian, eds. McGraw-Hill, New York.
- Zienkiewicz, O. C., S. Valliappan and I. P. King. 1969. "Elastic-Plastic Solutions of Engineering Problems 'Initial Stress', Finite Element Approach." Int. J. for Numerical Methods in Engineering 1:75-100.
- Zimmerman, H. 1982. "Investigation of Swelling of U-Pu Mixed Carbide." J. of Nucl. Mat. 150:56-61.

APPENDICES

APPENDIX A  
THERMAL ELASTOPLASTIC MODEL VERIFICATION

## THERMAL ELASTOPLASTIC MODEL VERIFICATION

Several test problems were run using slightly modified versions of the SPECKLE-III code. The modifications were mainly required to give constant mechanical properties for the fuel and the cladding and to remove some of the unnecessary calculations for the initial strain rate. These problems and results are described in this appendix.

### A.1 THERMAL-ELASTIC PROBLEM

This problem was chosen to represent the thermal-elastic behavior of a fuel pin. The problem geometry, shown in Figure A.1, consists of a solid fuel cylinder in contact with the cladding. The fuel and cladding mechanical properties are assumed to be constant and the temperature distribution in the pin is assumed to depend on the radial dimension only. The interface pressure developed between the cladding and the fuel is assumed to be constant, although slip is allowed to occur at the interface. The bottom end of the fuel and cladding are fixed, and the fuel and cladding are assumed to be in a state of generalized plain strain. These assumptions (except for the constant property assumptions) parallel those made for the thermal-elastic model described in this report.

#### A.1.1 Analytic Solution

An analytic solution was obtained for the above described problem as an extension of the single solid cylinder solution in Boley and Weiner (1960) and is outlined here. The Navier equations for axisymmetric geometry reduce to

$$(\lambda + 2G)e - (3\lambda + 2G) C_t \frac{dT}{dr} = 0 \quad \text{A.1}$$

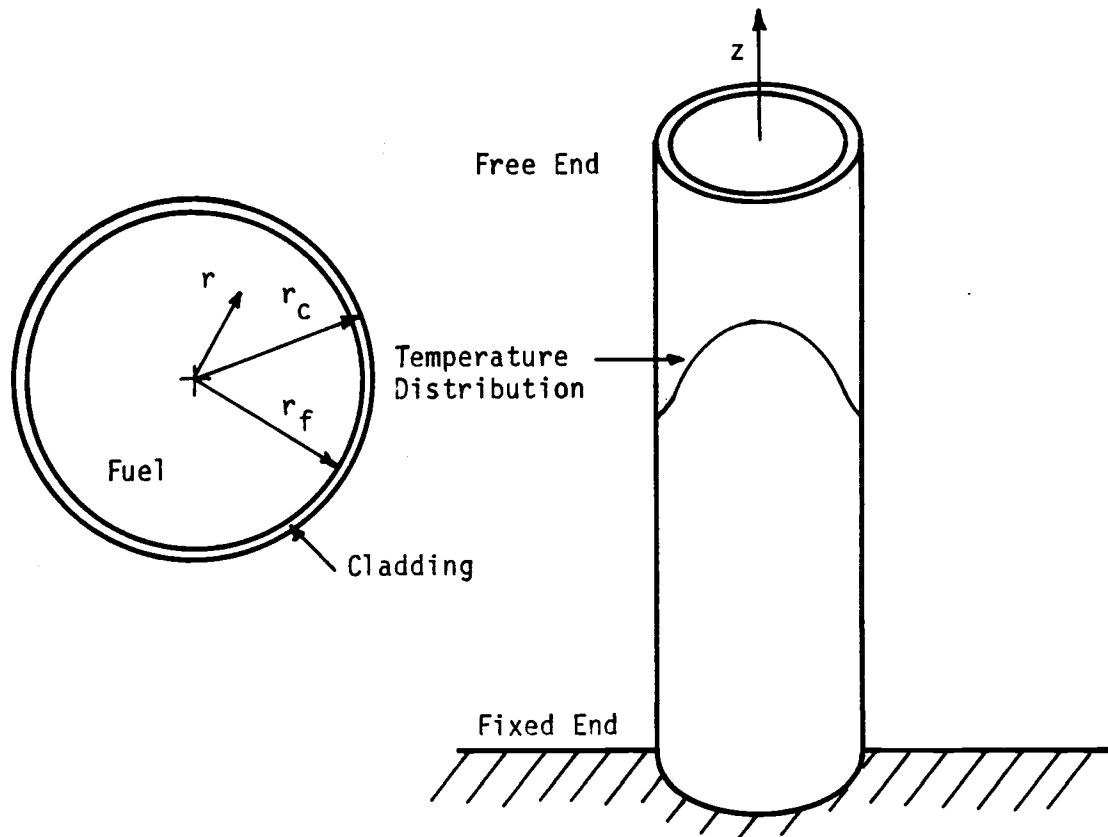


FIGURE A.1. Thermal-Elastic Check Problem Geometry

where  $\lambda$ ,  $G$  are Lamé's constants,  $e$  is the volumetric strain,  $r$  is the radial coordinate,  $C_t$  is the coefficient of thermal expansion, and  $T$  is the temperature. A plane strain solution is obtained first and then the generalized plane strain solution is arrived at by superposition of the negative of the average axial stress on the plane strain stress distribution. Using the strain displacement relations

$$\epsilon_r = du/dr$$

$$\epsilon_\theta = u/r$$

$$\epsilon_z = 0$$

A.2

where  $u$  is the radial displacement, Equation A.1 can be integrated twice to give

$$(\lambda + 2G)u = \frac{3K}{r} C_t \int_0^r T r dr + A_1 r + A_2/r \quad A.3$$

for the displacement solution. In Equation A.3,  $K$  is the bulk modulus given by

$$3K = 3\lambda + 2G$$

The boundary conditions for the fuel and cladding are

$$u_f (r=0) = 0$$

$$\sigma_{rf} (r = r_f) = - P_I$$

$$\sigma_{rc} (r = r_f) = - P_I$$

$$\sigma_{rc} (r = r_c) = 0$$

where the subscripts  $f$  and  $c$  refer to the fuel and cladding and  $P_I$  is the interface pressure (positive in compression). Application of these boundary conditions to obtain the integration constants results in

$$u_f = \frac{3 K_f C_{tf}}{(\lambda_f + 2G_f)r} \int_0^r T r dr + \frac{3 K_f C_{tf} G_f r}{(\lambda_f + G_f)(\lambda_f + 2G_f)r_f^2} \int_0^{r_f} T r dr - \frac{P_I r}{2(\lambda_f + G_f)}$$

A.4

and

$$u_c = \frac{3 K_c C_{tc}}{(\lambda_c + 2G_c)r} \int_{r_f}^r T r dr + \frac{3 K_c C_{tc} G_c r}{(\lambda_c + G_c)(\lambda_c + 2G_c)(r_{cf}^2 - 1)r_f^2} \int_{r_f}^{r_c} T r dr$$

$$+ \frac{P_I r_c^2 r}{(\lambda_c + G_c)(r_{cf}^2 - 1)2r_f^2} + \frac{3 K_c C_{tc}}{(\lambda_c + 2G_c)(r_{cf}^2 - 1)r} \int_{r_f}^{r_c} T r dr$$

$$= \frac{P_I r_c^2}{(r_{cf}^2 - 1)2G_c r} - \frac{P_I r}{2(\lambda_c + G_c)}$$

A.5

where  $r_{fc} = r_c/r_f$ .

These can be rewritten as

$$u_f = F_1/r \int_0^r T r dr + F_2 r + F_3 P_I r$$

A.6

and

$$u_c = C_1/r \int_{r_f}^r T r dr + C_2 r + C_3/r + C_4 P_I r + C_5 P_I/r$$

A.7

where the F and C constants are defined by comparison with Equations A.4 and A.5. This gives the plane strain displacement solution. To obtain the generalized plane strain solution the average axial stress in the fuel and cladding must be calculated. The plane strain stress-strain relations give

$$\sigma_z = \lambda(\epsilon_\theta + \epsilon_r) - 3K_t T \quad \text{A.8}$$

The net axial stress is given by

$$\bar{\sigma}_z = \frac{2\pi}{A} \int_{r_i}^{r_o} r \sigma_z dr \quad \text{A.9}$$

where A is the pertinent area and  $r_i$  and  $r_o$  are inner and outer radii respectively.

Combining Equations A.9, A.8, A.7, A.6 and A.2 gives

$$\bar{\sigma}_{zf} = 2\lambda_f(F_2 + F_3 P_I) + \frac{2(\lambda_f F_1 - 3K_f C_{tf})}{r_f^2} \int_0^{r_c} Tr dr \quad \text{A.10}$$

$$\bar{\sigma}_{zc} = 2\lambda_c(C_2 + C_4 P_I) + 2 \frac{2(\lambda_c C_1 - 3K_c C_{tc})}{r_c^2 - r_f^2} \int_{r_f}^{r_c} Tr dr \quad \text{A.11}$$

If there is not frictionless slip at the interface, equal and opposite shear loads will be applied to the fuel and the cladding. Since it is assumed that the fuel and cladding do not experience any shear strain (and therefore shear stress) the shear loads must be applied as effective axial loads. The axial stress for generalized plain strain can therefore be obtained from

$$\sigma_{zf}^g = \sigma_{zf} - \bar{\sigma}_{zf} + P_f$$

$$\sigma_{zc}^g = \sigma_{zc} - \bar{\sigma}_{zc} + P_c \quad \text{A.12}$$

where  $P_f$  and  $P_c$  are the axial stresses resulting from the interface shear loads. The radial and tangential stresses are not affected by the application of a uniaxial stress so that

$$\begin{aligned}\sigma_{rf}^g &= \sigma_{rf}, & \sigma_{\theta f}^g &= \sigma_{\theta f} \\ \sigma_{rc}^g &= \sigma_{rc}, & \sigma_{\theta c}^g &= \sigma_{\theta c}\end{aligned}\tag{A.13}$$

The quantities  $P_I$ ,  $P_f$ , and  $P_c$  are as yet unknown. A relation between these quantities can be obtained by requiring that

$$u_f^g (r = r_f) = u_c^g (r = r_f)\tag{A.14}$$

where  $u_f^g$  and  $u_c^g$  are the generalized plane strain deformations corresponding to the generalized plane strain stress field (Equations A.12 and A.13). The generalized plane strain radial deformations at  $r = r_f$  are given by

$$u_f^g = u_f + \frac{r_f \nu_f}{E_f} (\bar{\sigma}_{zf} - P_f)\tag{A.15}$$

$$u_c^g = u_c + \frac{r_f \nu_c}{E_c} (\bar{\sigma}_{zc} - P_c)$$

(i.e., the plane strain deformation plus the deformation resulting from the uniaxial stress).

Then, if Equations A.10 and A.11 are rewritten as

$$\bar{\sigma}_{zf} = F_1^i + F_2^i P_I\tag{A.16}$$

$$\bar{\sigma}_{zC} = C_1' + C_2' P_I \quad \text{A.17}$$

where the  $F'$  and  $C'$  constants are defined by comparison with Equations A.10 and A.11 and Equations A.6, A.7, A.15, A.16 and A.17 are substituted into Equation A.14, the resulting relationship between  $P_I$ ,  $P_f$ , and  $P_C$  is

$$\begin{aligned} & F_1/r_f \int_0^{r_f} T r dr + F_2 r_f + F_3 P_I r_f + \frac{r_f \nu_f F_1'}{E_f} + \frac{r_f \nu_f}{E_f} F_2' P_I - \frac{r_f \nu_f P_f}{E_f} \\ & = C_2 r_f + C_3/r_f + C_4 P_I r_f + C_5 P_I/r_f + r_f \frac{\nu_C}{E_C} C_1' + \frac{r_f \nu_C}{E_C} C_2' P_I - \frac{r_f \nu_C}{E_C} P_C \end{aligned}$$

A.18

If  $P_f$  and  $P_C$  are known then Equation A.18 can be solved for  $P_I$  and the generalized plane strain solution would be complete.  $P_f$  and  $P_C$  can be specified for three possible cases.

Case 1: Free slip - there is no interface shear load so

$$P_f = P_C = 0$$

Case 2: No slip - the axial displacements of the fuel and cladding must obey

$$\epsilon_{zf}^g = \epsilon_{zC}^g \quad \text{A.19}$$

Since the axial strains are due only to the superposed uniaxial loads, Equation A.19 becomes

$$\frac{1}{E_f} (P_f - \bar{\sigma}_{zf}) = \frac{1}{E_c} (P_c - \bar{\sigma}_{zc}) \quad \text{A.20}$$

Also the axial load on the fuel and cladding due to the interface must be equal and opposite giving

$$A_f P_f = - A_c P_c \quad \text{A.21}$$

where  $A_f$  and  $A_c$  are the fuel and cladding cross section areas. Then Equations A.18, A.20, and A.21 can be solved for  $P_I$ ,  $P_f$ , and  $P_c$  to complete the solution.

Case 3: Slip limited by friction - in this case the interface pressure is related to the cladding axial stress due to interface shear  
by

$$A_c P_c = P_I A_I \mu_I \quad \text{A.22}$$

where  $\mu_I$  is the interface friction factor. Here, again, Equation A.22 can be combined with Equations A.18 and A.21 to obtain  $P_I$ ,  $P_f$ , and  $P_c$ .

For a given friction factor the Case 2 solution can be compared to the Case 3 solution to determine whether or not the slip is limited by friction. Assuming that in the free slip case  $\epsilon_{zf}^g > \epsilon_{zc}^g$  then if  $P_{f \text{ case 3}} > P_{f \text{ case 2}}$  (an impossible situation) it must be concluded that the slip is not friction limited.

### A.1.2 SPECKLE-III Solution

The thermal-elastic problem described in Section A.1 was also solved using the SPECKLE-III code. For this solution the code was modified so that the only initial strain rate was that due thermal expansion. Plastic flow was not allowed except in the interface element, and the fuel and cladding material properties were set to constants. A single axial section was modeled with ten ring elements in the fuel and two in the cladding.

### A.1.3 Comparison for Thermal-Elastic Problem

Analytic and SPECKLE-III solutions were obtained for the particular case where the temperature profile was that resulting from a uniform power density in the fuel. The physical parameters used for the fuel and cladding are given in Table A.1.

Figure A.2 shows the analytic and code-predicted tangential stress normalized by the cladding elastic modulus with  $\mu_I = 0.008$ . Figure A.3 shows the fuel and cladding axial strains from the analytic and code solutions as a function of the interface friction factor. The agreement between the two results is excellent including the prediction of the point at which slip begins ( $\mu = 0.0082$ ). These results show, in particular, that the special interface element can accurately model the frictional slip condition. It should be noted that these results do not give any information concerning the fuel/cladding slip and interface friction factor for sphere-pac fuel but are relevant only for the particular parameters given in Table A.1.

TABLE A.1. Parameters for Thermal-Elastic Check Problem

$E_f$	6.9 E4 MPa
$E_c$	2.07 E5 MPa
$\nu_f$	0.3
$\nu_c$	0.3
$C_{tf}$	1.E-5 1/C
$C_{tc}$	2.E-5 1/C
$r_f$	0.254 cm
$r_c$	0.280 cm
Pin length	25.4 cm
Fuel conductivity	0.1 W/cm-C
Cladding conductivity	0.2 W/cm-C
Power	900 W/cm
Outer cladding temperature	500°C

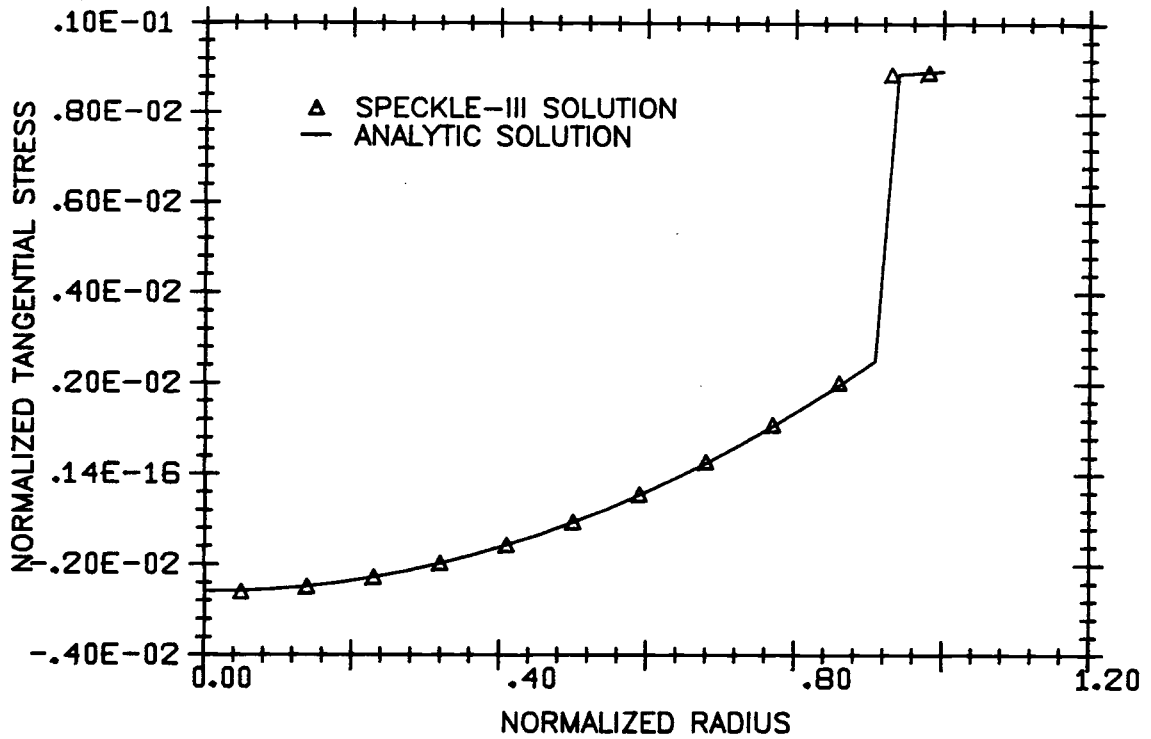


FIGURE A.2. Comparison of Analytic and SPECKLE-III Solutions for Tangential Stress in Thermal-Elastic Check Problem

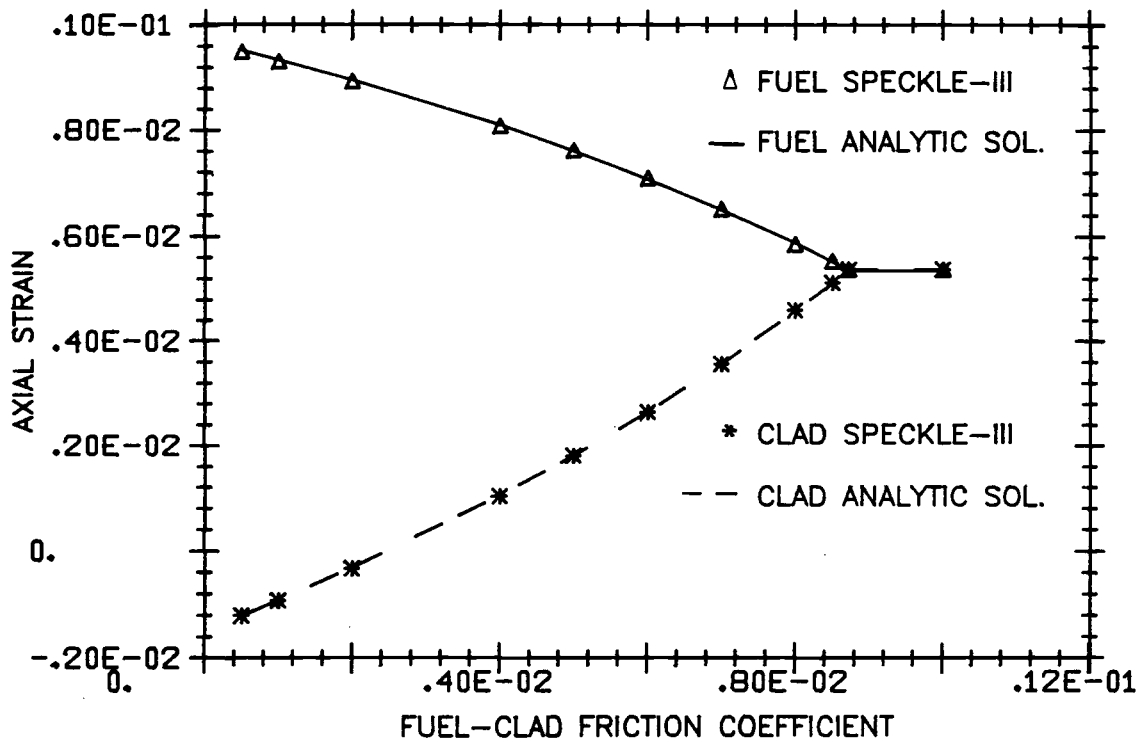


FIGURE A.3. Comparison of Analytic and SPECKLE-III Solutions for Axial Strain in Thermal Elastic Check Problem

## A.2 PLASTICITY PROBLEM

A simple elastoplastic problem was chosen to verify the SPECKLE-III solution techniques and coding. The problem geometry, shown in Figure A.4, consists of a hollow cylinder open on the ends. The inside of the cylinder is loaded by a uniform compressive stress,  $P_0$ . The cylinder is assumed to be in a state of plane strain and yields according to the von Mises law with associated flow.

### A.2.1 Finite-Difference Solution to Plasticity Problem

Hodge and White (1950) obtained a solution to the above problem using a finite-difference scheme for the particular parameters shown in Table A.2. In Table A.2,  $S_g$  is the yield strength in pure shear,  $G$  is the shear modulus, and  $\nu$  is Poisson's ratio.

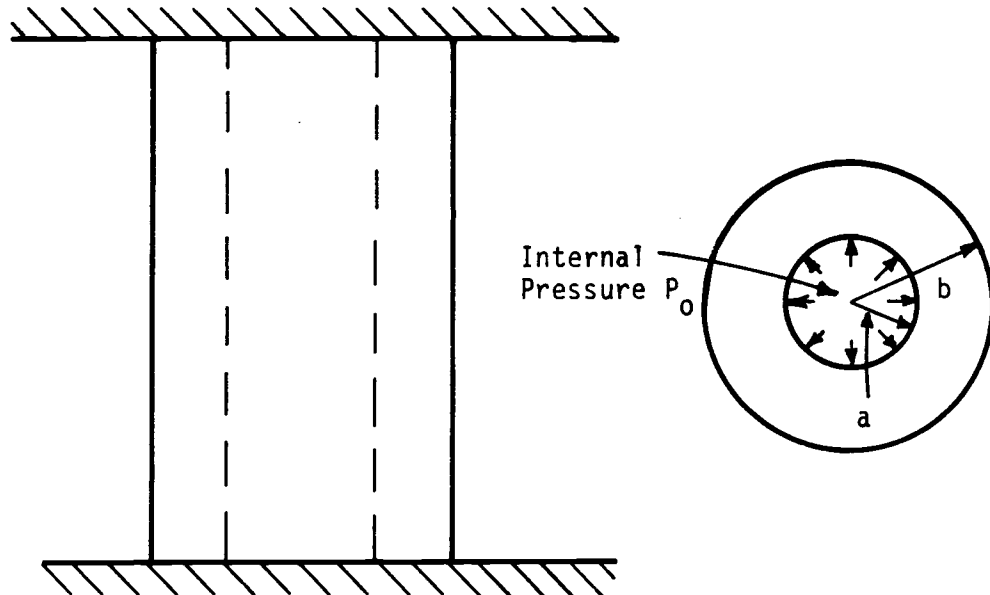


FIGURE A.4. Elastoplastic Check Problem Geometry

TABLE A.2. Plasticity Problem Parameters

$$P_0/S_g = 1.25$$

$$R_0/R_i = 2.0$$

$$G/S_g = 333.33$$

$$\nu = 0.3$$

### A.2.2 SPECKLE-III Solution to Plasticity Problem

The SPECKLE-III code was modified to solve the problem described in Section A.2. The plane strain assumption was incorporated by not allowing any axial displacement. One element was used for the fuel and eight elements were used for the cladding. To model a hollow cylinder, Young's modulus for the fuel element was set to a very small value. The cladding elastic properties were set to values corresponding to those given in Table A.2. The load on the interior of the cylinder was applied in the same manner as the gas pressure load in actual pin calculations (see Section 7.1) and the initial strain rate was set to zero.

### A.2.3 Comparison for Plasticity Problem

The radial, tangential, and axial stress profiles from the Hodge and White solution and from the SPECKLE-III code are shown in Figure A.5. The agreement is excellent for the radial and axial stresses and the elastic-plastic transition point. There is a slight discrepancy in the tangential stress in the plastic region. Since the SPECKLE-III results satisfy the von Mises yield law and the radial and axial stresses are in close agreement, the discrepancy is attributed to inaccuracies in the graphical representation of Hodge and White's results.

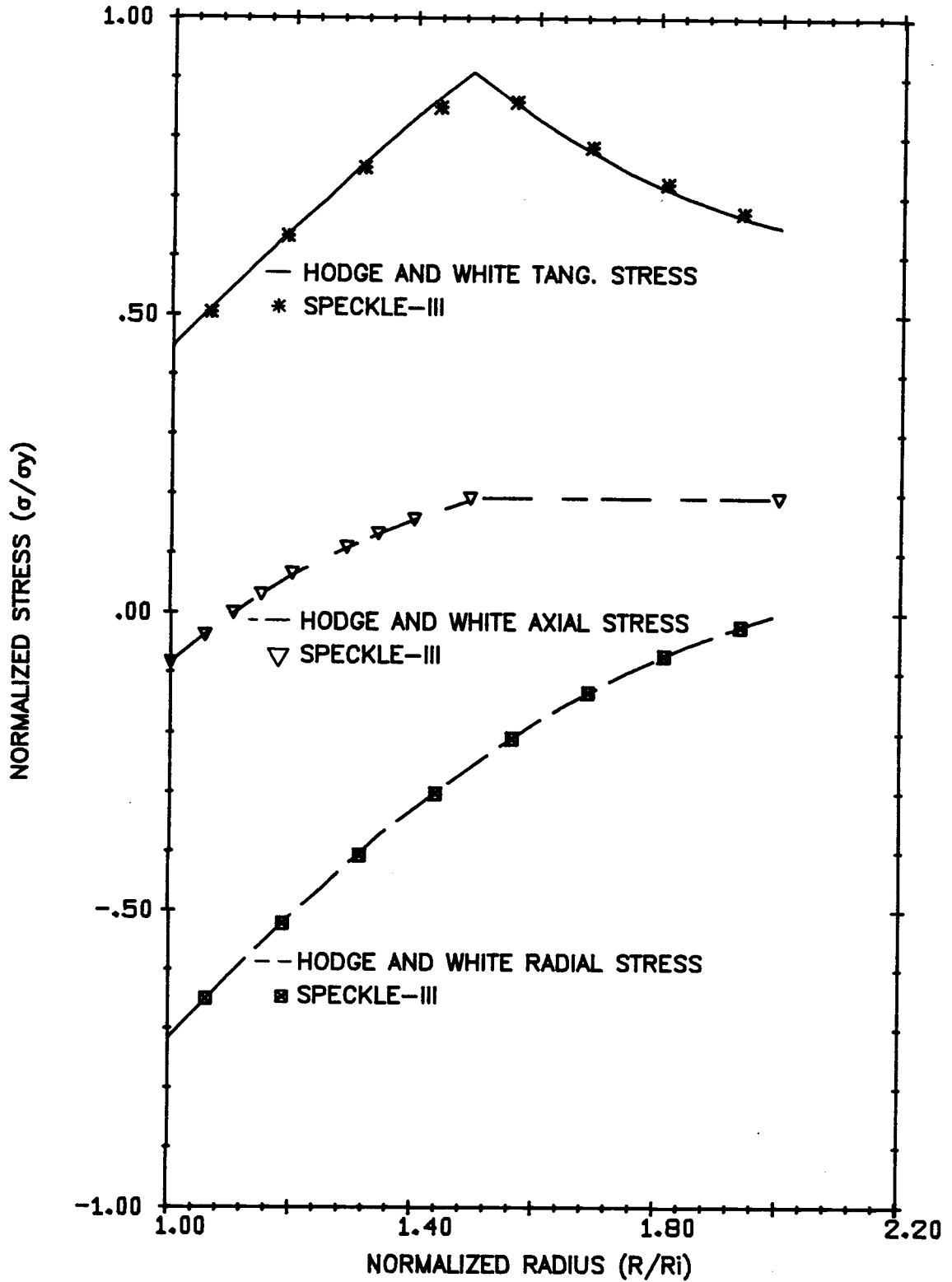


FIGURE A.5. Comparison of Hodge and White and SPECKLE-III Solution for Elastoplastic Check Problem

Another plasticity problem was solved to check the extended von Mises yield law for frictional material. The problem was similar to that described in Section A.2 except that the applied load was external, rather than internal, compression. The SPECKLE-III code results were compared with results from the NONSAP (Bathe, et al. 1974) code. The stress profiles and the elastic-plastic transition point again were in excellent agreement.

APPENDIX B  
TRIAxIAL COMPRESSION TESTS

## TRIAXIAL COMPRESSION TESTS

Some triaxial compression tests were performed on various samples of randomly packed sphere arrays to obtain a better understanding of the plastic behavior of the granular material and the effect on strength when two sphere sizes are combined.

A description of a triaxial compression test can be found in any standard text on solid mechanics, so only a brief description is presented here to give the details that relate to the sphere pac

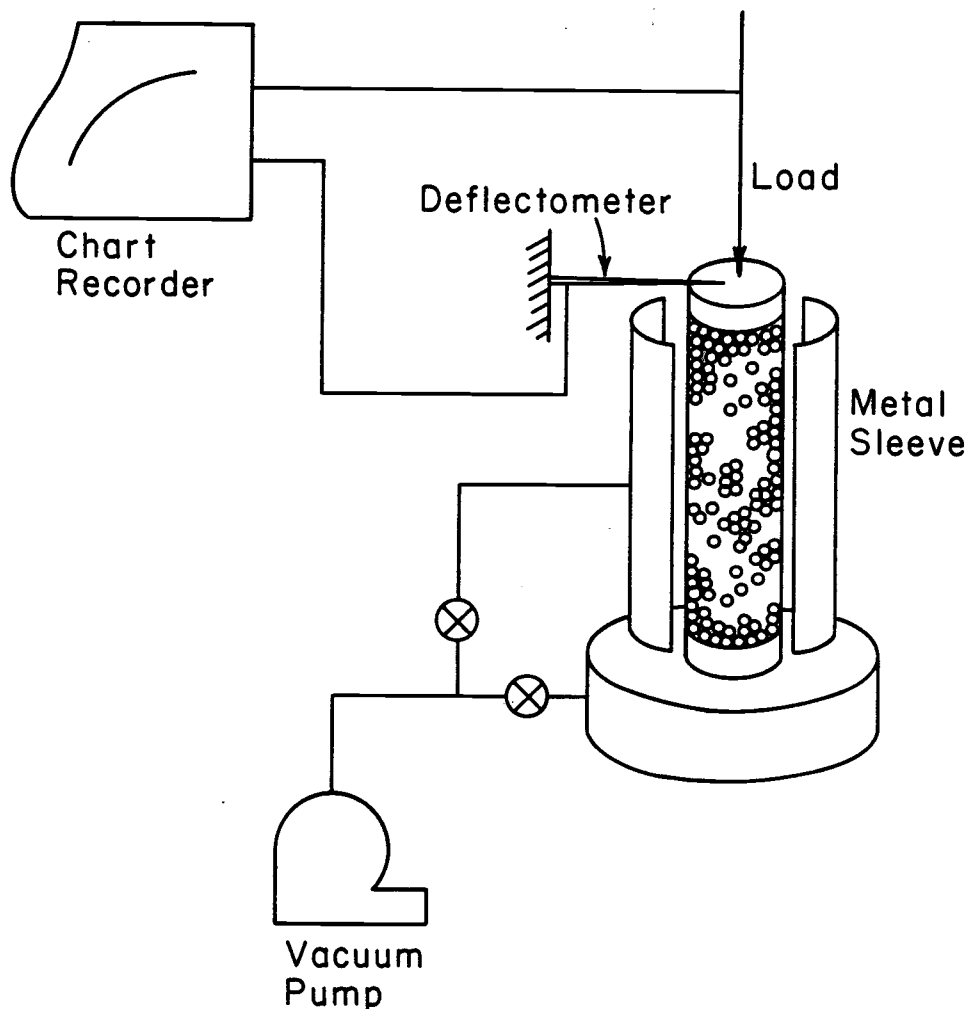


FIGURE B.1. Schematic Diagram of Triaxial Compression Test Equipment

fuel. The test equipment is shown schematically in Figure B.1. In a typical test, a thin rubber membrane is placed inside a metal sleeve. A vacuum is drawn between the inside of the sleeve and the membrane and the spheres poured into the membrane. The sample is then vibrated for approximately 30 seconds. If a second infiltrating sphere size is included in the sample, they are loaded into the already packed large sphere array. A weight is placed on the top of the sample and the sample again vibrated, adding more small spheres as necessary to fill the membrane. An end piece is then placed on the sample and the membrane pulled up over it and secured with rubber bands. The interior of the membrane is evacuated providing a compressive load on the sample of approximately one atmosphere. At this time the sample is rigid and the metal sleeve can be removed. Additional hydrostatic stress can be applied by enclosing the sample in a second container and pressurizing the container using stored compressed air.

The sample is loaded axially using a standard tensile testing machine in the compressive mode. For tests above atmospheric pressure the sample is loaded by a frictionless piston that penetrates the outside container. The axial deformation is recorded as a function of the axial load using a deflectometer attached to a chart recorder. The load is increased until the sample begins to experience large deformation with only small load increases.

Typical load-deflection behavior is shown in Figure B.2. For this particular test the sample was unloaded at point A and then reloaded starting at point B. It is evident that plastic deformation occurs upon unloading and that there is some kinematic hardening of the sample. A rough approximation of the strength of the sample can be related to the load at which very large deformations begin as indicated in Figure B.2.

Table B.1 lists the relevant tests made. To simulate the large spheres of the EIR fuel, 0.123 cm diameter steel spheres were used. The small spheres were simulated using 0.0079 cm alumina spheres.

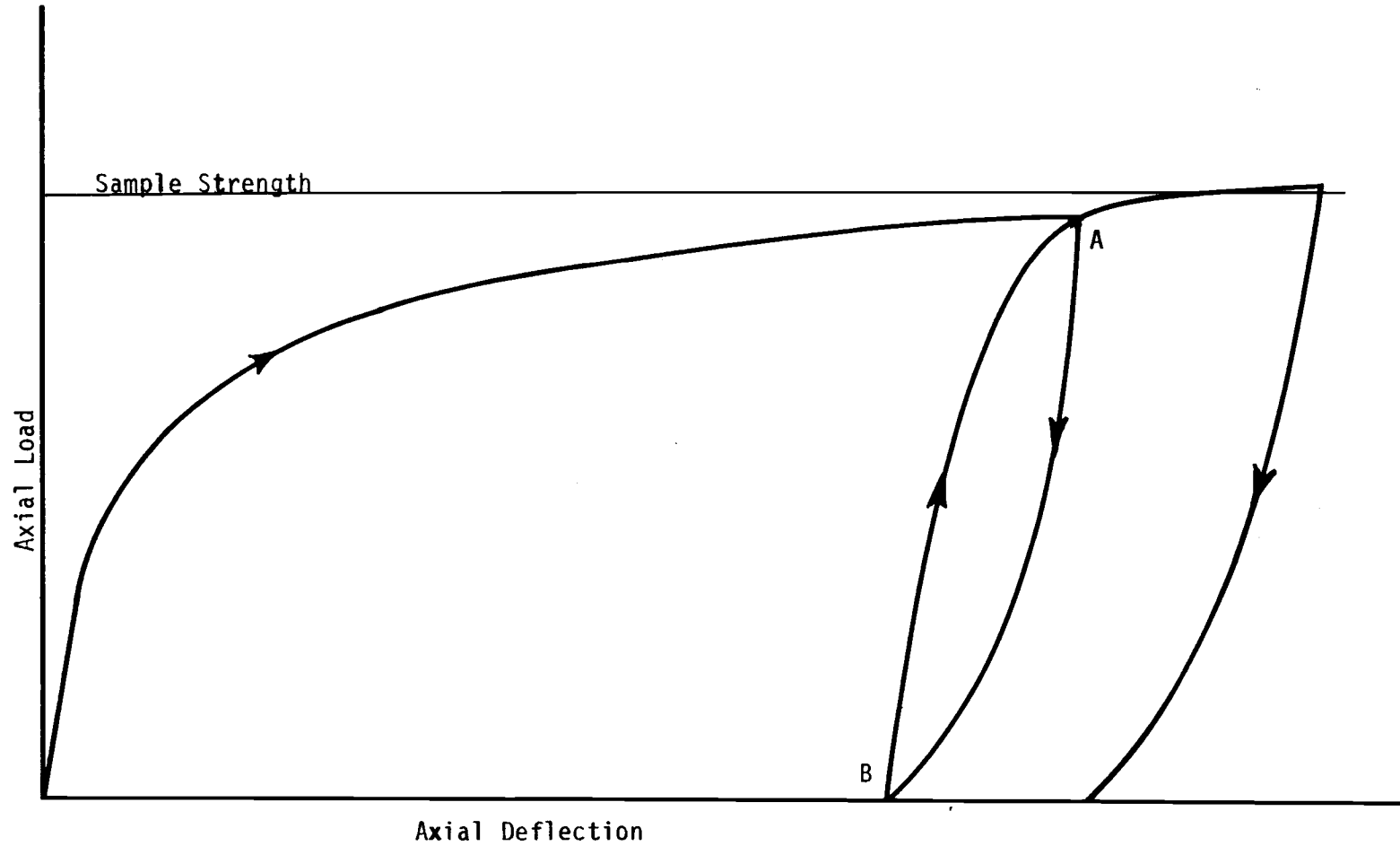


FIGURE B.2. Load Deflection Behavior for a Typical Triaxial Compression Test on a Random Array of Uniform Steel Spheres

TABLE B.1. Triaxial Compression Tests

<u>Test No.</u>	<u>Sphere Size (cm)</u>	<u>Confining Pressure (MPa)</u>
4	0.123	0.10
5	0.123	0.34
6	0.123	0.10
7	0.123	0.10
8	0.123	0.10
9	0.123	0.21
10	0.123	0.21
11	0.123	0.42
14	0.0079	0.10
15	0.123/0.0079	0.10
16	0.123/0.0079	0.10
17	0.123/0.0079	0.10
18	0.123/0.0079	0.42
20	0.0079	0.21
21	0.0079	0.10
22	0.0079	0.10
23	0.123/0.0079	0.10
24	0.123	0.10
25	0.123	0.10
26	0.123	0.21
27	0.123	0.42
28	0.0079	0.42

Tests were made on each of these sphere sizes separately and mixed together as in the EIR fuel. The internal friction angle can be obtained by plotting the Mohr circle for each test at the failure point. The Mohr-Coulomb yield criteria is given by the envelope of these circles and the friction angle is the angle that the envelope makes with the principal stress axis. Figure B.3 shows the Mohr circles for the separate and mixed size sphere tests and also shows the Mohr-Coulomb envelopes and friction angles. The friction angle for the large and small sphere mixture is considerably larger than for either of the sphere types alone.

Tests of this nature should be performed on the EIR fuel to provide better estimates for the unrestructured fuel internal friction angle required for the fuel plasticity model.

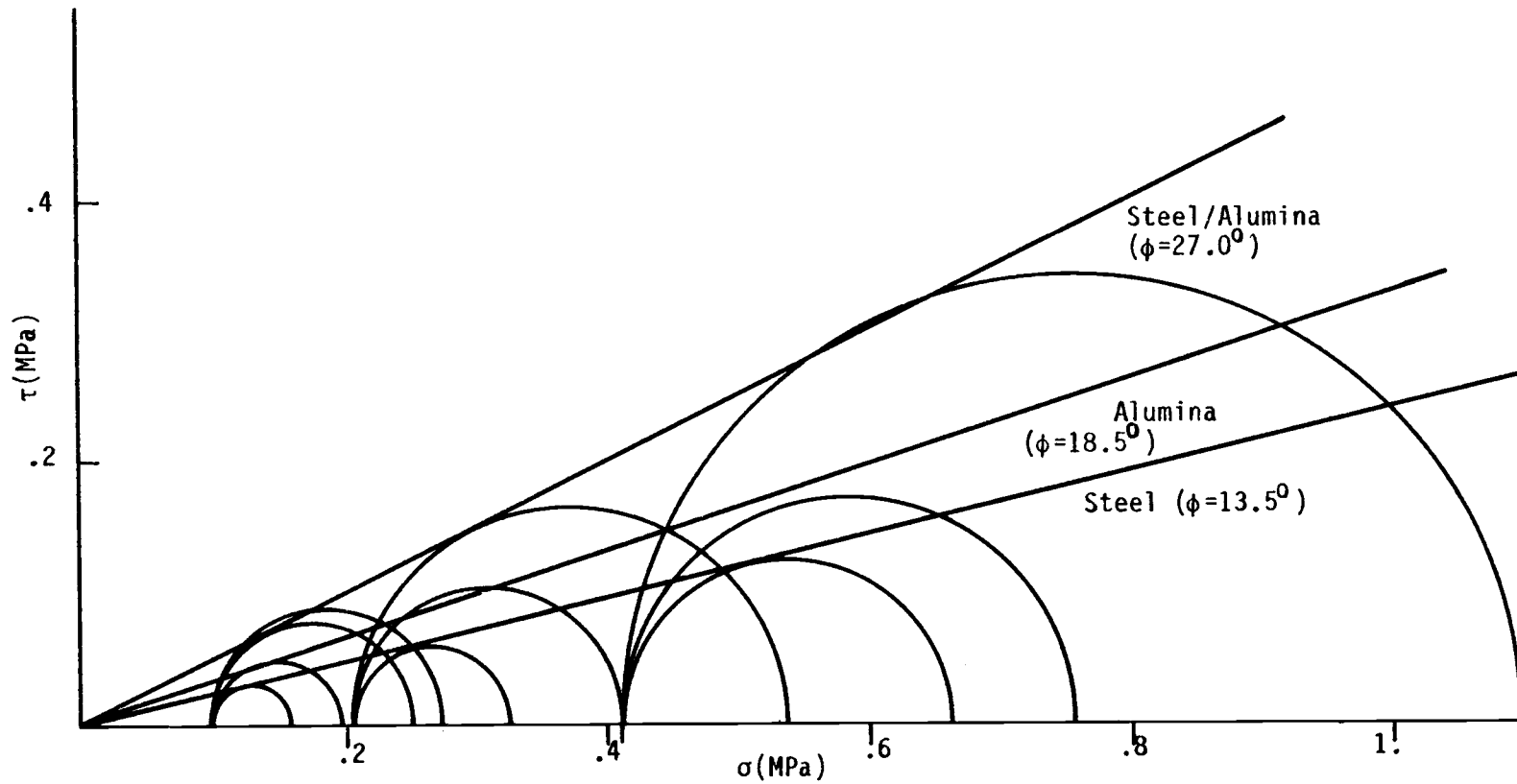


FIGURE B.3. Mohr-Coulomb Envelopes for Triaxial Compression Tests on Sphere Arrays

APPENDIX C  
DERIVATIONS OF SELECTED EQUATIONS

## DERIVATIONS OF SELECTED EQUATIONS

Equation 3.7 - The sphere surface area inside one-half of a unit cell is given by

$$A(\beta) = \int_{-\beta}^{\beta} \int_{-\omega(\theta_1)}^{\omega(\theta_1)} R^2 \cos \theta_2 d\theta_2 d\theta_1 \quad \text{C.1}$$

where the coordinates  $\theta_1$  and  $\theta_2$  are as shown in Figure C.1. From geometry, the range on  $\theta_2$  ( $\pm\omega$ ) is given by

$$\tan[\omega(\theta_1)] = \cos\theta_1 \tan\beta \quad \text{C.2}$$

Then integrating Equation C.1 once and substituting Equation C.2 gives

$$A(\beta) = 2R^2 \int_{-\beta}^{\beta} \sin[\tan^{-1}(\cos\theta_1 \tan\beta)] d\theta_1 \quad \text{C.3}$$

Finally, by symmetry

$$A(\beta) = 4R^2 \int_0^{\beta} \sin[\tan^{-1}(\cos\theta_1 \tan\beta)] d\theta_1 \quad \text{C.4}$$

Equation 3.8 - The solid volume of one half a unit cell is

$$V_S = \frac{4\pi R^3}{3CN} \quad \text{C.5}$$

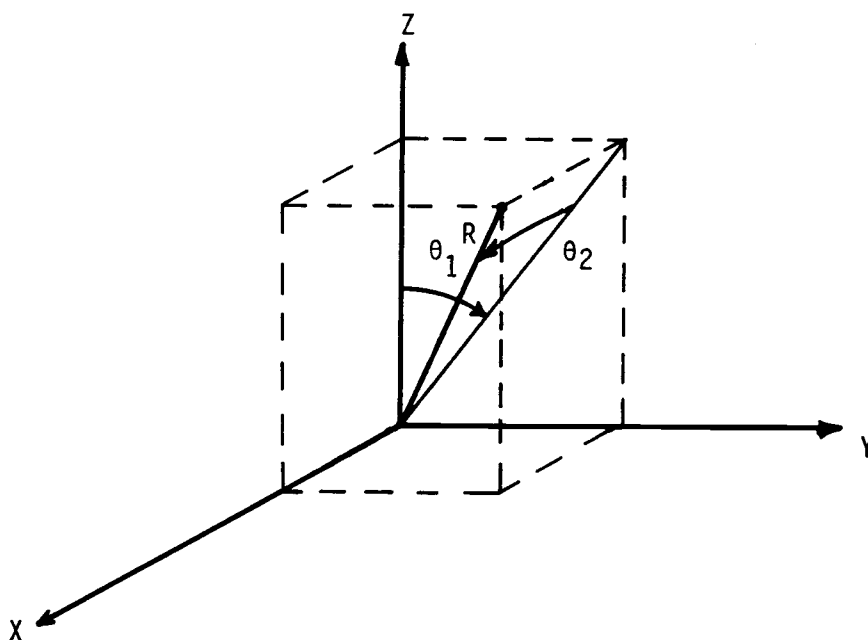


FIGURE C.1. Coordinate System for Derivation of Equation 3.7

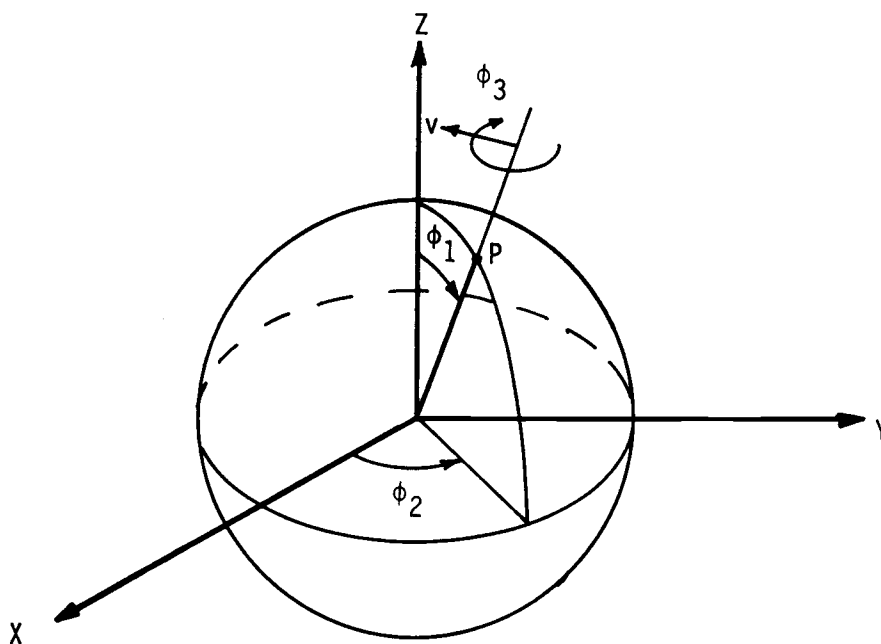


FIGURE C.2. Coordinate System for Derivation of Equation 3.12

where CN is the coordination number. The volume of one half a unit cell is the volume of a pyramid and is given by

$$V_T = \frac{1}{3} s^2 R \quad \text{C.6}$$

The side length S is

$$s = 2R \tan \beta \quad \text{C.7}$$

Then the packing factor can be obtained from

$$pf = V_S / V_T = \frac{\pi}{CN \tan^2 \beta} \quad \text{C.8}$$

Equation 3.12 - The various cell orientations can be represented by vectors tangent to the surface of a unit sphere as shown in Figure C.2. The point P defines the coordinates  $\phi_1$  and  $\phi_2$  and the direction of vector  $\vec{v}$  defines  $\phi_3$ . For each element of surface area of the unit sphere, the coordinate  $\phi_3$  can take on all values between 0 and  $2\pi$ . Equating the integrated value of the average incremental strain energy to the integrated incremental strain energy gives

$$\int_0^{2\pi} \int_0^{2\pi} \int_0^{\pi} dh^0 \sin \phi_1 d\phi_1 d\phi_2 d\phi_3 = \int_0^{2\pi} \int_0^{2\pi} \int_0^{\pi} dh(\phi_1, \phi_2, \phi_3) \sin \phi_1 d\phi_1 d\phi_2 d\phi_3$$

C.9

Then assuming  $dh^0$  is independent of the orientation, the average strain energy is

$$dh^0 = \frac{1}{8\pi^2} \int_0^{2\pi} \int_0^{2\pi} \int_0^\pi dh \sin\phi_1 d\phi_2 d\phi_3 \quad C.10$$

Equation 3.21 - To establish Equation 3.16 for an orthotropic unit cell it is helpful to use matrix notation rather than tensor notation since so many of the components of  $D_{ijkl}$  are zero. Vectors and matrices with an overbar are referenced to the fixed coordinate system and those without are referenced to the rotating coordinate system attached to the unit cell. The unit cell stress strain relation can be written as

$$\{d\epsilon\} = [D]\{d\sigma\} \quad C.11$$

and the incremental strain energy is given by

$$dh = \{\sigma\}^T \{d\epsilon\} = \{\sigma\}^T [D] \{d\sigma\} \quad C.12$$

Denote the tensor equivalent of  $\{\sigma\}$  by  $[\sigma]$ . Then the stress tensor referenced to the rotating coordinate system is related to the stress tensor referenced to the fixed coordinate system by

$$[\sigma] = [a][\bar{\sigma}][a]^T \quad C.13$$

where

$$[a] = \begin{bmatrix} a_{11} & a_{12} & a_{13} \\ a_{21} & a_{22} & a_{23} \\ a_{31} & a_{32} & a_{33} \end{bmatrix}$$

and the components of  $[a]$  are the direction cosines of the rotating coordinate system axes. If the multiplication of Equation C.13 is carried out the transformation matrix for the vector representation of the stress can be obtained and is given by

$$\{\sigma\} = [q]\{\bar{\sigma}\} \quad \text{C.14}$$

where

$$[q] = \begin{bmatrix} a_{11}^2 & a_{12}^2 & a_{13}^2 & 2a_{11}a_{12} & 2a_{11}a_{13} & 2a_{12}a_{13} \\ a_{21}^2 & a_{22}^2 & a_{23}^2 & 2a_{22}a_{21} & 2a_{23}a_{21} & 2a_{23}a_{22} \\ a_{31}^2 & a_{32}^2 & a_{33}^2 & 2a_{31}a_{32} & 2a_{33}a_{31} & 2a_{33}a_{32} \\ 2a_{11}a_{21} & 2a_{22}a_{12} & 2a_{23}a_{13} & a_{12}a_{21} + a_{11}a_{22} & a_{13}a_{21} + a_{11}a_{23} & a_{13}a_{22} + a_{12}a_{23} \\ 2a_{11}a_{31} & 2a_{12}a_{32} & 2a_{13}a_{33} & a_{12}a_{31} + a_{11}a_{32} & a_{13}a_{31} + a_{11}a_{33} & a_{32}a_{13} + a_{12}a_{33} \\ 2a_{21}a_{31} & 2a_{32}a_{22} & 2a_{33}a_{23} & a_{22}a_{31} + a_{21}a_{32} & a_{23}a_{31} + a_{21}a_{33} & a_{23}a_{32} + a_{22}a_{33} \end{bmatrix}$$

Then substituting Equation C.14 into Equation C.12 gives

$$dh = \{\bar{\sigma}\}^T [q]^T [D] [q] \{\bar{\sigma}\}$$

By analogy with Equation 3.16 the compliance matrix for the isotropic aggregate is

$$[D^0] = \frac{1}{8\pi^2} \int_0^{2\pi} \int_0^{2\pi} \int_0^\pi [q]^T [D] [q] \sin\phi d\phi d\phi_2 d\phi_3 \quad C.15$$

The compliance matrix for the isotrope can be completely established if  $D_{11}^0$  and  $D_{12}^0$  are known. To obtain  $D_{11}^0$  the matrix multiplication is carried out giving

$$D_{11}^0 = \frac{1}{8\pi^2} \int_0^{2\pi} \int_0^{2\pi} \int_0^\pi (q_{11}^2 D_{11} + q_{21}^2 D_{22} + q_{31}^2 D_{33} + 2q_{11}q_{21}D_{21} + 2q_{11}q_{31}D_{31} + 2q_{21}q_{31}D_{32} + q_{41}^2 D_{44} + q_{51}^2 D_{55} + q_{61}^2 D_{66}) \sin\phi d\phi_1 d\phi_2 d\phi_3 \quad C.16$$

The components of  $[D]$  are independent of cell orientation so it is only necessary to consider the integrals of the  $q$  coefficients. Since all possible orientations of the unit cell are considered,  $q_{11}$ ,  $q_{21}$ , and  $q_{31}$  will all take on the same values over the range of integration. The integral of  $q_{11}^2$  results in

$$\frac{1}{8\pi^2} \int_0^{2\pi} \int_0^{2\pi} \int_0^{\pi} q_{11}^2 \sin\phi_1 d\phi_1 d\phi_2 d\phi_3 = \frac{1}{8\pi^2} \int_0^{2\pi} \int_0^{2\pi} \int_0^{\pi} \cos^4\phi \sin\phi_1 d\phi_1 d\phi_2 d\phi_3 = \frac{1}{5}$$

C.17

Similarly, the coefficients on  $D_{12}$ ,  $D_{23}$ , and  $D_{13}$  are equal as are those on  $D_{44}$ ,  $D_{55}$ , and  $D_{66}$ . The integration could be carried out but it is simpler to realize that if  $[D]$  is for an isotropic material then  $[D^0] = [D]$ .  $D_{11}^0$  can be expressed as

$$D_{11}^0 = \frac{1}{5} (D_{11} + D_{22} + D_{33}) + a(D_{12} + D_{13} + D_{23}) + b(D_{44} + D_{55} + D_{66})$$

C.18

where  $a$  and  $b$  are the coefficients resulting from the integration of Equation C.16.

If  $[D]$  is for an isotropic material then

$$D_{11} = D_{22} = D_{33} = 1/E$$

$$D_{12} = D_{13} = D_{23} = -\nu/E$$

$$D_{44} = D_{55} = D_{66} = 2(1-\nu)/E$$

C.19

and

$$D_{11}^0 = 1/E$$

Substituting these expressions into Equation C.18 and matching the coefficients on  $E$  and  $\nu$  gives two equations that can be solved for  $a$  and  $b$  resulting in

$$\begin{aligned} a &= 2/15 \\ b &= 1/15 \end{aligned} \tag{C.20}$$

A similar analysis can be applied to  $D_{12}^0$  giving

$$D_{11}^0 = \frac{1}{5} (D_{11} + D_{22} + D_{33}) + \frac{2}{15} (D_{12} + D_{23} + D_{13}) + \frac{1}{15} (D_{44} + D_{55} + D_{66})$$

$$D_{12}^0 = \frac{1}{5} (D_{11} + D_{22} + D_{33}) + \frac{4}{15} (D_{12} + D_{23} + D_{13}) - \frac{1}{30} (D_{44} + D_{55} + D_{66})$$

$$D_{44}^0 = 2 (D_{11} - D_{12})$$

C.19

Equation 3.28 - The surface area of one side of the unit cell octahedron is (see Figure C.3)

$$A = \frac{1}{2} s R / \cos \beta = R^2 \sin \beta / \cos^2 \beta \tag{C.22}$$

The area of the exposed sphere material on one side of the octahedron is approximated by the area of the triangle ABC and is given by

$$A_S = \frac{1}{2} s_s R = R^2 \sin \beta \tag{C.23}$$

The ratio of the areas is then

$$A/A_S = 1/\cos^2 \beta \tag{C.24}$$

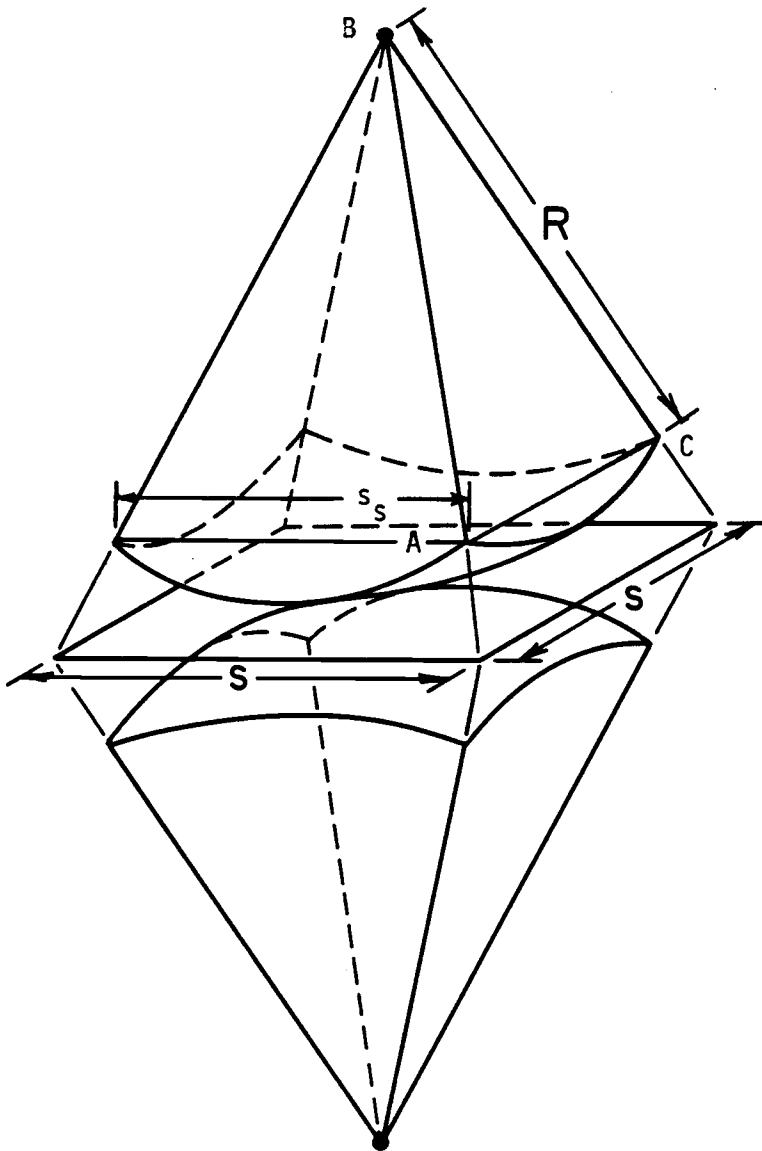


FIGURE C.3. Random Sphere Array Unit Cell

and the ratio of the projected areas onto the orthongonal coordinate planes is the same as that given in Equation C.24.

Equations 3.40 - Using Equation C.22 the projected areas in the x and z directions of one side of the octahedron are

$$\begin{aligned}
 A_x &= A \cos \beta = R^2 \tan \beta \\
 \text{and } A_z &= A \sin \beta = R^2 \tan^2 \beta
 \end{aligned}
 \tag{C.25}$$

The total projected area in the x-direction is from two sides of the octahedron and in the z-direction is from four sides of the octahedron giving Equations 3.40.

Equation 3.43 - The only nonzero terms in  $[D_{CN}]$  are multiplied by  $A_z$ . The coefficient on  $[D_{CN}]$  is therefore

$$A_{CN} = \frac{A_z^2}{VR} \tag{C.26}$$

Substituting Equations 3.40, C.6 and C.7 gives

$$A_{CN} = \frac{16R^4 \tan^4 \beta}{8R^2 \tan^2 \beta R^2} = 6 \tan^2 \beta \tag{C.27}$$

The volume of the solid body portion of the unit cell is

$$V_s = V_{\text{sphere}} - \frac{2}{3} \pi R^3 (1 - \cos \beta)^2 (2 + \cos \beta) \tag{C.28}$$

where  $V_{\text{sphere}}$  is the sphere volume in the unit cell. Then from Equations 3.42, C.24, C.6, C.7, and C.8, the coefficient on  $[D_m]$  is

$$\begin{aligned}
 A_m &= \left[ \frac{V_{\text{sphere}}}{V} - \frac{2\pi R^3 (1 - \cos\beta)^2 (2 + \cos\beta) 3}{3 R^3 8R^2 \tan^2\beta} \right] \frac{1}{\cos^4\beta} \\
 &= \frac{1}{\cos^4\beta} \left[ \text{pf} - \frac{\pi}{4} \frac{(1 - \cos\beta)^2 (2 + \cos\beta)}{\tan^2\beta} \right]
 \end{aligned}
 \tag{C.29}$$

Equation 5.38 - It is required to find a two-point quadrature formula that integrates terms of the form  $a + b\lambda^{-1/3}$  exactly. The base points are arbitrarily chosen as .1 and .9 times the integration interval. The quadrature formula is of the form

$$\int_{z_1}^{z_2} f(z) dz = w_1 f(.1(b-a)) + w_2 f(.9(b-a))
 \tag{C.30}$$

Without loss of generality it may be assumed that  $z_1=0$  and  $z_2=1$  since any limits can be reduced to these by an appropriate change of variables. The weighting factors  $w_1$  and  $w_2$  are chosen so that each of the required terms is integrated exactly. This gives two equations for  $w_1$  and  $w_2$ .

$$\int_0^1 a dz = a = w_1 a + w_2 a$$

C.31

$$\int_0^1 b z^{-1/3} dz = 1.5b = w_1 b(.1)^{-1/3} + w_2 b(.9)^{-1/3}$$

Solving Equations C.31 for the  $w_1$  and  $w_2$  gives

$$w_1 = .4149993$$

$$w_2 = .5850007$$

C.32